Electronic Theses and Dissertations

Theses, Dissertations, and Major Papers

1-1-2006

On the origins of NMR interaction tensors: Observations and theoretical models.

Cory M. Widdifield
University of Windsor

Follow this and additional works at: https://scholar.uwindsor.ca/etd

On the Origins of NMR Interaction Tensors:

Observations and Theoretical Models

By

Cory M. Widdifield

A Thesis
Submitted to the Faculty of Graduate Studies and Research
through Chemistry and Biochemistry
in Partial Fulfillment of the Requirements for the
Degree of Master of Science at the
University of Windsor

Windsor, Ontario, Canada

2006

© 2006 Cory M. Widdifield

Canada

Abstract

Solid-state NMR experiments are conducted on four linear polymeric alkali-metal metallocenes: CpK, Cp*K, CpNa, and a mixed CpNa/CpNa·THF sample. QCPMG is applied in order to observe broad and highly unreceptive ^{39}K NMR signals. *Ab Initio* studies are used to correlate observed NMR parameters to molecular structure. Discussion of temperature-dependent structural changes in CpK is also provided.

Echo experiments are used to acquire ^{23}Na NMR signals of the polymeric sodium species. NMR parameters are associated with molecular structure. The crystal structure of CpNa·THF is proposed. Literature ^{23}Na NMR data on CpNa, along with VT pXRD experiments and *Ab Initio* studies, allow for comments upon the motion of the metal atom in CpNa.

Using modern DFT, accounts of the CS tensor parameters for several simple molecules ($\underline{C}_2H_4$, $H\underline{F}$, $\underline{P}F_3$, and $H_2\underline{O}$; an underline represents the observe nucleus) are presented. Group theory techniques are applied for the first time to determine which MOs are symmetry-allowed to contribute to paramagnetic CS. In addition, a few literature accounts are revisited.

Acknowledgements

I would like thank Prof. Robert W. Schurko for giving me the opportunity to work in his lab for the last four years (two as an undergraduate student and two as a graduate). Although the size of the group increased from 3 to 10 over the course of my tenure, his door remained open and he was always there to help me along with things when I got myself stuck.

I would like to thank all the other members of my committee: Profs. C. L. B. Macdonald and T. J. Reddish for attending my defense and reading through my thesis, as well as the chair, Prof. J. Wang.

While a member of this group, I met a handful of people whom I would like to recognize in some form or another for their helpful discussions pertaining to NMR or a variety of other subjects. First, "the undergrads": Andre Sutrisno, Bryan Lucier, Graham Briscoe, Jenna Pawlowski and Josh Mutus and second "the grads": Andy Lo, Joel Tang, Aaron Rossini and Hiyam Hamaed.

I also acknowledge Prof. C. L. B. Macdonald, who, in some respects, acted in the capacity of "pseudo-advisor." He provided guidance in several areas, ranging from synthesis to crystal structure determination to feedback regarding the temperature-dependent structural models that were considered by me and Rob.

I would like to extend an additional thank you to Dr. Ivan Hung (Warwick), who taught me the majority of what I learned about NMR (and Kajira) while I was an undergraduate. Lastly, I would like to thank my family (Mom, Dad, Tim) for paying my way through University and letting me stay at home (rent free too!) for as long as they have.

Statement of Originality

I certify that this thesis, and the research to which it refers, are the product of my own work, and that any ideas or quotations from the work of other people, published or otherwise, are fully acknowledged in accordance with the standard referencing practices of the discipline. I acknowledge the helpful guidance and support of my supervisor, Professor Robert W. Schurko.

Chapter 2 of this thesis is based on the following publication:

C. M. Widdifield and R. W. Schurko. A Solid-State ^{39}K and ^{13}C NMR Study of Polymeric Potassium Metallocenes. J. Phys. Chem. A., 2005, 109, 6865-6876; DOI: 10.1021/jp0580591.

Contents

List of Tables

List of Figures

-xvi-

List of Abbreviations

2D	two-dimensional
ADF	Amsterdam Density Functional
AO	atomic orbital (plural: AOs)
B3LYP	Becke's three parameter hybrid functional using the correlation functional of Lee, Yang, and Parr
BLYP	Becke's exchange functional with the correlation functional of Lee, Yang, and Parr
CI	configuration interaction
CP	cross-polarization
Cp	cyclopentadienyl ligand, $C_5H_5^-$
Cp*	pentamethylcyclopentadienyl ligand, $C_5Me_5^-$
Cp$'$	cyclopentadienyl ligand of variable configuration
Cp$_{cent}$	geometric centre point of cyclopentadienyl ring
CS	chemical shielding
CSA	chemical shielding anisotropy
CT	central-transition
DFS	double-frequency sweep
DFT	density-functional theory
DZ	double-zeta
ECMO	embedded cluster molecular orbital

EFG	electric field gradient (plural: EFGs)
Et	ethyl group, $C_2H_5^-$
FO	fragment orbital
FT	Fourier transform
GooF	goodness of fit
GIAO	gauge-including atomic orbitals
HB	Herzfeld-Berger
*i*Pr	isopropyl group, $i\text{-}C_3H_7^-$
IR	infrared spectroscopy
KS	Kohn and Sham
M	alkali (group IA) metal atom
MAS	magic-angle spinning
MCHF	multiconfiguration Hartree-Fock
Me	methyl group, CH_3^-
MG	Meiboom-Gill
MO	molecular orbital (plural: MOs)
MQ	mulitple-quantum
NMR	nuclear magnetic resonance
occ	occupied molecular orbital
o.d.	outer diameter
OPBE	exchange functional of Cohen and Handy with correlation functional of Perdew, Burke and Ernzerhof

OPTX	exchange functional of Cohen and Handy
PAS	principal axis system
PBE	correlation functional of Perdew, Burke and Ernzerhof
ppm	parts per million
pXRD	powder X-ray diffraction
QCPMG	quadrupolar Carr-Purcell Meiboom-Gill
QM	quantum mechanical
RAPT	rotor-assisted population-transfer
RMS	root-mean-square
rf	radiofrequency
RHF	restricted Hartree-Fock
SCF	self-consistent field
S/N	signal-to-noise
SSNMR	solid-state nuclear magnetic resonance
STO	Slater-type orbital
tBu	t-butyl group, t-$C_4H_9^-$
THF	tetrahydrofuran, C_4H_8O
TMEDA	tetramethylethylenediamine, $C_6H_{16}N_2$
TMS	tetramethylsilane, $SiMe_4$
TZ	triple-zeta
vir	unoccupied (virtual) molecular orbital
VT	variable-temperature

WTBS   well-tempered basis set

XRD   X-ray diffraction

ZORA   zeroth-order regular approximation

List of Symbols

$\leftrightarrow$	molecular orbital mixing
$\hat{1}$	identity operator
A	double-frequency sweep adiabaticity
$\alpha_c, \beta_c, \gamma_c$	crystallographic unit cell angles
$\alpha_e, \beta_e, \gamma_e$	Euler angles
$\lvert \alpha \rangle, \lvert \beta \rangle$	nuclear spin eigenstate labels
γ	magnetogyric ratio
ΔE	energy difference between two eigenstates
Δ_{pc}	greatest difference between principal component values
δ	chemical shift parameter
δ_{Cp}	isotropic chemical shift of cyclopentadienyl ring carbon atom
δ_{ij}	general chemical shift tensor matrix element
δ_{ij}^{KD}	Krönecker delta function
δ_{iso}	isotropic chemical shift parameter
$\delta_{iso, ref}$	isotropic chemical shift value of a well-characterized sample
δ_{Me}	isotropic chemical shift of methyl carbon atom
$\tilde{\delta}$	frame independent chemical shift tensor
δ_r	reduced anisotropy
$\tilde{\delta}_{solids}$	chemical shift tensor in Cartesian frame of a molecule
$\tilde{\delta}_{solids}^{PAS}$	chemical shift tensor in shift principal axis system
$\delta_{11}, \delta_{22}, \delta_{33}$	principal components of the chemical shift tensor

η^5	bonding interaction with hapticity of five.
η_Q	electric field gradient tensor asymmetry parameter
θ	angle between interaction principal axis system and external magnetic field or the "magic-angle"
κ	chemical shift tensor skew parameter
λ	double-frequency sweep rate
ν_0	spin precession (Larmor) frequency (units of s^{-1})
ν_1	spin precession about the magnetic field associated with an on-resonance radiofrequency pulse
ν_Q	quadrupolar frequency (units of s^{-1})
ν_{iso}	isotropic nuclear spin precession frequency (units of s^{-1})
$\nu_{iso,ref}$	isotropic nuclear spin precession frequency of a well-characterized sample (units of s^{-1})
ν_{off}	offset frequency
ν_{rot}	magic-angle spinning sample rotation frequency
$\rho_{|\alpha\rangle}$	spin state population of eigenstate α
$\rho_{|\beta\rangle}$	spin state population of eigenstate β
$\sigma_{11}, \sigma_{22}, \sigma_{33}$	principal components of the chemical shielding tensor
σ	chemical shielding parameter
σ^d	diamagnetic chemical shielding parameter
σ_{ij}^d	general diamagnetic chemical shielding tensor matrix element
σ^p	paramagnetic chemical shielding parameter

-xxix-

σ_{ij}^{p}	general paramagnetic chemical shielding tensor matrix element
σ_{ij}	general chemical shielding tensor matrix element
σ_{iso}	isotropic chemical shielding value
σ_{iso}'	scaled isotropic chemical shielding value
$\sigma_{iso, ref}$	isotropic chemical shielding value of a well-characterized sample
$\tilde{\sigma}_{solids}$	chemical shielding tensor in Cartesian frame of a molecule
$\tilde{\sigma}_{solids}^{PAS}$	chemical shielding tensor in shielding principal axis system
$\sigma_{xx}, \sigma_{yy}, \sigma_{zz}$	principal components of the chemical shielding tensor, Haeberlen convention
$\hat{\sigma}_{X}$	Pauli spin operator, x-component
$\hat{\sigma}_{Y}$	Pauli spin operator, y-component
$\hat{\sigma}_{Z}$	Pauli spin operator, z-component
$\sigma_{\parallel}$	chemical shielding tensor principal component parallel to bond axis
$\sigma_{\perp}$	chemical shielding tensor principal component perpendicular to bond axis
$\tau_1, \tau_2, \tau_3, \tau_4$	experiment delay periods
τ_a	NMR signal acquisition time
τ_p	radiofrequency pulse duration
τ_{rapt}	rotor-assisted population-transfer delay period
μ	value of a nuclear spin magnetic moment
$\boldsymbol{\mu}$	nuclear spin magnetic moment
$\boldsymbol{\mu}_i$	nuclear spin magnetic moment of particle i
φ_p	radiofrequency pulse phase

$\varphi(\mathbf{r})$	Slater-type orbital function
$\varphi_\mu(\mathbf{r}, \mathbf{B}_0)$	gauge-including Slater-type orbital function
ψ_0	ground-state wave function
ψ_a, ψ_b	generic single-electron wave functions (reserved for mixing)
ψ_k	spatial portion of a one-electron wave function
ψ_n	excited-state wave function
ψ_p	generic single-electron wave function
ω_0	spin precession (Larmor) frequency (units of rad s^{-1})
ω_{rf}	radiofrequency pulse frequency (units of rad s^{-1})
ω_Q	quadrupolar frequency (units of rad s^{-1})
Ω	chemical shielding/shift tensor span
a_i, b_i	generic weighting coefficients
a, b, c	crystallographic unit cell lengths
$|A\rangle$	generic basis state
$\mathbf{B}_0$	constant external magnetic field
B_0^z	external magnetic field, z-component
$\mathbf{B}_1$	magnetic field associated with radiofrequency pulse
$\mathbf{B}_{eff}$	effective magnetic field
$\mathbf{B}_{ind}$	magnetic field induced by the external magnetic field
$\mathbf{B}_{nuc}$	magnetic field at the nucleus
$C_4(I, m)$	multiple-quantum magic-angle spinning parameter relating the central- and symmetric multiple-quantum transitions

C_Q	nuclear quadrupolar coupling constant
E_0	eigenvalue associated with ground electronic state
E_n	eigenvalue associated with excited electron state
$E_{XC}[\rho]$	electron exchange and correlation functional
e	electric charge of a proton
F_o	experimentally observed structure factor
F_w	formula weight
$\hbar$	the Planck constant (units of J s rad^{-1})
h, k, l	Miller indices
$\hat{\mathcal{H}}_{1,e}$	internal one-spin electronic Hamiltonian
$\hat{\mathcal{H}}_{1,m}$	internal one-spin magnetic Hamiltonian
$\hat{\mathcal{H}}_{2,e}$	internal two-spin electronic Hamiltonian
$\hat{\mathcal{H}}_{2,m}$	internal two-spin magnetic Hamiltonian
$\hat{\mathcal{H}}_{CS}^{iso}$	isotropic chemical shielding Hamiltonian
$\hat{\mathcal{H}}_{CS}^{solids}$	chemical shielding Hamiltonian for solid-state samples
$\hat{\mathcal{H}}_{D}$	direct dipole-dipole coupling Hamiltonian
$\hat{\mathcal{H}}_{e}$	total electronic Hamiltonian
$\hat{\mathcal{H}}_{e-ext}$	electronic Hamiltonian due to external interactions
$\hat{\mathcal{H}}_{int}$	total internal Hamiltonian
$\hat{\mathcal{H}}_{J}$	indirect dipole-dipole coupling Hamiltonian
$\hat{\mathcal{H}}_{m}$	total magnetic Hamiltonian
$\hat{\mathcal{H}}_{m-ext}$	magnetic Hamiltonian due to external interactions

-xxxii-

$\hat{\mathcal{H}}_Q$	quadrupolar Hamiltonian
$\hat{\mathcal{H}}_{rf}(t)$	time-dependent radiofrequency Hamiltonian
$\hat{\mathcal{H}}_{spin}$	total spin Hamiltonian
$\hat{\mathcal{H}}_{SR}$	spin-rotation Hamiltonian
$\hat{\mathcal{H}}_Z$	Zeeman Hamiltonian
$\mathbf{I}$	nuclear spin angular momentum vector
$\hat{\mathbf{I}}$	nuclear spin angular momentum operator
I	nuclear spin quantum number
$\hat{I}_X$	spin angular momentum operator, x-component
$\hat{I}_Y$	spin angular momentum operator, y-component
$\hat{I}_Z$	spin angular momentum operator, z-component
J	indirect dipolar interaction constant
k	chemical shielding scaling factor
k_B	Boltzmann constant
$\hat{L}_{ki}$	i-component orbital angular momentum operator (about gauge origin)
$\hat{L}_{Nkj}$	j-component orbital angular momentum operator (about nucleus)
$\hat{L}_y$	component orbital angular momentum operator, y-component
$\hat{L}_z$	component orbital angular momentum operator, z-component
$\mathbf{M}$	bulk nuclear spin magnetic moment or magnetization
m	nuclear spin angular momentum quantum number
m_e	electron mass value
Q	nuclear electric quadrupole moment

R_1, wR_2	residual factors
$\hat{R}_z, \hat{R}_{y'}, \hat{R}_{z''}$	set of rotational operators used for inter-coordinate system transformations
$\hat{R}_x, \hat{R}_y, \hat{R}_z$	set of rotational operators used in molecular orbital transformations
$\hat{R}_n$	rotational operator, n-axis
r_{NK}	electron-nucleus distance
S'	coordinating solvent
T_1	spin-lattice relaxation parameter
T_2	spin-spin relaxation parameter (pure molecular)
T_2^*	spin-spin relaxation parameter (inhomogeneous)
$\tilde{V}_{EFG}$	electric field gradient tensor in Cartesian frame of a molecule
$\tilde{V}_{EFG}^{PAS}$	electric field gradient tensor in electric field gradient principal axis system
V_{11}, V_{22}, V_{33}	principal components of the electric field gradient tensor
V_{ij}	general element of an electric field gradient tensor
X	generic dilute nucleus
Z	number of formula units in crystallographic unit cell

Chapter 1

Introduction to Nuclear Magnetic Resonance

1.1 Initial Observations

The phenomenon of nuclear magnetic resonance (NMR) was first observed in a beam of LiCl molecules in 1937 and was proposed as an alternative method for determining the value of a nuclear spin magnetic moment (μ).[1] Although initial attempts at applying the resonance technique to bulk materials failed,[2,3] technical improvements led to two research groups observing bulk NMR in early 1945.[4,5] By 1951, better experimental resolution allowed for the observation that resonance values were often sample-dependent.[6-10] This "sample-dependent shift" was later termed the chemical shift (δ), which is the parameter most often associated with NMR experiments. Today, NMR is employed in many scientific fields to determine and elucidate a range of atomic and molecular properties and processes.[11] This thesis highlights the usefulness of solid-state NMR (SSNMR), especially when coupled with other methodologies such as X-ray diffraction (XRD) and *ab initio* calculations. Several alkali-metal metallocene systems are characterized in detail using the above methods. Group symmetry techniques are used to discuss the chemical shielding observed in simple molecules, with applications to relevant solids.

1.2 Physical Background

The spin physics which governs NMR has been outlined in detail in a number of

-1-

sources[12-15] and anything beyond the most elementary items is considered to be beyond the scope of this text. Specific theoretical background discussions will also be included within each topic, as required.

1.2.1 The Classical Motion of Isolated† Nuclear Spins

A nucleus which possesses non-zero nuclear spin angular momentum (represented vectorially with I) will also have a nuclear spin magnetic moment (μ), as the two quantities are linearly related through the magnetogyric ratio (γ), with $\mu = \gamma I$. Using a classical vector model, both quantities can be pictured as in Figure 1.1.

γ is positive γ is negative
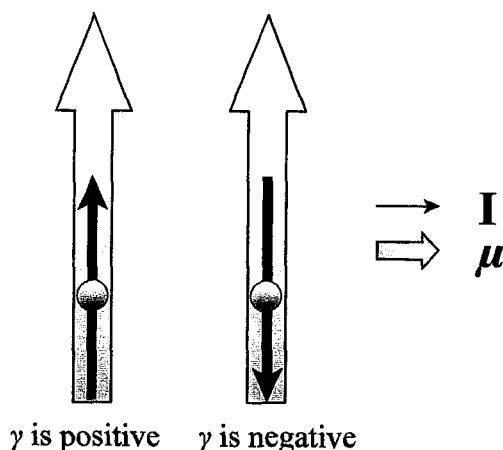
Figure 1.1 Vector representation of the nuclear spin angular momentum (I) and nuclear spin magnetic moment (μ). If the two vectors are collinear, then the magnetogyric ratio (γ) is positive and if they are antiparallel, γ is negative.

If a diamagnetic sample is outside of an external magnetic field, the individual μ's point along any spatial direction (i.e., a random distribution) and a bulk nuclear spin

---

† Isolated will mean a nuclide which is interacting with, at most, a constant external magnetic field (B_0).

-2-

magnetic moment (**M**) does not arise. When an ensemble of nuclear spins experience a

constant external magnetic field (**B**$_0$), contrary to popular belief,[16] there is no reorientation

of the magnetic moments of the individual spins into $I + \frac{1}{2}$ spatial eigenstates, where I is the

nuclear spin quantum number. Rather, they begin to precess about the applied field. The

sense of rotation is determined by the sign of the magnetogyric ratio (Figure 1.2).

γ is positive γ is negative
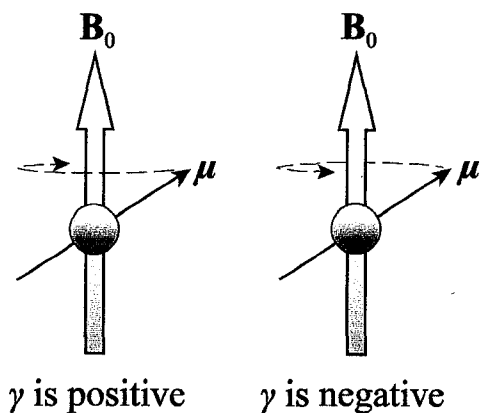
Figure 1.2 Precession about **B**$_0$ may be either clockwise ($\gamma > 0$) or counterclockwise ($\gamma < 0$).[15]

The frequency of precession (the Larmor frequency, ω_0) for a given nuclide is simply

the negative of the product of the magnetogyric ratio and magnetic field strength, as

$\omega_0 = -\gamma \mathbf{B}_0$. Note that ω_0 is in units of rad s^{-1}, so in order to determine the value in Hz (v_0),

this value must be divided by 2π.

1.2.2 Nuclear Spin Interactions

The preceding section used a classical vector model to present the motion of an

isolated nuclear spin when it interacts with an external magnetic field (it is traditionally

assumed that **B**$_0$ lies along the z-axis). This section uses quantum mechanics to determine

-3-

the nuclear spin state eigenvalues (i.e., energy levels) for both the isolated scenario and when the nuclear spin is coupled to additional items.

1.2.2.1 Coupling to an External Magnetic Field

Although the quantum-mechanical (QM) treatments for spin angular momentum and orbital angular momentum are similar,[17,18] they should not be thought of in the same sense. Spin angular momentum is usually described as an intrinsic property of the electron and many nuclides, which contrasts with the conventional descriptions of orbital angular momentum. When an isolated nuclear spin of arbitrary I value is subjected to $\mathbf{B_0}$, $2I + 1$ energy eigenstates are possible. Quite often, these are referred to as Zeeman (or hyperfine) eigenstates. The case where $I = \frac{1}{2}$ is treated in a number of introductory texts[19-22] and will serve as the starting point. The eigenstates of nuclear spin angular momentum along the axis in which the magnetic field is applied are denoted according to the convention of Dirac:[23]

$$| \text{state} \rangle = | I, m \rangle$$

$$| \alpha \rangle = | \frac{1}{2}, +\frac{1}{2} \rangle = \begin{bmatrix} 1 \\ 0 \end{bmatrix}$$

$$| \beta \rangle = | \frac{1}{2}, -\frac{1}{2} \rangle = \begin{bmatrix} 0 \\ 1 \end{bmatrix}$$

[1.1]

where m is the nuclear spin angular momentum quantum number and α and β serve as arbitrary eigenstate labels. The Zeeman Hamiltonian ($\hat{\mathcal{H}}_z$) describes the quantum dynamics of the nuclear spin states under the conditions outlined above:

$$\hat{\mathcal{H}}_z = \hbar \omega_0 \hat{I}_z = \frac{\hbar}{2} \omega_0 \hat{\sigma}_z$$

[1.2]

-4-

with $\hat{I}_Z$ as the spin angular momentum operator along the direction of the applied field (a caret (^) will denote QM operators) and where $\hat{\sigma}_Z$ is one of the conventional Pauli Spin Operators,[24] which together with the identity operator ($\hat{1}$) form the basis of the spin space:

$$\hat{\sigma}_X = \begin{bmatrix} 0 & +1 \\ -1 & 0 \end{bmatrix} \qquad \hat{\sigma}_Y = \begin{bmatrix} 0 & -i \\ +i & 0 \end{bmatrix} \qquad \hat{\sigma}_Z = \begin{bmatrix} +1 & 0 \\ 0 & -1 \end{bmatrix} \qquad \hat{1} = \begin{bmatrix} +1 & 0 \\ 0 & +1 \end{bmatrix}$$

When the Zeeman Hamiltonian operates upon the spin states in [1.1], the relative energies of the two states are obtained:

$$\hat{\mathcal{H}}_Z |\alpha\rangle = \hbar\omega_0 \hat{I}_Z |\alpha\rangle = \frac{\hbar}{2}\omega_0 |\alpha\rangle = -\frac{\hbar}{2}\gamma \mathbf{B}_0 |\alpha\rangle \qquad [1.3]$$

$$\hat{\mathcal{H}}_Z |\beta\rangle = \hbar\omega_0 \hat{I}_Z |\beta\rangle = -\frac{\hbar}{2}\omega_0 |\beta\rangle = +\frac{\hbar}{2}\gamma \mathbf{B}_0 |\beta\rangle \qquad [1.4]$$

It is seen that two states, each depending upon the nuclear property γ and the strength of the applied magnetic field, result. Assuming a constant value for γ, the energy separation between these two states increases with increasing magnetic field strength (Figure 1.3):
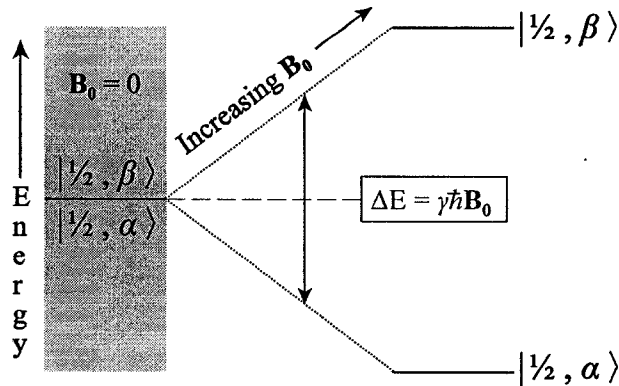
Figure 1.3 When a nuclear spin experiences $\mathbf{B}_0$, the spin-states, $|\alpha\rangle$ and $|\beta\rangle$, lose their degeneracy. The number of states formed is equal to $(2I + 1)$ and the energy difference between adjacent spin-states is $\gamma\hbar\mathbf{B}_0$. The case illustrated above is for nuclides possessing $I = \frac{1}{2}$ and $\gamma > 0$. If $\gamma < 0$, $|\beta\rangle$ would be lower in energy.

-5-

As hinted at earlier when using a classical vector model to describe the motion of an isolated nuclear spin, a given nuclear spin is not restricted to being either "pure $| \alpha \rangle$" or "pure $| \beta \rangle$", rather, they are usually found in a superposition of those two states:

$$| A \rangle = a_i | \alpha \rangle + b_i | \beta \rangle \qquad \qquad \textbf{[1.5]}$$

where a_i and b_i are generic weighting coefficients. The above process may also be utilized to determine the eigenstates for nuclides where $I \neq \frac{1}{2}$, in each case leading to $2I + 1$ states (Figure 1.4):
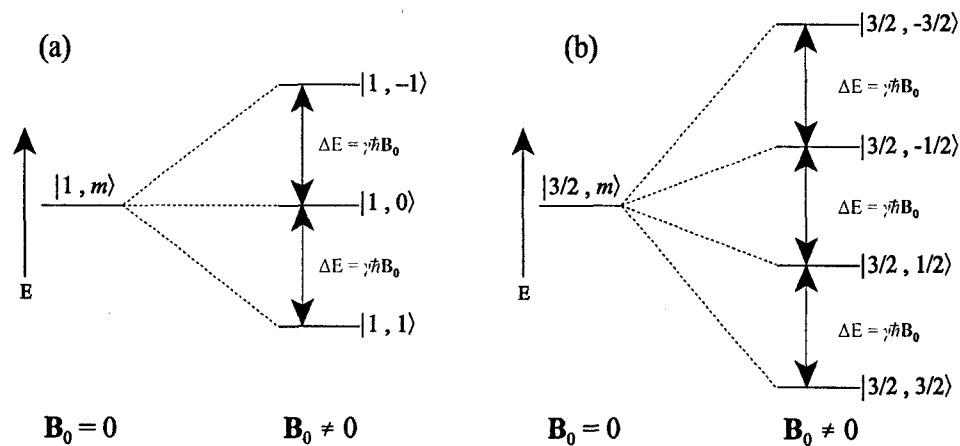
Figure 1.4 Nuclear spin state energy levels for the cases where (a) a spin-1 nuclide and (b) a spin-3/2 nuclide are coupled to B_0 (γ is taken as positive).

1.2.2.2 Thermal Equilibrium Populations

Although preceding discussions were often presented using a single nuclear spin, NMR spectroscopy requires the presence of an ensemble of spins. For the case where $I = \frac{1}{2}$ and $\gamma > 0$, the population of eigenstate α $(\rho_{| \alpha \rangle})$ is given according to a Boltzmann distribution:[20]

$$\rho_{| \alpha \rangle} = \rho_{| \beta \rangle} \exp \{ -\hbar \omega_0 / k_B T \} \qquad \qquad \textbf{[1.6]}$$

where $\rho_{|\beta\rangle}$ is the population of eigenstate β and k_B is the Boltzmann constant. Relative to other types of spectroscopy, in NMR the energy separation between adjacent eigenstates is small, leading to very similarly populated states and hence low experimental sensitivity.

1.2.2.3 Response to Radiofrequency (rf) Pulses

The bulk nuclear spin magnetic moment (or magnetization, **M**) is determined by summing the individual nuclear spin magnetic moments (μ_i), i.e., $\mathbf{M} = \sum \mu_i$. When the α state is preferentially populated, it is said that **M** points along the applied field and when the β state is preferentially populated, **M** points anti-parallel to the applied field.

The NMR signal of a nuclide under study is typically prepared (i.e., transformed into a state which is measurable) by applying an oscillating rf pulse. This rf pulse produces its own magnetic field (**B₁**), which is considerably smaller in magnitude than **B₀**. When the frequency of the oscillating pulse (ω_{rf}) matches ω_0 ("on-resonance"), the large external magnetic field is, in effect, removed, leaving only **B₁** to interact with the ensemble of nuclear spins. As a result, **M** will precess about the **B₁** axis with a frequency ν_1 (Figure 1.5a). As long as $\omega_0 \approx \omega_{rf}$, **M** will interact with the applied field and precess about **B**$_{eff}$ (Figure 1.5b):

$$\mathbf{B}_{eff} = (\mathbf{B}_0 + \omega_{rf}/\gamma) + \mathbf{B}_1 \tag{1.7}$$

The degree of precession is determined by **B₁** and the duration of the pulse applied (the pulse width, τ_p) The on-resonance time-dependent rf Hamiltonian ($\hat{\mathcal{H}}_{rf}(t)$) is provided below:[24]

$$\hat{\mathcal{H}}_{rf}(t) = -\hbar\gamma\mathbf{B}_1 [\cos(\omega_{rf}t + \varphi_p)\hat{I}_X \pm \sin(\omega_{rf}t + \varphi_p)\hat{I}_Y] \tag{1.8}$$

where φ_p is the phase of the rf pulse. The Hamiltonian expressed in **[1.8]** represents the applied rf field as two circularly polarized fields: one rotates at the Larmor frequency of the

-7-

nuclide while the other rotates at $-\omega_0$. The component that interacts with **M** is clearly dependent upon the sign of γ and hence some sources suggest that **[1.8]** be multiplied by a factor of ½, as half of the applied pulse is never used.[15]

(a)

(b)

$\mathbf{B}_0$ along z

$\omega_0 = \omega_{\mathrm{rf}}$

$\omega_0 \approx \omega_{\mathrm{rf}}$
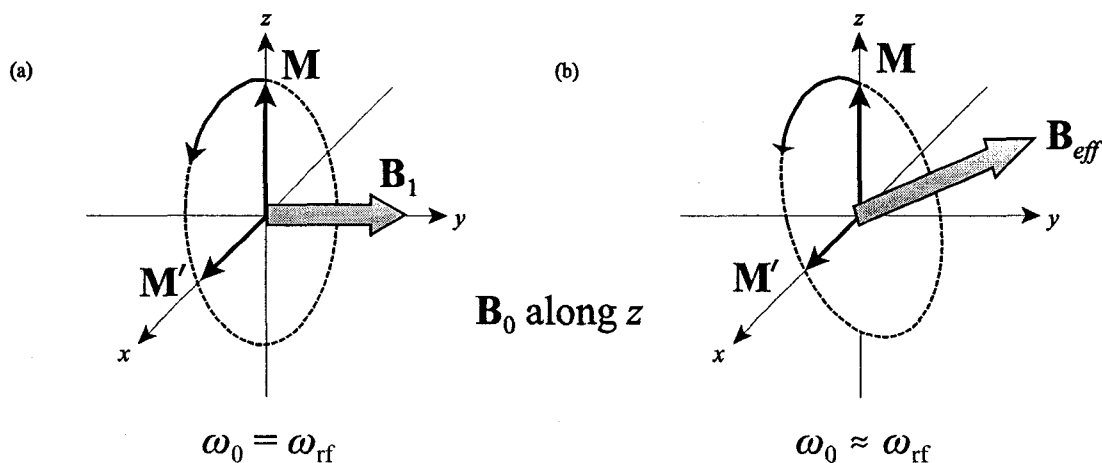
Figure 1.5 (a) If $\omega_0 = \omega_{\mathrm{rf}}$, the application of an rf pulse along the y-axis will result in **M** precessing about $\mathbf{B}_1$. (b) As long as $\omega_0 \approx \omega_{\mathrm{rf}}$, the rf pulse will still interact with **M**, but the precession will be about $\mathbf{B}_{\mathit{eff}}$, as given in **[1.7]**. If $\omega_0 \neq \omega_{\mathrm{rf}}$, **M** will not interact with the applied field and will maintain its orientation. The initial state of **M** is idealized, in that all nuclear spins find themselves in $|\alpha\rangle$.

1.2.2.4 Chemical Shielding

In addition to the two external interactions, a number of internal nuclear spin interactions exist and are measurable using NMR experiments. The chemical shielding (or chemical shift) interaction results from the coupling between the nuclear spin angular momentum and a local magnetic field which is produced by $\mathbf{B}_0$-induced electron circulation. This means that the total field experienced at the nucleus ($\mathbf{B}_{nuc}$) is not usually equal to the applied field. This effect is commonly seen when studying atoms and molecules, with the total and external fields being related through the chemical shielding parameter (σ):

-8-

$$\mathbf{B}_{nuc} = (1 - \sigma)\mathbf{B}_0 \qquad [1.9]$$

The value which σ assumes is usually very small for diamagnetic samples and is typically denoted in units of parts per million (ppm) of $\mathbf{B}_0$. Although useful from a theoretical standpoint, chemical shielding is not often measured experimentally, but rather, a chemical shift value (δ) is measured. Chemical shift values for samples in isotropic media (δ_{iso}) are expressed relative to a well-characterized sample, known as the reference:[25]

$$\delta_{iso} \equiv \frac{v_{iso} - v_{iso,ref}}{v_{iso,ref}} \qquad [1.10]$$

where v_{iso} and $v_{iso, ref}$ are the isotropic nuclear spin precession frequencies (in Hz) of the sample under study and the reference, respectively. The measured chemical shift value may be related to a chemical shielding value if an absolute shielding scale (*vide infra*) has been established for that particular element:[26]

$$\delta_{iso} = \frac{\sigma_{iso,ref} - \sigma_{iso}}{1 - \sigma_{iso,ref}} \approx \sigma_{iso,ref} - \sigma_{iso} \qquad [1.11]$$

If $\delta > 0$, then the sample under study is said to be deshielded relative to the standard and if $\delta < 0$, the sample is shielded relative to the standard. The isotropic chemical shift Hamiltonian ($\hat{\mathcal{H}}_{CS}^{iso}$) is defined as:

$$\hat{\mathcal{H}}_{CS}^{iso} = -\hbar\gamma\delta_{iso}\mathbf{B}_0\hat{I}_Z \qquad [1.12]$$

Thus, it is clear that the amount by which the chemical shift Hamiltonian alters the eigenvalue of a spin state is linearly dependent on γ and $\mathbf{B}_0$ and that the change in energy is small, based upon the usual magnitude of δ_{iso}. Due to this, the effects of $\hat{\mathcal{H}}_{CS}^{iso}$ may be treated as a perturbation upon $\hat{\mathcal{H}}_Z$ eigenstates.

-9-

1.2.2.5 The Quadrupolar Interaction

If $I \geq 1$, the electric charge of the nucleus is not distributed uniformly and the nucleus can no longer be adequately modelled using a sphere; rather, it is better described using an ellipsoid (Figure 1.6). This physical characteristic gives rise to another nuclear property, known as the nuclear electric quadrupole moment (Q), which interacts with local electric-field gradients (EFGs) of the molecule. The magnitude of this (quadrupolar) interaction is typically found to be on the order of hundreds of kHz, leaving the Zeeman interaction as the most dominant for many nuclides. The quadrupolar Hamiltonian ($\hat{\mathcal{H}}_Q$) under the first-order secular approximation is:[27]

$$\hat{\mathcal{H}}_Q = \frac{\omega_Q}{3}(3\hat{I}_z^2 - \hat{I} \cdot \hat{I}) \qquad [1.13]$$

with ω_Q representing the quadrupolar frequency. Thus, to first order, the change in energy of the Zeeman eigenstates is linearly proportional to ω_Q. In isotropic media, $\hat{\mathcal{H}}_Q$ is averaged to zero, however, the quadrupolar interaction will still contribute to nuclear spin relaxation. Efficient relaxation leads to signal broadening in frequency-domain spectra, in some cases to the point where the signal is too broad to detect.

(a)   (b)

$I = \frac{1}{2}$ $I > \frac{1}{2}$
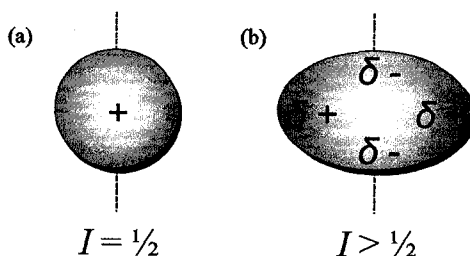
Figure 1.6 Nuclides which possess $I = \frac{1}{2}$ (a) do not interact with local electric field gradients (EFGs) as the nuclear charge is distributed spherically, but for $I > \frac{1}{2}$, (b) a non-spherical distribution of charge leads to a net electric quadrupole moment, which interacts with local EFGs.

-10-

1.2.2.6 Other Interactions and the Total Spin Hamiltonian

A number of other interactions may be observed in NMR spectra, and are mentioned at this time for completeness, but they are not focussed upon in subsequent discussions (Figure 1.7).
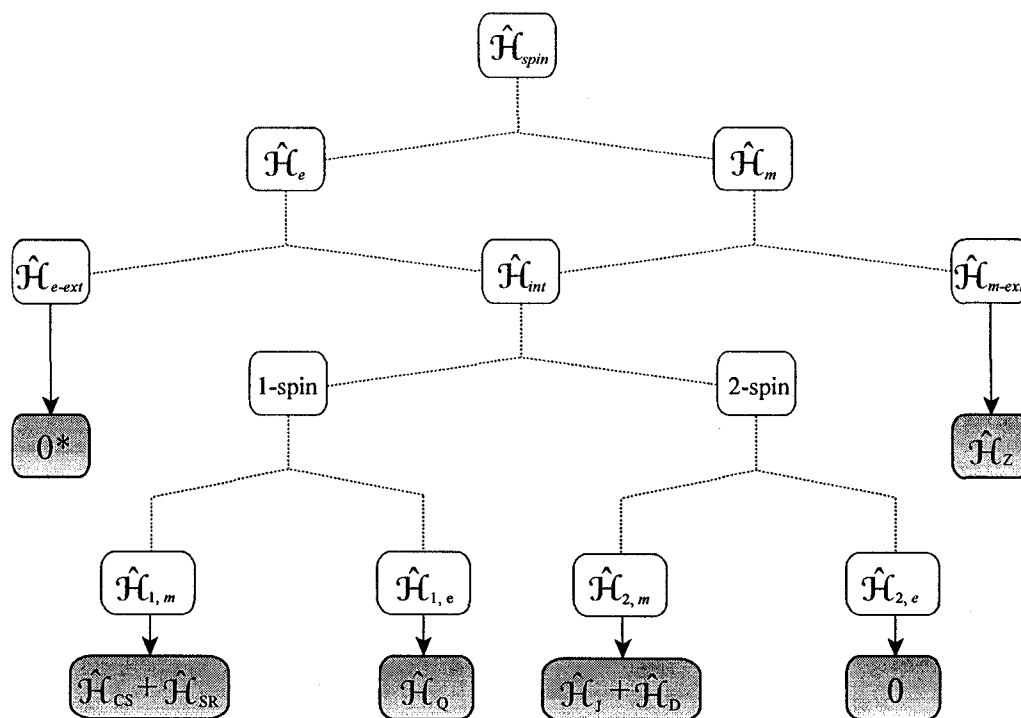
Figure 1.7 Breakdown of the total spin Hamiltonian into its contributing parts.[15] Definitions for undefined Hamiltonian terms can be found in the list of symbols. (*Diamagnetic samples)

They include: (i) the direct dipole-dipole interaction ($\hat{\mathcal{H}}_D$), which represents the coupling between the nuclear spin angular momenta of two proximate nuclei through space; (ii) the indirect (J) dipole-dipole interaction ($\hat{\mathcal{H}}_J$), which represents the coupling between the nuclear spin angular momenta of two nuclei through bonding electrons and; (iii) the spin-rotation interaction ($\hat{\mathcal{H}}_{SR}$), which represents the coupling between I and the magnetic field generated by molecular rotation. All interactions can be considered as perturbations upon

-11-

the Zeeman interaction and the total spin Hamiltonian ($\hat{\mathcal{H}}_{spin}$) is formed by taking a linear combination of all the time-independent Hamiltonian terms in the Zeeman frame:

$$\hat{\mathcal{H}}_{spin} = \hat{\mathcal{H}}_Z + \hat{\mathcal{H}}_{CS} + \hat{\mathcal{H}}_D + \hat{\mathcal{H}}_J + \hat{\mathcal{H}}_Q + \hat{\mathcal{H}}_{SR} \qquad [1.14]$$

1.2.3 Anisotropic NMR Interactions

When conducting NMR experiments upon samples which are not in isotropic media (e.g., solid-state samples), the sensitivity and resolution of the acquired spectra are expected to decrease. This is because many of the previously mentioned NMR interactions are orientation-dependent. Individual crystallites of a powder in the solid-state are oriented randomly with respect to the applied magnetic field, which typically distributes the total NMR signal over a range of precession frequencies (Figure 1.8).
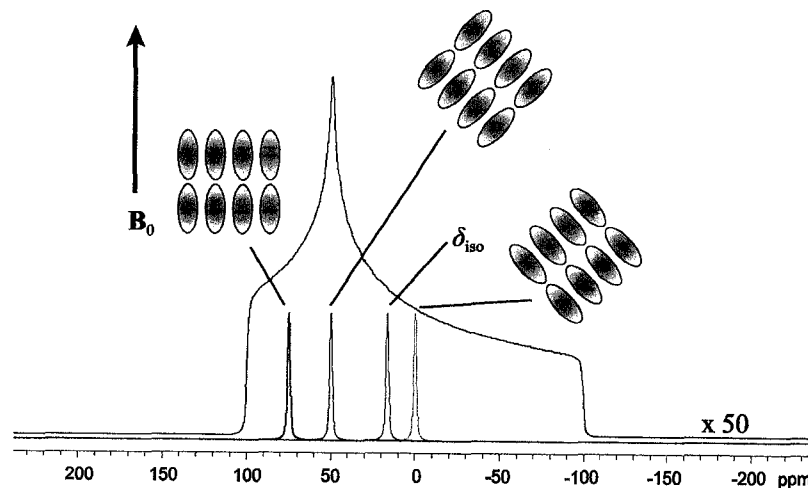
Figure 1.8 Chemical shielding, one example of an orientation-dependent NMR interaction, manifests as chemical shielding anisotropy (CSA) in solids. Each microcrystalline region (represented above as octets of ovals) gives rise to a solution-like resonance; however, as each crystallite is ordered randomly in a powdered sample, the total NMR signal is a composite of many resonances. The vertical scale of the broad signal (powder pattern) has been increased by a factor of 50.

-12-

1.2.3.1 Chemical Shielding Anisotropy (CSA)

Except for cases where the chemical environment is of very high symmetry, the isotropic chemical shift value (δ_{iso}) defined earlier is not adequate for describing the observed NMR signal (powder pattern) of solid-state samples. Rather, a second-rank Cartesian tensor is used, which may be represented using a 3 × 3 matrix:[28]

$$\tilde{\delta}_{solids} = \begin{bmatrix} \delta_{xx} & \delta_{xy} & \delta_{xz} \\ \delta_{yx} & \delta_{yy} & \delta_{yz} \\ \delta_{zx} & \delta_{zy} & \delta_{zz} \end{bmatrix} \qquad \text{[1.15]}$$

where each element of the matrix (δ_{ij}, $i, j = x, y, z$) describes the shift which results from an external magnetic field applied along the j-axis and inducing a magnetic field which possesses a component along the i-axis of the lab frame. As $\mathbf{B}_0$ is along the z-axis, things are simplified when one wishes to determine the induced magnetic field vector ($\mathbf{B}_{ind}$) using the chemical shift tensor: $\mathbf{B}_{ind} = \tilde{\delta}_{solids} \cdot \mathbf{B}_0$:

$$\mathbf{B}_{ind} = \begin{bmatrix} \delta_{xx} & \delta_{xy} & \delta_{xz} \\ \delta_{yx} & \delta_{yy} & \delta_{yz} \\ \delta_{zx} & \delta_{zy} & \delta_{zz} \end{bmatrix} \cdot \begin{bmatrix} 0 \\ 0 \\ B_0^z \end{bmatrix} = \begin{bmatrix} \delta_{xz} B_0^z \\ \delta_{yz} B_0^z \\ \delta_{zz} B_0^z \end{bmatrix} \qquad \text{[1.16]}$$

Thus, the induced magnetic field is fully described using a three component column vector, with each element being proportional to the applied magnetic field. Under the secular approximation, only the element containing δ_{zz} is retained, and [1.12] can be re-expressed in a form suitable for solid-state samples:[15]

$$\hat{\mathcal{H}}_{CS}^{solids} = -\hbar\gamma\delta_{zz}(\Theta)B_0^z \hat{I}_Z \qquad \text{[1.17]}$$

where (Θ) indicates that this is an orientation-dependent Hamiltonian.

-13-

The matrix representing the observable portion of the chemical shift tensor is symmetric ($\delta_{ij} = \delta_{ji}$) and can be diagonalized, a process which provides information regarding the relative orientation between the Cartesian frame of the molecule and the principal axis system (PAS) of the shift tensor. When in its own PAS, all off-diagonal elements of the chemical shift tensor are zero, and the diagonal elements (the eigenvalues) are known as the principal components:

$$\tilde{\delta}_{solids}^{PAS} = \begin{bmatrix} \delta_{11} & 0 & 0 \\ 0 & \delta_{22} & 0 \\ 0 & 0 & \delta_{33} \end{bmatrix} \qquad \textbf{[1.18]}$$

where $\delta_{11} \geq \delta_{22} \geq \delta_{33}$. If the chemical shift tensor is known in any reference frame, δ_{iso} may be determined by taking the average of the diagonal components of the tensor matrix:

$$\delta_{iso} = \frac{1}{3}(\delta_{xx} + \delta_{yy} + \delta_{zz}) = \frac{1}{3}(\delta_{11} + \delta_{22} + \delta_{33}) \equiv \frac{1}{3}\text{Tr}\{\tilde{\delta}\} \qquad \textbf{[1.19]}$$

where $\tilde{\delta}$ is a chemical shift tensor when the frame of reference is not of importance.

Observed chemical shift/shielding powder patterns are currently described using three conventions.[29] The Herzfeld-Berger (HB) convention,[30,31] which will be primarily used herein, uses three parameters to characterize a CSA powder pattern in terms of a chemical shift tensor (Ω, κ and δ_{iso}):

$$\Omega = \delta_{11} - \delta_{33} \quad ; \quad \kappa = \frac{3(\delta_{22} - \delta_{iso})}{\Omega} \qquad \textbf{[1.20]}$$

where Ω is the span, which specifies the breadth of the powder pattern (in ppm) in the frequency domain and κ is the skew, which ranges from -1 to $+1$ and represents the degree

-14-

of axial symmetry of the pattern. A general CSA powder pattern denoted according to the HB convention is provided in Figure 1.9.
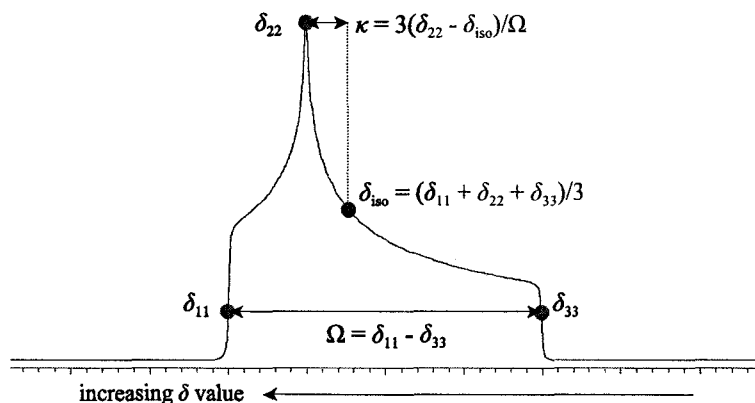
Figure 1.9 A schematic example of a CSA-dominated NMR signal.[32] Parameter definitions according to the HB convention are provided.

1.2.3.2 Quadrupolar Interaction in Solids

As was the case with CSA, unless the atom is in a highly symmetric environment, electric field gradients (EFGs) in solids are conveniently expressed using a symmetric second-rank tensor ($\tilde{V}_{EFG}$) of trace zero:

$$\tilde{V}_{EFG} = \begin{bmatrix} V_{xx} & V_{xy} & V_{xz} \\ V_{yx} & V_{yy} & V_{yz} \\ V_{zx} & V_{zy} & V_{zz} \end{bmatrix} \qquad [1.21]$$

where V_{ij} are the elements of the EFG tensor. As the matrix is traceless, the elements along the diagonal are such that $V_{xx} + V_{yy} + V_{zz} = 0$. The EFG tensor may be diagonalized, which allows one to determine the relative orientation between the EFG PAS and the Cartesian frame of the molecule. When in its own PAS, the matrix takes the following form:

-15-

$$\tilde{V}_{EFG}^{PAS} = \begin{bmatrix} V_{11} & 0 & 0 \\ 0 & V_{22} & 0 \\ 0 & 0 & V_{33} \end{bmatrix} \qquad \text{[1.22]}$$

where $|V_{33}| \geq |V_{22}| \geq |V_{11}|$ and the sum of the diagonal components is still zero. The principal

component with the largest absolute value (V_{33}) is related to the quadrupolar frequency:[33]

$$\omega_Q(\Theta) = \frac{3eQ}{4\hbar I(2I - 1)} V_{33}(\Theta) \qquad \text{[1.23]}$$

where e is the electric charge of a proton and (Θ) again denotes that the interaction bears an

orientation dependence. The quadrupolar interaction is not averaged out in solid-state

samples, hence the quadrupolar Hamiltonian will alter the eigenstates of the system[34]

(Figure 1.10 shows the effect to first-order).

It is important to note that the central-transition (CT) of half-integer quadrupolar

nuclei $(m = + 1/2 \rightarrow - 1/2)$ is unaffected to first-order by the quadrupolar interaction and that

the value of ω_Q can be determined directly from the spacing between one of the satellite-

transitions (either $m = - 1/2 \rightarrow - 3/2$ or $m = + 3/2 \rightarrow + 1/2$) and the CT in a frequency-domain

spectrum. Once ω_Q is known, it can be related to the nuclear quadrupolar coupling constant

(C_Q), a commonly reported parameter:

$$\omega_Q = \frac{3\pi C_Q}{2I(2I - 1)} \qquad \text{[1.24]}$$

where C_Q is directly related to the largest component of the EFG tensor in its PAS:

$$C_Q = \frac{eQV_{33}}{h} \qquad \text{[1.25]}$$

-16-

(a)

$|3/2, -3/2\rangle$

$\Delta E = \hbar \{\gamma B_0 + \omega_Q(\Theta)\}$

$\Delta E = \gamma \hbar B_0$

$|3/2, m\rangle$

E

$\Delta E = \gamma \hbar B_0$

$|3/2, -1/2\rangle$

$\Delta E = \gamma \hbar B_0$

$\Delta E = \gamma \hbar B_0$

$|3/2, 1/2\rangle$

$\Delta E = \hbar \{\gamma B_0 - \omega_Q(\Theta)\}$

$\Delta E = \gamma \hbar B_0$

$|3/2, 3/2\rangle$

$\mathcal{H}_z + \mathcal{H}_Q$

$\mathcal{H}_z$

(b)

ν_Q ν_Q

ν_0
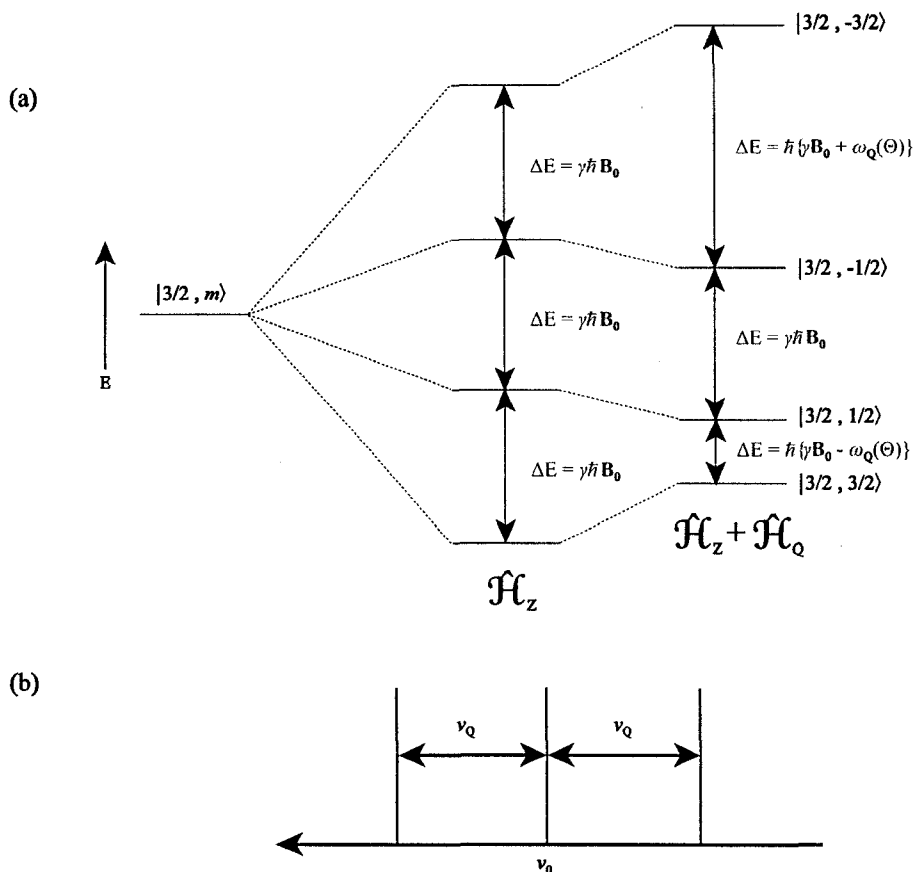
Figure 1.10 The quadrupolar interaction, to first-order, alters the energy levels of the system as shown in (a). For the case where $I = 3/2$, this results in three NMR signals that are equally spaced about the Lamour frequency by $\pm \nu_Q$, as shown in (b). In this example it is assumed that $\omega_Q > 0$ and ν_Q is the quadrupolar frequency in units of s^{-1}.

In order to completely specify the EFG tensor, one additional piece of information is required, which is provided by the EFG tensor asymmetry parameter (η_Q):

$$\eta_Q = \frac{V_{11} - V_{22}}{V_{33}}$$

[1.26]

The above discussion is valid for the regime where $\nu_0 \gg \nu_Q$, but many cases exist where this is not the case.[34,35] When this occurs, the expansion of the quadrupolar Hamiltonian must be done to second-order, which produces a more complicated expression,

-17-

but one may now determine C_Q and η_Q through analysis of the central-transition only (Figure 1.11). This is very important, as it is typically very difficult to directly detect the satellite-transitions in this regime: only the CT is usually observable.
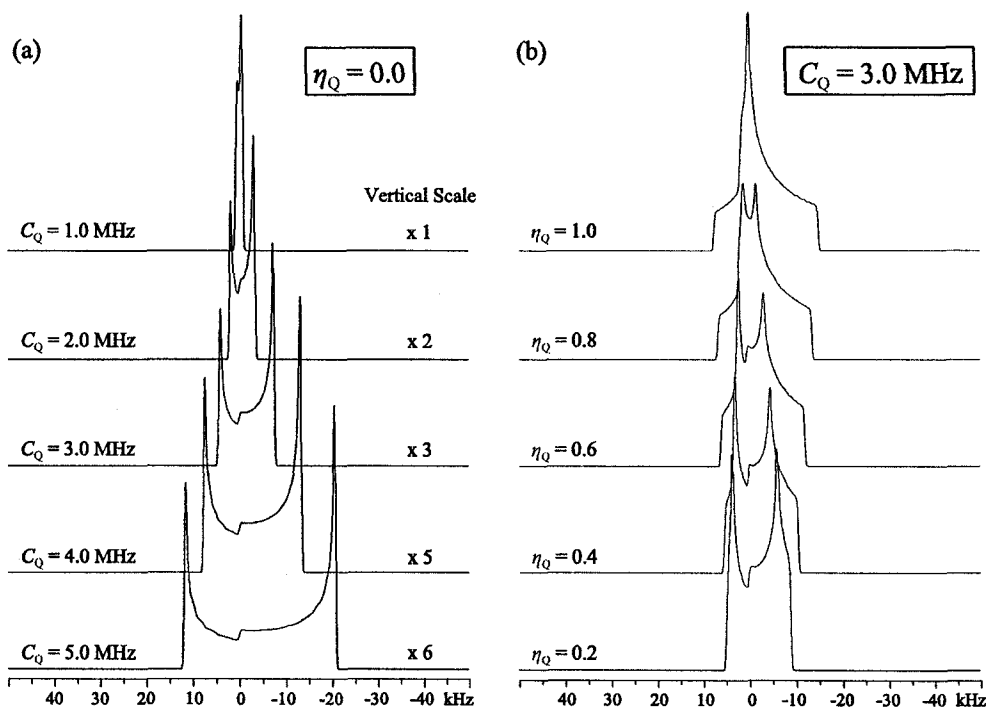
Figure 1.11 Analytical WSolids[32] simulations of theoretical solid-state ^{23}Na NMR powder patterns under static (i.e., non-MAS, *vide infra*) sample conditions. For all simulations, $\nu_0(^{23}$Na$) = 100$ MHz and 500 Hz of Gaussian line-broadening was used. If $\eta_Q(^{23}$Na$)$ is kept constant (a), one notes that $C_Q(^{23}$Na$)$ has a pronounced effect upon the breadth of the spectrum, while the shape is fairly consistent; however, if one keeps $C_Q(^{23}$Na$)$ constant (b) and varies $\eta_Q(^{23}$Na$)$, the width of the CT signal varies only slightly and the most significant effect is on the shape of the pattern. The vertical scale of the patterns in (a) have been increased by the factors shown.

1.2.3.3 Euler Angles

As both the CS and EFG matrices can be diagonalized, the orientation of each interaction PAS with respect to the Cartesian frame of the molecule can be determined by

-18-

conducting NMR experiments upon single-crystals.[36,37] When conducting SSNMR experiments upon microcrystalline samples where both the shielding anisotropy and quadrupolar interactions contribute significantly to the overall powder pattern, it is only possible to experimentally determine the *relative* orientation between the two interaction principal axis systems.[38,39] This relative orientation is provided by three parameters (α_e, β_e, γ_e)[†], known collectively as the Euler angles,[40] which specify the angle of positive (counter-clockwise) rotation about axes which are related to an arbitrarily chosen origin frame. The EFG PAS, which is represented by three mutually orthogonal axes (x, y, z), is chosen to be the origin frame with the final frame being the CS PAS, which is represented by its own triad of mutually orthogonal axes (1, 2, 3). The origin frame is transformed into the final frame by three successive rotations (Figure 1.12).

$$\hat{R}_z(\alpha_e) \qquad \hat{R}_{y'}(\beta_e) \qquad \hat{R}_{z''}(\gamma_e)$$
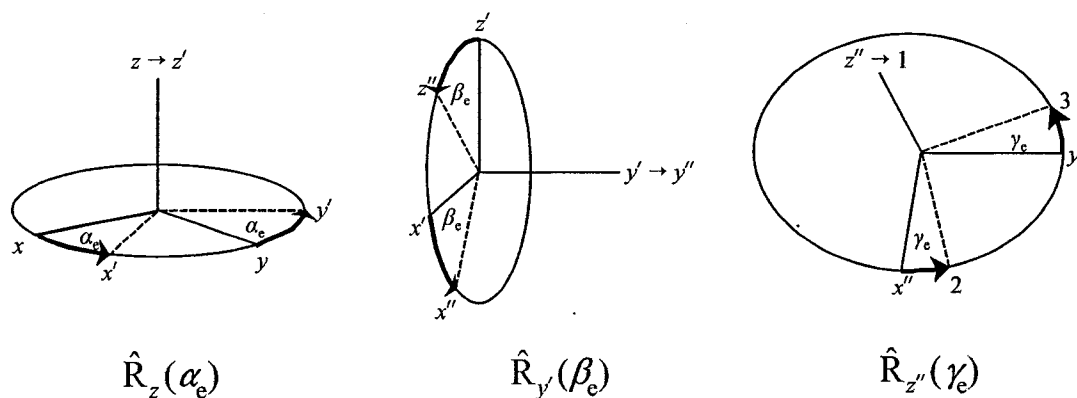
Figure 1.12 Three rotational operators ($\hat{R}_z$, $\hat{R}_{y'}$, $\hat{R}_{z''}$) transform the EFG PAS into the CS PAS. The angle of rotation is determined by the value of the Euler angles. Intermediate frames are denoted as (x', y', z') and (x'', y'', z'') after the application of the $\hat{R}_z$ and $\hat{R}_{y'}$ operators, respectively.

[†] Traditionally, the parameters are α, β, γ. The symbolism chosen here is done so to reduce ambiguity.

-19-

1.3 Experimental Background

As in any scientific discipline, NMR has many specialized experimental procedures which are used in order to carry out data acquisition in an efficient manner. The biggest challenge to overcome when conducting SSNMR experiments is the inherently poor experimental sensitivity and resolution. A number of techniques have been developed in order to deal with these issues; only the ones which pertain to subsequent discussions are outlined below.

1.3.1 Resolution Enhancement

1.3.1.1 Magic-Angle Spinning (MAS)

In solution-state NMR experiments, isotropic molecular tumbling renders unobservable the anisotropic portion of the interactions that are observed in SSNMR experiments. A number of NMR interactions, including chemical shielding, direct dipole-dipole and first-order quadrupolar, have essentially the same orientational dependence[41] and can be averaged to their isotropic values by mechanically rotating the sample at the so-called "magic-angle." This angle is found by solving for the root of $3\cos^2\theta = 1$, where θ represents the angle between the direction associated with the largest principal component of a given interaction tensor (e.g., δ_{33}) and $\mathbf{B}_0$. Therefore, if θ is set to $54.74°$, the anisotropy will at least partially average, which usually results in significant NMR line-narrowing (Figure 1.13).[42-44] Most conventional SSNMR probes can reach sample rotation frequencies (v_{rot}) of approximately $10 - 20$ kHz,[45] although a number of specialized probes that can rotate samples at frequencies of over 50 kHz have been developed.[46]

-20-
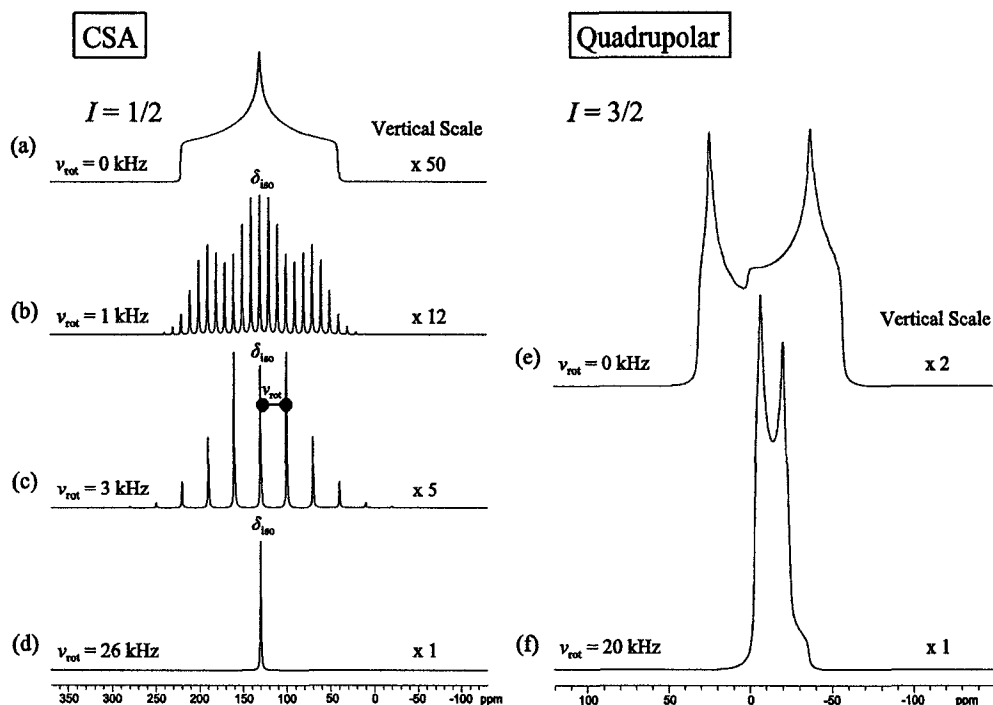
Figure 1.13 Analytical WSolids simulations illustrating the effect of magic-angle spinning (MAS) on CSA-dominated (a-d) and quadrupole-dominated (e-f) spectra. The low resolution static powder pattern that is produced as a result of CSA (a), is partitioned into the isotropic peak plus a number of sidebands (b-c), assuming MAS conditions and $v_{rot} < \Omega$. The sidebands flank the isotropic peak at integer multiples of v_{rot} (highlighted in (c)). If $v_{rot} \gg \Omega$, a solution-like peak is observed (d). When $\hat{\mathcal{H}}_Q$ represents the dominant interaction and cannot be truncated to first-order, MAS will only narrow a CT powder pattern by a factor of ca. $2-3$ (f). This is because the second-order quadrupolar interaction is too complex to completely average using MAS only. Note the various vertical scale enhancements employed in the spectra. Parameters used for simulations: (a-d) $I = 1/2$, $v_0 = 100$ MHz, $\delta_{11} = 220$ ppm, $\delta_{22} = 130$ ppm, $\delta_{33} = 40$ ppm; (e-f) $I = 3/2$, $v_0 = 100$ MHz, $C_Q = 2.4$ MHz, $\eta_Q = 0.2$.

1.3.1.2 Multiple-Quantum MAS (MQMAS)

For samples where the second-order quadrupolar interaction must be considered (v_0 no longer $\gg$ than v_Q), more advanced line-narrowing techniques are required. Generally speaking, two techniques are used to remove second-order quadrupolar broadening:

-21-

(i) mechanical sample rotation about two axes[47,48] or (ii) two-dimensional (2D) correlation experiments done under MAS conditions.[49,50] The multiple-quantum MAS (MQMAS) experiment correlates the CT with any symmetrical (i.e., $+ m \rightarrow - m$) multiple-quantum (MQ) transition (Figure 1.14a). Typical MAS conditions are used to eliminate any first-order quadrupolar, direct dipole-dipole and chemical shielding anisotropies. Due to the fashion in which the second-order quadrupolar Hamiltonian perturbs the Zeeman eigenstates, the symmetric MQ transitions and CT are related by a scalar value ($C_4(I,m)$; Table 1.1).[49] This relationship leads to a ridge-like structure in a frequency-domain MQMAS spectrum along the line $y = C_4(I,m)x$. A shearing transformation is then applied, leading to a typical MAS spectrum along one dimension and an isotropic spectrum in the second (Figure 1.14b).
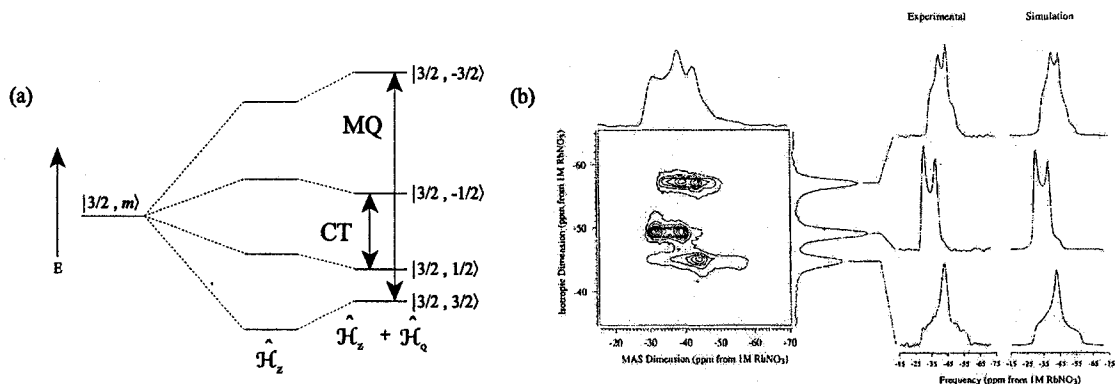
Figure 1.14 The MQMAS experiment removes second-order quadrupolar broadening by correlating a symmetrical MQ transition ($+ m \rightarrow - m$; $\Delta m = 3, 5, 7, 9$) with the CT ($m = + \frac{1}{2} \rightarrow - \frac{1}{2}$). A schematic showing a MQ transition where $\Delta m = 3$ is provided in (a). A correlation between the MQ transition and CT as in (a) would initially produce a ridge-like structure along $y = - 7/9x$ in the frequency domain, which, after appropriate processing, allows for the removal of anisotropic broadening along one dimension of the resultant spectrum, as shown in the solid-state [87]Rb MQMAS spectrum ($I(^{87}Rb) = 3/2$) of a microcrystalline sample of RbNO$_3$ (b).[51]

-22-

Table 1.1 $C_4(I,m)$ values for cases where $I = 3/2, 5/2, 7/2$ and $9/2$

I	m	$C_4(I,m)$	I	m	$C_4(I,m)$
3/2	3/2	$-7/9$	7/2	7/2	$-161/45$
5/2	3/2	19/12	9/2	3/2	91/36
5/2	5/2	$-25/12$	9/2	5/2	95/36
7/2	3/2	101/45	9/2	7/2	2/13
7/2	5/2	11/9	9/2	9/2	$-31/6$

1.3.2 Sensitivity Enhancement

1.3.2.1 Cross-Polarization (CP)

Many chemically interesting nuclides with $I = \frac{1}{2}$ (^{13}C, ^{15}N, ^{29}Si, etc.) have low natural abundances. Additionally, these nuclei typically have inefficient spin-lattice relaxation properties (i.e., a large T_1 value, for discussions pertaining to nuclear spin relaxation, the reader is directed to a number of resources[15,16,20,25,52]), thereby making the direct acquisition of solid-state NMR spectra of these nuclei a fairly challenging endeavour. Many cases exist where the desired NMR active nucleus is dipolar coupled to at least one ^{1}H atom, a nuclide which typically possesses very favourable NMR properties (large γ, small T_1 value). The cross-polarization (CP) experiment[53-56] serves to reduce experimental time in two ways: (i) transfer of $M(^1H)$ from the abundant ^{1}H nuclei to the dilute spins and (ii) usage of $T_1(^1H)$ as opposed to $T_1(X)$, where X denotes a generic dilute nucleus. Using $M(^1H)$ rather than $M(X)$ reduces experiment time by increasing experimental sensitivity in a fashion proportional to $\gamma(^1H)^2/\gamma(X)^2$ (recall, $M \propto \gamma$)[53] and thus the observable NMR signal per scan is increased. Additionally, due to the generally lower T_1 of the protons, more scans may be done per unit

-23-

time. The CP experiment is commonly coupled with MAS, leading to both increased resolution and sensitivity (Figure 1.15(a-d)).
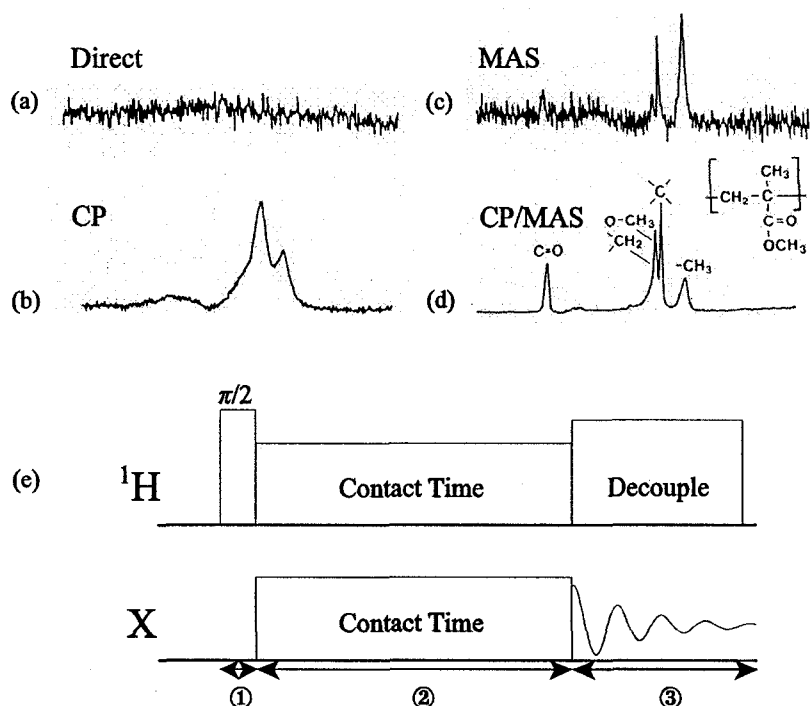
Figure 1.15 (a-d) ^{13}C SSNMR spectra of a sample of poly(methylmethacrylate), acquired using a variety of techniques.[57] (a) While a direct static ^{13}C NMR experiment does not result in the detection of a signal, sensitivity and resolution are recovered individually by using (b) CP and (c) MAS techniques, respectively. (d) Maximum gains in both sensitivity and resolution are achieved with the CP/MAS experiment, which couples the CP pulse sequence with MAS. All spectra in (a-d) employed a 1 second pulse delay and acquisition of 250 transients. (e) The basic CP experiment involves three steps: ① – preparation, ② – mixing and ③ – detection. Proton decoupling is usually required during detection on the X channel.

The CP experiment is quite elegant (Figure 1.15e), involving three stages: preparation, mixing and detection. Preparation requires a single $\pi/2$ pulse on the ^{1}H channel, which will rotate the magnetization associated with the ^{1}H spins from the z-axis into the xy-plane. The mixing portion of the sequence serves to pass the spin magnetization from the ^{1}H nuclei to

-24-

the dilute spins, the duration of which is called the contact time. In order to maximize the amount of magnetization transferred, the Hartmann-Hahn match must be satisfied, which states that $\gamma(^1H)B_1(^1H) = \gamma(X)B_1(X)$.[58] After the contact time, the signal is detected on the X channel with some form of decoupling typically being employed on the ^1H channel.

1.3.2.2 The Quadrupolar Carr-Purcell Meiboom-Gill (QCPMG) Experiment

When conducting SSNMR experiments upon nuclei where $I > \frac{1}{2}$, the time-domain signal produced after preparation will become decoherent (a T_2^* decay) relatively quickly due to quadrupolar relaxation mechanisms. Sometimes, the NMR signal will decay in such an efficient manner that it cannot be meaningfully interpreted by the receiver. A traditional solution to this problem is found by applying the Hahn-echo pulse sequence (Figure 1.16a).[59] After a preparatory $\pi/2$ pulse, the magnetization is allowed to decay for a period of time (τ_1), after which a π pulse is applied. The π pulse serves to almost completely refocus the magnetization after a second delay period (τ_2). At this point, the receiver is turned on and data acquisition begins. While this sequence does allow for the acquisition of previously undetectable NMR signals, a number of situations exist where it is not useful. This lack of utility is typically due to poor experimental sensitivity (and hence low signal-to-noise (S/N)), which can arise from any of the previously mentioned factors.

The quadrupolar Carr-Purcell Meiboom-Gill (QCPMG) pulse sequence was developed in the 1950's and is a modified version of the Hahn-echo sequence that includes additional acquisition and delay portions (Figure 1.16a).[60,61] It was initially used to measure T_2 values and address such items as homonuclear dipolar couplings[62-64] and molecular

-25-

dynamics,[65-69] and was not applied with the goal of experimental sensitivity enhancement until recently.[70] The sequence increases sensitivity if individual T_2^* decays are much shorter than the T_2 decay of the sample (see Figure 1.16 caption for a brief explanation of T_2 and T_2^* decays). Additional details are provided elsewhere,[60,61] but it enhances sensitivity by acquiring what is termed as a "train" of system response echos (the number of which is determined by the number of Meiboom-Gill (MG) loops), as opposed to just a single echo as is the case with the Hahn-Echo experiment (Figure 1.16b).
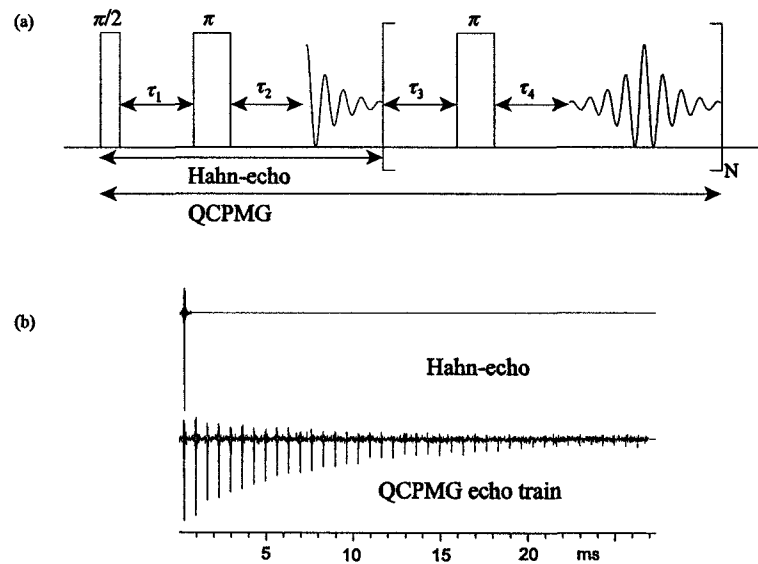
Figure 1.16 (a) The QCPMG sequence is a modified Hahn-echo experiment that includes additional delay (τ_3, τ_4) and acquisition periods. The portion inside the brackets is called a Meiboom-Gill (MG) loop and is repeated N times. (b) Qualitative illustration of Hahn-echo and QCPMG system responses in the time-domain. The Hahn-echo sequence collects only a single system response (one T_2^* decay), while the QCPMG sequence collects several (as seen by the numerous spikelets; the train of echos is one T_2 decay).

-26-

1.3.2.3 Additional Enhancement Sequences

In addition to the CP and QCPMG techniques, several other pulse sequences may be used to enhance experimental sensitivity. The pulse sequences briefly discussed herein have been used both in isolation,[71-76] as well as in tandem with the QCPMG experiment,[77] although they themselves are never used together. The pulse sequence for rotor-assisted population-transfer (RAPT)[78] is a train of repeating $\varphi_p - \overline{\varphi}_p$ pulses, followed by a delay period (τ_{rapt}) and the Hahn-echo sequence (Figure 1.17a). RAPT must be run under MAS conditions and will enhance the sensitivity by a maximum factor of (I + ½). The enhancement is due to the saturation of the satellite-transitions (Figure 1.17b), which leads to increased magnetization being associated with the CT. Additional details are available.[75]
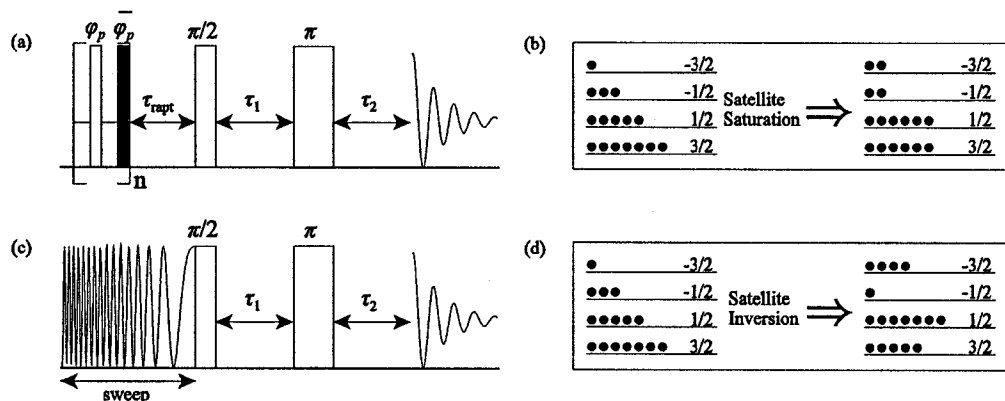
Figure 1.17 (a) The RAPT pulse sequence consists of an initial train of pulses (repeated n times), which serve to saturate the satellite-transitions, followed by a delay (τ_{rapt}) and the Hahn-echo sequence. (b) The RAPT sequence leads to a theoretical increase in experimental sensitivity proportional to (I + ½). (c) The DFS sequence consists of two frequency sweeps (accomplished over the time denoted by sweep) and is followed by the Hahn-echo experiment. DFS inverts the satellite-transitions (d), leading to a theoretical signal enhancement proportional to $2I$.

As was the case with RAPT, the double-frequency sweep (DFS) pulse sequence (Figure

-27-

1.17c) also involves manipulation of the nuclear spin state populations.[71,72] Unlike RAPT, DFS inverts the satellite-transition populations (Figure 1.17d) through the use of adiabatic frequency sweeps prior to the Hahn-echo portion of the sequence. DFS is more time consuming to optimize experimentally as compared to RAPT, but offers additional sensitivity gains (proportional to $2I$).

1.4 Context of Research

The portions of this thesis which pertain to metallocenes (chapters 2 and 4) are, for the most part, an extension of the solid-state NMR studies carried out by previous members of our research group. Dr. Ivan Hung (Warwick) applied solid-state NMR techniques in the study of a number of main group- and transition-metal metallocene systems, including $[Cp_2Al]^+$,[79] Cp_2Mg,[80] Cp_2ZrCl_2,[81] as well as a few boron[82] and beryllium[83] metallocenes. Contributions towards the understanding of several sodium metallocenes were also made by Mr. Mathew Willans (Alberta).[84] These accounts were not the first time in which NMR techniques had been applied to metallocene systems but are noteworthy as the NMR experiments were conducted in the solid-state and focussed on the central metal nucleus, rather than the Cp ring systems: prior to this, NMR studies of metallocenes were typically conducted on solution state samples with the point of interest being the Cp ring carbons (studied using ^1H and ^{13}C NMR).[85,86]

These solid-state NMR studies showed that metal nuclei EFG tensor parameters could be related to molecular structure and dynamics in metallocenes. The first studies were conducted on microcrystalline samples whose solid-state crystal structures were known (e.g.,

-28-

$[Cp_2Al]^+$ and $[Cp*_2B]^+$). With known structures, relationships between NMR interaction tensor parameters and solid-state structures could be made with very high confidence. With regard to base-free alkali-metal metallocenes, structure determination is usually carried out using powder XRD experiments, followed by Rietveld analysis;[87] hence, definitive solid-state structures for these types of metallocenes are not known. Previous knowledge of the relationships between EFG tensor parameters and structure may therefore by used to propose structures where crystal data is not available.

In chapter 2, potassium-containing polymeric metallocenes are studied in order to extend the discussion upon the relationship between NMR interaction tensors and molecular structure to include CpK and Cp*K. Solid-state ^{39}K NMR experiments have never been conducted upon a metallocene and are very rarely used to study microcrystalline powder samples due to the very low receptivity of this nuclide to NMR experiments. By correlating measured NMR parameters with structure, we are able to propose a structure for Cp*K, which had not been established previously, even through pXRD/Rietveld methods. The relationships between NMR interaction tensor parameters and structure becomes very important when developing a model to relate the temperature-dependent NMR parameters with potential temperature-dependent structural changes in CpK. Chapter 4 uses XRD techniques and *ab initio* calculations to compliment solid-state ^{23}Na NMR experiments. All three techniques help to develop a very convincing model for the temperature-dependent structural changes in CpNa.

Chapter 3 advances discussion on the relationships between chemical shielding (CS) tensor parameters and molecular structure. Although many previous accounts exist which

-29-

discuss the relationships between structure and CS tensor parameters,[79,88-103] the presentation herein is unique as it uses group theory to evaluate which MOs are allowed by symmetry to contribute to chemical shielding. It is hoped that the methodology developed here would be instructive and clear enough so that the anisotropic nature of CS becomes clear even to non-specialists and that it helps to elucidate the relationships which exist between the CS tensor and molecular symmetry.

-30-

Bibliography

[1]   Rabi, I. I.; Zacharias, J. R.; Millman, S.; Kusch, P. *Physical Review* **1938**, *53*, 318.

[2]   Gorter, C. J. *Physica* **1936**, *3*, 995.

[3]   Gorter, C. J.; Broer, L. J. F. *Physica* **1942**, *9*, 591.

[4]   Purcell, E. M.; Torrey, H. C.; Pound, R. V. *Physical Review* **1946**, *69*, 37.

[5]   Bloch, F.; Hansen, W. W.; Packard, M. *Physical Review* **1946**, *69*, 127.

[6]   Dickinson, W. C. *Physical Review* **1950**, *77*, 736.

[7]   Lindstrom, G. *Physical Review* **1950**, *78*, 817.

[8]   Proctor, W. G.; Yu, F. C. *Physical Review* **1950**, *77*, 717.

[9]   Thomas, H. A. *Physical Review* **1950**, *80*, 901.

[10]   Arnold, J. T.; Dharmatti, S. S.; Packard, M. E. *Journal of Chemical Physics* **1951**, *19*, 507.

[11]   *Encyclopedia of Nuclear Magnetic Resonance*; Grant, D. M.; Harris, R. K., Eds.; Wiley: New York, 1996, pp 6470.

[12]   Abragam, A. *The Principles of Nuclear Magnetism*; Oxford University Press: London, 1961.

[13]   Slichter, C. P. *Principles of Magnetic Resonance*; Harper & Row: New York, 1963.

[14]   Ernst, R. R.; Bodenhausen, G.; Wokaun, A. *Principles of Nuclear Magnetic Resonance in One and Two Dimensions*; Oxford University Press: London, 1990.

[15]   Levitt, M. H. *Spin Dynamics: Basics of Nuclear Magnetic Resonance*; John Wiley & Sons Ltd: Sussex, 2003.

[16] Yoder, C. H.; Schaeffer, C. D. *Introduction to Multinuclear NMR*; Benjamin/Cummings: Menlo Park, 1987.

[17] Edmonds, A. R. *Angular Momentum in Quantum Mechanics*; Princeton University Press: Princeton, 1960; Vol. 4.

[18] Feenberg, E.; Pake, G. E. *Notes on the Quantum Theory of Angular Momentum*; Stanford University Press: Stanford, 1959.

[19] Atkins, P.; de Paula, J. *Physical Chemistry*, 7th ed.; W. H. Freeman and Company: New York, 2002.

[20] Nelson, J. H. *Nuclear Magnetic Resonance Spectroscopy*; Prentice Hall: Upper Saddle River, 2003.

[21] Lambert, J. B.; Shurvell, H. F.; Lightner, D.; Cooks, R. G. *Introduction to Organic Spectroscopy*; Macmillan: New York, 1987.

[22] Claridge, T. D. W. *High-Resolution NMR Techniques in Organic Chemistry*, 1 ed.; Pergamon: New York, 1999; Vol. 19.

[23] Dirac, P. A. M. *The Principles of Quantum Mechanics*, 4 ed.; Oxford University Press: Oxford, 1958; Vol. 27.

[24] Mehring, M.; Weberrub, V. A. *Object-Oriented Magnetic Resonance: Classes and Objects, Calculations and Computations*; Academic Press: New York, 2001.

[25] *Multinuclear NMR*; Mason, J., Ed.; Plenum Press: New York, 1987.

[26] Duer, M. J. *Introduction to Solid-State NMR Spectroscopy*; Blackwell Publishing: Cornwall, 2004.

[27] Man, P. P. Quadrupole Couplings in Nuclear Magnetic Resonance, General. In

Encyclopedia of Analytical Chemistry; Meyers, R. A., Ed.; John Wiley & Sons Ltd: Chichester, 2000; pp 12224

[28]   Mehring, M. *Principles of High Resolution NMR in Solids*, 2nd ed.; Springer-Verlag: New York, 1983.

[29]   Grant, D. M. Chemical Shift Tensors. In *Encyclopedia of Nuclear Magnetic Resonance*; Grant, D. M., Ed.; Wiley: New York, 1996; pp 1298

[30]   Herzfeld, J.; Berger, A. E. *Journal of Chemical Physics* **1980**, *73*, 6021.

[31]   Mason, J. *Solid State Nuclear Magnetic Resonance* **1993**, *2*, 285

[32]   Eichele, K.; Wasylishen, R. E. WSolids; 2.2.13 ed.; Dalhousie University: Halifax, N.S., 1998.

[33]   Vega, A. J. Quadrupolar Nuclei in Solids. In *Encyclopedia of Nuclear Magnetic Resonance*; Grant, D. M., Ed.; Wiley: New York, 1996; pp 3869

[34]   Lucken, E. A. C. *Nuclear Quadrupole Coupling Constants*; Academic Press: London, 1969.

[35]   Smith, M. E.; Van Eck, E. R. H. *Progress in Nuclear Magnetic Resonance Spectroscopy* **1999**, *34*, 159.

[36]   Kroeker, S.; Eichele, K.; Wasylishen, R. E.; Britten, J. F. *Journal of Physical Chemistry B* **1997**, *101*, 3727.

[37]   Vosegaard, T.; Skibsted, J.; Jakobsen, H. J. *Journal of Physical Chemistry A* **1999**, *103*, 9144.

[38]   Chu, P. J.; Gerstein, B. C. *Journal of Chemical Physics* **1989**, *91*, 2081.

[39]   Power, W. P.; Wasylishen, R. E.; Mooibroek, S.; Pettitt, B. A.; Danchura, W. *Journal*

-33-

of Physical Chemistry **1990**, *94*, 591.

[40]   Zare, R. N. *Angular Momentum: Understanding Spatial Aspects in Chemistry and Physics*; John Wiley & Sons: Toronto, 1988.

[41]   Brown, S. P.; Lyndon, E. *Handbook of Spectroscopy*; Wiley: Toronto, 2003; Vol. 2.

[42]   Gutowsky, H. S.; Pake, G. E. *Journal of Chemical Physics* **1950**, *18*, 162.

[43]   Andrew, E. R.; Newing, R. A. *Proceedings of the Physical Society, London* **1958**, *72*, 959.

[44]   Lowe, I. J. *Physical Review Letters* **1959**, *2*, 285.

[45]   Bryce, D. L.; Bernard, G. M.; Gee, M.; Lumsden, M. D.; Eichele, K.; Wasylishen, R. E. *Canadian Journal of Analytical Sciences and Spectroscopy* **2001**, *46*, 46.

[46]   Ernst, M. *Journal of Magnetic Resonance* **2003**, *162*, 1.

[47]   Llor, A.; Virlet, J. *Chemical Physics Letters* **1988**, *152*, 248.

[48]   Samoson, A.; Lippmaa, E.; Pines, A. *Molecular Physics* **1988**, *65*, 1013.

[49]   Frydman, L.; Harwood, J. S. *Journal of the American Chemical Society* **1995**, *117*, 5367.

[50]   Gan, Z. *Journal of the American Chemical Society* **2000**, *122*, 3242.

[51]   Massiot, D.; Touzo, B.; Trumeau, D.; Coutures, J. P.; Virlet, J.; Florian, P.; Grandinetti, P. J. *Solid State Nuclear Magnetic Resonance* **1996**, *6*, 73.

[52]   Fyfe, C. A. *Solid State NMR for Chemists*; C.F.C. Press: Guelph, 1983.

[53]   Pines, A.; Gibby, M. G.; Waugh, J. S. *Journal of Chemical Physics* **1973**, *59*, 569.

[54]   Pines, A.; Gibby, M. G.; Waugh, J. S. *Chemical Physics Letters* **1972**, *15*, 373.

[55]   Gibby, M. G.; Pines, A.; Waugh, J. S. *Journal of the American Chemical Society*

1972, *94*, 6231.

[56]   Pines, A.; Gibby, M. G.; Waugh, J. S. *Journal of Chemical Physics* **1972**, *56*, 1776.

[57]   Fyfe, C. A.; Dudley, R. L.; Stephenson, P. J.; Deslandes, Y.; Hamer, G. K.; Marchessault, R. H. *Journal of Macromolecular Science, Reviews in Macromolecular Chemistry and Physics* **1983**, *C23*, 187.

[58]   Hartmann, S. R.; Hahn, E. L. *Physical Review* **1962**, *128*, 2042.

[59]   Hahn, E. L. *Physical Review* **1949**, *76*, 145.

[60]   Carr, H. Y.; Purcell, E. M. *Physical Review* **1954**, *94*, 630.

[61]   Meiboom, S.; Gill, D. *Review of Scientific Instruments* **1958**, *29*, 688.

[62]   Garroway, A. N. *Journal of Magnetic Resonance* **1977**, *28*, 365.

[63]   Engelsberg, M.; Yannoni, C. S. *Journal of Magnetic Resonance* **1990**, *88*, 393.

[64]   Lizak, M. J.; Gullion, T.; Conradi, M. S. *Journal of Magnetic Resonance* **1991**, *91*, 254.

[65]   Vega, A. J. *Journal of Magnetic Resonance* **1985**, *65*, 252.

[66]   Marchetti, P. S.; Bhattacharyya, L.; Ellis, P. D.; Brewer, C. F. *Journal of Magnetic Resonance* **1988**, *80*, 417.

[67]   Bank, S.; Bank, J. F.; Ellis, P. D. *Journal of Physical Chemistry* **1989**, *93*, 4847.

[68]   Cheng, J. T.; Ellis, P. D. *Journal of Physical Chemistry* **1989**, *93*, 2549.

[69]   Mueller, K.; Poupko, R.; Luz, Z. *Journal of Magnetic Resonance* **1990**, *90*, 19.

[70]   Larsen, F. H.; Jakobsen, H. J.; Ellis, P. D.; Nielsen, N. C. *Journal of Physical Chemistry A* **1997**, *101*, 8597.

[71]   Haase, J.; Conradi, M. S. *Chemical Physics Letters* **1993**, *209*, 287.

[72]   Haase, J.; Conradi, M. S.; Grey, C. P.; Vega, A. J. *Journal of Magnetic Resonance, Series A* **1994**, *109*, 90.

[73]   Kentgens, A. P. M.; Verhagen, R. *Chemical Physics Letters* **1999**, *300*, 435.

[74]   Madhu, P. K.; Goldbourt, A.; Frydman, L.; Vega, S. *Chemical Physics Letters* **1999**, *307*, 41.

[75]   Kwak, H. T.; Prasad, S.; Yao, Z.; Grandinetti, P. J.; Sachleben, J. R.; Emsley, L. *Journal of Magnetic Resonance* **2001**, *150*, 71.

[76]   Prasad, S.; Kwak, H.-T.; Clark, T.; Grandinetti, P. J. *Journal of the American Chemical Society* **2002**, *124*, 4964.

[77]   Schurko, R. W.; Hung, I.; Widdifield, C. M. *Chemical Physics Letters* **2003**, *379*, 1.

[78]   Yao, Z.; Kwak, H. T.; Sakellariou, D.; Emsley, L.; Grandinetti, P. J. *Chemical Physics Letters* **2000**, *327*, 85.

[79]   Schurko, R. W.; Hung, I.; Macdonald, C. L. B.; Cowley, A. H. *Journal of the American Chemical Society* **2002**, *124*, 13204.

[80]   Hung, I.; Schurko, R. W. *Solid State Nuclear Magnetic Resonance* **2003**, *24*, 78.

[81]   Hung, I.; Schurko, R. W. *Journal of Physical Chemistry B* **2004**, *108*, 9060.

[82]   Schurko, R. W.; Hung, I.; Schauff, S.; Macdonald, C. L. B.; Cowley, A. H. *Journal of Physical Chemistry A* **2002**, *106*, 10096.

[83]   Hung, I.; Macdonald, C. L. B.; Schurko, R. W. *Chemistry--A European Journal* **2004**, *10*, 5923.

[84]   Willans, M. J.; Schurko, R. W. *Journal of Physical Chemistry B* **2003**, *107*, 5144.

[85]   Jutzi, P.; Burford, N. *Chemical Reviews (Washington, D. C.)* **1999**, *99*, 969.

[86]   Siemeling, U. *Chemical Reviews (Washington, D. C.)* **2000**, *100*, 1495.

[87]   Harder, S. *Coordination Chemistry Reviews* **1998**, *176*, 17.

[88]   Karplus, M.; Pople, J. A. *Journal of Chemical Physics* **1963**, *38*, 2803.

[89]   Rozhenko, A. B.; Schoeller, W. W.; Povolotskii, M. I. *Magnetic Resonance in Chemistry* **1999**, *37*, 551.

[90]   Zilm, K. W.; Conlin, R. T.; Grant, D. M.; Michl, J. *Journal of the American Chemical Society* **1980**, *102*, 6672.

[91]   Chesnut, D. B.; Quin, L. D. *Journal of the American Chemical Society* **1994**, *116*, 9638.

[92]   Barrie, P. J.; Groombridge, C. J.; Mason, J.; Moore, E. A. *Chemical Physics Letters* **1994**, *219*, 491.

[93]   Wiberg, K. B.; Hammer, J. D.; Keith, T. A.; Zilm, K. *Tetrahedron Letters* **1997**, *38*, 323.

[94]   Wiberg, K. B.; Hammer, J. D.; Keith, T. A.; Zilm, K. *Journal of Physical Chemistry A* **1999**, *103*, 21.

[95]   Chesnut, D. B. *Chemical Physics* **1997**, *224*, 133.

[96]   Kaupp, M.; Malkina, O. L. *Journal of Chemical Physics* **1998**, *108*, 3648.

[97]   Gilbert, T. M.; Ziegler, T. *Journal of Physical Chemistry A* **1999**, *103*, 7535.

[98]   Wiberg, K. B.; Hammer, J. D.; Zilm, K. W.; Cheeseman, J. R.; Keith, T. A. *Journal of Physical Chemistry A* **1998**, *102*, 8766.

[99]   Grutzner, J. B. *Chemical Shift Theory. Orbital Symmetry and Charge Effects on Chemical Shifts*; Norell Press: Landisville, 1987.

[100]   Arduengo, A. J.; Dixon, D. A.; Kumashiro, K. K.; Lee, C.; Power, W. P.; Zilm, K. W. *Journal of the American Chemical Society* **1994**, *116*, 6361.

[101]   Wiberg, K. B.; Hammer, J. D.; Zilm, K. W.; Cheeseman, J. R. *Journal of Organic Chemistry* **1999**, *64*, 6394.

[102]   Wiberg, K. B.; Hammer, J. D.; Zilm, K. W.; Keith, T. A.; Cheeseman, J. R.; Duchamp, J. C. *Journal of Organic Chemistry* **2004**, *69*, 1086.

[103]   Forgeron, M. A. M.; Wasylishen, R. E. *Journal of the American Chemical Society* **2006**, *128*, 7817.

Chapter 2

A Solid-State ^{39}K and ^{13}C NMR Study of Polymeric Potassium Metallocenes

2.1 Introduction

Cyclopentadienyl-alkali metal complexes are linear polymeric organometallic compounds of the form $[Cp'M]_n$ (herein referred to as Cp'M), where M is an alkali metal and Cp' is a cyclopentadienyl anion of the form $C_5R_5^-$ or $C_5R_xH_{5-x}^-$, with R = H, Me, iPr, etc. These metallocenes have been of significant interest for over a century, due to their fascinating structural types, utility as starting reagents and roles in monomeric anion chemistry.[1,2] While the synthesis and isolation of cyclopentadienyl potassium (CpK) was first reported by Thiele in 1901,[3] structural characterization of Cp'M complexes did not commence until the 1950s: early NMR[4,5] and IR[6] investigations revealed their highly ionic nature and the η^5-bonding interaction between the aromatic π-system(s) of the ring(s) and the alkali metal (Figure 2.1).
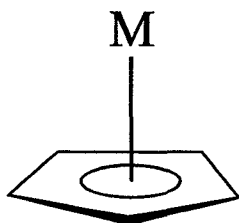
Figure 2.1 A schematic highlighting the η^5 interaction between a Cp ligand and a metal (M).

In addition to being only occasionally soluble in polar solvents, Cp'M complexes are

rarely soluble in non-polar and non-coordinating solvents. When certain Cp′M compounds are recrystallized from polar solvents, the solid-state structure often changes from unsolvated linear polymers (Figure 2.2(a,b)) to solvated linear polymers or monomers with markedly different structures (Figure 2.2(c,d)).[2] Crystal structures have been determined for a number of linear, potassium-containing, solvated polymers, including $(Me_3Si)CpK$,[7] $(tBuNH)Me_2SiCpK·THF$ (THF = tetrahydrofuran; C_4H_8O),[8] $Cp*K·(pyridine)_2$ $(Cp* = C_5Me_5^-)$,[9] $CpK·Et_2O$,[10] $Cp*K·nTHF$ ($n = 1, 2$),[11] and $(MeH_4C_5)K$.[12] Unfortunately, the structures of numerous Cp′M complexes (e.g., CpLi, CpNa, Cp*Na, CpK, Cp*K, etc.) cannot be determined by single-crystal X-ray diffraction (XRD) techniques as they can be isolated only as microcrystalline powders. Recently, synchrotron powder X-ray diffraction (pXRD) experiments, in combination with Rietveld analyses,[13] have been utilized to probe the structures of microcrystalline Cp′M polymers, including CpLi, CpNa and CpK,[14] as well as $Cp*Li$[15] and $Cp*Na$.[16]

Cp′M polymers are extremely reactive and sensitive to contact with air and moisture. As a result, when used as starting materials for organometallic synthesis, there are often disordered impurity phases which cannot be identified by pXRD techniques, which speaks to the limitations of such techniques for their accurate structural characterization. Solid-state NMR experiments, including those from the perspective of the central metal nucleus, have proven to be an ideal tool for characterizing alkali-metal metallocenes, including those in microcrystalline solids. Solid-state NMR studies of metal nuclei in polymeric metallocenes include ^{7}Li NMR experiments on lithium metallocenes and other organometallic complexes,[17] as well as ^{23}Na NMR studies of CpNa·TMEDA (TMEDA = tetramethyl-

-40-

ethylenediamine; $C_6H_{16}N_2$),[18] an assortment of organosodium complexes[19] and a variety

of Cp′Na complexes.[20]
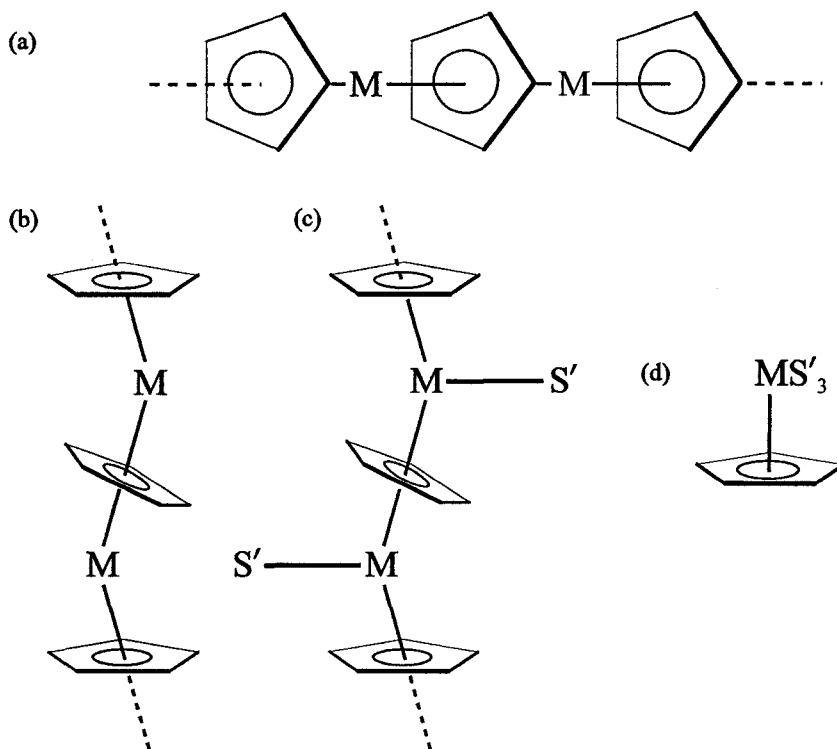
Figure 2.2 Examples of solvent-free alkali-metal metallocenes in the commonly observed (a) straight and (b) bent or "zigzagging" conformations. When placed in contact with a coordinating solvent (S′), the zigzagging conformation (c) is typically adopted, although the polymeric structure does occasionally break down into monomers (d).

Potassium has three NMR active isotopes, ^{39}K, ^{40}K and ^{41}K, all of which are quadrupolar nuclei ($I >$ ½): ^{39}K and ^{41}K are spin-3/2 nuclei while ^{40}K is a spin-4 nucleus. ^{39}K is the most receptive NMR nucleus of the trio, largely because of its high natural abundance (93.1 %) and relatively small nuclear quadrupole moment (accepted values range from $+ 0.055$ to 0.1×10^{-28} m^2).[21-24] However, ^{39}K has a very small γ relative to nuclei like ^{1}H and

-41-

[13]C, making the acquisition of high-quality solid-state ^{39}K NMR spectra a challenging endeavour.[25] Even more challenging is the acquisition of solid-state ^{39}K NMR spectra of potassium nuclides within nonspherically symmetric electronic environments, which is the case for systems such as CpK and Cp*K. In such systems, significant EFGs often lead to large quadrupolar interactions which can broaden the single quantum transitions of NMR powder patterns to such a degree that they are undetectable via conventional NMR experiments or at standard magnetic field strengths.[26-28]

Due to the prominence of potassium in a variety of inorganic complexes, biological systems, and technologically relevant materials, ^{39}K NMR experiments have been conducted on many solid systems. Early ^{39}K NMR experiments were used to measure Knight shifts in potassium metal and potassium-containing alloys[29,30] and chemical shifts in solid potassium halides.[21] The combination of spin–echo sequences and higher magnetic field strengths enabled comprehensive ^{39}K NMR studies on a variety of potassium-containing microcrystalline powders.[31,32] Those initial studies led to further research using ^{39}K NMR to probe a variety of systems,[33,34] including hydrated K$^+$ ions in smectites,[35] potassium ions in buckminsterfullerides,[23,36] alkali-metal superoxides,[37] Hungarian clay,[38] and KTiOPO$_4$, a nonlinear optical crystal.[39] Recently, ^{39}K NMR has been used in the study of biological solids,[40] including a high-field study of K$^+$ ions in G-quadruplex structures.[41,42]

Thus, even though the rapid acquisition of solid-state ^{39}K NMR spectra would be indispensable in a number of areas, published ^{39}K NMR experiments on nonsymmetric potassium sites remain uncommon. It was recently demonstrated that the QCPMG pulse sequence may be used to enhance the signal-to-noise (S/N) ratio in the NMR spectra of half-

-42-

integer quadrupolar nuclei by up to two orders of magnitude.[43,44] QCPMG NMR experiments have been performed on a variety of inorganic and organometallic compounds (^{27}Al, ^{67}Zn and ^{93}Nb NMR),[44-46], minerals ($^{47/49}$Ti and ^{87}Sr NMR),[47,48] organic hydrochloride salts (^{35}Cl NMR),[49] biological solids (^{25}Mg and ^{67}Zn NMR),[50-52] and metallocenes (^{25}Mg and ^{91}Zr NMR).[53,54] The QCPMG sequence has also been used for the detection of the direct dimension in the MQMAS/QCPMG NMR experiment[55] and has been coupled with the DFS[56,57] and RAPT[58] pulse sequences for further signal enhancements.[59]

In this chapter, the first solid-state ^{39}K NMR spectra of organometallic complexes are presented: CpK and Cp*K. The DFS/QCPMG pulse sequence is applied at a standard external magnetic field strength ($\mathbf{B}_0$ = 9.4 T; $v_0(^{39}$K) = 18.65 MHz) to obtain high S/N ^{39}K NMR spectra of very broad CT powder patterns. The spectra are simulated to obtain $\delta_{iso}(^{39}$K), $C_Q(^{39}$K), and $\eta_Q(^{39}$K). Variable-temperature (VT) ^{39}K NMR experiments are conducted to monitor changes in NMR parameters and molecular structure as a function of temperature. ^{13}C CP/MAS NMR experiments are used to measure the carbon chemical shielding (CS) tensors. Theoretical calculations of ^{39}K EFG tensors and potassium and carbon CS tensors are utilized to correlate NMR parameters to molecular structure. The above techniques support the proposed solid-state structure of CpK and qualitatively predict the structure of Cp*K, while also showing their utility as practical probes of sample purity.

2.2 Experimental

2.2.1 Syntheses of C$_5$H$_5$K (CpK) and C$_{10}$H$_{15}$K (Cp*K)

Reagents were handled under a nitrogen atmosphere and all reactions were conducted

-43-

using a Schlenk line. The syntheses of CpK[60] and Cp*K[61] were based upon those in the literature. Purity of both samples was confirmed by solid-state ^{13}C CP/MAS NMR[5,9] (*vide infra*) and pXRD[14,62] (see Appendix A, Figures A.1.1 and A.1.2) experiments.

2.2.2 Solid-State NMR Spectroscopy

2.2.2.1 General NMR Parameters

All samples were ground into fine powders under nitrogen atmosphere and packed into 4 mm (for ^{13}C CP/MAS and ^{39}K MAS NMR experiments) and 5 mm (for ^{39}K static NMR experiments) outer diameter (o.d.) zirconium oxide rotors. All rotors were sealed with airtight caps. Solid-state ^{13}C and ^{39}K NMR spectra were obtained using a Varian Infinity Plus NMR spectrometer with an Oxford 9.4 T ($v_0(^1H)$ = 400 MHz) wide-bore magnet at Larmor frequencies of $v_0(^{13}C)$ = 100.52 MHz and $v_0(^{39}K)$ = 18.65 MHz. CT selective pulse widths used for ^{39}K NMR experiments are equal to the non-selective solution pulse widths scaled by a factor of $(I + 1/2)^{-1}$. For all ^{39}K NMR experiments, tuning and matching the probe circuit was achieved through the use of a Varian/Chemagnetics low-gamma tuning box. A Varian/Chemagnetics 4 mm double-resonance MAS probe was used for all MAS experiments, and a Varian/Chemagnetics 5 mm double-resonance static wideline probe was used for all static ^{39}K NMR experiments.

^{13}C chemical shifts were referenced to TMS (δ_{iso} = 0.0 ppm) by using the high-frequency signal of adamantane as a secondary reference (δ_{iso} = 38.57 ppm). All ^{39}K chemical shifts were referenced to a saturated solution of KBr (δ_{iso} = 0.0 ppm). For all ^{13}C NMR experiments, the experimental pulse delay used was 5.0 s. For ^{39}K NMR experiments,

-44-

calibrated pulse delays utilized were 3.0 – 6.0 and 0.3 s, for CpK and Cp*K, respectively. VT NMR experiments were conducted at temperatures ranging from –120 to 60 °C.

2.2.2.2 ^{13}C CP/MAS NMR

Experiments on Cp*K were optimized using a $\pi/2$ proton pulse width of 6.75 μs ($v_1(^1H) = 37.0$ kHz), a spectral width of 40 kHz and a contact time of 13 ms. The number of transients collected for each of these experiments (at $v_{rot} = 2.0$ kHz and 2.7 kHz) was 48. For CpK, all parameters are the same as above, except that a proton $\pi/2$ pulse width of 5.5 μs ($v_1(^1H) = 45.5$ kHz) was used, 20 transients were collected in each experiment, and $v_{rot} = 2.3$ kHz and 3.0 kHz.

2.2.2.3 ^{39}K QCPMG NMR of CpK

All ^{39}K NMR experiments were conducted using variations of the QCPMG pulse sequence,[43] due to the low receptivity of the ^{39}K nucleus. For static experiments, a CT selective $\pi/2$ pulse width of 2.75 μs ($v_1(^{39}K) = 45.4$ kHz) and spectral width of 150 kHz were used. 18,000 acquisitions were required to achieve reasonable S/N. Interpulse and interacquisition delays τ_1, τ_2, τ_3 and τ_4 were all set to 60 μs. 57 MG loops, each comprised of 70 time-domain points, were acquired, and after the application of a Fourier transform (FT), each QCPMG spikelet was separated by 2,143 Hz.

For the MAS/QCPMG experiment, the number of MG loops and echo size were set equal to 40 and 100, respectively, and 18,496 transients were acquired. A CT-selective $\pi/2$ pulse of 2.5 μs ($v_1(^{39}K) = 50$ kHz) and a spectral width of 80 kHz were applied. The

-45-

MAS/QCPMG pulse sequence requires one to pay special attention to the acquisition of rotor-synchronized data (Figure 2.3): (i) the initial half-echo acquisition is synchronized in the usual MAS-echo manner ($\tau_1 + \frac{1}{2}\pi = \tau_{rot}$) and (ii) the $[\tau_3\text{-}\pi\text{-}\tau_4\text{-}\tau_a]_N$ portion of the sequence must be set equal to $2N\tau_{rot}$.[63] For this experiment, $\tau_{rot} = 55.56$ μs, resulting in $\tau_1 = \tau_2 = 55.56$ μs and $\tau_3 = \tau_4 = 205.8$ μs.
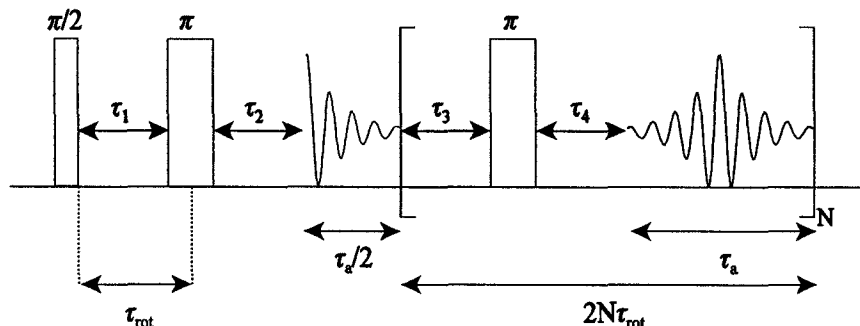
Figure 2.3 The MAS/QCPMG pulse sequence requires rotor-synchronized data acquisition as outlined above. τ_a represents the NMR signal acquisition time.

2.2.2.4 ^{39}K QCPMG NMR of Cp*K

For ^{39}K NMR experiments on Cp*K, the QCPMG pulse sequence was used in a fashion similar to that of the CpK experiments; however, due to the large width of the CT powder pattern (*vide infra*), the spectrum was acquired in a piecewise fashion using transmitter frequencies of $v = 18.71, 18.65, 18.59$ and 18.53 MHz. These four spectra were combined in the frequency domain using co-addition[64-66] and skyline[52] methods. For each piece, a $\pi/2$ pulse width of 2.25 μs ($v_1(^{39}$K) $= 55.6$ kHz) was used, 99,008 transients were acquired, and a spectral width of 150 kHz was employed. All other QCPMG parameters were the same as the static CpK experiment, except that $\tau_1 = \tau_2 = \tau_3 = \tau_4 = 70$ μs.

-46-

2.2.2.5 ^{39}K DFS/QCPMG NMR of CpK

The DFS/QCPMG pulse sequence was optimized and run as previously described.[59] All significant QCPMG parameters were kept the same as those in the static ^{39}K QCPMG NMR experiment on CpK. 800 transients were acquired to build an acceptable ratio of S/N in the static VT experiments, and 18,000 were acquired in the static experiments. Sweeps began 1.40 MHz and ended 0.15 MHz from the centre of gravity of the CT. These sweeps occurred over a period of 850 μs and were divided into 2,720 steps, translating into a sweep rate of $\lambda = 1470.6$ MHz s^{-1} and a sweep adiabaticity ($A = v_1^2/\lambda$) of 0.351.

2.2.2.6 Spectral Simulations

^{39}K EFG parameters were determined using both analytical and numerical simulation methods. All experimental spectra were simulated using the analytical simulation package WSolids.[67] WSolids incorporates the space-tiling method of Alderman and co-workers to generate frequency domain solid-state NMR spectra.[68] Numerical simulations were carried out using the SIMPSON simulation package.[69] All SIMPSON simulations were done via the *direct* method of powder averaging using the *zcw4180* crystal file provided with the package, the start and detect operators were set to I_{1z} and I_{1c}, respectively, and the number of gamma angles were set to 1 and 20 for static and MAS simulations, respectively. Error bounds were determined through bidirectional variation of individual NMR parameters, and best-fit spectra were obtained by comparison of root-mean-square difference spectra.

-47-

2.2.3 Theoretical Calculations

The atomic coordinates of CpK were taken from the refined structure obtained from powder XRD.[14] Calculations were carried out on relatively small CpK clusters ($Cp_2K^-/Cp_2K_3^+/Cp_2K_3/Cp_4K_3^-/Cp_4K_4$) (see Appendix A, Tables in A.2.1 and A.2.2) using two Dell Precision workstations running Red Hat Linux. Gaussian 98[70] and Gaussian 03[71] calculations employed either restricted Hartree-Fock (RHF) or hybrid density functional theory (Becke's three parameter hybrid functional with the correlation functional of Lee, Yang, and Parr (B3LYP)),[72,73] using several standard polarized double-ζ and triple-ζ basis sets provided with the Gaussian software packages (6-31G**/6-311G**/6-311+G**/6-311++G**). Selected calculations used a well-tempered basis set (WTBS) on the potassium atom(s).[74-76] The ^{39}K quadrupolar coupling constant was converted from atomic units into $Hz^{[77,78]}$ by utilizing the formula $C_Q = (eV_{33}Q/h) \times 9.71736 \times 10^{21}$ V m^{-2}, where $Q(^{39}K) = $ + 0.055 $\times$ 10^{-28} m^2,[21] $e = 1.602188 \times 10^{-19}$ C, $h = 6.6260755 \times 10^{-34}$ J s. Potassium CS tensors were calculated using the gauge-including atomic orbitals (GIAO) method[79,80] and referenced against the theoretical isotropic shift ($\delta_{iso} = 0.0$ ppm) of $K(OH_2)_6^+$. The absolute potassium CS of $K(OH_2)_6^+$ was calculated from a structure that was geometry-optimized using the same methodology/basis set combination (see Tables in A.2.3 of the Appendix for optimized structures). Embedded cluster molecular orbital (ECMO) calculations used point charges generated from crystallographically determined atomic coordinates in a 20 Å sphere about a central potassium atom both with (2794 point charges) and without (1521 point charges) explicit proton point charges. Standard (e.g., K = +1.00) as well as calculated Mulliken charges were used. Using the MOLDEN software package,[81] a z-matrix of an

-48-

idealized $Cp_2K_3^+$ crystal structure with C_s point symmetry was constructed in an effort to model temperature-dependent structural changes. For these calculations only, both self-consistent field (SCF) = direct and SCF = tight input commands were used (see A.2.4 of the Appendix for the format of z-matrix used).

2.3 Results and Discussion

2.3.1 ^{39}K NMR of CpK

2.3.1.1 Static and MAS NMR Experiments

QCPMG and DFS/QCPMG pulse sequences were applied to acquire high S/N ^{39}K NMR spectra. The DFS pulse sequence offers theoretical signal enhancement proportional to $2I$ when dealing with single-crystals[82] and slightly less when dealing with microcrystalline powders. Before applying DFS/QCPMG, a preliminary QCPMG spectrum was acquired in order to estimate the values of $C_Q(^{39}K)$ and $\eta_Q(^{39}K)$ (Appendix, Figure A.1.3). These parameters (especially C_Q) must be roughly known, as they determine the high- and low-frequency offset bounds of the frequency sweeps. Optimized ^{39}K static NMR spectra of CpK, acquired with the QCPMG and DFS/QCPMG pulse sequences, as well as analytical and numerical simulations of the powder pattern, are shown in Figure 2.4. When simulating static QCPMG spectra, there are two alternatives: (i) one may match the outer manifold of echo spikelets in the experimental spectrum with a simulated static powder pattern or (ii) the echoes in the QCPMG time-domain may be co-added and processed to produce a powder pattern which is then directly compared to that of a simulation (Figure 2.5). Methods (i) and (ii) are similar, as they very closely match the same simulated powder

-49-

pattern: $C_Q(^{39}K) = 2.55(6)$ MHz, $\eta_Q(^{39}K) = 0.28(3)$, and $\delta_{iso}(^{39}K) = -100(20)$ ppm (potassium

CSA is neglected in the simulation, *vide infra*).
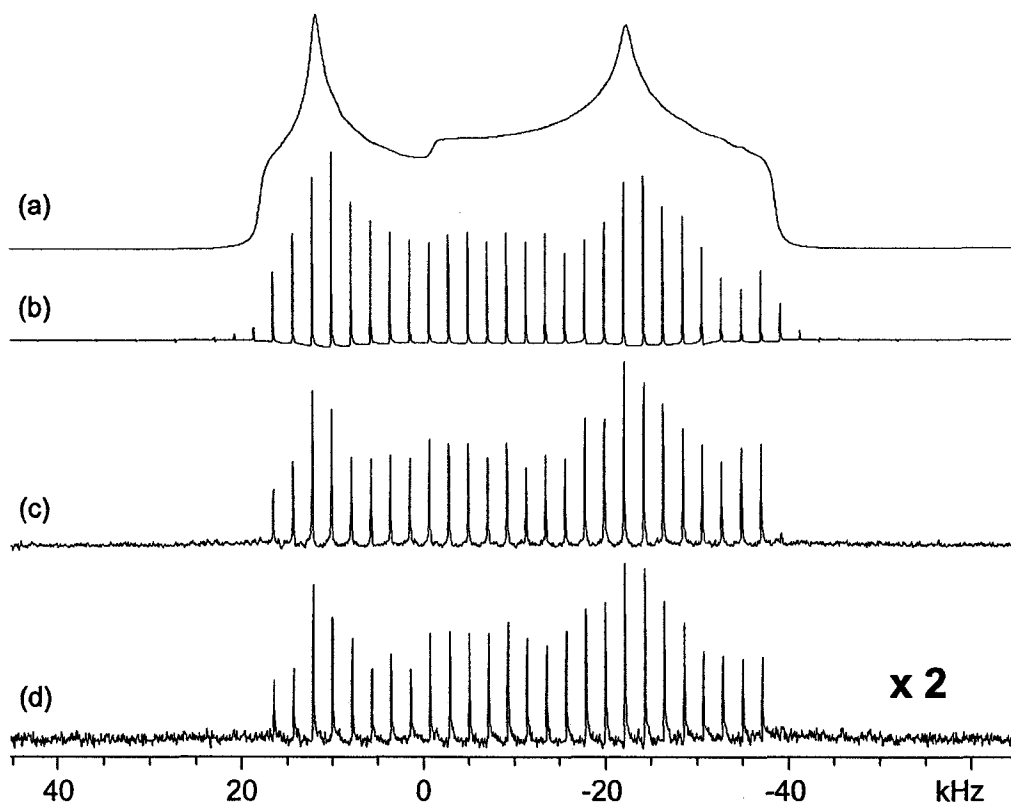
Figure 2.4 All traces depict static ^{39}K NMR signals of CpK at $v_0(^{39}K) = 18.65$ MHz. (a) Analytical simulation using WSolids; NMR parameters used: $C_Q(^{39}K) = 2.55(6)$ MHz, η_Q $(^{39}K) = 0.28(3)$, and $\delta_{iso} = -100(20)$ ppm. (b) Numerical SIMPSON simulation using the same parameters as in (a). For comparison, both (c) DFS/QCPMG and (d) QCPMG spectra were acquired using the same QCPMG parameters, and they clearly depict that the DFS/QCPMG sequence provides higher S/N. Note that the vertical scale of (d) has been increased by a factor of 2.

When comparing experimental and simulated powder patterns of Figure 2.5, there is not an exact match between the experimental and simulated manifolds; however, the discontinuities and shoulders in the experimental powder pattern can be precisely identified,

-50-

thereby yielding accurate NMR parameters. Possible reasons for the less than perfect

agreement include (i) low S/N, (ii) insufficient number of points comprising the spin–echo,

and/or (iii) nonuniform excitation of the CT powder pattern.[83-85] The last explanation may

be discarded, as the CT-selective $\pi/2$ pulse width used in the QCPMG and DFS/QCPMG

experiments was 2.75 μs ($v_1(^{39}K)$ = 45.5 kHz), well within the acceptable range for uniform

excitation of an approximately 55 kHz wide powder pattern.[86]
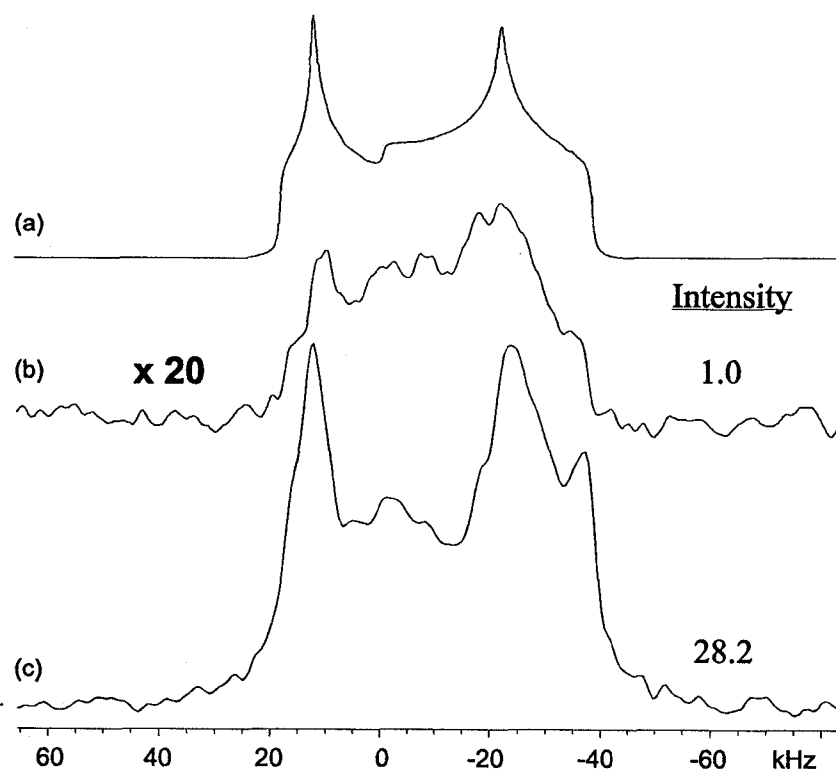
Figure 2.5 Comparison of integrated intensities between (b) the Hahn-echo and (c) the
DFS/QCPMG pulse sequences. For this comparison, the vertical scale of (b) was increased by a
factor of 20 and given a normalized integrated intensity of 1.0.

Regardless of the minor issues outlined above, the S/N ratios, as well as the system

responses isolated from the QCPMG and DFS/QCPMG experiments, are superior to the

conventional Hahn-echo experiment (Figure 2.5). It is clear that the Hahn-echo sequence is not suitable for solid-state [39]K NMR experiments when the electronic environment about the potassium nucleus is not near spherical symmetry. Even after increasing the vertical scale by a factor of 20, the Hahn-echo trace appears nearly void of features, making quantitative NMR analysis very difficult. Overall enhancement, normalized with respect to the integrated intensity of the Hahn-echo experiment, is 28.2 through application of the DFS/QCPMG sequence and 15.2 for the QCPMG pulse sequence. Integrated intensities were obtained by co-adding the CPMG echo trains until a single spin-echo was isolated.[87]

[39]K MAS NMR experiments on CpK were conducted to confirm quadrupolar parameters and to aid in quantifying the contribution of potassium CSA to the static spectra. A 4 mm od rotor was chosen over a 5 mm od rotor due to the relatively high spinning frequency required to separate the spinning sidebands from the CT. A [39]K MAS/QCPMG NMR spectrum acquired with a spinning frequency of ν_{rot} = 18 kHz is shown in Figure 2.6. Spectral simulations using SIMPSON and WSolids reveal C_Q([39]K) = 2.67(8) MHz and η_Q ([39]K) = 0.29(3), in good agreement with the corresponding static [39]K NMR spectra (spinning sidebands are not entirely resolved due to insufficient S/N). The slightly larger C_Q measured in the MAS spectrum is likely the result of frictional sample heating, as opposed to potassium CSA, as the C_Q of alkali metals in unsolvated Cp'M complexes are known to increase with increasing temperature (see reference 18 and VT [39]K NMR data below). Analytical simulations including the effect of potassium CSA (Ω = 100 ppm; Appendix, Figure A.1.4) suggest that its effect on static [39]K NMR spectra is negligible at $\mathbf{B}_0$ = 9.4 T and that the powder patterns are dominated by the quadrupolar interaction. In addition,

-52-

theoretical calculations (*vide infra*) suggest an upper limit to the potassium CSA of about 60 ppm, representing a contribution of less than 2 % of the total breadth of the static pattern at $B_0 = 9.4$ T. For accurate elucidation of CS tensor parameters, spectral acquisitions at very high magnetic fields (e.g., $B_0 = 18.8$ T or higher) may be required.
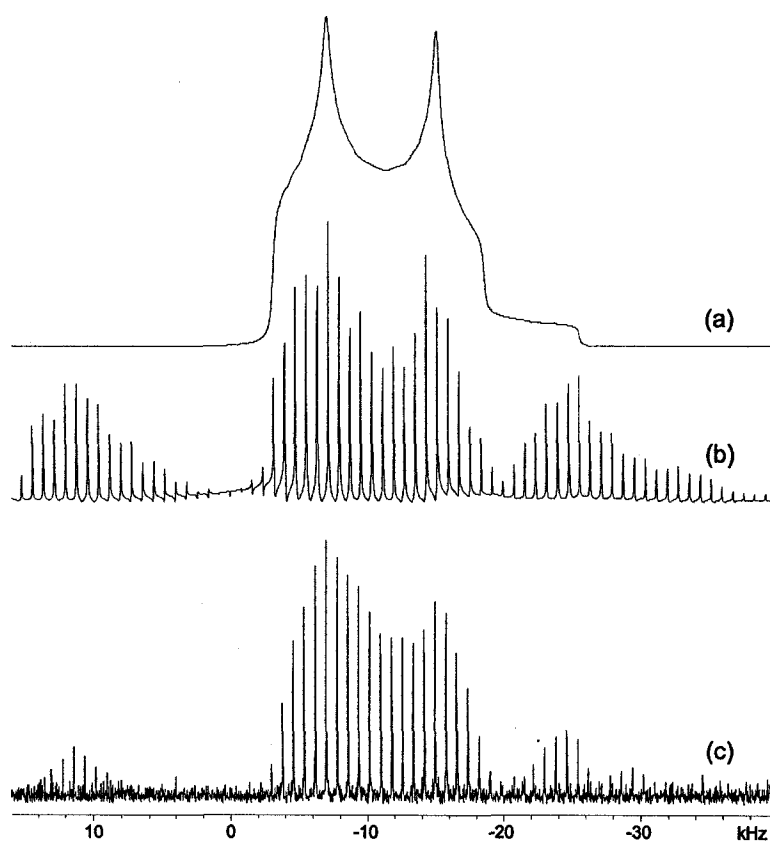
Figure 2.6 All traces depict ^{39}K MAS NMR signals of CpK at $v_0(^{39}$K$) = 18.65$ MHz; (a) assumes an infinite spinning frequency, while (b) and (c) were done at $v_{rot} = 18$ kHz. (a) Analytical WSolids simulation using the following parameters: $C_Q(^{39}$K$) = 2.67(8)$ MHz, η_Q (^{39}K$) = 0.29(3)$, and $\delta_{iso} = -75(30)$ ppm. (b) Numerical SIMPSON simulation using the same NMR parameters as (a). (c) Experimental MAS/QCPMG powder pattern of CpK, requiring 18,496 transients (experiment time ~16 h).

According to pXRD studies, smaller alkali metals such as Li and Na often result in

linear chains when they are constituents of Cp'M complexes, whereas the extended structure of CpK is proposed to be a long zigzagging chain. Solid-state ^{23}Na NMR experiments on straight linear Cp'Na complexes[20] reveal, in all cases, a near zero value for $\eta_Q(^{23}\text{Na})$, reflecting the axial symmetry of the sodium environments. In this same study, solid-state ^{23}Na NMR experiments were conducted on CpNa·THF, establishing that $\eta_Q(^{23}\text{Na}) = 0.39(2)$. It was postulated that the non-zero η_Q value corresponded to a zigzagging linear polymeric structure, a finding which is confirmed using refined single-crystal XRD data (vide infra, Chapter 4). Hence, the non-zero η_Q for CpK is consistent with a zigzagging polymeric structure and a non-axial ground-state electronic environment about the potassium nucleus, in support of previous pXRD findings.[14]

The low-frequency shift ($\delta_{\text{iso}}(^{39}\text{K})$) of CpK with respect to the aqueous standard is similar to that observed for a variety of main-group metallocenes, such as in ^{27}Al NMR spectra of Cp_2Al^+,[88] ^{11}B NMR spectra of Cp_2B^+,[89] and ^{23}Na NMR spectra of Cp'Na complexes.[20] Similar chemical shifts have also been observed for Na^+ and K^+ cations which are coordinated to π-electron systems in solid $Na[BPh_4]$ and $K[BPh_4]$.[34] In addition, although there is a considerable difference between the powder pattern breadths in the ^{39}K NMR spectra of CpK and ^{23}Na NMR spectra of CpNa (55 kHz and 14 kHz, respectively at $\mathbf{B}_0 = 9.4$ T), their C_Q values are comparable: 2.55 MHz for CpK and 2.97 MHz for CpNa. The increased breadth of the powder pattern in the ^{39}K NMR spectrum results from a combination of (i) low $\nu_0(^{39}\text{K})$ and (ii) much larger EFGs (i.e., larger V_{33}) in CpK (as the eQ for ^{39}K is almost half that of ^{23}Na).

-54-

2.3.1.2 Variable-Temperature (VT) NMR Experiments

When acquiring VT ^{39}K NMR data for CpK, conventional Hahn-echo experiments cannot be used as they do not offer enough sensitivity. The QCPMG sequence offers significant S/N enhancement, reducing experimental times to about 5 h per temperature point; however, the DFS/QCPMG pulse sequence is used here as it is even more efficient. By reducing the experimental time to 1 h per temperature point, it reduces wear on the NMR probe and the consumption of cryogens. Thus, even though several steps (outlined earlier) are required to obtain an optimized DFS/QCPMG spectrum, this method is faster than the conventional spin-echo experiment by more than an order of magnitude: it is estimated that the same set of VT data would take almost a week a gather using the spin-echo sequence.

The number of scans in the VT DFS/QCPMG spectra is decreased with respect to the room temperature static experiment presented earlier in an effort to reduce experimental time, while still providing a reasonably accurate estimate of changes in quadrupolar parameters with temperature. As the temperature is decreased, the value of C_Q is observed to decrease from 2.60 MHz at +60 °C to 2.35 MHz at −120 °C (Table 2.1; Figure 2.7). Similar temperature-dependent behaviour was observed for VT ^{23}Na NMR experiments on linear Cp′Na complexes as with decreasing temperature, $C_Q(^{23}$Na) is observed to decrease. The EFG asymmetry parameter ($\eta_Q(^{39}$K)) is observed to increase from 0.27 to 0.36 as the temperature is decreased from +60 °C to −120 °C. This change is similar to, though more modest than, the temperature-dependent change of $\eta_Q(^{23}$Na) in the VT ^{23}Na NMR spectra of CpNa·THF. Correlation between observed NMR parameter changes and temperature-dependent structural changes will be addressed in the theoretical section of the discussion.

-55-

Table 2.1 Experimental ^{39}K Chemical Shift and Quadrupolar Parameters [a]

experiment	temp (K)	molecule	C_Q (MHz)	η_Q	δ_{iso} (ppm)
Static	293	CpK	2.55(6)	0.28(3)	−100(20)
MAS [b]	293	CpK	2.67(8)	0.29(3)	−75(30)
VT - Static	333	CpK	2.60(8)	0.27(3)	−100(30)
VT - Static	273	CpK	2.51(8)	0.28(3)	−100(30)
VT - Static	213	CpK	2.44(8)	0.29(3)	−100(30)
VT - Static	153	CpK	2.35(8)	0.36(3)	−100(30)
Static	293	Cp*K	4.69(8)	0.30(3)	−140(40)

[a] Parameter definitions can be found in chapter 1.

[b] MAS rotation frequency, v_{rot} = 18 kHz.
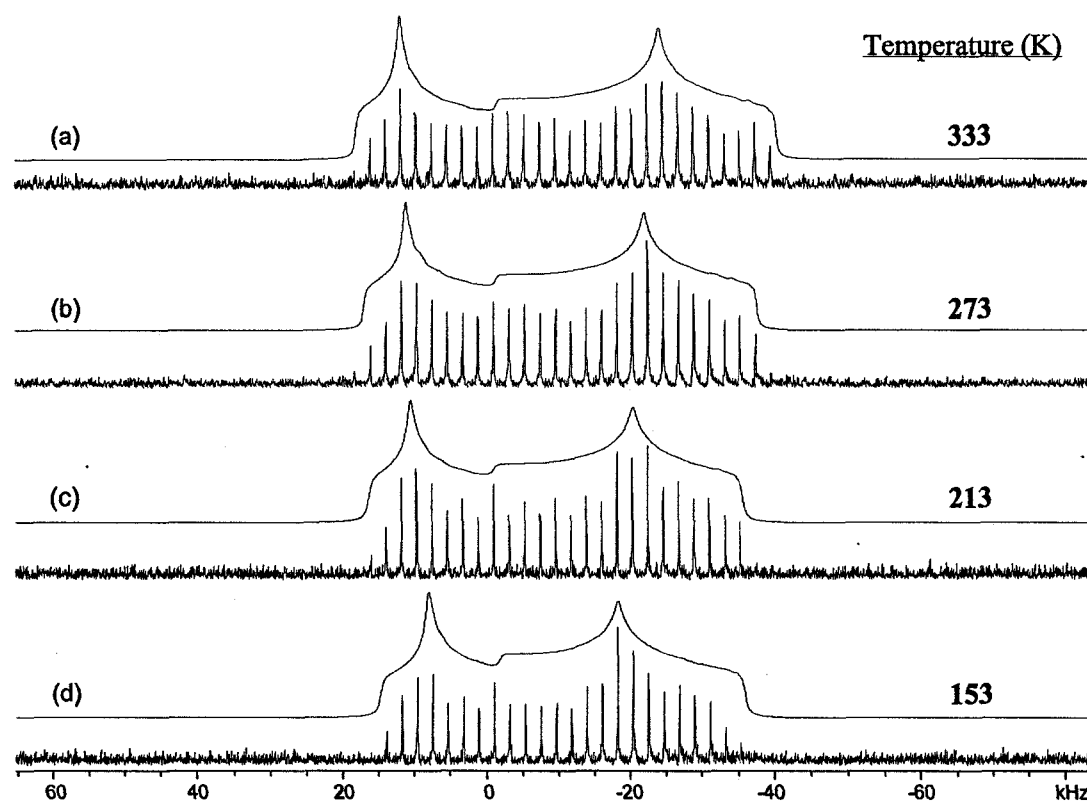
Figure 2.7 VT ^{39}K NMR spectra of CpK at (a) 333 K, (b) 273 K, (c) 213 K, and (d) 153 K. In all cases, the top trace is the corresponding WSolids analytical simulation of the experimental bottom trace. Simulation parameters are given in Table 2.1.

-56-

2.3.2 ^{39}K NMR of Cp*K

Initial static ^{39}K NMR experiments on Cp*K revealed that the CT powder pattern exceeded any achievable excitation bandwidth. The small magnetogyric ratio of ^{39}K greatly limits the selective excitation of this extremely broad CT powder pattern. As QCPMG experiments enhance the rate at which broad powder patterns can be acquired, a piecewise acquisition of the entire powder pattern should be possible. The wide-line NMR experiment employed here is much like the usual NMR experiment, but differs such that the final NMR spectrum presented is the sum of several "sub-spectra".[64-66] An initial spectrometer frequency of 18.65 MHz was used due to its proximity to the reference, and then, with the aid of Maple 7,[90] several offset frequencies (v_{off}) are theoretically tested to ensure uniform excitation over the entire wide-line spectrum (Figure 2.8). Once a reasonable offset frequency has been established, sub-spectra are acquired along both frequency-domain directions until the system response at a particular transmitter frequency is significantly reduced; at this point, the lack of response is taken to denote the edge of the central-transition. The sub-spectra are then individually subjected to a Fourier transformation and co-added in the frequency domain. Individual slices, as well as the co-added spectrum, are provided in Figure 2.9a. This methodology is considerably more efficient than the so-called "point-by-point" method,[91] which involves plotting the echo intensity as a function of offset frequency and thereby requires many more data points (each corresponding to an NMR experiment) to be collected. Aside from the co-addition method outlined above, it is also possible to produce a skyline projection of the spectra[52] (Figure 2.9b, middle trace, asterisk denotes an impurity at ca. 0 ppm, which is likely due to the presence of an inorganic

-57-

potassium salt).
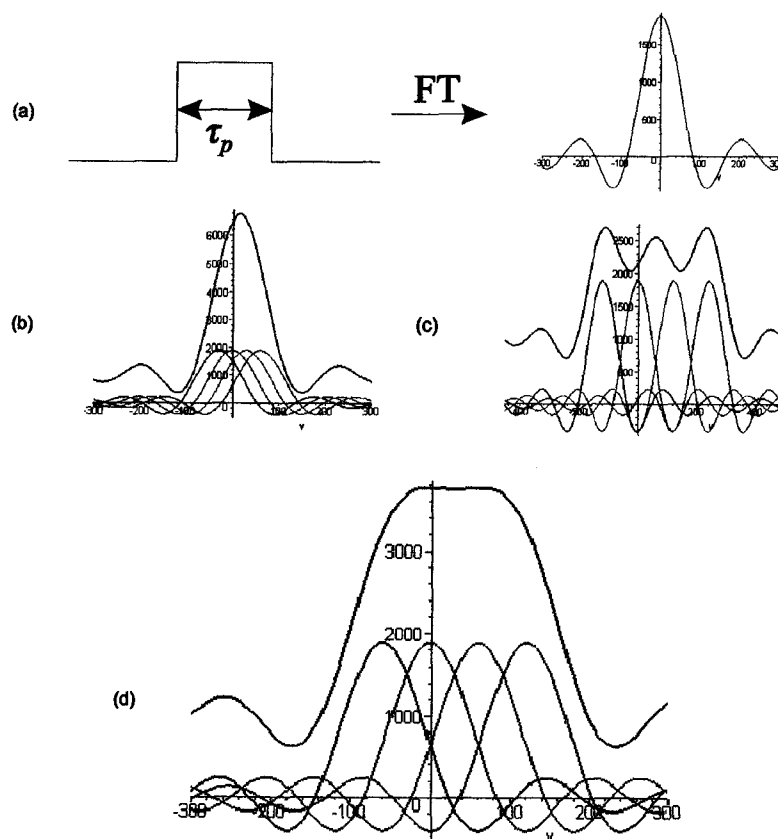
Figure 2.8 Maple 7 renderings of pulses. (a) Ideal square pulse and corresponding excitation pattern (described by a sinc function) after Fourier transformation. Various offset frequencies are shown, including (b) $v_{off} = 30$ kHz, (c) $v_{off} = 120$ kHz, and (d) $v_{off} = 60$ kHz. In (b-d), the co-added pulse is offset above the rest of the pulses. If the offset between sinc functions is too small or too large (as in (b) and (c), respectively), the co-added excitation profile will not be ideal. When the sum of the individual pieces form a shape exhibiting uniform excitation (as in (d)), that offset frequency is chosen.

Regardless of the processing method used, the NMR parameters isolated from analytical simulations are very similar to one another: $C_Q(^{39}K) = 4.69(8)$ MHz, $\eta_Q(^{39}K) = 0.30(3)$, and $\delta_{iso} = -140(40)$ ppm. As with CpK, the nonzero η_Q value should correspond to

-58-

a zigzagging polymeric structure. Additionally, the increased $C_Q(^{39}K)$ value for Cp*K relative to CpK can be interpreted as resulting from a decrease in the K–Cp$_{cent}$ distance (Cp$_{cent}$ = geometric centre point of Cp ring), as substitution of the Cp' ring with alkyl groups has been correlated to a decrease in M–Cp$_{cent}$ distance (see reference 2 and the discussion below dealing with the effects of structural changes on CpK tensor parameters). Solid-state NMR is the only experimental technique for which Cp*K structural information has been elucidated, as no structure has been obtained from the available X-ray data.
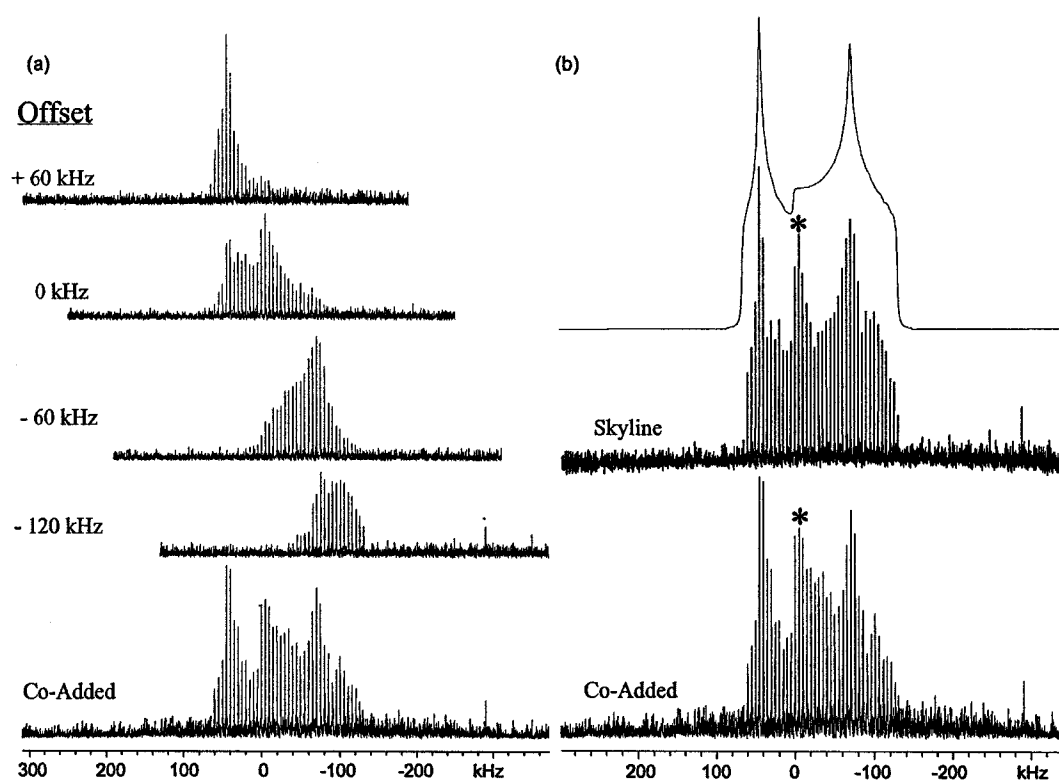
Figure 2.9 All traces depict static ^{39}K NMR signals of Cp*K. (a) Four static Cp*K ^{39}K NMR sub-spectra, each having a different transmitter offset frequency, are co-added in the frequency-domain, producing the bottom trace. (b) WSolids analytical simulation (top trace) using the following parameters: $C_Q(^{39}K)$ = 4.69(8) MHz, $\eta_Q(^{39}K)$ = 0.30(3), and δ_{iso} = –140(40) ppm. Corresponding experimental patterns, each composed of four sub-spectra, are produced using the skyline (middle trace) and co-addition (bottom trace) processing methods.

-59-

2.3.3 ^{13}C CP/MAS NMR

Carbon-13 CP/MAS NMR experiments were conducted on both CpK and Cp*K in order to measure carbon CS tensors. Presented in Figure 2.10 are ^{13}C CP/MAS NMR spectra of CpK and Cp*K. In the case of CpK, a single isotropic peak (δ_{Cp} = 106.2 ppm) is observed as the carbon atoms of the Cp ring are undergoing rapid 5-fold reorientations (*vide infra*). For Cp*K, two isotropic peaks are isolated, one corresponding to the five carbon atoms that comprise the cyclopentadienyl ring (δ_{Cp} = 106.8 ppm), and one belonging to the carbon atoms that are part of the five equivalent methyl groups (δ_{Me} = 11.0 ppm). Herzfeld–Berger analysis[92] was conducted to determine the carbon CS tensors for the aromatic Cp' carbons. For both CpK and Cp*K, the results clearly show a carbon CS tensor that is very close to being perfectly axially symmetric (i.e., $\delta_{11} \cong \delta_{22}$ according to the standard convention, see Table 2.2), analogous to the Cp$_2$Mg[53] and CpNa[20] systems, among others.[88,93,94]

Table 2.2 Experimental Carbon CS Tensor Parameters ^{a}

molecule	carbon	δ_{11} (ppm)	δ_{22} (ppm)	δ_{33} (ppm)	δ_{iso} (ppm)	Ω (ppm)	κ
CpK	Cp	146.7	144.3	27.7	106.2	119.0	0.97
Cp*K	Cp	142.6	142.6	35.0	106.8	107.6	1.00
	Me	—	—	—	11.0	—	—

^{a} Parameter definitions can be found in chapter 1.
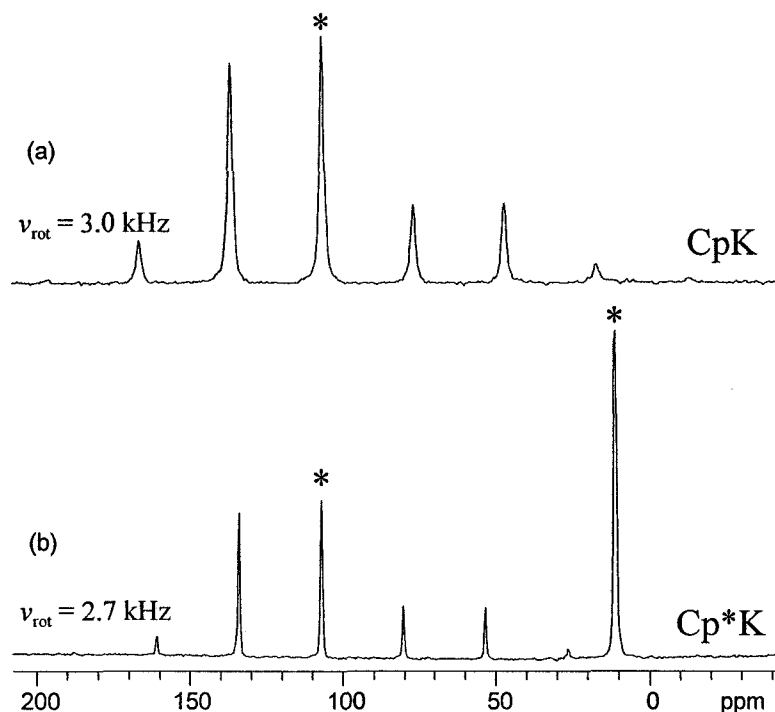
Figure 2.10 ^{13}C CP/MAS NMR experiments on (a) CpK (v_{rot} = 3.0 kHz) depict a single, isotropic peak (δ_{Cp} = 106.2 ppm), while similar mechanical rotation conditions (b) (v_{rot} = 2.7 kHz) show two isotropic peaks (δ_{Cp} = 106.8 ppm; δ_{Me} = 11.0 ppm) for Cp*K.

2.3.4 Detection of Impurity Phases via NMR

Polymeric metallocenes are in general very sensitive to air and moisture. Solid-state ^{13}C and ^{39}K NMR experiments can be used to confirm sample purity and potentially identify decomposition products (Appendix, Figures A.1.5 and A.1.6). ^{13}C CP/MAS NMR experiments on a sample of CpK which had been exposed to the atmosphere show no trace of resonances corresponding to Cp ring carbons. The broad peak at ca. 133 ppm corresponds to free cyclopentadiene, while the sharper peaks at 169 and 162 ppm likely correspond to functional groups containing C=O bonds.[95] In addition, ^{39}K NMR spectra reveal a relatively narrow powder pattern, indicating that the potassium is in a completely distinct chemical

-61-

environment from CpK. If the second-order quadrupolar interaction is taken into account, then the isotropic shift is near 0 ppm, which indicates the presence of a simple potassium salt. The observations of completely different chemical compositions are further supported by powder XRD experiments, which reveal distinct powder patterns for the fresh and exposed samples of CpK (Appendix, Figure A.1.7).

2.3.5   Theoretical Calculations of NMR Tensor Parameters

Calculations were conducted on CpK only, as a refined crystal structure has been proposed from Rietveld analysis of a powder XRD pattern.[14] Several calculations used a WTBS on each potassium atom, corresponding to 26 functions describing each of the four s-orbitals and 16 functions describing each of two p-orbitals.

2.3.5.1 ^{39}K Quadrupolar Coupling Constant, $C_Q(^{39}K)$

Calculated ^{39}K EFG parameters which most closely match the experimental findings for the CpK complex can be found in Table 2.3 (see Table A.2.5.1 in the Appendix for the rest of the data set). When considering calculations that did not employ the WTBS, C_Q values vary between 1.25 and 4.10 MHz, with no one set of calculations approaching the experimental value of 2.55 MHz. Both precision and accuracy are increased when calculations included a WTBS: C_Q values converge into the 1.38 to 2.65 MHz range; however, there is a corresponding increase in computational time by a factor of 4 to 8. When the WTBS is used on the potassium atoms, cluster size does not appear to affect calculated EFG tensor parameters significantly, though cluster size is a significant parameter when

-62-

WTBSs are not used. Independent of the basis set applied, cluster charge variance along the series +1, 0, −1 results in a steady increase in C_Q. Neither the RHF nor B3LYP method appears to be far superior to the other in predicting the experimental C_Q value when considering all calculations. It is therefore suggested that the calculated values depend most strongly upon (i) molecular charge and, to a lesser extent, (ii) basis set. The RHF method, when used in tandem with anionic clusters and the WTBS on the potassium atoms, has proven to be the best at predicting $C_Q(^{39}K)$.

Table 2.3 Experimental and Theoretical ^{39}K EFG Tensor Parameters for CpK

cluster	method	basis set [a]	V_{11} (au)	V_{22} (au)	V_{33} (au)	$|C_Q|$ (MHz)	η_Q
CpK	exp	static	—	—	—	2.55(6)	0.28(3)
CpK	exp	MAS	—	—	—	2.67(8)	0.29(3)
Cp_2K^-	RHF	6-31G**	−0.0747	−0.1240	0.1987	2.568	0.2481
$Cp_2K_3^+$	RHF	6-31G**	−0.0651	−0.1173	0.1824	2.357	0.2862
Cp_3K_3	RHF	6-31G**	−0.0671	−0.1181	0.1852	2.394	0.2750
$Cp_4K_3^-$	RHF	6-31G**	−0.0694	−0.1191	0.1884	2.435	0.2639
Cp_4K_4	RHF	6-31G**	−0.0685	−0.1185	0.1870	2.417	0.2671
Cp_2K^-	RHF	6-311G**	−0.0753	−0.1298	0.2051	2.651	0.2659
$Cp_2K_3^+$	RHF	6-311G**	−0.0639	−0.1239	0.1878	2.427	0.3192
Cp_3K_3	RHF	6-311G**	−0.0665	−0.1249	0.1915	2.474	0.3049
$Cp_4K_3^-$	RHF	6-311G**	−0.0696	−0.1262	0.1959	2.531	0.2891
Cp_4K_4	RHF	6-311G**	−0.0684	−0.1255	0.1939	2.506	0.2947

[a] Carbon and hydrogen atoms only; a WTBS was used on potassium atoms.

2.3.5.2 ^{39}K EFG Tensor

As long as certain minimal requirements (polarized triple-ζ basis set on all atoms and $Cp_2K_3^+$ cluster) are satisfied, the ^{39}K EFG tensor orientation is consistent and appears

-63-

insensitive to any methodology, cluster size/charge or basis set changes. In contrast with sodocene analogues, the major component of the tensor, V_{33}, does not point at the centroid of either of the Cp rings (Figure 2.11). Rather, V_{33} lies very close to the c-axis of the crystallographic unit cell (which is of space group $P\bar{4}2_1c$), which is nearly coincident with the direction of CpK propagation. Consequences of these orientations are evident when considering the temperature-dependent changes in the CpK structure (*vide infra*).

(a) $V_{33} \parallel$ to pg; V_{11}/V_{22} 45° to pg   **(b)** $V_{33} \perp$ to pg
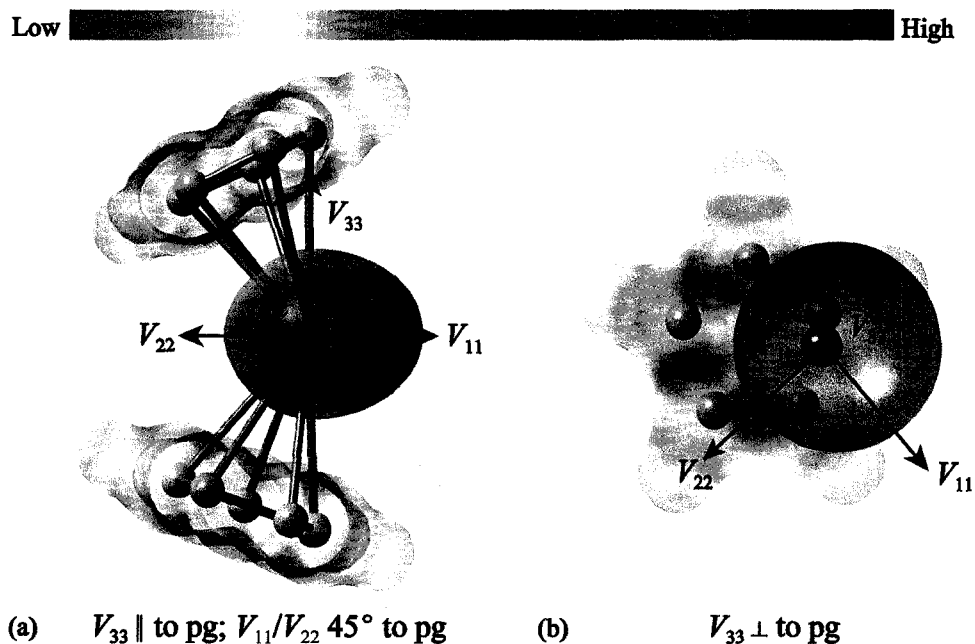
Figure 2.11 GaussView[96] renderings of the electron density mapped onto the electrostatic potential of a Cp_2K^- fragment, along with ^{39}K EFG tensor orientations when (a) V_{33} is parallel to the plane of the page and when (b) V_{33} is perpendicular to the plane of the page. Note that the crystallographic c-axis is nearly coincident with V_{33}. In order to enhance clarity, (a) is presented without protons and (b) is provided with the top Cp ring, as well as all protons and atomic bonds, removed.

2.3.5.3 Asymmetry Parameter, $\eta_Q(^{39}K)$

Regardless of the basis set and calculation method, all calculations predict a non-zero value for η_Q, indicating a slight to moderate deviation from axial symmetry about the

-64-

potassium atom and supporting a zigzagging polymeric structure. Calculations using a polarized double- or triple-ζ basis set on all atoms consistently underestimate η_Q, predicting values between 0.10 and 0.21. Neither the use of larger basis sets of this type nor variations in computational methodology result in close agreement with the experimental η_Q. When a WTBS is used on the potassium atoms, significant improvement is usually observed and is most dramatic when using the RHF method. Cluster charge also appears to be a significant factor in predicting η_Q: as the charge of the cluster changes in the series $+1, 0, -1$, the calculated η_Q value decreases in a steady manner. The best agreement between experiment and theory is found when employing the RHF method and the WTBS on the potassium atoms, as η_Q is predicted to be between 0.25 and 0.35.

According to the refined XRD structure, every potassium atom is ca. 3.33 to 3.66 Å away from two carbon atoms in neighbouring CpK chains, thus it is possible that these nearby chains influence the asymmetry parameter. Embedded cluster molecular orbital (ECMO) calculations were conducted as they may better approximate the electrical environment about the potassium nucleus. Analysis of the results (Table A.2.5.1) demonstrate that η_Q values are not approximated any better using this approach, strongly implying that the dominant influences on the ^{39}K EFG tensor are intramolecular. ECMO calculations predict a decrease for the C_Q in all cases and afford a marginally higher correlation between experiment and theory.

2.3.5.4 Effects of Ring Dynamics and Structural Changes on CpK Tensor Parameters

In an effort to correlate the NMR parameters observed in the ^{13}C CP/MAS NMR and

VT ^{39}K NMR experiments with Cp ring dynamics and temperature-dependent structural changes, a computational study was carried out to simulate (i) Cp ring rotation, (ii) lengthening and shortening of the Cp_{cent}–K distance, and (iii) variation in the Cp_{cent}–K–Cp_{cent} angle. Although it may account for minor changes in EFG parameters, the Cp ring "tip angle" (i.e., the angle a plane defined by the Cp ring makes with a vector parallel to the direction of the Cp_{cent}–K bond) was always kept constant at an idealized value of 90 °. The atoms of the Cp rings were input as being planar in an effort to reduce computational time (the crystal structure does show a slight deviation from planarity). A single structural parameter (as outlined above) was adjusted in a given set of calculations while holding all other structural parameters fixed, to draw simple qualitative correlations between the adjustable parameter and changes in the appropriate tensor. For all calculations, the $Cp_2K_3^+$ cluster was used with the B3LYP method and 6-311+G** basis set, as this combination provided very good agreement between experiment and theory. This permits comprehensive sets of calculations to be done, while not being overly computationally expensive.

It is quite reasonable to expect rapid Cp ring rotation at room temperature on the time scale of the NMR experiment.[97] Theoretical results presented here strongly support this notion (Figure 2.12). The barrier associated with ring rotation is slight at about 0.093 kJ mol^{-1} (35.4 μHartrees), which is similar to the theoretically determined value for CpNa. Changes in ^{39}K EFG tensor parameters due to rapid Cp ring rotation are negligible, $\Delta C_Q(^{39}K)$ = 0.0015(1) MHz; $\Delta \eta_Q(^{39}K)$ = 0.004(1), and should not account for any discrepancy between experimental and theoretical parameters.

-66-
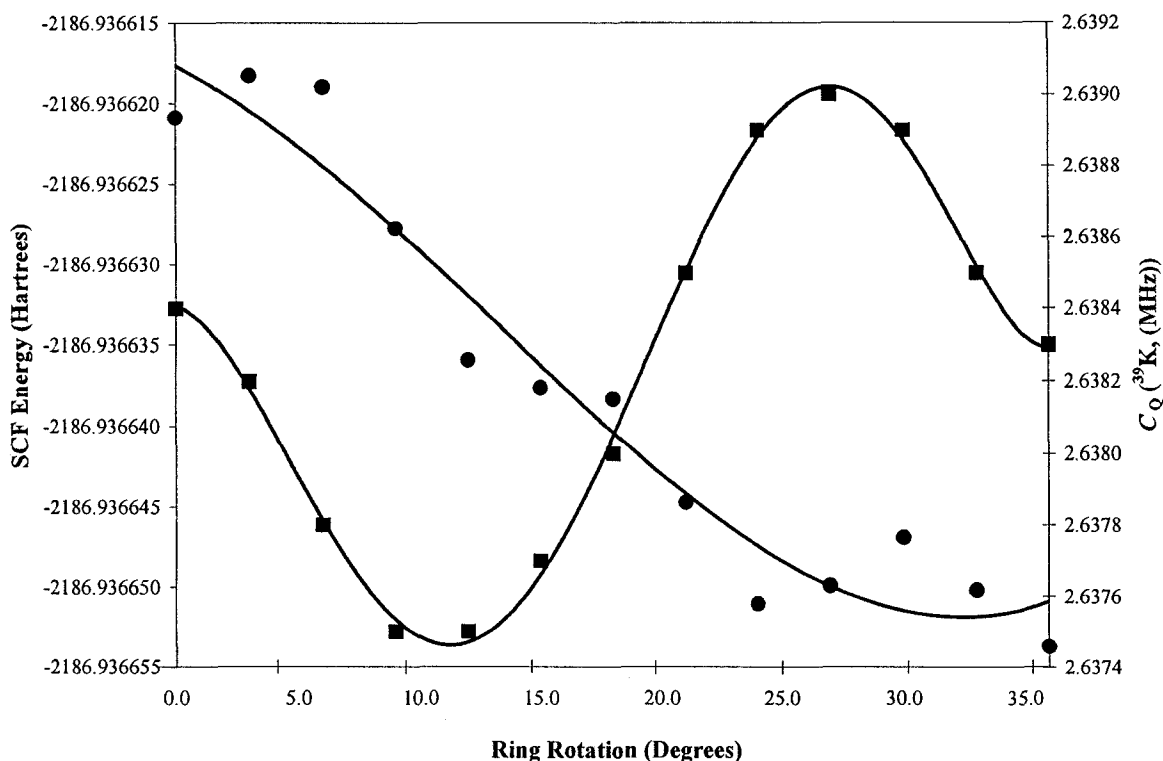
Figure 2.12 Theoretical calculations indicate the feasibility of rapid Cp ring rotation at ambient temperatures. Results show the C_Q (■) and SCF energy (●) changes are very slight as the Cp ring is rotated from an eclipsed ($\theta = 0°$) to staggered ($\theta = 36°$) conformation. Calculations were carried out on an isolated $Cp_2K_3^+$ chain using the B3LYP method and 6-311+G** basis set on all atoms.

We postulate that the changing ^{39}K quadrupolar parameters in the VT ^{39}K NMR experiments presented above arise from temperature-dependent structural changes in CpK, most likely from temperature-induced alterations in the Cp_{cent}–K bond length and/or Cp_{cent}–K–Cp_{cent} bond angle. According to the EFG parameters obtained from theoretical modelling, a decrease in C_Q may arise from an increasing Cp_{cent}–K bond distance and/or a decreasing Cp_{cent}–K–Cp_{cent} angle, while an increase in η_Q may be attributed to a decrease in the Cp_{cent}–K–Cp_{cent} angle (Figure 2.13). The experimentally observed change in η_Q from 0.27

-67-

to 0.36, when compared to changes in η_Q that were calculated, shows that the angle variance is slight: the decrease in the Cp_{cent}–K–Cp_{cent} angle from its experimentally determined value is likely in the range 3° to 6° as the temperature is decreased from 333 to 153 K. As V_{33} of the EFG tensor points nearly along the c-axis of the unit cell, this likely means that as the temperature of the CpK system increases, the linear polymeric structure of CpK becomes increasingly straight. The temperature-dependent behaviour seen here is similar to what was predicted for Cp′Na systems when studied via ^{23}Na NMR, though it is less pronounced in the [39]K NMR parameters due to the orientation of the [39]K EFG tensor.[20] VT pXRD experiments will be utilized to confirm the proposed models of behaviour in forthcoming studies (VT pXRD data on two of the linear polymeric sodocenes are provided in Chapter 4).

2.3.5.5 Potassium Chemical Shielding

As mentioned earlier, the contribution of potassium CSA to the observed [39]K NMR powder patterns does not appear to be particularly significant. In full support of the experimental findings, calculated potassium CSA values (Tables 2.4 and A.2.5.2) predict very minimal CSA-based powder pattern broadening. Theoretical values are relatively close to one another considering the overall breadth of the CpK powder pattern (9 ppm < Ω < 63 ppm), showing a general independence to the method, basis set, cluster size, and cluster charge used in the calculation. Non-WTBS, RHF calculations with short chains predict the most significant CSA, while WTBS calculations using small basis sets on all other atoms predict the smallest CSA.

-68-
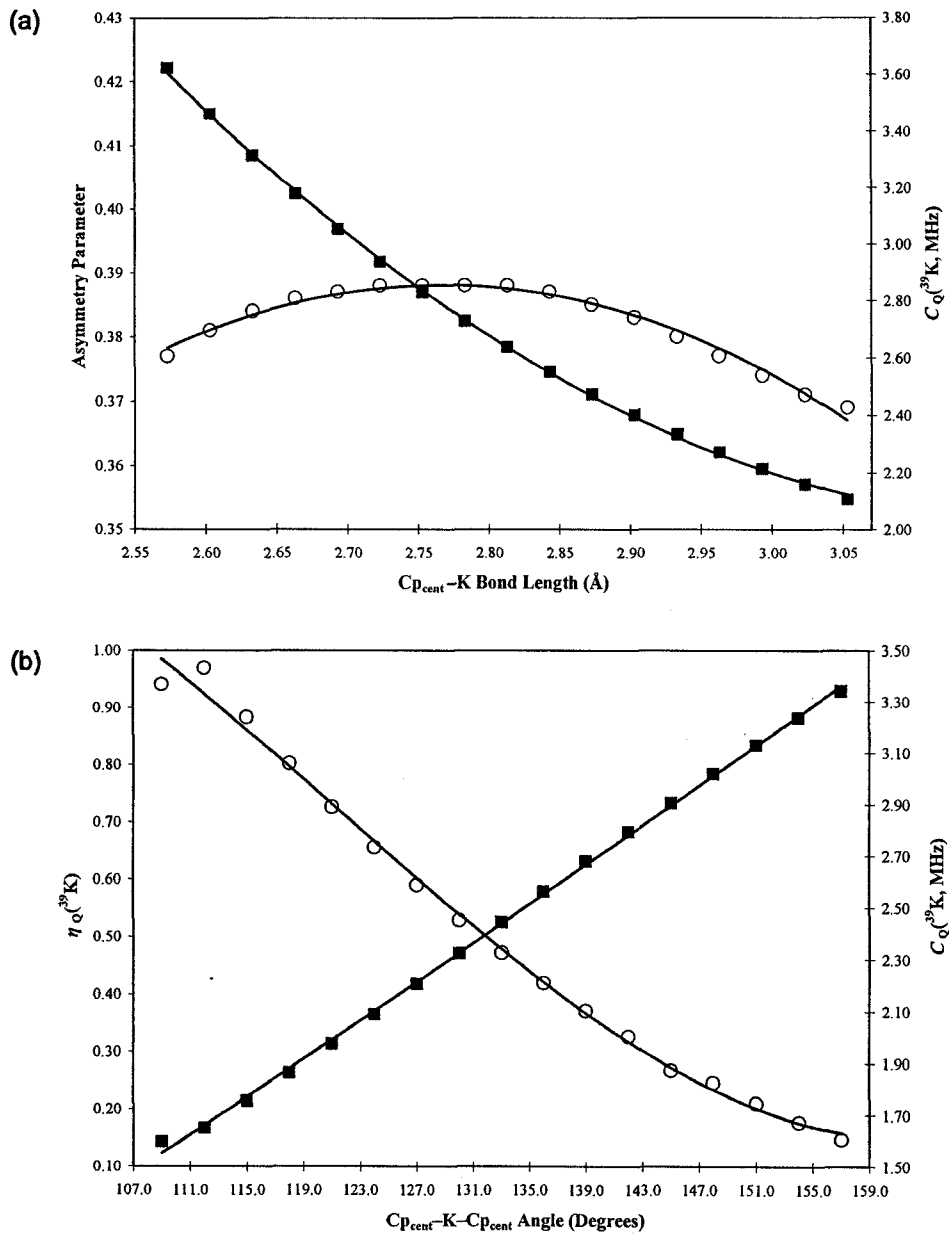
Figure 2.13 Theoretical calculations showing (a) the change in η_Q (O) and C_Q (■) when the Cp_{cent}–K bond length is modified and (b) the change in η_Q (O) and C_Q (■) when the Cp_{cent}–K–Cp_{cent} angle is altered. Calculations were carried out upon an isolated $Cp_2K_3^+$ chain using the B3LYP method and 6-311+G** basis set on all atoms.

-69-

Table 2.4 Experimental and Theoretical Potassium Chemical Shielding Tensor Parameters for CpK

cluster	method	basis set	δ_{11} (ppm)	δ_{22} (ppm)	δ_{33} (ppm)	δ_{iso} (ppm)	σ_{iso} (ppm)	Ω (ppm)	κ
CpK	exp	static	—	—	—	−100(20)	—	—	—
CpK	exp	MAS	—	—	—	−75(30)	—	—	—
$Cp_2K_3^+$	RHF	6-31G**	−68.70	−109.66	−110.91	−96.42	1367.32	42.21	−0.94
$Cp_2K_3^+$	RHF	6-31G** [a]	−32.85	−37.43	−43.41	−37.90	1335.18	10.56	0.13
$Cp_2K_3^+$	RHF	6-311G**	−83.61	−127.44	−129.74	−113.59	1365.96	46.13	−0.90
$Cp_2K_3^+$	RHF	6-311G** [a]	−37.48	−45.65	−53.03	−45.38	1336.65	15.56	−0.05
$Cp_2K_3^+$	RHF	6-311+G**	−87.23	−123.24	−126.32	−112.27	1361.85	39.09	−0.84
$Cp_2K_3^+$	RHF	6-311+G** [a]	−67.90	−90.98	−94.91	−84.60	1355.02	27.01	−0.71
$Cp_2K_3^+$	RHF	6-311++G**	−87.96	−121.71	−126.90	−112.19	1360.84	38.94	−0.73
$Cp_2K_3^+$	RHF	6-311++G** [a]	−71.03	−90.38	−91.96	−84.46	1354.92	20.93	−0.85
$Cp_2K_3^+$	B3LYP	6-31G**	−86.45	−131.52	−133.71	−117.23	1364.20	47.26	−0.91
$Cp_2K_3^+$	B3LYP	6-31G** [a]	−27.80	−34.88	−42.09	−34.92	1335.41	14.29	0.01
$Cp_2K_3^+$	B3LYP	6-311G**	−110.90	−139.21	−143.86	−131.32	1344.89	32.96	−0.72
$Cp_2K_3^+$	B3LYP	6-311G** [a]	−30.08	−37.58	−49.31	−38.99	1328.54	19.23	0.22
$Cp_2K_3^+$	B3LYP	6-311+G**	−111.07	−132.93	−138.96	−127.65	1342.51	27.89	−0.57
$Cp_2K_3^+$	B3LYP	6-311+G** [a]	−85.97	−110.79	−115.05	−103.94	1353.15	29.08	−0.71
$Cp_2K_3^+$	B3LYP	6-311++G**	−112.85	−133.64	−143.44	−129.98	1343.05	30.59	−0.36
$Cp_2K_3^+$	B3LYP	6-311++G** [a]	−94.35	−109.16	−114.58	−106.03	1349.91	20.23	−0.46

[a] A WTBS on the potassium atom(s).

2.3.5.6 Carbon Chemical Shielding

Unlike the ^{39}K NMR experiments, carbon CSA effects can be observed experimentally and theoretically calculated in a relatively accurate manner using any parameter combination presented in this discussion (Tables 2.5 and A.2.5.3). Before accounting for rapid 5-fold ring reorientation, the skew (κ) values are greatly underestimated and span (Ω) values greatly overestimated in all cases. Previous studies upon analogous complexes[20,53,88,93,94] have proven that, for Cp$'$ ring carbons, (i) the δ_{11} and δ_{22} components of the carbon CS tensor lie nearly parallel to the plane defined by the Cp$'$ ring and (ii) the Cp$'$ ring itself undergoes rapid 5-fold reorientations, causing δ_{11} and δ_{22} to be averaged. After accounting for this type of motion, the correlation between experimental and calculated values is substantially higher in all cases, most notably when using the B3LYP method and 6-31G** basis set on carbon and hydrogen atoms.

-71-

Table 2.5 Experimental and Theoretical Carbon Chemical Shielding Parameters for CpK

cluster	method	basis set	δ_{11} (ppm)	δ_{22} (ppm)	δ_{33} (ppm)	δ_{iso} (ppm)	σ_{iso} (ppm)	Ω (ppm)	κ	$(\delta_{11}+\delta_{22})/2$ (ppm)	Ω' [a] (ppm)
CpK	exp	MAS	146.7	144.3	27.7	106.2	—	119.0	0.97	—	—
$Cp_2K_3^+$	RHF	6-31G**	173.34	103.57	5.16	94.03	103.56	168.18	0.17	138.46	133.29
$Cp_2K_3^+$	RHF	6-31G** [b]	172.63	110.37	5.00	96.00	101.59	167.64	0.26	141.50	136.51
$Cp_2K_3^+$	RHF	6-311G**	176.60	101.25	−4.55	91.10	88.31	181.15	0.17	138.92	143.47
$Cp_2K_3^+$	RHF	6-311G** [b]	176.67	99.96	−4.92	90.57	88.84	181.59	0.16	138.32	143.23
$Cp_2K_3^+$	RHF	6-311+G**	178.34	103.23	−4.35	92.41	87.11	182.68	0.18	140.78	145.13
$Cp_2K_3^+$	RHF	6-311+G** [b]	178.23	101.23	−4.69	91.59	87.93	182.92	0.16	139.73	144.42
$Cp_2K_3^+$	RHF	6-311++G**	178.43	103.28	−4.42	92.43	87.09	182.85	0.18	140.86	145.27
$Cp_2K_3^+$	RHF	6-311++G** [b]	178.23	101.51	−4.79	91.70	87.82	183.17	0.16	139.95	144.73
$Cp_2K_3^+$	B3LYP	6-31G**	174.67	109.78	18.64	101.03	96.30	156.03	0.17	142.23	123.59
$Cp_2K_3^+$	B3LYP	6-31G** [b]	173.40	117.02	18.09	102.84	94.49	155.31	0.27	145.21	127.12
$Cp_2K_3^+$	B3LYP	6-311G**	178.94	106.84	5.34	97.04	77.74	173.60	0.17	142.89	137.55
$Cp_2K_3^+$	B3LYP	6-311G** [b]	179.25	103.65	4.76	95.89	78.89	155.31	0.27	145.21	127.12
$Cp_2K_3^+$	B3LYP	6-311+G**	181.24	110.08	6.38	99.23	76.56	174.86	0.19	145.66	139.28
$Cp_2K_3^+$	B3LYP	6-311+G** [b]	180.77	106.33	5.82	97.64	78.15	174.95	0.15	143.55	137.73
$Cp_2K_3^+$	B3LYP	6-311++G**	181.15	109.70	6.37	99.07	76.72	174.78	0.18	145.43	139.06
$Cp_2K_3^+$	B3LYP	6-311++G** [b]	180.62	106.12	6.69	97.81	77.98	173.93	0.14	143.37	136.68

[a] Ω' calculated using averaged value of $(\delta_{11}+\delta_{22})/2$ in place of δ_{11}.

[b] A WTBS on the potassium atom(s).

2.4 Conclusions

Solid-state ^{39}K and ^{13}C NMR experiments on linear polymeric potassium metallocenes, along with theoretically calculated NMR tensors, have proven useful for correlating molecular structure to NMR tensor parameters, as well as for observing temperature-dependent structural changes at the molecular level. The application of pulse sequences such as QCPMG and DFS/QCPMG is shown to be invaluable for the acquisition of ^{39}K NMR spectra of CpK and will find much use in the future for acquiring similar spectra of ^{39}K nuclei (along with other low-γ, half-integer quadrupolar nuclei) in asymmetric environments. A methodology for efficient, uniform, piecewise acquisition of ^{39}K QCPMG NMR spectra for broad powder patterns which exceed the maximum excitable bandwidth is also demonstrated. ^{39}K NMR quadrupolar parameters obtained for CpK support the zigzagging linear polymeric structure proposed from powder XRD data, and similar parameters obtained for Cp*K are used to infer a structure for this hitherto uncharacterized system. The optimized DFS/QCPMG pulse sequence enables the rapid acquisition of VT ^{39}K NMR spectra of CpK, and from these spectra, temperature-dependent structural changes are intimated from changes in the observed values of $C_Q(^{39}K)$ and $\eta_Q(^{39}K)$. ^{13}C CP/MAS NMR experiments on CpK and Cp*K were used to determined carbon CS tensor orientations and confirm the presence of rapid 5-fold Cp ring reorientations. Theoretical calculations on CpK clusters predict ^{39}K NMR parameters relatively well, especially those conducted with large well-tempered basis sets on the potassium atoms. Clear relationships are shown to exist between the zigzagging nature of the $[Cp'K]_n$ chains and the theoretically calculated ^{39}K EFG tensors (i.e., both the magnitude of principal components and orientations of the

-73-

EFG tensors). Idealized $Cp_2K_3^+$ clusters were used to see if temperature-dependent structural changes could be correlated to the VT NMR data. It was determined that as temperature is increased, the decreasing value of $\eta_Q(^{39}K)$ and increasing value of $C_Q(^{39}K)$ could be correlated to the increasing linearity of the CpK chains. NMR experiments are also useful in identifying the decomposition of CpK and may play a useful role in identifying impurity phases in a variety of potassium-containing materials.

Bibliography

[1]   Weiss, E. *Angewandte Chemie-International Edition in English* **1993**, *32*, 1501.

[2]   Harder, S. *Coordination Chemistry Reviews* **1998**, *176*, 17.

[3]   Thiele, J. *Berichte der Deutschen Chemischen Gesellschaft* **1901**, *34*, 68.

[4]   Cox, R. H.; Terry, H. W.; Harrison, L. W. *Journal of the American Chemical Society* **1971**, *93*, 3297.

[5]   Fischer, P.; Stadelhofer, J.; Weidlein, J. *Journal of Organometallic Chemistry* **1976**, *116*, 65.

[6]   Fritz, H. P.; Schafer, L. *Chemische Berichte* **1964**, *97*, 1829.

[7]   Jutzi, P.; Leffers, W.; Hampel, B.; Pohl, S.; Saak, W. *Angewandte Chemie-International Edition in English* **1987**, *26*, 583.

[8]   Schaefer, W. P.; Cotter, W. D.; Bercaw, J. E. *Acta Crystallographica Section C-Crystal Structure Communications* **1993**, *49*, 1489.

[9] ·   Rabe, G.; Roesky, H. W.; Stalke, D.; Pauer, F.; Sheldrick, G. M. *Journal of Organometallic Chemistry* **1991**, *403*, 11.

[10]   Jordan, V.; Behrens, U.; Olbrich, F.; Weiss, E. *Journal of Organometallic Chemistry* **1996**, *517*, 81.

[11]   Evans, W. J.; Brady, J. C.; Fujimoto, C. H.; Giarikos, D. G.; Ziller, J. W. *Journal of Organometallic Chemistry* **2002**, *649*, 252.

[12]   Bai, G.; Roesky, H. W.; Muller, P. *Bulletin of the Polish Academy of Sciences, Chemistry* **2002**, *50*, 1.

[13] Rietveld, H. M. *Journal of Applied Crystallography* **1969**, *2*, 65.

[14] Dinnebier, R. E.; Behrens, U.; Olbrich, F. *Organometallics* **1997**, *16*, 3855.

[15] Dinnebier, R. E.; Schneider, M.; van Smaalen, S.; Olbrich, F.; Behrens, U. *Acta Crystallographica Section B-Structural Science* **1999**, *55*, 35.

[16] Tedesco, C.; Dinnebier, R. E.; Olbrich, F.; van Smaalen, S. *Acta Crystallographica Section B-Structural Science* **2001**, *57*, 673.

[17] Johnels, D.; Boman, A.; Edlund, U. *Magnetic Resonance in Chemistry* **1998**, *36*, S151.

[18] Pietrass, T.; Burkert, P. K. *Inorganica Chimica Acta* **1993**, *207*, 253.

[19] Jost, S.; Gunther, H. *Magnetic Resonance in Chemistry* **2003**, *41*, 373.

[20] Willans, M. J.; Schurko, R. W. *Journal of Physical Chemistry B* **2003**, *107*, 5144.

[21] Sahm, W.; Schwenk, A. *Zeitschrift fur Naturforschung A: Journal of Physical Sciences* **1974**, *29*, 1754.

[22] Kello, V.; Sadlej, A. J. *Chemical Physics Letters* **1998**, *292*, 403.

[23] Sasaki, S.; Matsuda, A.; Chu, C. W. *Physica C: Superconductivity (Amsterdam)* **1998**, *302*, 319.

[24] Grecu, M. N.; Constantinescu, S. *Applied Magnetic Resonance* **1999**, *16*, 373.

[25] Smith, M. E. Recent Progress in Solid-State NMR of Low-Gamma Nuclei. In *Annual Reports on NMR Spectroscopy*, 2001; Vol. 43; pp 121.

[26] Freude, D.; Haase, J. *Quadrupole Effects in Solid-State Nuclear Magnetic Resonance*; Springer-Verlag: Berlin, 1993; Vol. 29.

[27] Vega, A. J. *Quadrupolar Nuclei in Solids*; Wiley: New York, 1996.

[28] Smith, M. E.; van Eck, E. R. H. *Progress in Nuclear Magnetic Resonance Spectroscopy* **1999**, *34*, 159.

[29] Van der Lugt, W.; Knol, J. S. *Physica Status Solidi* **1967**, *23*, K83.

[30] Van der Molen, S. B.; Van der Lugt, W.; Draisma, G. G.; Smit, W. *Physica (Amsterdam)* **1968**, *38*, 275.

[31] Kunwar, A. C.; Turner, G. L.; Oldfield, E. *Journal of Magnetic Resonance* **1986**, *69*, 124.

[32] Bastow, T. J. *Journal of the Chemical Society, Faraday Transactions* **1991**, *87*, 2453.

[33] Bastow, T. J. *Zeitschrift fur Naturforschung A: Journal of Physical Sciences* **1994**, *49*, 320.

[34] Wong, A.; Whitehead, R. D.; Gan, Z.; Wu, G. *Journal of Physical Chemistry A* **2004**, *108*, 10551.

[35] Lambert, J. F.; Prost, R.; Smith, M. E. *Clays and Clay Minerals* **1992**, *40*, 253.

[36] Apostol, M. *Journal of Physical Chemistry* **1996**, *100*, 3175.

[37] Krawietz, T. R.; Murray, D. K.; Haw, J. F. *Journal of Physical Chemistry A* **1998**, *102*, 8779.

[38] Carroll, D. L.; Kemp, T. F.; Bastow, T. J.; Smith, M. E. *Solid State Nuclear Magnetic Resonance* **2005**, *28*, 31.

[39] Thomas, P. A.; Baldwin, A.; Dupree, R.; Blaha, P.; Schwarz, K.; Samoson, A.; Gan, Z. H. *Journal of Physical Chemistry B* **2004**, *108*, 4324.

[40] Wu, G. *Biochemistry and Cell Biology* **1998**, *76*, 429.

[41] Wu, G.; Wong, A.; Gan, Z.; Davis, J. T. *Journal of the American Chemical Society*

2003, *125*, 7182.

[42]   Wu, G.; Wong, A. *NMR Spectroscopy of Biological Solids* **2006**, 317.

[43]   Larsen, F. H.; Jakobsen, H. J.; Ellis, P. D.; Nielsen, N. C. *Journal of Physical Chemistry A* **1997**, *101*, 8597.

[44]   Larsen, F. H.; Skibsted, J.; Jakobsen, H. J.; Nielsen, N. C. *Journal of the American Chemical Society* **2000**, *122*, 7080.

[45]   Lo, A. Y. H.; Bitterwolf, T. E.; Macdonald, C. L. B.; Schurko, R. W. *Journal of Physical Chemistry A* **2005**, *109*, 7073.

[46]   Tang, J. A.; Masuda, J. D.; Boyle, T. J.; Schurko, R. W. *ChemPhysChem* **2006**, *7*, 117.

[47]   Larsen, F. H.; Farnan, I.; Lipton, A. S. *Journal of Magnetic Resonance* **2006**, *178*, 228.

[48]   Bowers, G. M.; Lipton, A. S.; Mueller, K. T. *Solid State Nuclear Magnetic Resonance* **2006**, *29*, 95.

[49]   Bryce, D. L.; Gee, M.; Wasylishen, R. E. *Journal of Physical Chemistry A* **2001**, *105*, 10413. .

[50]   Lipton, A. S.; Sears, J. A.; Ellis, P. D. *Journal of Magnetic Resonance* **2001**, *151*, 48.

[51]   Lipton, A. S.; Buchko, G. W.; Sears, J. A.; Kennedy, M. A.; Ellis, P. D. *Journal of the American Chemical Society* **2001**, *123*, 992.

[52]   Lipton, A. S.; Wright, T. A.; Bowman, M. K.; Reger, D. L.; Ellis, P. D. *Journal of the American Chemical Society* **2002**, *124*, 5850.

[53]   Hung, I.; Schurko, R. W. *Solid State Nuclear Magnetic Resonance* **2003**, *24*, 78.

[54]   Hung, I.; Schurko, R. W. *Journal of Physical Chemistry B* **2004**, *108*, 9060.

[55]   Larsen, F. H.; Nielsen, N. C. *Journal of Physical Chemistry A* **1999**, *103*, 10825.

[56]   Kentgens, A. P. M.; Verhagen, R. *Chemical Physics Letters* **1999**, *300*, 435.

[57]   Iuga, D.; Schafer, H.; Verhagen, R.; Kentgens, A. P. M. *Journal of Magnetic Resonance* **2000**, *147*, 192.

[58]   Yao, Z.; Kwak, H. T.; Sakellariou, D.; Emsley, L.; Grandinetti, P. J. *Chemical Physics Letters* **2000**, *327*, 85.

[59]   Schurko, R. W.; Hung, I.; Widdifield, C. M. *Chemical Physics Letters* **2003**, *379*, 1.

[60]   Wagner, B. O.; Ebel, H. F. *Tetrahedron* **1970**, *26*, 5155.

[61]   Schumann, H.; Albrecht, I.; Loebel, J.; Hahn, E.; Hossain, M. B.; Helm, D. *Organometallics* **1986**, *5*, 1296.

[62]   Dinnebier, R. E., Private Communication.

[63]   Larsen, F. H.; Jakobsen, H. J.; Ellis, P. D.; Nielsen, N. C. *Journal of Magnetic Resonance* **1998**, *131*, 144.

[64]   Bastow, T. J.; Smith, M. E. *Solid State Nuclear Magnetic Resonance* **1992**, *1*, 165.

[65]   Massiot, D.; Farnan, I.; Gautier, N.; Trumeau, D.; Trokiner, A.; Coutures, J. P. *Solid State Nuclear Magnetic Resonance* **1995**, *4*, 241.

[66]   Medek, A.; Frydman, V.; Frydman, L. *Journal of Physical Chemistry A* **1999**, *103*, 4830.

[67]   Eichele, K.; Wasylishen, R. E. WSolids; 2.2.13 ed.; Dalhousie University: Halifax, N.S., 1998.

[68]   Alderman, D. W.; Solum, M. S.; Grant, D. M. *Journal of Chemical Physics* **1986**, *84*,

3717.

[69]   Bak, M.; Rasmussen, J. T.; Nielsen, N. C. *Journal of Magnetic Resonance* **2000**, *147*, 296.

[70]   Frisch, M. J.; Trucks, G. W.; Schlegel, H. B.; Scuseria, G. E.; Robb, M. A.; Cheeseman, J. R.; Zakrzewski, V. G.; Montgomery, J., J. A.; Stratmann, R. E.; Burant, J. C.; Dapprich, S.; Millam, J. M.; Daniels, A. D.; Kudin, K. N.; Strain, M. C.; Farkas, O.; Tomasi, J.; Barone, V.; Cossi, M.; Cammi, R.; Mennucci, B.; Pomelli, C.; Adamo, C.; Clifford, S.; Ochterski, J.; Petersson, G. A.; Ayala, P. Y.; Cui, Q.; Morokuma, K.; Malick, D. K.; Rabuck, A. D.; Raghavachari, K.; Foresman, J. B.; Cioslowski, J.; Ortiz, J. V.; Baboul, A. G.; Stefanov, B. B.; Liu, G.; Liashenko, A.; Piskorz, P.; Komaromi, I.; Gomperts, R.; Martin, R. L.; Fox, D. J.; Keith, T.; Al-Laham, M. A.; Peng, C. Y.; Nanayakkara, A.; Challacombe, M.; Gill, P. M. W.; Johnson, B.; Chen, W.; Wong, M. W.; Andres, J. L.; Gonzalez, C.; Head-Gordon, M.; Replogle, E. S.; Pople, J. A. Gaussian 98; Revision A.9 ed.; Gaussian, Inc.: Pittsburgh, PA, 1998.

[71]   Frisch, M. J.; Trucks, G. W.; Schlegel, H. B.; Scuseria, G. E.; Robb, M. A.; Cheeseman, J. R.; Montgomery, J., J. A.; Vreven, T.; Kudin, K. N.; Burant, J. C.; Millam, J. M.; Iyengar, S. S.; Tomasi, J.; Barone, V.; Mennucci, B.; Cossi, M.; Scalmani, G.; Rega, N.; Petersson, G. A.; Nakatsuji, H.; Hada, M.; Ehara, M.; Toyota, K.; Fukuda, R.; Hasegawa, J.; Ishida, M.; Nakajima, T.; Honda, Y.; Kitao, O.; Nakai, H.; Klene, M.; Li, X.; Knox, J. E.; Hratchian, H. P.; Cross, J. B.; Adamo, C.; Jaramillo, J.; Gomperts, R.; Stratmann, R. E.; Yazyev, O.; Austin, A. J.; Cammi, R.; Pomelli, C.; Ochterski, J. W.; Ayala, P. Y.; Morokuma, K.; Voth, G. A.; Salvador, P.; Dannenberg, J. J.; Zakrzewski, V. G.; Dapprich,

S.; Daniels, A. D.; Strain, M. C.; Farkas, O.; Malick, D. K.; Rabuck, A. D.; Raghavachari, K.; Foresman, J. B.; Ortiz, J. V.; Cui, Q.; Baboul, A. G.; Clifford, S.; Cioslowski, J.; Stefanov, B. B.; Liu, G.; Liashenko, A.; Piskorz, P.; Komaromi, I.; Martin, R. L.; Fox, D. J.; Keith, T.; Al-Laham, M. A.; Peng, C. Y.; Nanayakkara, A.; Challacombe, M.; Gill, P. M. W.; Johnson, B.; Chen, H.; Wong, M. W.; Gonzalez, C.; Pople, J. A. Gaussian 03; Rev. B.03 ed.; Gaussian, Inc.: Pittsburgh, 2003.

[72]   Becke, A. D. *Physical Review A* **1988**, *38*, 3098.

[73]   Lee, C.; Yang, W.; Parr, R. G. *Physical Review B* **1988**, *37*, 785.

[74]   Huzinaga, S.; Miguel, B. *Chemical Physics Letters* **1990**, *175*, 289.

[75]   Huzinaga, S.; Klobukowski, M. *Chemical Physics Letters* **1993**, *212*, 260.

[76]   Basis sets were obtained from the Extensible Computational Chemistry Environment Basis Set Database, V., as developed and distributed by the Molecular Science Computing Facility, Environmental and Molecular Sciences Laboratory which is part of the Pacific Northwest Laboratory, P.O. Box 999, Richland, Washington 99352, USA, and funded by the U.S. Department of Energy. The Pacific Northwest Laboratory is a multiprogram laboratory operated by Battelle Memorial Institute for the U.S. Department of Energy under contract DE-AC06-76RLO 1830. Contact David Feller or Karen Schuchardt for further information.

[77]   Brown, R. D.; Head-Gordon, M. P. *Molecular Physics* **1987**, *61*, 1183.

[78]   Cummins, P. L.; Bacskay, G. B.; Hush, N. S. *Molecular Physics* **1987**, *62*, 193.

[79]   Ditchfield, R. *Molecular Physics* **1974**, *27*, 789.

[80]   Wolinski, K.; Hinton, J. F.; Pulay, P. *Journal of the American Chemical Society* **1990**, *112*, 8251.

[81]   Schaftenaar, G.; Noordik, J. H. *Journal of Computer-Aided Molecular Design* **2000**, *14*, 123.

[82]   Schafer, H.; Iuga, D.; Verhagen, R.; Kentgens, A. P. M. *Journal of Chemical Physics* **2001**, *114*, 3073.

[83]   Fenzke, D.; Freude, D.; Froehlich, T.; Haase, J. *Chemical Physics Letters* **1984**, *111*, 171.

[84]   Man, P. P. *Physical Review B: Condensed Matter* **1995**, *52*, 9418.

[85]   Dumazy, Y.; Amoureux, J.-P.; Fernandez, C. *Molecular Physics* **1997**, *90*, 959.

[86]   Schmidt-Rohr, K.; Spiess, H. W. *Multidimensional Solid-State NMR and Polymers*; Harcourt Brace: Toronto, 1994.

[87]   Lefort, R.; Wiench, J. W.; Pruski, M.; Amoureux, J. P. *Journal of Chemical Physics* **2002**, *116*, 2493.

[88]   Schurko, R. W.; Hung, I.; Macdonald, C. L. B.; Cowley, A. H. *Journal of the American Chemical Society* **2002**, *124*, 13204.

[89]   Schurko, R. W.; Hung, I.; Schauff, S.; Macdonald, C. L. B.; Cowley, A. H. *Journal of Physical Chemistry A* **2002**, *106*, 10096.

[90]   Monagan, M. B.; Geddes, K. O.; Heal, K. M.; Labahn, G.; Vorkoetter, S. M.; McCarron, J.; DeMarco, P. Maple; 7 ed.; Waterloo Maple, Inc., 2001.

[91]   Zhao, P.; Prasad, S.; Huang, J.; Fitzgerald, J. J.; Shore, J. S. *Journal of Physical Chemistry B* **1999**, *103*, 10617.

[92]   Herzfeld, J.; Berger, A. E. *Journal of Chemical Physics* **1980**, *73*, 6021.

[93]   Wemmer, D. E.; Ruben, D. J.; Pines, A. *Journal of the American Chemical Society*

1981, *103*, 28.

[94]   Kwon, O.; McKee, M. L. *Journal of Physical Chemistry A* **2001**, *105*, 10133.

[95]   Kalinowsky, H.-O.; Berger, S.; Braun, S. *^{13}C NMR Spectroskopie*; Verlag: Stuttgart, 1984.

[96]   Roy Dennington II; Todd Keith; John Millam; Ken Eppinnett; W. Lee Hovell; Gilliland, R. GaussView; 3.09 ed.; Semichem Inc.: Shawnee Mission, 2003.

[97]   Orendt, A. M.; Facelli, J. C.; Jiang, Y. J.; Grant, D. M. *Journal of Physical Chemistry A* **1998**, *102*, 7692.

Chapter 3

Understanding Chemical Shielding Using Group Symmetry Representations, MO Analysis and Modern Density-Functional Theory

3.1 Introduction

The chemical shift, δ, a hallmark of nuclear magnetic resonance (NMR) spectroscopy for the past 50 years, is considered by many chemists to be the primary NMR parameter associated with the structural characterization of matter at the molecular level.[1,2] Chemically induced resonance shifts were rationalized through physical modelling[3-7] shortly after initial observations;[8,9] however, the accurate calculation of unknown chemical shift values proved significantly more daunting. *Ab initio* computations return a chemical shielding value (σ) a quantity which can be related to a chemical shift as was shown in [1.11]. Thus, for a chemical shift value to be determined theoretically, shielding values for both the unknown and a reference compound are required. Absolute shielding scales, which organize information much like chemical shift scales (see Figure 3.1 for a comparison of the two scales), have been determined for several nuclides using experimental data or one of a number of hybrid experimental-theoretical methods.[10-13] Purely computational approaches have not developed to the point where they may be used to quantitatively produce an absolute shielding scale; however calculated shielding values are constantly improving,[14-18] as solutions pertaining to gauge variance,[19-24] relativistic effects[25-28] and electron correlation[29,30] problems have been formulated and improvements in computational capacity

-84-

allow one to use increasingly complex basis sets.

direction of increasing σ $\longrightarrow$

| -100 | 0 | 100 | 200 | 300 | 400 | 500 | 600 | 700 σ (ppm) |

85% H_3PO_4

P^{15+} PCl_3 PF_3 PMe_3 PH_3

| 400 | 300 | 200 | 100 | 0 | -100 | -200 | -300 | δ (ppm) |

$\longleftarrow$ direction of increasing δ
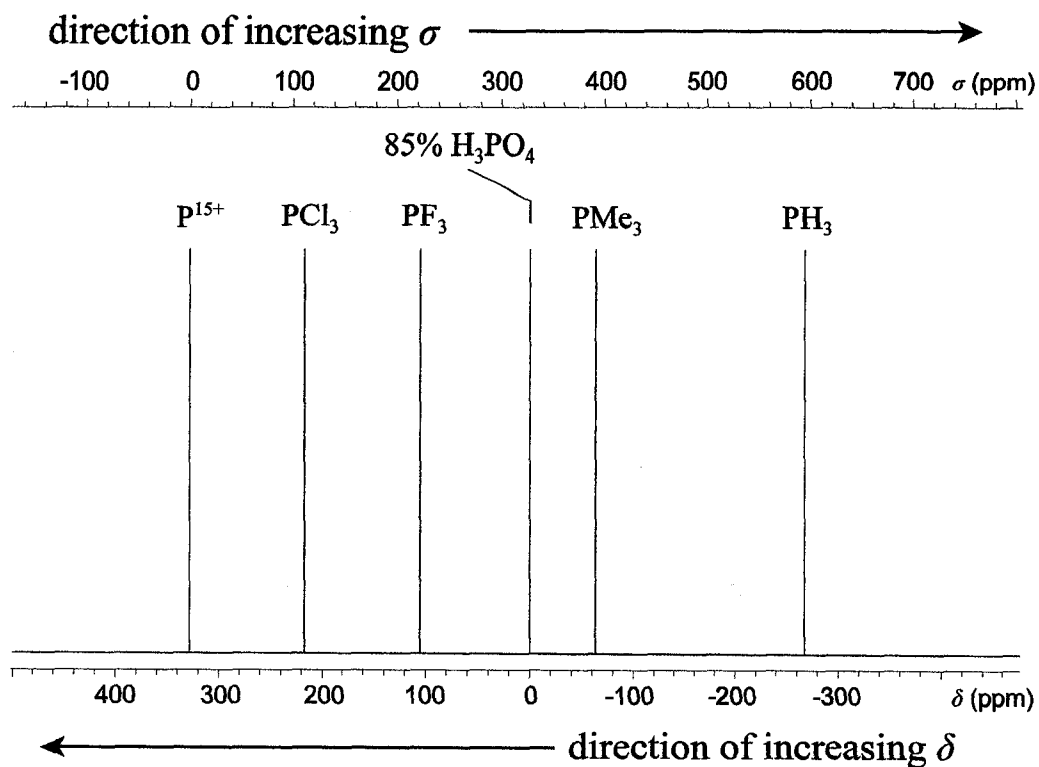
Figure 3.1 Comparison of chemical shielding (σ) and chemical shift (δ) scales using a portion of the phosphorus absolute shielding scale provided by Jameson et al.[31] The scales are calibrated such that $\sigma(P^{15+}) = 0.0$ ppm and $\delta(85\ \%\ H_3PO_{4(aq)}) = 0.0$ ppm.

Therefore, although very significant progress has been made in the theoretical prediction of chemical shielding, there appears to be a relative dearth of information regarding its origin in a number of systems. Perhaps even more notable is the sparse amount of data pertaining to its generally anisotropic nature of origin in molecules. It is envisioned that having a systematic procedure to explain the anisotropic origins of chemical shielding in molecules would be very beneficial. This discussion is motivated by the ever-increasing applicability of solid-state NMR (SSNMR) experiments, which unlike solution-state NMR

-85-

experiments, can be used to measure the anisotropy of several NMR interactions.

Here, an intuitive method based upon molecular symmetry is presented in order to rationalize the chemical shifts and chemical shielding anisotropy (CSA) in several simple molecules. Calculations employing gauge-including atomic orbital (GIAO)[19] basis sets in the context of modern density-functional theory (DFT) methods[32-34] are used in order to support the symmetry-based arguments on chemical shielding. The general procedure is rather simple: the total observed chemical shift tensor may be related to a calculated shielding tensor, which can be decomposed according to Ramsey[3] into various contributing mechanisms. Consideration of the point group symmetry representations for both the quantum mechanical rotation operators and molecular orbitals (MOs) greatly facilitate the ease with which one may determine which MOs will contribute to observable shielding and the direction of the shielding. Theoretical analyses are performed, which determine the degree of contribution of each MO to the chemical shielding tensor components, thereby quantifying the simple symmetry-based relationships.

3.2 Background

As outlined in Chapter 1, B_0 induces local magnetic fields in the molecule which depend upon the orientation of the molecule with respect to B_0. The chemical shielding interaction is therefore anisotropic and for a microcrystalline sample, each magnetically distinct nucleus gives rise to a unique powder pattern in a SSNMR spectrum. Although the powder pattern is rich in information pertaining to molecular structure, the main effect of the anisotropic interaction is to reduce the S/N and resolution in the NMR spectrum.

3.2.1 Chemical Shielding in Anisotropic Environments - Models

In section **1.2.3.1**, a number of items pertaining to the chemical shift tensor ($\tilde{\delta}$) were discussed. The presentation of that section was geared towards the commonly observable NMR parameter, δ. As this chapter relies heavily upon the theoretical calculation of chemical shielding (σ), some of the expressions must be reintroduced in terms of chemical shielding, beginning with the tensor representation of chemical shielding:[35]

$$\tilde{\sigma}_{solids} = \begin{bmatrix} \sigma_{xx} & \sigma_{xy} & \sigma_{xz} \\ \sigma_{yx} & \sigma_{yy} & \sigma_{yz} \\ \sigma_{zx} & \sigma_{zy} & \sigma_{zz} \end{bmatrix}. \qquad \textbf{[3.1]}$$

Each element (σ_{ij}; $i, j = x, y, z$) represents the i-component of shielding when $\mathbf{B}_0$ is along the j-axis. The observable shielding tensor is symmetric[36] ($\sigma_{ij} = \sigma_{ji}$) and diagonalizable into its own PAS. A shielding tensor in its PAS may be fully expressed using three values (the principal components), which are located along the diagonal of the matrix:

$$\tilde{\sigma}_{solids}^{PAS} = \begin{bmatrix} \sigma_{11} & 0 & 0 \\ 0 & \sigma_{22} & 0 \\ 0 & 0 & \sigma_{33} \end{bmatrix} \qquad \textbf{[3.2]}$$

where $\sigma_{11} \leq \sigma_{22} \leq \sigma_{33}$. This means that σ_{11} is the least shielded component of the tensor, while σ_{33} is the most shielded. The isotropic shielding value may be determined by evaluating 1/3 of the trace of the matrix in **[3.2]**, hence $\sigma_{iso} \equiv (\sigma_{11} + \sigma_{22} + \sigma_{33})/3$.

The conventions that were used to describe chemical shift tensors are also applicable to chemical shielding tensors, although subtle differences do exist. The span (Ω) and skew (κ) parameters associated with the Herzfeld-Berger convention are now defined such that:[37]

-87-

$$\Omega = \sigma_{33} - \sigma_{11} \quad ; \quad \kappa = \frac{3(\sigma_{iso} - \sigma_{22})}{\Omega} . \quad\quad\quad [3.3]$$
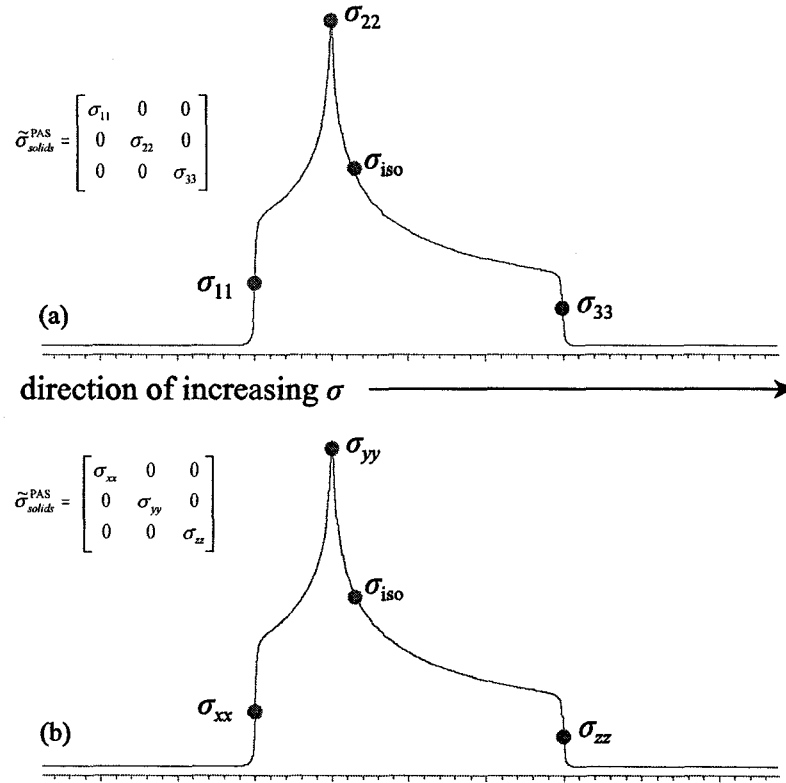
Figure 3.2 Comparison of the shielding tensor conventions used. (a) Principal components as per the Herzfeld-Berger method. (b) Principal components according to the Haeberlen convention.

The Haeberlen tensor convention[38] introduces the anisotropy ($\Delta\sigma$) and asymmetry (η) parameters, with principal components that are defined differently in comparison to the Herzfeld-Berger method (Figure 3.2):

$$|\Delta\sigma| = \sigma_{zz} - \frac{\sigma_{xx} + \sigma_{yy}}{2} \quad ; \quad \eta = \frac{\sigma_{yy} - \sigma_{xx}}{\delta_r} \quad\quad [3.4]$$

where $|\sigma_{zz} - \sigma_{iso}| \geq |\sigma_{xx} - \sigma_{iso}| \geq |\sigma_{yy} - \sigma_{iso}|$, and δ_r is the reduced anisotropy, defined as $\sigma_{zz} - \sigma_{iso}$. Further details regarding the Haeberlen convention can be found in the

-88-

literature.[38,39]

The shielding tensor may be visualized geometrically as an ellipsoid (Figure 3.3),[40] although an equivalent treatment using ovaloids has been developed.[41] The magnitude of the ellipsoid semi-axes, commonly denoted as a, b and c, are related to the principal components of the tensor such that:

$$d = 1/\sqrt{\sigma_{ii}} \qquad d = a,b,c \quad ; \quad i = x,y,z \ \text{ or } \ 1,2,3 \ . \qquad [3.5]$$
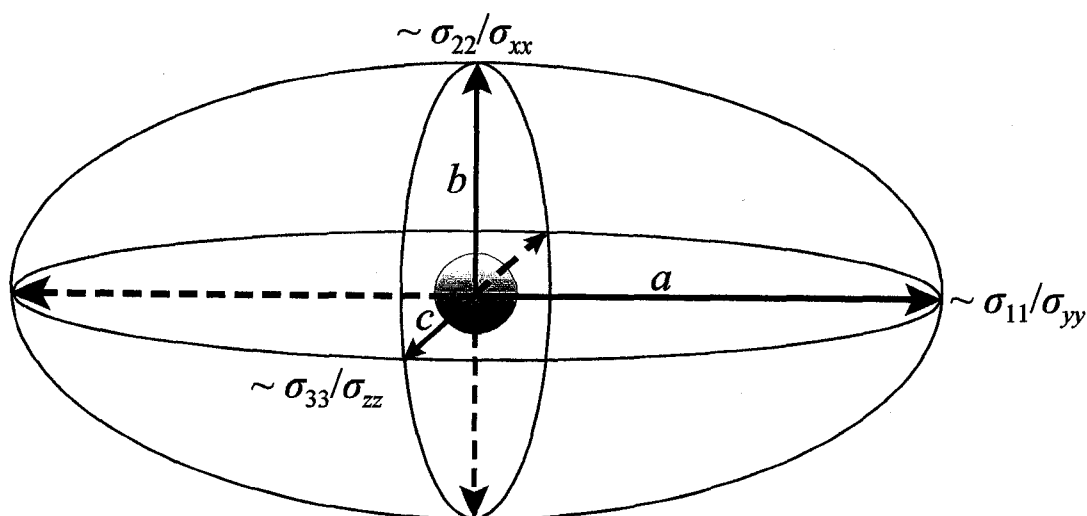
Figure 3.3 The relationship between the semi-axes of an ellipsoid with the principal components of the chemical shielding tensor. The principal components may be represented as vectors within the ellipsoid. Due to the symmetry inherent to an ellipse, each principal component is equivalently represented with either the solid arrow or the dashed arrow.

The principal components (as in Figure 3.3), and the orientation of the shielding tensor in the molecular frame, are often determined by the molecular symmetry elements: they lie along rotational axes, are contained within mirror planes, etc.[35,38] In cases where symmetry elements are either not apparent or are absent, computational techniques have been shown to be extremely reliable in predicting the orientation of the tensor, as confirmed by

-89-

comparison with experimentally determined chemical shielding tensors (i.e., single-crystal NMR techniques[42-44] or separated-local-field[45] and CS recoupling experiments[46,47] for microcrystalline powder samples).

3.2.2   Diamagnetic and Paramagnetic Shielding

Chemical shielding effects for NMR active nuclei are understood to arise through a number of mechanisms. Ramsey's theory for magnetic shielding in molecules decomposes shielding contributions into diamagnetic (σ^d) and paramagnetic (σ^p) portions, such that $\sigma = \sigma^d + \sigma^p$.[3] The proposed mechanism of diamagnetic shielding involves an applied magnetic field inducing electronic current circulation, which in turn creates a small magnetic field at the nucleus that opposes the applied field. A more detailed account of this mechanism has been provided previously by Slichter.[48] The diamagnetic portion of chemical shielding is easily calculated,[49] since it relies strictly upon the ground electronic state as expressed below:[50]

$$\sigma_{ij}^d \;=\; \frac{e^2 \mu_0}{8\pi m_e} \left\langle \psi_0 \,\Big|\, \sum_k \frac{r_{Nk}^2 \delta_{ij}^{KD} - r_{Nki} r_{Nkj}}{r_{Nk}^3} \,\Big|\, \psi_0 \right\rangle \qquad i,j = x,y,z \qquad [3.6]$$

where σ_{ij}^d is element i, j of a diamagnetic shielding tensor, ψ_0 is a ground-state wave function (i.e., MO), δ_{ij}^{KD} is the Krönecker delta function and r_{Nk} is the distance of electron k from nucleus N. Contributions of all k electrons are considered, the equation is in MKS units and the origin of the magnetic vector potential is taken to be at the nucleus.

The paramagnetic mechanism can be thought of as magnetic dipole-allowed mixing of wave functions/MOs induced by application of an external magnetic field. Contributions

-90-

to σ^p are considerably more difficult to calculate than those of σ^d, since the former rely upon accurate descriptions of excited electronic state wave functions:

$$\sigma_{ij}^p = -\frac{e^2\mu_0}{8\pi m_e^2} \sum_n \frac{1}{E_n - E_0} \left[\langle \psi_0 | \sum_k \hat{L}_{ki} | \psi_n \rangle \langle \psi_n | \sum_k \frac{\hat{L}_{Nkj}}{r_{Nk}^3} | \psi_0 \rangle + \text{c.c.} \right] \qquad [3.7]$$

where σ_{ij}^p is element i,j of the paramagnetic shielding tensor, E_n and E_0 are the eigenvalues associated with an excited and a ground electronic state, $\hat{L}_{ki}$ and $\hat{L}_{Nkj}$ are component angular momentum operators, corresponding to the rotation of electronic charge about the gauge (vector potential) origin and nucleus, respectively and c.c. represents the complex conjugate. The component angular momentum operator applies a rotational transformation upon a given MO, which may alter its symmetry,[51] but conserves its angular momentum. The resulting matrix element is a scalar value describing the degree of overlap between the two mixing states. The effects of the rotation operators upon atomic orbitals (AOs) have been described previously (Figure 3.4) and the fashion in which they contribute to paramagnetic chemical shielding has been described using both MO and valence-bond theories.[51] If, after the rotational transformation, a pair of MOs are of the appropriate symmetry (*vide infra*), they will mix and potentially contribute to σ^p. Conversely, if the MOs are not of the appropriate symmetry, they make no contribution to σ^p (i.e., magnetic dipole-allowed mixing is forbidden). Contributions are proportional to the degree of MO overlap and inversely proportional to the energetic separation (ΔE) between the two MOs. This mechanism has been schematised before for F_2, as in Figure 3.5.
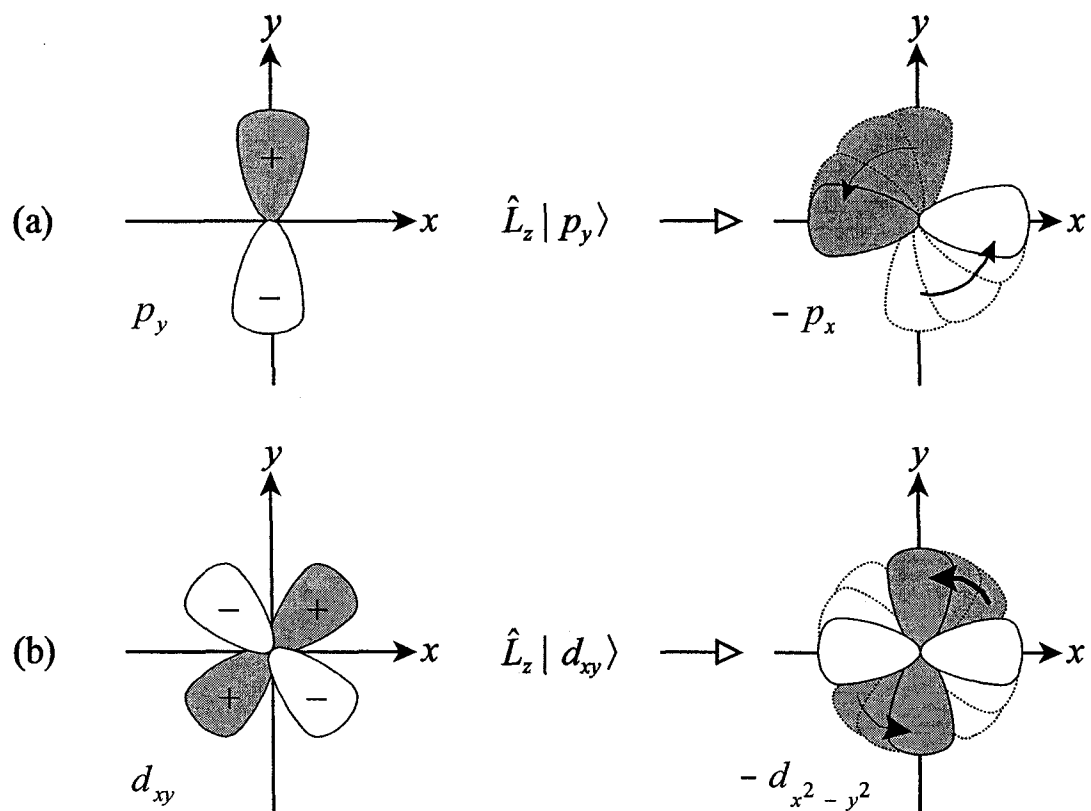
Figure 3.4 Considering symmetry only, when $\hat{L}_z$ operates upon the (a) p_y and (b) d_{xy} AOs, the effect is adequately described in terms of a rotation transformation, leaving the magnitude of angular momentum unchanged.

3.2.3 Determination of Allowed Transitions

As with other forms of spectroscopy,[52] one may determine if a transition (and hence a contribution to chemical shielding) is allowed based upon symmetry considerations. In order for a pair of MOs to contribute to chemical shielding, the following integral must result in a non-zero matrix element:

$$\langle \psi_b | \hat{R}_n | \psi_a \rangle \quad = \quad \int \psi_b \, \hat{R}_n \, \psi_a \, d\tau \quad \neq \quad 0 \qquad \textbf{[3.8]}$$

-92-

where ψ_b and ψ_a are single-electron wave functions (MOs) and $\hat{R}_n$ is a rotational operator along the axis n.
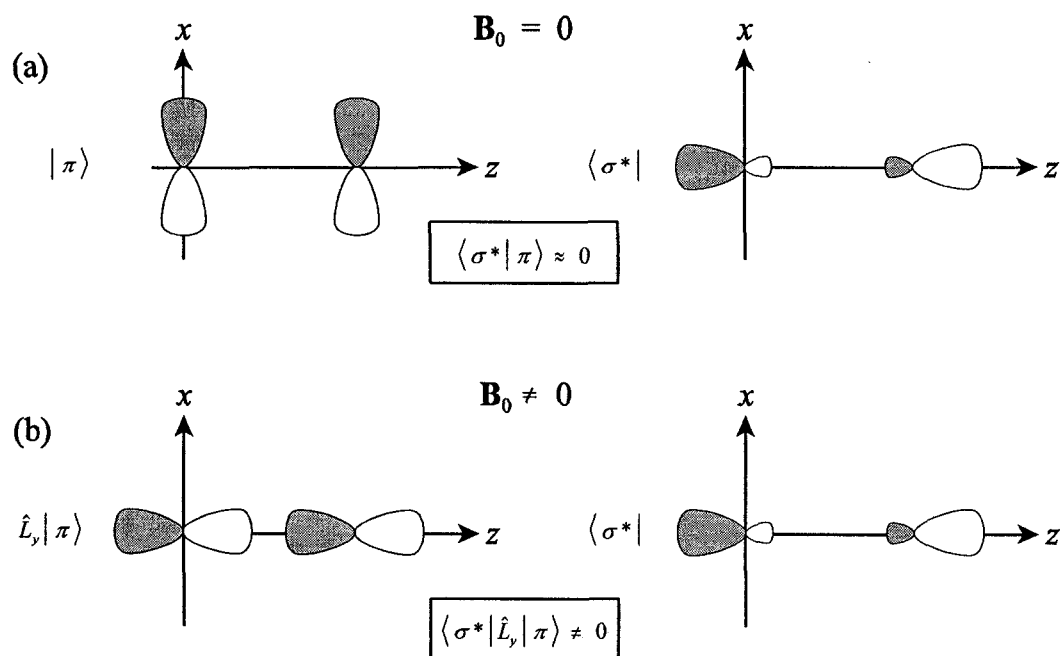
Figure 3.5 According to earlier reports,[34] the $\pi \rightarrow \sigma^*$ transition makes the most significant contribution to σ^p in the F_2 molecule. Before application of the external magnetic field (a), the two MOs clearly do not possess the correct symmetry to overlap and hence do not contribute to σ^p or total energy, however; after application of B_0 (b), induced diamagnetic electron circulation results in non-zero orbital overlap and hence a contribution to σ^p.

The evaluation of [3.8] can be simplified by considering the direct product of the symmetry representations of the wave functions and operator in the three-member integrand. If the integrand is equal to or contains the totally symmetric representation $(A)^{[53]}$ of a given point group, i.e.,

$$\Gamma(\psi_b) \otimes \Gamma(\hat{R}_n) \otimes \Gamma(\psi_a) \supseteq A \tag{3.9}$$

then the integral is non-zero and the transition is said to be magnetic-dipole allowed.[54] The

axis of the rotational operator corresponds to the direction of magnetic shielding. It is stressed that the evaluation of this integrand does not offer insight into the magnitude of the contribution to σ^P, but rather only if the transition is allowed by symmetry.

3.2.4 Contributions to Paramagnetic Shielding

The magnetic dipole-allowed MO mixing may be further decomposed into contributions from occupied - occupied (occ – occ) and occupied - virtual (occ – vir) MO mixing pairs:

$$\sigma^P = \sigma^P(occ - occ) + \sigma^P(occ - vir) . \qquad [3.10]$$

The contributions to paramagnetic shielding have been analysed according to pair-wise MO mixing several times before, although the analysis was often done using approximate or empirical methods,[55,56] qualitative discussions,[57-61] or schematised representations of the molecular orbitals.[62-64] More thorough treatments tend to account for observed isotropic chemical shielding values;[65] relatively few (compared to the total accounts of observed/calculated chemical shielding) can be found where this discussion is extended to include anisotropic chemical shielding.[66-71] Herein, several techniques will be used in tandem so as to provide a more complete picture of chemical shielding.

3.2.5 Calculating Shielding using the ADF/GIAO/DFT Methodology

Though the Ramsey formalism described earlier is quite instructive when rationalizing chemical shielding in molecules, different models are implemented by computational software for the calculation of σ. The Amsterdam Density Functional (ADF)

-94-

suite of programs[72-74] uses Slater-type orbital (STO) functions to describe the basis set elements (i.e., the AOs) which constitute the single-electron wave functions. They are of the form $\varphi(\mathbf{r}) = Y_{lm_l}(\Phi) r^l e^{-\bar{a}r}$, with $Y_{lm_l}(\Phi)$ describing the angular shape of the element and the remainder pertaining to radial decay. The GIAO formalism, widely regarded to be at least marginally superior to other gauge-including methods,[75] places individual gauges at the centre of each AO, resulting in a magnetic-field dependent basis, $\varphi(\mathbf{r}) \rightarrow \varphi_\mu(\mathbf{r}, \mathbf{B}_0)$, where the μ identifies that a gauge has been placed at the centre of the AO. The gauge is introduced through a complex exponential function, such that:

$$\varphi_\mu(\mathbf{r}, \mathbf{B}_0) = \exp\left[-\frac{i}{2}(\mathbf{B}_0 \wedge \mathbf{r}_N) \cdot \mathbf{r}_k\right] \varphi(\mathbf{r}) \qquad [3.11]$$

where $\mathbf{r}_N$ and $\mathbf{r}_k$ are the position vectors of the nucleus and electron, respectively, and [13] is in atomic units.

Density functional theory (DFT) according to the formalism of Kohn and Sham[76] (KS) proposes the following exact expression for the ground-state electronic energy of a system:[30,77]

$$E_0 = -\frac{1}{2}\sum_k \langle \psi_k | \nabla^2 | \psi_k \rangle - \int V(\mathbf{r}_N)\rho(\mathbf{r}_k)d\mathbf{r}_k$$
$$+ \frac{1}{2}\iint \frac{\rho(\mathbf{r}_k)\rho(\mathbf{r}_k')}{|\mathbf{r}_k - \mathbf{r}_k'|} d\mathbf{r}_k d\mathbf{r}_k' + E_{XC}[\rho] \qquad [3.12]$$

where ψ_k is the spatial portion of a one-electron wave function which represents an electron, k, $V(\mathbf{r})$ is an external (nuclear) potential function, $\rho(\mathbf{r})$ is the total electron density of the system and $E_{XC}[\rho]$ is a functional that describes electron exchange and correlation effects. If $E_{XC}[\rho]$ is known exactly, [3.12] would be exact and according to KS, all ground- and

-95-

excited-state electronic properties could be determined precisely. Unfortunately, $E_{XC}[\rho]$ is not exactly known, although much effort has gone into developing suitable representations.[78-87]

3.3   Experimental

Geometry optimizations were done at the self-consistent field (SCF) level and were conducted using the Amsterdam Density Functional (ADF) program, version 2005.01,[72,73,88] distributed by Scientific Computing and Modelling. NMR shielding calculations were carried out using the both the NMR[34,89,90] and EPR[91] modules provided within the ADF suite of programs. The NMR and EPR modules use the GIAO method to account for gauge variance encountered when using finite basis sets. DZ and TZ2P all-electron basis sets were used on all atoms, with values reported herein originating from calculations using the TZ2P basis. The DZ basis set is non-relativistic, double-ζ in the valence, while the TZ2P basis is non-relativistic, triple-ζ in the valence with two polarization functions. Both bases are double-ζ in the core. All DFT calculations used Becke's exchange functional[92] and the correlation functional proposed by Lee, Yang and Parr[93] (BLYP). Optimized geometries using the two different basis sets are provided in the appendix (see Appendix B, Table B.1).

3.4 Results and Discussion

3.4.1 Ethene, C_2H_4

3.4.1.1 Isotropic Carbon Chemical Shielding

The isotropic carbon chemical shielding value of a geometry-optimized (see Table B.1 for geometry) C_2H_4 molecule ($\sigma_{iso}(^{13}C)$) was calculated to be 51.71 ppm (Table 3.1). This value is in fair agreement with previous reports, based upon gas phase[11,94] ($\sigma_{iso}(^{13}C)$ = 64.5 ppm) and low-temperature solid-state[57] ($\sigma_{iso}(^{13}C)$ = 62.1 ppm) measurements. When using density-functional methods to calculate isotropic chemical shielding, it has been found that the calculated shielding values are often deshielded relative to the experimentally observed values. It has also been established that the largest discrepancies occur when the molecule has a very large isotropic σ^p value. It has been suggested by Chesnut that a semi-empirical relationship exists, such that:[95]

$$\sigma = \sigma^d + k\sigma^p \qquad [3.13]$$

where k is an empirically determined scaling factor, equal to 0.952 for carbon. The diamagnetic and paramagnetic shielding values are calculated to be 237.00 ppm and −185.29 ppm, respectively (Table 3.1). Using the empirical correction factor, this results in a scaled isotropic carbon shielding value (σ_{iso}') of 60.60 ppm, which is in better agreement with the experimental values. It is also clear that occ − vir mixing contributes more significantly to σ^p than does occ − occ mixing.

3.4.1.2 Anisotropic Carbon Chemical Shielding

Low-temperature solid-state NMR measurements of the carbon CSA in ethene

-97-

highlight a large, non-axially symmetric shielding tensor ($\Omega(^{13}C)$ = 210 ppm; $\kappa(^{13}C)$ =

−0.09).[57] The calculated carbon chemical shielding tensor parameters are in good

agreement with these values, particularly the calculated value for the skew: $\Omega(^{13}C)$ = 237.18

ppm; $\kappa(^{13}C)$ = −0.11. With respect to one another, the total diamagnetic carbon chemical

shielding (see Table 3.1) is found to be substantially less anisotropic than the total

paramagnetic carbon chemical shielding. The reasons for this considerable difference

depend strongly upon the mechanisms which give rise to σ^d and σ^p, as will be shown below.

Table 3.1 C_2H_4 - Contributions to Carbon Chemical Shielding (ppm) [a]

contribution	σ_{11} (ppm)	σ_{22} (ppm)	σ_{33} (ppm)	σ_{iso} (ppm)	Ω (ppm)	$\Delta\sigma$ [b] (ppm)	κ
σ^d (total)	247.32	247.26	216.43	237.00	—	—	—
σ^p (gauge)	0.00	0.00	−8.90	−2.97	—	—	—
σ^p (occ – occ)	47.80	80.98	192.65	107.14	—	—	—
σ^p (occ – vir)	−366.31	−267.90	−234.18	−289.47	—	—	—
σ^p (total)	−318.51	−186.92	−50.44	−185.29	—	—	—
σ (total)	−71.19	60.34	165.99	51.71	237.18	184.36	−0.11
experiment [c]	—	—	.—	63.3 [d]	210	162	−0.09
calculation [e]	—	—	—	65.68	—	—	—

[a] TZ2P all-electron basis set on all atoms, see **3.2** for parameter definitions.
[b] The anisotropy will assume a negative value only if σ_{zz} is to low frequency of σ_{iso}.
[c] See references [94], [11] and [57].
[d] Average of reported values.
[e] Previously calculated value which agrees well with experiment. See reference [96].

Ethene can be represented using the D_{2h} point group (see Table B.2 for character

table), and, as expected, the principal components of the shielding tensor are determined by

the symmetry of the molecule (Figure 3.6a). σ_{33} points out of the molecular plane (along one

of the twofold (C_2) rotational axes), with σ_{22} pointing parallel to the olefinic carbon-carbon

bond (also along a C_2 axis), while σ_{11} lies perpendicular to the double bond (parallel to the direction of the third C_2 axis). This orientation matches exactly with previous accounts and is the same for each of the two carbon atoms.[97]
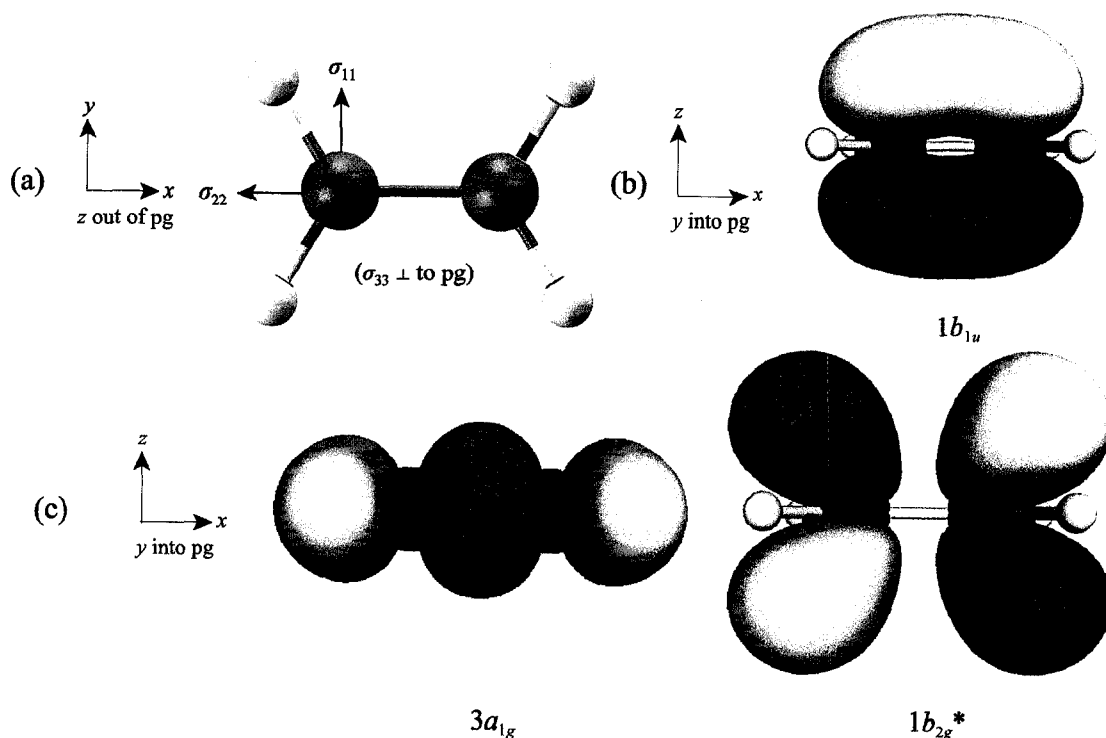
Figure 3.6 (a) Carbon chemical shielding tensor orientation of ethene in the molecular frame. (b) The $1b_{1u}$ MO, which is of high p_z AO character, contributes to σ^d in a relatively anisotropic fashion (dark shading represents negative contours, while light shading represents positive). (c) An example of symmetry-allowed MO mixing is provided by considering $3a_{1g} \leftrightarrow 1b_{2g}^*$ ($\leftrightarrow$ denotes MO mixing). The $\hat{R}_y$ operator acts such that it will rotate the MOs about the y-axis (centred on a carbon atom), and produce shielding parallel to this direction. As the y-axis is parallel to the σ_{11} principal component, the shielding is produced along σ_{11}.

The most significant contributions to diamagnetic shielding at the carbon atoms arise from molecular orbitals with high carbon AO character (see Table B.3 for fragment orbital

-99-

(FO) contributions to the MOs). It is also worth noting that essentially all (ca. 98 %) of the diamagnetic shielding arises from 4 MOs (Table 3.2). The low-lying $1a_{1g}$ and $1b_{3u}$ MOs contribute to shielding in a very isotropic manner, and it is noted that they are of high s-character. These two MOs are composed using a linear combination of the $1s$ AOs on the two carbon atoms: the $1a_{1g}$ is $\sqrt{0.5}\,1s(C_1) + \sqrt{0.5}\,1s(C_2)$ while the $1b_{3u}$ is $\sqrt{0.5}\,1s(C_1) - \sqrt{0.5}\,1s(C_2)$, where C_1 and C_2 represent the two olefinic carbon atoms. Increased anisotropic contributions to σ^d are seen to be due to MOs which are of lower s-character. For example, the $1b_{1u}$ MO (Figure 3.6b) is primarily a linear combination of the $2p_z$ AOs on the carbon atoms and possesses the largest difference between principal component values out of the four MOs which contribute in a substantial fashion to σ^d.

Table 3.2 C_2H_4 - Significant Diamagnetic Contributions to $\bar{\sigma}$, Arranged by MO

$\psi_p{}^a$	MO	σ_{11} (ppm)	σ_{22} (ppm)	σ_{33} (ppm)	σ_{iso} (ppm)	$\Delta_{pc}{}^b$ (ppm)	s char. (%)	p char. (%)
1	$1a_{1g}$	100.1	100.2	100.1	100.1	0.1	100.0	0.0
2	$1b_{3u}$	100.1	100.3	100.1	100.1	0.2	100.0	0.0
3	$2a_{1g}$	16.0	18.0	15.3	16.4	2.7	88.0	12.0
8	$1b_{1u}$	22.8	19.2	9.6	17.2	13.2	0.0	100.0
—	rem ^{c}	8.3	9.6	–8.7	3.2	—	—	—

^{a} Wave functions are numbered according to increasing energy, with 1 representing the lowest energy eigenstate.
^{b} The value of the greatest difference between principal component values.
^{c} Remaining contributions from all other MOs.

Paramagnetic contributions to the carbon chemical shielding tensor are principally due to occ – vir MO mixing, with the $3a_{1g} \leftrightarrow 1b_{2g}{}^*$ and $1b_{1g} \leftrightarrow 1b_{2g}{}^*$ MO pairs ($\leftrightarrow$ denotes that a pair of MOs are mixing) making the most significant contributions to σ^p (Table 3.3).

-100-

According to the calculation, $3a_{1g} \leftrightarrow 1b_{2g}*$ MO mixing leads to paramagnetic deshielding along σ_{11}. Using group theory, it will be shown why the mixing is allowed and why the shielding produced is oriented along σ_{11}. Three non-degenerate rotational operators are available in the D_{2h} point group, where $\Gamma(\hat{R}_x) = B_{3g}$, $\Gamma(\hat{R}_y) = B_{2g}$ and $\Gamma(\hat{R}_z) = B_{1g}$. The direct product of the symmetry representations evaluates as follows:

$$\Gamma(\psi_b) \otimes \Gamma(\hat{R}_n) \otimes \Gamma(\psi_a) = B_{2g} \otimes \begin{bmatrix} B_{3g} \\ B_{2g} \\ B_{1g} \end{bmatrix} \otimes A_{1g} = \begin{bmatrix} B_{1g} \\ A_{1g} \\ B_{3g} \end{bmatrix}. \qquad [3.14]$$

From [22], it is clear that only a rotational transformation about the y-axis will lead to magnetic dipole-allowed MO mixing. This is because only this matrix element equals or contains the totally symmetric representation of the D_{2h} point group (i.e., A_{1g}). By observing the orientation of the chemical shielding tensor in the frame of the molecule (Figure 3.6a), it is seen that y and σ_{11} are collinear. Hence, $3a_{1g} \leftrightarrow 1b_{2g}*$ is symmetry-allowed and must produce shielding along σ_{11}, in agreement with the calculated direction. To determine the magnitude of the shielding that is produced by this MO pair, a number of additional items must be considered, the two most important of which are the degree of overlap between the two MOs, and their separation in energy (ΔE). To help qualitatively visualize the overlap between the MO pair, see Figure 3.6c. By rotating the $3a_{1g}$ MO about the y-axis, it can be anticipated that a high degree of overlap with the $1b_{2g}*$ MO should result. Lastly, by observing Figure 3.7a, it is seen that these two MOs are energetically similar ($\Delta E = 9.18$ eV). Generally speaking, important occ – vir contributions commonly involve the HOMO, the LUMO, or MOs which are energetically similar to the HOMO and LUMO (i.e., valence

-101-

MOs).

Table 3.3 C_2H_4 - Significant Paramagnetic Contributions to $\tilde{\sigma}$, Arranged by MO

ψ_a[a]	MO	ψ_b	MO	σ_{11} (ppm)	σ_{22} (ppm)	σ_{33} (ppm)	σ_{iso} (ppm)	$\langle\psi_b\|R_n\|\psi_a\rangle$ [b]
Occupied - Occupied Molecular Orbital Mixing Contributions								
4	$2b_{3u}$	5	$1b_{2u}$	0.0	0.0	76.7	25.6	$\langle b_{2u}\|R_z\|b_{3u}\rangle$
4		8	$1b_{1u}$	47.5	0.0	0.0	15.8	$\langle b_{1u}\|R_y\|b_{3u}\rangle$
5	$1b_{2u}$	8	$1b_{1u}$	0.0	81.0	0.0	27.0	$\langle b_{1u}\|R_x\|b_{2u}\rangle$
6	$3a_{1g}$	7	$1b_{1g}$	0.0	0.0	122.3	40.8	$\langle b_{1g}\|R_z\|a_{1g}\rangle$
—	—	—	rem [b]	0.3	0.0	−6.4	−2.1	—
Occupied - Virtual Molecular Orbital Mixing Contributions								
5	$1b_{2u}$	15	$2b_{1u}$*	0.0	−38.3	0.0	−12.8	$\langle b_{1u}\|R_x\|b_{2u}\rangle$
5		24	$6b_{3u}$*	0.0	0.0	−37.0	−12.3	$\langle b_{3u}\|R_z\|b_{2u}\rangle$
6	$3a_{1g}$	9	$1b_{2g}$*	−219.4	0.0	0.0	−73.1	$\langle b_{2g}\|R_y\|a_{1g}\rangle$
6		19	$2b_{2g}$*	−46.9	0.0	0.0	−15.6	$\langle b_{2g}\|R_y\|a_{1g}\rangle$
6		23	$3b_{1g}$*	0.0	0.0	−28.5	−9.5	$\langle b_{1g}\|R_z\|a_{1g}\rangle$
7	$1b_{1g}$	9	$1b_{2g}$*	0.0	−126.3	0.0	−42.1	$\langle b_{2g}\|R_x\|b_{1g}\rangle$
7		10	$4a_{1g}$*	0.0	0.0	−31.2	−10.4	$\langle a_{1g}\|R_z\|b_{1g}\rangle$
7		18	$6a_{1g}$*	0.0	0.0	−36.0	−12.0	$\langle a_{1g}\|R_z\|b_{1g}\rangle$
7		19	$2b_{2g}$*	0.0	−47.5	0.0	−15.8	$\langle b_{2g}\|R_x\|b_{1g}\rangle$
—	—	—	rem [c]	−100.0	−55.8	−101.5	−85.9	—

[a] Wave functions are numbered according to increasing energy, with 1 representing the lowest energy eigenstate.

[b] Integrands which evaluate to non-zero matrix elements. To confirm MO mixing is symmetry allowed, evaluate the direct product of the symmetry representations of the MOs and rotational operator. For brevity, the operator caret symbol has been dropped when denoting rotational operators in tables.

[c] Remaining contributions from all other MOs.

If the same procedure is applied to predict the direction of shielding produced by the $1b_{1g} \leftrightarrow 1b_{2g}$* MO pair, one finds that the symmetry of the rotational operator must be represented by B_{3g}, which is a representation of $\hat{R}_x$. Thus, symmetry constrains the shielding that is produced by this MO pair to be along the x-direction of the molecule, which is

-102-

coincident with σ_{22}, exactly as predicted in Table 3.3. A number of additional contributions to σ^p do exist (see Figure 3.7 for a schematic of the important eigenstates, as well as ADFview renderings of a number of the MOs which contribute substantially to σ^p), but they roughly cancel one another out.
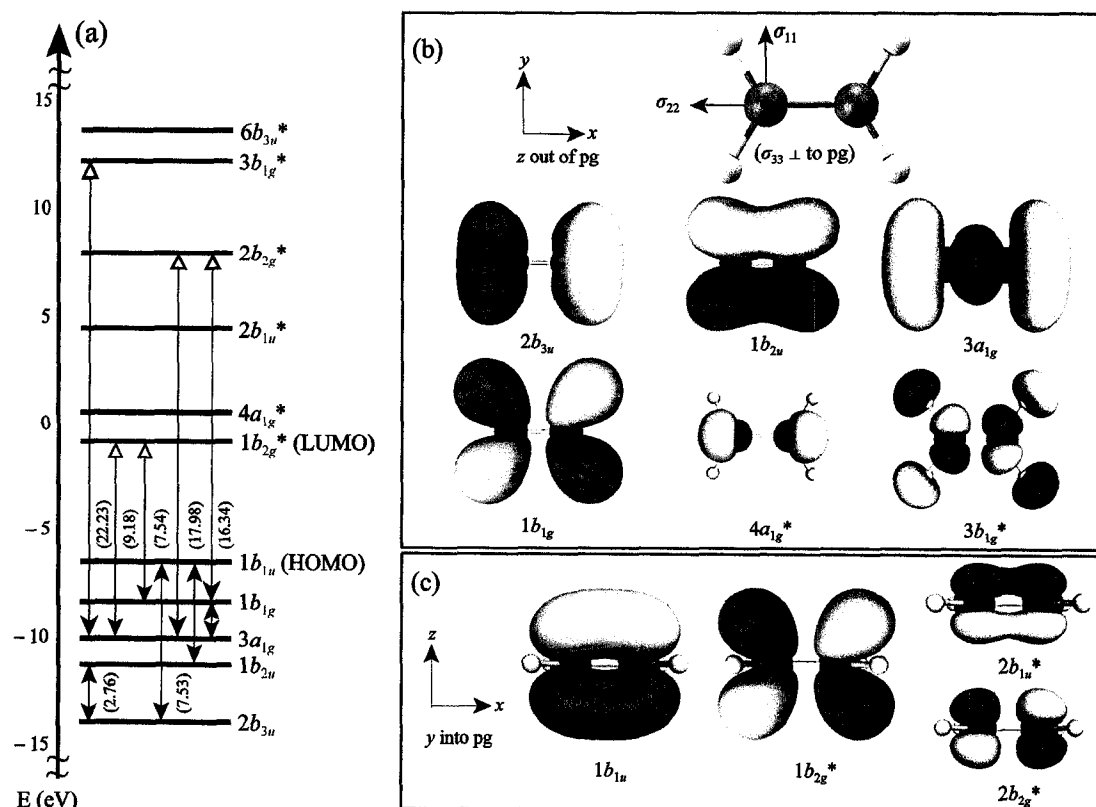
Figure 3.7 (a) Partial MO diagram for ethene, highlighting MOs that make significant contributions to σ^p (ΔE values in parentheses; open and closed arrowheads refer to virtual and occupied MOs, respectively). (b,c) Visual representations of MOs which contribute substantially to σ^p, as viewed along the z (b) and y (c) directions.

It is therefore clear that the $3a_{1g} \leftrightarrow 1b_{2g}^*$ and $1b_{1g} \leftrightarrow 1b_{2g}^*$ MO pairs are responsible to a great extent for the resultant span and skew values of the carbon chemical shielding tensor. Other MO pairs contribute more modestly to σ^p, due in large part to two reasons: (i) greater

-103-

ΔE values and (ii) while the occupied orbitals are typically of high carbon character, a number of the virtual orbitals have significant hydrogen character (see Table B.3), which would not be expected to lead to significant shielding at the carbon atoms (i.e., relatively small overlap coefficient magnitudes).

3.4.2 Hydrogen Fluoride, HF

3.4.2.1 Isotropic Fluorine Chemical Shielding

Using a geometry-optimized HF molecule (see Table B.1 for geometry), $\sigma_{iso}(^{19}F)$ is calculated to be 404.02 ppm (Table 3.4), in relatively good agreement with the experimental value determined for the gas-phase molecule ($\sigma_{iso}(^{19}F) = 410 \pm 6$ ppm).[98] In fact, the shielding value calculated herein appears to estimate σ_{iso} as well as high-level coupled-cluster (CCSD(T))[99] and relativistic Hartree-Fock[100,101] calculations, in line with earlier conclusions that electron-correlation and relativistic effects are not very significant in this molecule, each making maximal contributions to $\sigma_{iso}(^{19}F)$ of about 5 ppm.[102] In contrast to ethene, diamagnetic contributions dominate those of paramagnetic origin, with the total contributions to σ^d and σ^p being calculated as 470.56 ppm and −66.54 ppm, respectively. Due to the small magnitude of σ^p, a scaling calculation does not appear warranted.

3.4.2.2 Anisotropic Fluorine Chemical Shielding

There do not appear to be any comments in the literature regarding the direct measurement of fluorine shielding anisotropy in a ground-state HF molecule. High-resolution molecular-beam electron-resonance measurements taken from an excited state (v

-104-

= 0, J = 1) HF molecule infer an axially-symmetric $(\kappa(^{19}F) = +1.00)$ fluorine chemical shielding tensor with significant anisotropy in fluorine shielding when comparing directions perpendicular and parallel to the HF bond axis $(\Omega(^{19}F) = 108 \pm 9$ ppm).[103] It has been established that the shielding tensor differences between the ground and first excited rotational states are very minimal, on the order of 0.1 ppm.[104] DFT calculations conducted herein agree reasonably well with the previous account $(\Omega(^{19}F) = 116.24$ ppm; $\kappa(^{19}F) = +1.00$; Table 3.4).

Table 3.4 HF - Contributions to Fluorine Chemical Shielding (ppm) [a]

contribution	σ_{11} (ppm)	σ_{22} (ppm)	σ_{33} (ppm)	σ_{iso} (ppm)	Ω (ppm)	$\Delta\sigma$ (ppm)	κ
σ^d (total)	465.08	465.08	481.51	470.56	—	—	—
σ^p (gauge)	0.00	0.00	0.00	0.00	—	—	—
σ^p (occ – occ)	106.03	106.03	0.00	70.69	—	—	—
σ^p (occ – vir)	–205.84	–205.84	0.00	–137.23	—	—	—
σ^p (total)	–99.81	–99.81	0.00	–66.54	—	—	—
σ (total)	365.27	365.27	481.51	404.02	116.24	–116.24	1.00
experiment [b]	—	—	—	410(6)	108(9)	–108(9)	1.00
calculation [c]	—	—	—	418.4 [d]	—	—	—

[a] TZ2P all-electron basis set on all atoms, see **3.2** for parameter definitions.
[b] See references [98] and [103].
[c] Results from high-level calculations. See references [99-101].
[d] Average calculated value.

The fluorine shielding tensor elements of HF, a molecule which can be represented using the linear point group $C_{\infty v}$ (see Appendix, Table B.4 for character table), are oriented in a manner that is derived from the symmetry of the molecule: all find themselves in the infinite σ_v mirror "plane," with σ_{33} along the bonding and C_∞ rotational axes and σ_{11} and σ_{22} perpendicular to the infinite rotational axis (Figure 3.8b). Due to the axial symmetry of the

-105-

shielding tensor, the σ_{11} and σ_{22} labels may be interchanged and may be referred to simply

as $\sigma_\perp$ as they are perpendicular to the HF bonding axis (as well, σ_{33} may be denoted as $\sigma_\parallel$).

From the data in Table 3.4, it is seen that paramagnetic shielding does not contribute at all

to $\sigma_{33}/\sigma_\parallel$ (i.e., along the bond axis).
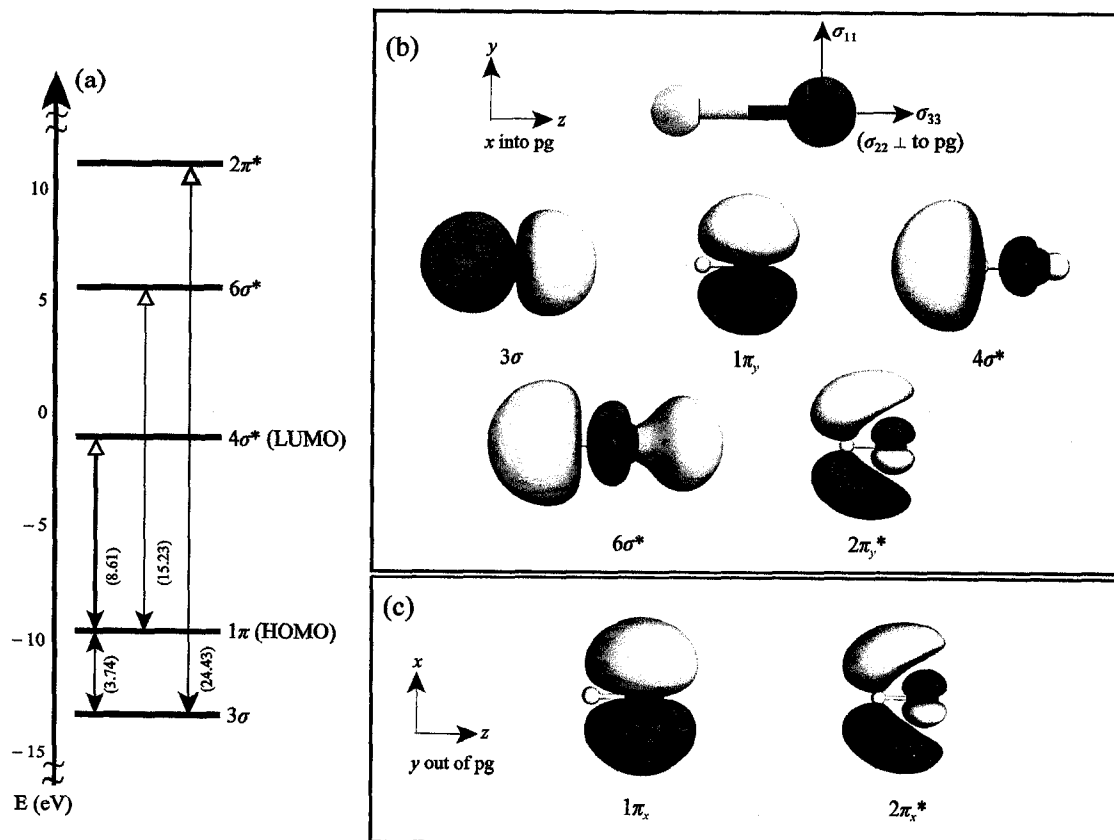
Figure 3.8 (a) Partial MO diagram for HF, highlighting MOs that make significant contributions to σ^p (ΔE values in parentheses). (b,c) Fluorine chemical shielding tensor orientation for HF in the molecular frame (top) along with visual representations of the MOs which contribute substantially to σ^p, as viewed along the x (b) and y (c) directions.

The diamagnetic contributions to fluorine chemical shielding (Table 3.5) share many

of the traits that were observed in the σ^d contributions in ethene. The largest contributions

are due to electron circulation in low-lying MOs (1σ, 2σ, etc.; the 5 MOs in Table 3.5

-106-

account for 100% of the calculated σ^d), they are considerably less anisotropic than σ^p components, and the contributions become less isotropic as the degree of MO s character is decreased (see Table B.5 for FO contributions to the HF MOs).

Table 3.5 HF - Significant Diamagnetic Contributions to $\tilde{\sigma}$, Arranged by MO

ψ_p	MO	σ_{11} (ppm)	σ_{22} (ppm)	σ_{33} (ppm)	σ_{iso} (ppm)	Δ_{pc} (ppm)	s char. (%)	p char. (%)
1	1σ	305.8	305.8	305.8	305.8	0.0	100.0	0.0
2	2σ	47.9	47.9	46.9	47.6	1.0	95.6	4.4
3	3σ	32.2	32.2	24.6	29.6	7.6	77.4	22.6
4	$1\pi_x$	52.9	26.3	52.1	43.8	26.6	0.0	100.0
5	$1\pi_y$	26.3	52.9	52.1	43.8	26.6	0.0	100.0
—	rem	0.0	0.0	0.0	0.0	—	—	—

From Table 3.6, it is seen that the fluorine paramagnetic shielding tensor does not have any significant contributions that arise from MO mixing due to $\hat{R}_z$ (in fact, there are not even trace contributions due to $\hat{R}_z$). Because of this, no paramagnetic deshielding is observed along this axis and it becomes clear that σ_{33} should be oriented along this direction. Using group theory, one can see why molecular symmetry constrains σ_{33} along this direction. From Table 3.6, it is seen that only $\sigma \leftrightarrow \pi$ type MO mixing contributes substantially to σ^p. The $1\pi \leftrightarrow 6\sigma^*$ MO pair (molecular orbital renderings are provided in Figure 3.8) will serve as the example. First, one notes that in addition to the previously-mentioned $\hat{R}_z$ operator ($\Gamma(\hat{R}_z) = A_2$), the $C_{\infty v}$ point group possesses a doubly-degenerate rotational operator ($\hat{R}_x, \hat{R}_y$) which belongs to the E_1 representation. The direct product of the symmetry representations for this MO pair evaluates as below:

-107-

$$\Gamma(\psi_b) \otimes \Gamma(\hat{R}_n) \otimes \Gamma(\psi_a) \;=\; A_1 \otimes \begin{bmatrix} E_1 \\ A_2 \end{bmatrix} \otimes E_1 \;=\; \begin{bmatrix} A_1 + A_2 + E_2 \\ E_1 \end{bmatrix} \qquad [3.15]$$

From [3.15], a σ and π MO are symmetry-allowed to mix only when the rotational operator may be represented by E_1, which is the $(\hat{R}_x, \hat{R}_y)$ operator. The $\hat{R}_z$ rotational operator is not symmetry-allowed to mix any of these types of MOs. Hence, there can be no resultant shielding along this direction, as predicted in the calculations. This ensures that the σ_{33} component of the shielding tensor points along the C_∞ axis.

Table 3.6 HF - Significant Paramagnetic Contributions to $\tilde{\sigma}$, Arranged by MO

ψ_a	MO	ψ_b	MO	σ_{11} (ppm)	σ_{22} (ppm)	σ_{33} (ppm)	σ_{iso} (ppm)	$\langle \psi_b | R_n | \psi_a \rangle$
Occupied - Occupied Molecular Orbital Mixing Contributions								
3	3σ	4	$1\pi_x$	97.9	0.0	0.0	32.6	$\langle \pi | (R_x R_y) | \sigma \rangle$
3		5	$1\pi_y$	0.0	97.9	0.0	32.6	$\langle \pi | (R_x R_y) | \sigma \rangle$
—	—	—	rem	8.1	8.1	0.0	5.5	—
Occupied - Virtual Molecular Orbital Mixing Contributions								
3	3σ	9	$2\pi_x{}^*$	−18.4	0.0	0.0	−6.1	$\langle \pi | (R_x R_y) | \sigma \rangle$
3		10	$2\pi_y{}^*$	0.0	−18.4	0.0	−6.1	$\langle \pi | (R_x R_y) | \sigma \rangle$
4	$1\pi_x$	6	$4\sigma^*$	−56.4	0.0	0.0	−18.8	$\langle \sigma | (R_x R_y) | \pi \rangle$
4		8	$6\sigma^*$	−75.7	0.0	0.0	−25.2	$\langle \sigma | (R_x R_y) | \pi \rangle$
5	$1\pi_y$	6	$4\sigma^*$	0.0	−56.4	0.0	−18.8	$\langle \sigma | (R_x R_y) | \pi \rangle$
5		8	$6\sigma^*$	0.0	−75.7	0.0	−25.2	$\langle \sigma | (R_x R_y) | \pi \rangle$
—	—	—	rem	−55.3	−55.3	0.0	−37.0	—

As each π MO can be broken into π_x and π_y components, it should be expected by symmetry that when they mix with a σ MO, the value that each MO pair (i.e., $\sigma \leftrightarrow \pi_x$ and $\sigma \leftrightarrow \pi_y$) contributes to shielding would be the same, as both the orbital overlap and ΔE variables are exactly the same in each case. Due to this, the fluorine chemical shielding

-108-

tensor must be axially-symmetric, in agreement with both observational data and calculations. As before, the actual amount that each MO pair contributes to shielding is typically most produced when the energy difference between the mixing MOs is small. It is observed that the most significant paramagnetic contributions to chemical shielding are due to the 1π (HOMO), the $4\sigma^*$ (LUMO), and a few other energetically similar MOs (i.e., 3σ, 6σ, etc.).

3.4.3 Trifluorophosphine, PF_3

3.4.3.1 Isotropic Phosphorus Chemical Shielding

The isotropic chemical shielding value at the phosphorus atom in a geometry-optimized PF_3 molecule ($\sigma_{iso}(^{31}P)$; see Table B.1 for geometry), was calculated to be 153.65 ppm (Table 3.7), clearly in poor agreement with the experimental value of 222.69 ppm reported by Jameson.[31] In contrast to HF, the phosphorus paramagnetic shielding term is of considerable magnitude ($\sigma^p = -803.20$ ppm) and therefore a scaling calculation is performed. The empirical scaling factor for phosphorus was determined to be 0.906 ± 0.008, leading to $\sigma_{iso}'(^{31}P) = 229.15$ ppm, in very good agreement with both the experimental findings as well as high-level CCSD(T) calculations.[105] In contrast to the chemical shielding values provided earlier for ethene and HF, contributions to σ^p at the phosphorus atom in PF_3 are dominated by occ – vir mixing to the point where occ – occ mixing is barely of significance.

3.4.3.2 Anisotropic Phosphorus Chemical Shielding

Phosphorus NMR measurements upon PF_3 highlight a very anisotropic shielding environment, with $\Omega(^{31}P)$ ranging from 181 ± 5 ppm to 228 ± 2 ppm when dissolved in smectic[106] and nematic[107] liquid crystal solvents, respectively. This span, which represents a significant fraction of the total phosphorus shielding range (currently about 1500 ppm for diamagnetic samples)[108] is confirmed by the calculations reported herein, as $\Omega(^{31}P) = 247.97$ ppm (Table 3.7). All previous experimental observations and theoretical treatments report an axially-symmetric phosphorus shielding tensor ($\kappa(^{31}P) = +1.00$), in agreement with our findings.

Table 3.7 PF_3 - Contributions to Phosphorus Chemical Shielding (ppm) [a]

contribution	σ_{11} (ppm)	σ_{22} (ppm)	σ_{33} (ppm)	σ_{iso} (ppm)	Ω (ppm)	$\Delta\sigma$ (ppm)	κ
σ^d (total)	958.79	958.79	952.98	956.85	—	—	—
σ^p (gauge)	−1.29	−1.29	−1.73	−1.44	—	—	—
σ^p (occ − occ)	−15.34	−15.34	−76.89	−35.86	—	—	—
σ^p (occ − vir)	−871.17	−871.17	−555.41	−765.91	—	—	—
σ^p(total)	−887.80	−887.80	−634.02	−803.20	—	—	—
σ (total)	70.99	70.99	318.96	153.65	247.97	−247.97	1.00
experiment [b]	—	—	—	222.69	182(5)	−182(5)	1.00
					228(2)	−228(2)	1.00
calculation [c]	—	—	—	235.24	273.95	−273.95	—

[a] TZ2P all-electron basis set on all atoms.

[b] Anisotropic parameters are given for PF_3 dissolved in smectic (top value) and nematic (bottom value) liquid crystal solvents. See references [31], [106] and [107].

[c] Results from high-level calculations. See reference [105].

PF_3 may be represented by the C_{3v} point group (Table B.6). As with ethene and HF, the orientation of the shielding tensor (Figure 3.9a) is determined by molecular symmetry:

-110-

σ_{33} lies along the C_3 axis (z-direction), with the other two principal components lying perpendicular to this axis (in the xy-plane, assuming the coordinate system origin to be at the phosphorus atom). Due to the axial symmetry of the tensor, the directions associated with the σ_{11} and σ_{22} components, as pictured in Figure 3.9a, may be interchanged (equivalently, they may be referred to as $\sigma_\perp$, as they both point perpendicular to the C_3 axis).
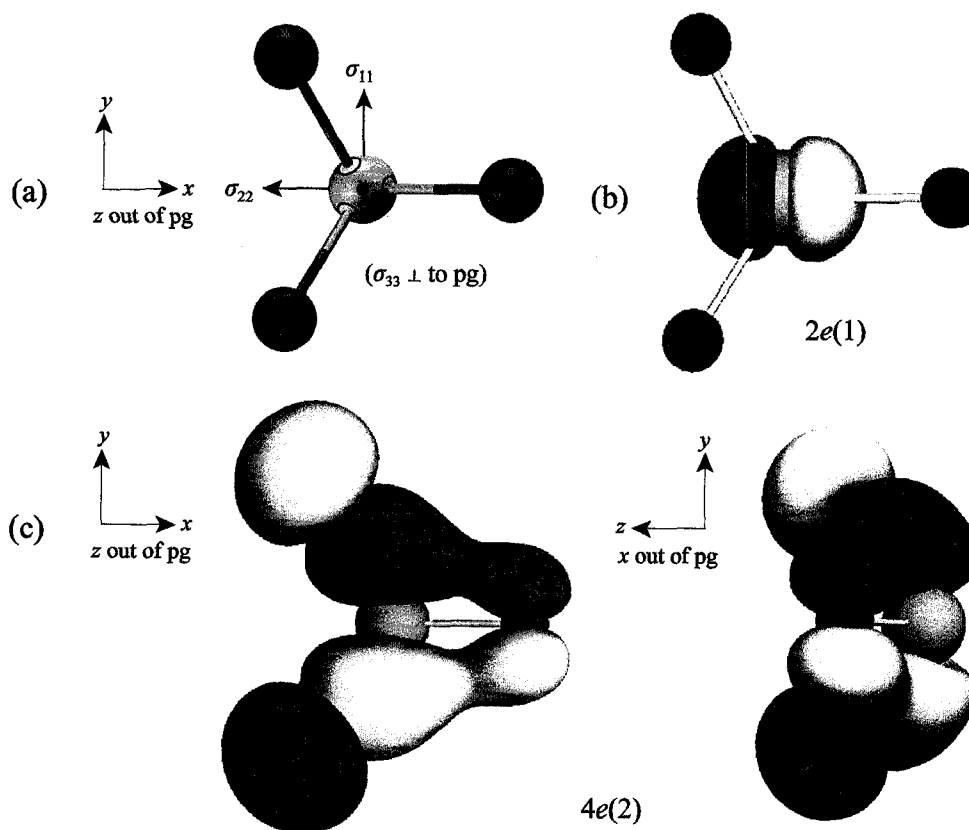
Figure 3.9 (a) Phosphorus chemical shielding tensor orientation of PF_3 in the molecular frame. ADFview renderings of the (b) $2e(1)$ and (c) $4e(2)$ MOs, which do not overlap with one another unless the z rotational operator is applied. In order to aid in visualization, the $4e(2)$ MO is provided from two points of view, one along the z axis (left) and one along the x axis (right).

The contributions to diamagnetic phosphorus shielding (Table 3.8) are seen to arise primarily from MOs with high phosphorus AO character (as expected; see Table B.7 for FO

-111-

contributions to the MOs), with the degree of anisotropy again being dependent upon the degree of s- and p-character of the MO. Nearly all of the diamagnetic shielding (94 %) can be accounted for by considering only the MOs shown in Table 3.8. Much the same can be said about the paramagnetic shielding contributions, as out of 112 MOs, only 9 (Table 3.9) need to be considered to account for the majority (ca. 63 %) of the paramagnetic shielding. Occ − occ contributions contribute only slightly to the net paramagnetic shielding tensor, and are seen to arise from MO mixing between $e \leftrightarrow e$ and $e \leftrightarrow a_1$ mixing pairs. The C_{3v} group contains only 2 rotational operators, $\hat{R}_z$ and $(\hat{R}_x, \hat{R}_y)$, whose representations are A_2 and E, respectively. By evaluating the selection rule for this point group, it is not immediately apparent why $e \leftrightarrow e$ leads to shielding along the z-direction only (as in Table 3.9):

$$\Gamma(\psi_b) \otimes \Gamma(\hat{R}_n) \otimes \Gamma(\psi_a) = E \otimes \begin{bmatrix} E \\ A_2 \end{bmatrix} \otimes E = \begin{bmatrix} 3E + A_2 + A_1 \\ E + A_2 + A_1 \end{bmatrix}. \qquad [3.16]$$

Table 3.8 PF_3 - Significant Diamagnetic Contributions to $\tilde{\sigma}$, Arranged by MO

ψ_p	MO	σ_{11} (ppm)	σ_{22} (ppm)	σ_{33} (ppm)	σ_{iso} (ppm)	Δ_{pc} (ppm)	s char. (%)	p char. (%)
1	$1a_1$	517.1	517.1	517.1	517.1	0.0	100.0	0.0
5	$3a_1$	99.6	99.6	99.6	99.6	0.0	100.0	0.0
6	$2e(1)$	115.1	57.6	115.1	96.0	57.5	0.0	100.0
7	$2e(2)$	57.6	115.1	115.1	96.0	57.5	0.0	100.0
8	$4a_1$	114.5	114.5	57.6	95.5	56.9	0.1	99.9
—	rem	54.9	54.9	48.5	52.7	—	—	—

According to the selection rule, shielding is allowed by symmetry along the x- and y-directions, in addition to the z-direction, which contrasts sharply with the calculated direction. The mixing between the $2e(1) \leftrightarrow 4e(2)$ MO pair will illustrate why the calculated

-112-

direction is correct. If the 2e(1) orbital is rotated about the x-axis, it is clear that its

orientation will not vary and it remains as pictured in Figure 3.9b. If one considers the

degree of overlap between the 2e(1) and 4e(2) MOs (Figure 3.9c), it is clear that there are

equal amounts of constructive and destructive orbital overlap, leading to zero net overlap.

Rotation of the 2e(1) MO about the y-axis leads to the same situation: there are equal

amounts of constructive and destructive MO overlap and therefore there is zero net overlap.

It must be concluded that this pair of MOs cannot contribute to chemical shielding along

either the x- or y-directions, based upon overlap (not magnetic dipole-allowed mixing)

arguments. On the other hand, if the 2e(1) MO is rotated about the z-axis, there are now

significant regions of positive and negative constructive overlap. Therefore, if both the

selection rule and the degree of overlap of the mixing MOs is considered, it can be

concluded that this MO pair will contribute to shielding along the z-axis only (along σ_{33}), in

agreement with the calculated direction.

Table 3.9 PF_3 - Significant Paramagnetic Contributions to $\tilde{\sigma}$, Arranged by MO

ψ_a	MO	ψ_b	MO	σ_{11} (ppm)	σ_{22} (ppm)	σ_{33} (ppm)	σ_{iso} (ppm)	$\langle \psi_b | R_n | \psi_a \rangle$
Occupied - Occupied Molecular Orbital Mixing Contributions								
6	2e(1)	14	4e(2)	0.0	0.0	−49.9	−16.6	$\langle e | R_z | e \rangle$
6		21	$8a_1$	−50.3	0.0	0.0	−16.8	$\langle a_1 | (R_x, R_y) | e \rangle$
7	2e(2)	13	4e(1)	0.0	0.0	−49.9	−16.6	$\langle e | R_z | e \rangle$
7		21	$8a_1$	0.0	−50.3	0.0	−16.8	$\langle a_1 | (R_x, R_y) | e \rangle$
8	$4a_1$	13	4e(1)	−57.4	0.0	0.0	−19.1	$\langle e | (R_x, R_y) | a_1 \rangle$
8		14	4e(2)	0.0	−57.4	0.0	−19.1	$\langle e | (R_x, R_y) | a_1 \rangle$
13	4e(1)	21	$8a_1$	66.8	0.0	0.0	22.3	$\langle a_1 | (R_x, R_y) | e \rangle$
14	4e(2)	21	$8a_1$	0.0	66.8	0.0	22.3	$\langle a_1 | (R_x, R_y) | e \rangle$
—	—	—	rem	25.6	25.6	22.9	24.6	—

ψ_a	MO	ψ_b	MO	σ_{11} (ppm)	σ_{22} (ppm)	σ_{33} (ppm)	σ_{iso} (ppm)	$\langle\psi_b|R_n|\psi_a\rangle$
Occupied - Virtual Molecular Orbital Mixing Contributions								
13	$4e(1)$	23	$7e(2)^*$	0.0	0.0	−138.9	−46.3	$\langle e|R_z|e\rangle$
13		28	$11a_1^*$	−88.8	0.0	0.0	−29.3	$\langle a_1|(R_x,R_y)|e\rangle$
14	$4e(2)$	22	$7e(1)^*$	0.0	0.0	−138.9	−46.3	$\langle e|R_z|e\rangle$
14		28	$11a_1^*$	0.0	−88.8	0.0	−29.3	$\langle a_1|(R_x,R_y)|e\rangle$
21	$8a_1$	22	$7e(1)^*$	−493.2	0.0	0.0	−164.4	$\langle e|(R_x,R_y)|a_1\rangle$
21		23	$7e(2)^*$	0.0	−493.2	0.0	−164.4	$\langle e|(R_x,R_y)|a_1\rangle$
—	—	—	rem	−290.0	−290.0	−277.6	−285.9	—

$$7e(1) \otimes (\hat{R}_x, \hat{R}_y) \otimes 8a_1 = E \otimes E \otimes A_1 \supseteq A_1$$
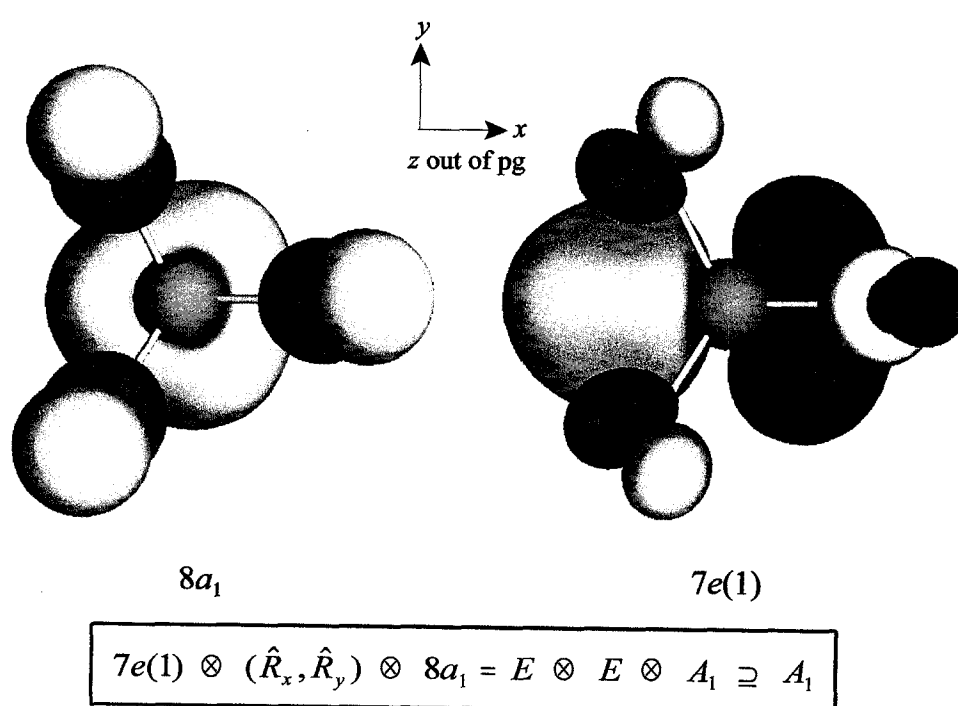
Figure 3.10 The most significant contribution to σ^p along the σ_{11} direction is due to $8a_1 \leftrightarrow 7e(1)$. As outlined in the box, the doubly-degenerate rotational operator possesses the correct symmetry for the magnetic dipole-allowed mixing of these two MOs. If the $8a_1$ MO is rotated about the y-axis, there is clearly overlap with the $7e(1)$ MO, and as σ_{11} and the y-axis are parallel, this pair should produce shielding along σ_{11}, in agreement with the calculated direction.

σ^d often varies little as one changes the environment about an atom (*vide infra*) and therefore

will not usually determine the resultant chemical shielding. In PF_3, it is seen that the occ – vir contributions to σ^p dominate the occ – occ contributions by a factor of ca. 20:1. Due to the pronounced anisotropic fashion in which pairwise MO mixing contributes to σ^p, the observed isotropic shielding value, as well as the magnitude of the shielding anisotropy, can be rationalized by considering the occ – vir contributions to σ^p. The 6 pairs of MOs disclosed in Table 3.9 account for approximately 63 % of all occ – vir contributions to the isotropic shielding value, and within this set, it is clear that $8a_1$ (HOMO) $\leftrightarrow$ $7e^*$ (LUMO) mixing contributes very significantly along the σ_{11} and σ_{22} directions (Figure 3.10), with other MO pairs making less significant provisions along σ_{33}. Therefore, it is primarily this MO pair which leads to the pronounced shielding anisotropy observed in the phosphorus NMR spectra of PF_3, in agreement with earlier findings.[109] The contribution that this MO pair makes is expected to be quite substantial, as $7e^*$ has very high phosphorus character (92.1 % of this MO is from either the $3p_x$ or $3p_y$ AOs of the phosphorus, Table B.7).

-115-
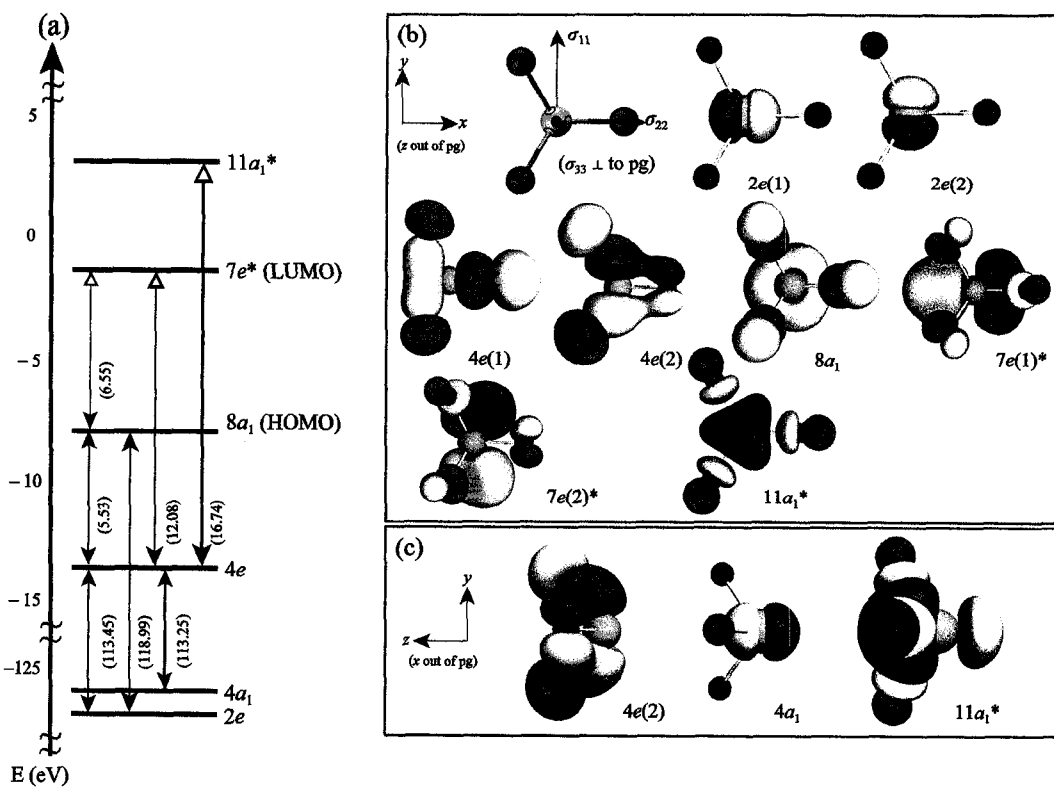
Figure 3.11 (a) Partial MO diagram for PF_3, showing MOs that make significant contributions to σ^p. (b) Renderings of these key MOs are provided as viewed along the z (b) and x (c) directions.

In addition, HOMO/LUMO mixing necessarily means that ΔE is at its minimum value (for occ – vir mixing). This can be contrasted with the shielding produced due to $4e \leftrightarrow 11a_1{}^*$. This pair contributes in a more modest fashion to σ^p due to the decreased phosphorus character of the occupied orbital, as well as a significantly larger ΔE (16.74 eV, as compared to 6.55 eV for $8a_1 \leftrightarrow 7e^*$). A partial MO diagram for PF_3, highlighting the MOs which contribute substantially to σ^p, as well as pictures of many of the important paramagnetic shielding MOs, are provided in Figure 3.11.

-116-

3.4.4   Water, H_2O

3.4.4.1   Isotropic Oxygen Chemical Shielding

The isotropic chemical shielding value at the oxygen atom in a geometry-optimized water molecule ($\sigma_{iso}(^{17}O)$) is calculated to be 322.75 ppm (Table 3.10; see Table B.1 for the optimized-geometry), in very good agreement with previously reported experimental[110,111] and high-level *ab initio*[112] values. The diamagnetic and paramagnetic portions of chemical shielding are calculated to be 384.65 ppm and –61.90 ppm, respectively. Oxygen chemical shielding calculations were also carried out upon CO and H_2CO (Table 3.10). It is observed that while σ^d varies only slightly ($\Delta\sigma^d$ is ca. 15 ppm for the set of three molecules), the total magnetic shielding at the nucleus can change by very significant amounts. In fact, $\sigma_{iso}(^{17}O$, H_2CO) is nearly 800 ppm less than in H_2O. It is abundantly clear that paramagnetic deshielding is the source of this variation: while it is very modest in H_2O, it is clearly the dominant feature in the total oxygen shielding in CO and H_2CO. The most notable change in σ^p is from the occ – vir component, while the changes in occ – occ are less pronounced, but still significant.

Table 3.10 Contributions to Isotropic Oxygen Chemical Shielding (ppm) [a]

contribution	H$_2$O [111,112]	CO [111,112]	H$_2$CO [99,113,114]
σ^d	384.65	400.69	399.56
σ^p (gauge)	−0.66	0.00	−1.41
σ^p (occ − occ)	160.28	−16.94	−13.15
σ^p (occ − vir)	−221.50	−459.85	−833.75
σ^p (total)	−61.90	−476.79	−848.30
σ_{iso} (total)	322.75	−76.10	−448.74
experimental	323.6 ± 0.6	−62.74 ± 0.59	−427.1 ± 100
calculation [b]	324.0 ± 1.5	−62.3 ± 1.5	−383.1

[a] TZ2P all-electron basis set on all atoms, see theoretical section for parameter definitions.

[b] Results from high-level calculations.

3.4.4.2 Anisotropic Oxygen Chemical Shielding

Experimental measurements of the oxygen shielding tensor in water have not been reported; rather we will attempt to rationalize the theoretically calculated tensor. The span of the oxygen shielding tensor (Table 3.11) is calculated to be 59.07 ppm, with both diamagnetic and paramagnetic shielding mechanisms making significant contributions. The near zero skew value (κ(^{17}O) = 0.16) reflects that all of the principal components are distinct and that the powder pattern (neglecting quadrupolar broadening) is distributed nearly centrosymmetrically about σ_{iso}. Water may be represented using the C_{2v} point group (see Table B.8 for character table). The calculated orientation (Figure 3.12a) of the oxygen shielding tensor is again constrained by molecular symmetry: σ_{11} points perpendicular to the molecular plane and lies in the xz-mirror plane, σ_{22} lies along the C_2 axis and in the xz- and yz-mirror planes, with σ_{33} in the yz-mirror plane. Diamagnetic shielding is most pronounced along the σ_{33} direction, while the most significant paramagnetic contributions are along σ_{11}.

Table 3.11 H_2O - Contributions to Oxygen Chemical Shielding (ppm) [a]

contribution	σ_{11} (ppm)	σ_{22} (ppm)	σ_{33} (ppm)	σ_{iso} (ppm)	Ω (ppm)	$\Delta\sigma$ (ppm)	κ
σ^d (total)	370.61	379.47	403.88	384.65	—	—	—
σ^p (gauge)	−1.97	0.00	0.00	−0.66	—	—	—
σ^p (occ − occ)	226.80	204.52	49.51	160.28	—	—	—
σ^p (occ − vir)	−300.68	−264.32	−99.57	−221.50	—	—	—
σ^p (total)	−75.85	−59.80	−50.05	−61.90	—	—	—
σ (total)	294.76	319.67	353.83	322.75	59.07	−46.62	0.16
experiment [b]	—	—	—	323.6	—	—	—
calculation [c]	—	—	—	324.0	—	—	—

[a] TZ2P all-electron basis set on all atoms.

[b] See reference [111].

[c] Results from high-level calculations. See reference [112].
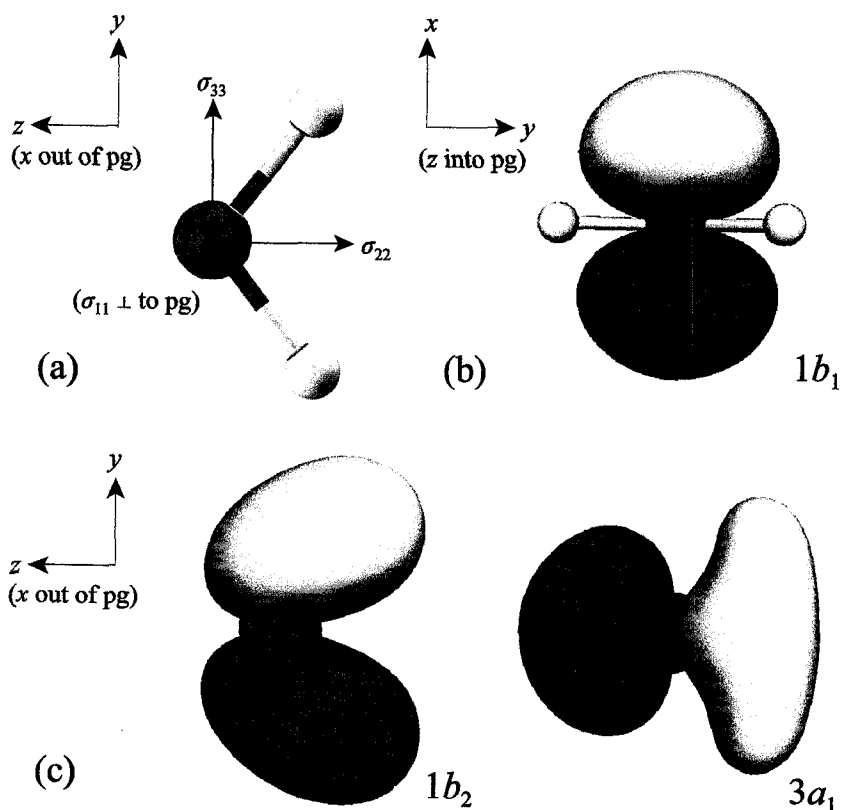
Figure 3.12 (a) Oxygen chemical shielding tensor of water in the frame of the molecule. (b,c) ADFview renderings of important chemical shielding MOs: the $1b_2 \leftrightarrow 3a_1$ and $1b_2 \leftrightarrow 1b_1$ MO pairs contribute significantly to σ^p along the σ_{11} and σ_{22} shielding directions, respectively.

-119-

The total diamagnetic shielding is again observed to be heavily dependent upon core MOs which possess high oxygen character (Table 3.12), with the most significant offering (270.6 ppm) provided by the $1a_1$ MO, which is essentially the $1s$ AO on the oxygen (see Table B.9 for FO contributions to the MOs). The four MOs listed in Table 3.12 account for 98 % of the total diamagnetic shielding. The degree of anisotropy of each contribution again appears to increase with decreasing MO s-character.

Table 3.12 H_2O - Significant Diamagnetic Contributions to $\tilde{\sigma}$, Arranged by MO

ψ_p	MO	σ_{11} (ppm)	σ_{22} (ppm)	σ_{33} (ppm)	σ_{iso} (ppm)	Δ_{pc} (ppm)	s char. (%)	p char. (%)
1	$1a_1$	270.6	270.6	270.6	270.6	0.0	100.0	0.0
2	$2a_1$	39.5	39.3	37.4	38.7	2.1	93.0	7.0
4	$3a_1$	35.1	23.3	34.3	30.9	11.8	85.0	14.0
5	$1b_1$	22.3	44.9	44.3	37.2	22.6	1.0	99.0
—	rem	3.1	1.4	17.3	7.3	—	—	—

The total oxygen paramagnetic shielding has a few very important contributors (Table 3.13). Nearly all (95 %) of the σ^p(occ − occ) contributions can be accounted for using three MO pairs, with each pair contributing shielding along a unique direction. The $1b_2 \leftrightarrow 3a_1$ and $1b_2 \leftrightarrow 1b_1$ pairs make the most pronounced contributions to σ^p (see Figure 3.12(b,c) for renderings of these three MOs). Using group theory, it will be shown that $1b_2 \leftrightarrow 3a_1$ must produce shielding along σ_{11}, while $1b_2 \leftrightarrow 1b_1$ leads to shielding along σ_{22}. The C_{2v} point group has rotational transformations of B_2, B_1 and A_2 symmetry for rotations about the x-, y- and z-axes, respectively.

Table 3.13 H_2O - Significant Paramagnetic Contributions to $\bar{\sigma}$, Arranged by MO

ψ_a	MO	ψ_b	MO	σ_{11} (ppm)	σ_{22} (ppm)	σ_{33} (ppm)	σ_{iso} (ppm)	$\langle\psi_b|R_n|\psi_a\rangle$
Occupied - Occupied Molecular Orbital Mixing Contributions								
3	$1b_2$	4	$3a_1$	209.4	0.0	0.0	69.8	$\langle a_1|R_x|b_2\rangle$
3		5	$1b_1$	0.0	204.5	0.0	68.2	$\langle b_1|R_z|b_2\rangle$
4	$3a_1$	5	$1b_1$	0.0	0.0	42.4	14.1	$\langle b_1|R_y|a_1\rangle$
—	—	—	rem	17.4	0.0	7.1	8.2	—
Occupied - Virtual Molecular Orbital Mixing Contributions								
3	$1b_2$	6	$4a_1{}^*$	−31.6	0.0	0.0	−10.5	$\langle a_1|R_x|b_2\rangle$
3		8	$5a_1{}^*$	−35.7	0.0	0.0	−11.9	$\langle a_1|R_x|b_2\rangle$
3		10	$6a_1{}^*$	−74.7	0.0	0.0	−24.9	$\langle a_1|R_x|b_2\rangle$
3		11	$2b_1{}^*$	0.0	−108.9	0.0	−36.3	$\langle b_1|R_z|b_2\rangle$
4	$3a_1$	9	$3b_2{}^*$	−68.0	0.0	0.0	−22.7	$\langle b_2|R_x|a_1\rangle$
5	$1b_1$	6	$4a_1{}^*$	0.0	0.0	−31.7	−10.6	$\langle a_1|R_y|b_1\rangle$
5		8	$5a_1{}^*$	0.0	0.0	−50.3	−16.8	$\langle a_1|R_y|b_1\rangle$
5		9	$3b_2{}^*$	0.0	−98.4	0.0	−32.8	$\langle b_2|R_z|b_1\rangle$
—	—	—	rem	−90.7	−57.0	−17.6	−55.0	—

The direct products are evaluated in the usual manner (first for $1b_2 \leftrightarrow 3a_1$, followed by $1b_2 \leftrightarrow 1b_1$):

$$\Gamma(\psi_b) \otimes \Gamma(\hat{R}_n) \otimes \Gamma(\psi_a) = A_1 \otimes \begin{bmatrix} B_2 \\ B_1 \\ A_2 \end{bmatrix} \otimes B_2 = \begin{bmatrix} A_1 \\ A_2 \\ B_1 \end{bmatrix} \qquad [3.17]$$

$$\Gamma(\psi_b) \otimes \Gamma(\hat{R}_n) \otimes \Gamma(\psi_a) = B_1 \otimes \begin{bmatrix} B_2 \\ B_1 \\ A_2 \end{bmatrix} \otimes B_2 = \begin{bmatrix} B_1 \\ B_2 \\ A_1 \end{bmatrix} \qquad [3.18]$$

[3.17] and [3.18] evaluate to contain the totally symmetric representation only when the $\hat{R}_x$

and $\hat{R}_z$ operators are applied, individually. By observing the shielding tensor orientation in

-121-

the molecular frame (Figure 3.12a), it is seen that σ_{11} is along x and σ_{22} is along z. Thus, $1b_2$ $\leftrightarrow$ $3a_1$ may only produce shielding along σ_{11} and $1b_2$ $\leftrightarrow$ $1b_1$ can contribute chemical shielding along σ_{22}, in agreement with the calculated directions. In addition to being allowed by symmetry, it is expected that these MO pairs will produce large σ^P (occ − occ) magnitudes, due to relatively small ΔE values (only 5.83 eV separates the $1b_1$ from the $1b_2$) coupled with high oxygen MO character(s) and the presence of a substantial amount of non-bonding electron density.
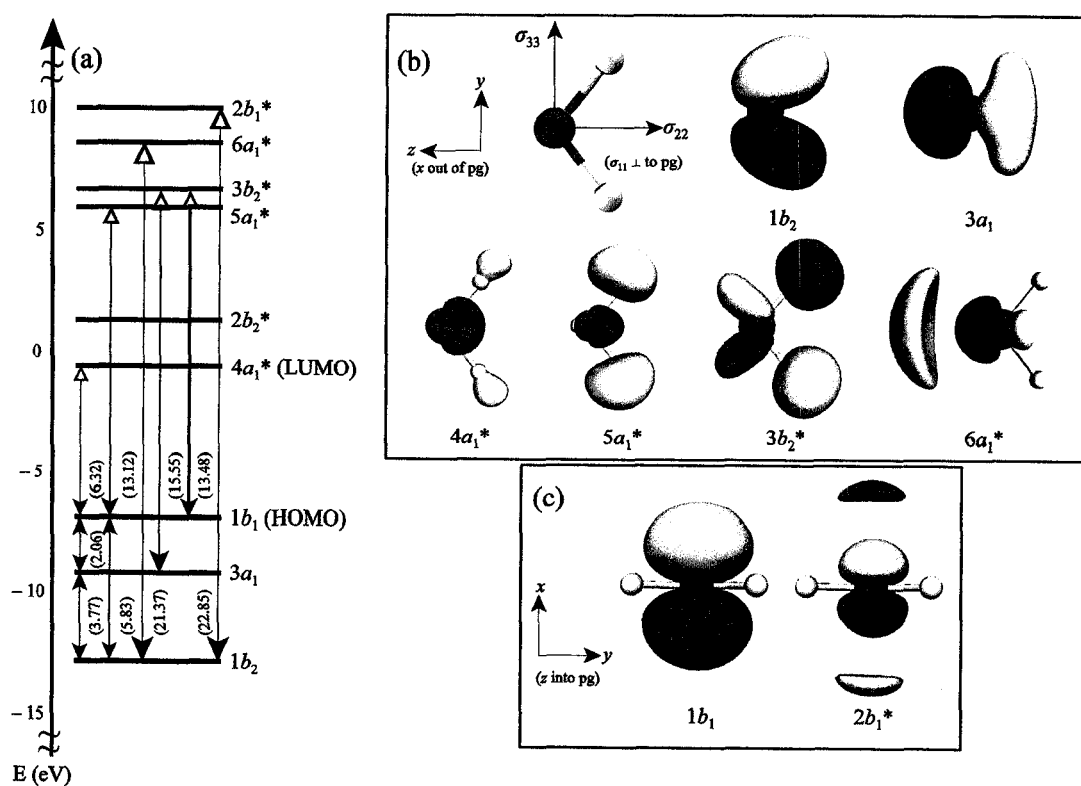
Figure 3.13 (a) Partial MO diagram for water, highlighting MOs that make significant contributions to σ^P. (b) Visual representations of the important σ^P MOs generated using the ADFview software along the (b) x and (c) z directions.

The small separation in energy between the $1b_2$, $3a_1$ and $1b_1$ MOs is likely why the total σ^P

(occ – occ) contributions are similar in magnitude to those that are due to occ – vir MO

mixing, in contrast with ethene and PF_3. From Figure 3.13a, it is seen that the HOMO-

LUMO energy gap ($\Delta E = 6.32$ eV) is larger than the energy separation between the three

important occupied orbitals. The most pronounced occ – vir contributions (i.e., $1b_2 \leftrightarrow 2b_1{}^*$,

$1b_1 \leftrightarrow 3b_2{}^*$) to σ^p arise from MOs with moderate to high oxygen p-character in both the

occupied and virtual MOs. Smaller magnitudes of occ – vir shielding are provided by the

same occupied MOs, but the mixing occurs with virtual MOs that are of high H s-character

(e.g., the $4a_1{}^*$ and $5a_1{}^*$ MOs). Pictures of MOs which contribute significantly to σ^p are

provided in Figure 3.13(b,c).

3.4.5 Selected Literature Examples Revisited

As documented in section **3.2**, a number of literature examples exist which possess

some of the elements of the chemical shielding discussions presented here. MO-by-MO

analysis and/or the concept of wavefunctions being subjected to rotational transformations

by angular momentum operators are usually presented. Rarely is the aspect of group theory

even mentioned,[54,115] and no case can be found where the direct products of the symmetry

representations of the MOs and rotational operators are evaluated. As the fundamental basis

for all of the chemical shielding arguments (i.e., Ramsey's equations) remains unchanged,

it is thought to be instructive to revisit a few of the similar accounts in the literature, in order

to (briefly) apply the group theory aspect of the treatment that has been presented herein.

-123-

3.4.5.1 Acetylene (Ethyne), C_2H_2

The anisotropic carbon chemical shielding of acetylene has been discussed in detail from a theoretical standpoint on at least two other occasions,[66,68] motivated by the experimental observations of Grant and co-workers.[116] Acetylene can be represented using the $D_{\infty h}$ point group which possesses two rotational operators: one doubly-degenerate operator $((\hat{R}_x, \hat{R}_y))$ which can be associated with the Π_g representation, and a $\hat{R}_z$ operator, which can be expressed using the Σ_g^- representation. The experimentally measured carbon chemical shielding tensor in acetylene is axially symmetric ($\kappa(^{13}C) = +1.00$) with a substantial span value of 240 ppm. As the molecule can be represented using a linear point group, there is no paramagnetic shielding along the z-axis of the molecule (see Figure 3.14a for the shielding tensor orientation in the molecular frame). It was reported that the experimental spectrum can be rationalized by considering the mixing between an occupied σ_g MO, whose symmetry representation in $D_{\infty h}$ is Σ_g^+, and two virtual π_g MOs, which may be represented as Π_g. The direct product of the symmetry representations of these important shielding MOs with the two rotational operators is now evaluated:

$$\Gamma(\psi_b) \otimes \Gamma(\hat{R}_n) \otimes \Gamma(\psi_a) \quad = \quad \Pi_g \otimes \begin{bmatrix} \Pi_g \\ \Sigma_g^- \end{bmatrix} \otimes \Sigma_g^+ \quad = \quad \begin{bmatrix} \Sigma_g^+ + \Sigma_g^- + \Delta_g \\ \Pi_g \end{bmatrix} \quad \text{[3.19]}$$

As Σ_g^+ is the totally symmetric representation of this point group, a transition of this sort is allowed by symmetry only when the $(\hat{R}_x, \hat{R}_y)$ operator is used. Thus, paramagnetic shielding contributions are allowed only along the x- and y-directions, in agreement with the calculated direction of Wiberg et al. (explicit discussions in this account pertained to σ_{xx} shielding; σ_{yy} was assumed based upon symmetry arguments).[68] By observing the fashion in which the

-124-

σ_g and π_g MOs transform under the $\hat{L}_x$ operator, it was established in the previous accounts that $\sigma_g \leftrightarrow \pi_g$ will lead to positive overlap with one another and hence contribute to shielding. Due to the symmetry of the doubly-degenerate π_g orbitals, the magnitude of paramagnetic deshielding will be equal along the x and y directions. As $\sigma_g \leftrightarrow \pi_g$ is the dominant MO pair, it should be expected that the resultant shielding tensor would be axially-symmetric, in accordance with the experimental findings. The actual value which the span assumes is determined by the degree of overlap between the mixing MO pairs, in addition to ΔE, but it is worth noting that the two pairs of MOs mentioned in this section account for about 95 % of the calculated span value.[68]

3.4.5.2 PtX$_4$$^{2-}$ Series

In a recent publication by Ziegler et al., the zeroth-order relativistic approximation (ZORA) was shown to be quite accurate in the calculation of ^{195}Pt NMR chemical shielding tensors for a series of *cis-* and *trans-*PtX$_2$L$_2$ (X = halogen; L = NH$_3$, PMe$_3$, SMe$_2$, or AsMe$_3$) complexes (i.e., within 2–3 % of the total platinum chemical shielding range).[64] Theoretical platinum chemical shielding calculations were also carried out upon PtX$_4$$^{2-}$ dianions, and it was noted that two MO pairs, leading to platinum chemical shielding along z, are responsible for approximately 40 % of the calculated paramagnetic shielding in the series where X = Cl, Br, I. Both of these transitions were of $d_{xy} \leftrightarrow d_{x^2-y^2}$ type (a pure d-orbital model for the platinum valence was used in their discussion). Each of the complexes may be represented using the D_{4h} point group, (see Figure 3.14b for the shielding tensor orientation), hence, $\Gamma(d_{xy}) = B_{2g}$ and $\Gamma(d_{x^2-y^2}) = B_{1g}$. Available rotational operators and their representations

-125-

(in brackets) are $(\hat{R}_x, \hat{R}_y)$, (E_g) and $\hat{R}_z$ (A_{2g}). The direct product is evaluated as below:

$$\Gamma(\psi_b) \otimes \Gamma(\hat{R}_n) \otimes \Gamma(\psi_a) = B_{1g} \otimes \begin{bmatrix} E_g \\ A_{2g} \end{bmatrix} \otimes B_{2g} = \begin{bmatrix} 2E_g \\ A_{1g} \end{bmatrix} \qquad [3.20]$$
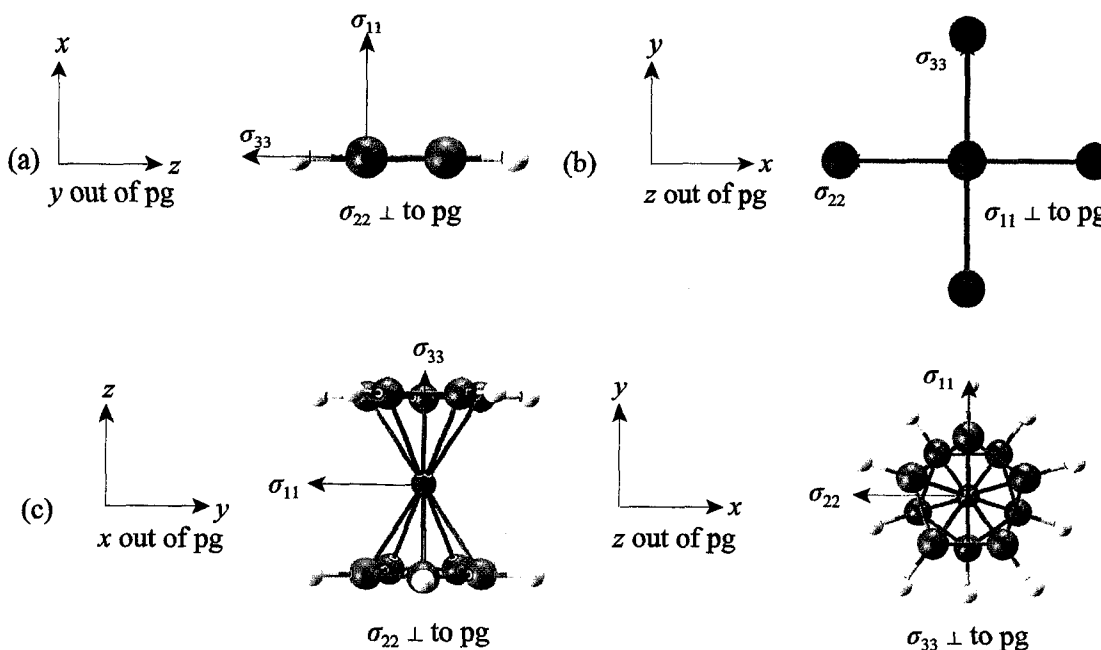
Figure 3.14 Various chemical shielding tensor orientations in appropriate molecular frames. (a) The carbon CS tensor orientation of acetylene. (b) The platinum CS tensor orientation of $PtCl_4^{2-}$. (c) The aluminum CS tensor orientation of $[Cp_2Al]^+$ (which is the molecule that was used in computations by Schurko et al., the tensor orientation is thought to be equivalent in $[Cp^*_2Al]^+$), as viewed perpendicular (left) and parallel (right) to the C_5 axis of the molecule.

The totally symmetric representation in D_{4h} is A_{1g}, hence only $\hat{R}_z$ may produce magnetic shielding via $d_{xy} \leftrightarrow d_{x^2-y^2}$, in complete agreement with the calculated direction in the earlier report. The two $d_{xy} \leftrightarrow d_{x^2-y^2}$ MO pairs are calculated to contribute 10,000 ppm to σ^p along the z-direction in $PtCl_4^{2-}$ (slightly less for the other two complexes in this series), constraining σ_{11} to point $\perp$ to the molecular plane. Due to the symmetry of the

-126-

molecule, the calculated shielding tensor will be axially symmetric, but this is the first case in this manuscript where $\kappa = -1.00$. This value is due in large part to the pronounced uniaxial deshielding of the two MO pairs discussed here. Other conclusions made in this previous report mirror ours: (i) a greater ΔE between mixing MO pairs will typically lead to decreasing contributions to $\sigma^p(^{195}Pt)$ and (ii) orbital overlap must be considered in order to explain the magnitudes of contributions to σ^p when ΔE values are very similar. Along the series from X = Cl, Br, and I, it was established that σ^p sequentially decreased. Going down the series, it was established that ΔE values decreased very slightly (less than 1 eV).[64] Due to the dominant nature of $d_{xy} \leftrightarrow d_{x^2-y^2}$ type MO mixing, the decreased deshielding was attributed almost entirely to the decreasing platinum character of the key mixing MOs, in full support of one of the major points of our manuscript.

3.4.5.3 The Decamethylaluminocenium Cation, $[Cp*_2Al]^+$

The aluminum shielding anisotropy for this complex was found to be rather substantial and nearly axially-symmetric,[69] as $\Omega(^{27}Al) = 108.1$ ppm and $\kappa(^{27}Al) = +0.88$ (a picture of the chemical shielding tensor in the molecular frame is provided in Figure 3.14c). For this study, the molecular symmetry chosen by the authors was D_{5d} (although D_{5h} would have been just as appropriate, considering the dynamic C_5 reorientational motions of the Cp rings). Due to the presence of axial molecular symmetry, an observed skew value of approximately +1.00 is unsurprising and will not be discussed further. The pronounced span can be attributed to a number of mixing MO pairs (i.e., there is no dominant MO pair; the magnitude which each significant MO pair contributes is roughly the same), although it

appears that the prominent σ^p (occ – occ) contributions are all due to the $2e_{1u}$ MO mixing

with a virtual orbital of a_{2u} symmetry. In each case, a contribution was found to be made

along the $\sigma_\perp$ direction (equivalently, σ_{11} or σ_{22}). Once again, the group theory aspect outlined

in this manuscript will be used to show that shielding is symmetry-allowed along this

direction (it will be assumed that there is finite overlap between the mixing MOs). Available

rotation operators (symmetry representations in brackets) are seen to be ($\hat{R}_x, \hat{R}_y$) (E_{1g}) and $\hat{R}_z$

(A_{2g}). Evaluation of the appropriate direct product proceeds as follows:

$$\Gamma(\psi_b) \otimes \Gamma(\hat{R}_n) \otimes \Gamma(\psi_a) \;=\; A_{2u} \otimes \begin{bmatrix} E_{1g} \\ A_{2g} \end{bmatrix} \otimes E_{1u} \;=\; \begin{bmatrix} A_{1g} + A_{2g} + E_{2g} \\ E_{1g} \end{bmatrix} \qquad \textbf{[3.21]}$$

In complete agreement with the findings of the previous account, mixing of this type of MO

pair is not symmetry-allowed if the $\hat{R}_z$ operator is used and hence no shielding can be

produced along the C_5 axis of the molecule (i.e., the z-direction or $\sigma_\parallel/\sigma_{33}$). Mixing of these

types of orbitals is only symmetry allowed perpendicular to the axis of rotation (i.e., the xy-

plane or $\sigma_\perp$). The magnitude that each $e_{1u} \leftrightarrow a_{2u}$ pair contributes to σ^p (occ – vir) is only

moderate, due to quite sizeable ΔE values, of which in this series of MOs, the smallest value

is 71.76 eV (i.e., 6.92 MJ mol^{-1}). In this previous report, it was found that only $e_{1u} \leftrightarrow e_{1u}$

type MO mixing leads to shielding along $\sigma_\parallel$ (σ_{33}). Due to the presence of more available a_{2u}

MOs, (5 are deemed significant) relative to e_{1u} MOs (2 are found to be important to σ^p), it

must be concluded that $e_{1u} \leftrightarrow a_{2u}$ type deshielding must contribute more to σ^p than $e_{1u} \leftrightarrow e_{1u}$.

Therefore, the aluminum shielding tensor must be oriented as presented in figure 3.14c, in

agreement with the *ab initio* calculations included in the literature account.

-128-

3.5 Conclusions

Experimentally observed and theoretically calculated chemical shielding tensor parameters are intimately related to molecular symmetry. If symmetry elements are present in a molecule, the orientation of the principal components of the shielding tensor will be determined by them. In a number of cases, diamagnetic shielding does not vary in a pronounced fashion as one changes the chemical environment about the nucleus; however, the observed chemical shielding value is often very sensitive to the local environment. Variation in chemical shielding is attributed nearly completely to changes in paramagnetic shielding, which is the result of pairwise MO mixing, either between two occupied MOs, or an occupied MO and a virtual MO. The presence of symmetry elements allows one to use group theory in order to comment upon which MOs may potentially contribute to chemical shielding. This is done by evaluating the direct product of the symmetry representations of the mixing MOs and the available rotational operators. Only if the totally symmetric representation is contained in the resulting expression, is MO mixing allowed by symmetry. The direction of symmetry-allowed shielding is also determined using this procedure. Orbital overlap must also exist for the mixing to contribute to shielding. Actual magnitudes are best determined using computational techniques, although the theoretically determined magnitudes can be rationalized by considering the energy separation (ΔE) between the mixing MOs, as well as the atomic characters of both mixing MOs. It is confirmed that an increasing ΔE value will typically reduce the contribution which an MO pair makes to σ^p and that significant contributions to the shielding at nucleus X (X = arbitrary nucleus) usually result only if element X provides substantial character to both of the mixing MOs.

-129-

Bibliography

[1]   *Encyclopedia of Nuclear Magnetic Resonance*; Grant, D. M.; Harris, R. K., Eds.; Wiley: New York, 1996, pp 6470.

[2]   Butler, L. G. An Introduction to Solution, Solid-State, and Imaging NMR Spectroscopy. In *Handbook of Spectroscopy*; Gauglitz, G., Vo-Dinh, T., Eds.; John Wiley & Sons: New York, 2003.

[3]   Ramsey, N. F. *Physical Review* **1950**, *78*, 699.

[4]   Ramsey, N. F. *Physical Review* **1951**, *83*, 540.

[5]   Ramsey, N. F. *Physical Review* **1952**, *86*, 243.

[6]   Pople, J. A. *Proc. Roy. Soc. (London)* **1957**, *A239*, 541.

[7]   Pople, J. A. *Discussions of the Faraday Society* **1962**, *No. 34*, 7.

[8]   Proctor, W. G.; Yu, F. C. *Physical Review* **1950**, *77*, 717.

[9]   Dickinson, W. C. *Physical Review* **1950**, *77*, 736.

[10]   Jameson, C. J.; Jameson, A. K.; Burrell, P. M. *Journal of Chemical Physics* **1980**, *73*, 6013.

[11]   Jameson, A. K.; Jameson, C. J. *Chemical Physics Letters* **1987**, *134*, 461.

[12]   Laaksonen, A.; Wasylishen, R. E. *Journal of the American Chemical Society* **1995**, *117*, 392.

[13]   Gee, M.; Wasylishen, R. E.; Laaksonen, A. *Journal of Physical Chemistry A* **1999**, *103*, 10805.

[14]   Cheeseman, J. R.; Trucks, G. W.; Keith, T. A.; Frisch, M. J. *Journal of Chemical*

Physics **1996**, *104*, 5497.

[15]   Alkorta, I.; Elguero, J. *Structural Chemistry* **1998**, *9*, 187.

[16]   Auer, A. A.; Gauss, J.; Stanton, J. F. *Journal of Chemical Physics* **2003**, *118*, 10407.

[17]   Clawson, J. S.; Anderson, K. L.; Pugmire, R. J.; Grant, D. M. *Journal of Physical Chemistry A* **2004**, *108*, 2638.

[18]   Facelli, J. C. *Concepts in Magnetic Resonance, Part A* **2004**, *20A*, 42.

[19]   Ditchfield, R. *Molecular Physics* **1974**, *27*, 789.

[20]   Keith, T. A.; Bader, R. F. W. *Chemical Physics Letters* **1993**, *210*, 223.

[21]   Kutzelnigg, W. *Israel Journal of Chemistry* **1980**, *19*, 193.

[22]   Schindler, M.; Kutzelnigg, W. *Journal of Chemical Physics* **1982**, *76*, 1919.

[23]   Lipscomb, W. N. In *Advances in Magnetic Resonance*; Waugh, J. S., Ed.; Academic Press: New York, 1966; Vol. 2; pp 138.

[24]   Hansen, A. E.; Bouman, T. D. *Journal of Chemical Physics* **1985**, *82*, 5035.

[25]   Fukui, H.; Baba, T.; Inomata, H. *Journal of Chemical Physics* **1996**, *105*, 3175.

[26]   van Lenthe, E.; Baerends, E. J.; Snijders, J. G. *Journal of Chemical Physics* **1993**, *99*, 4597.

[27]   van Lenthe, E.; Baerends, E. J.; Snijders, J. G. *Journal of Chemical Physics* **1994**, *101*, 9783.

[28]   Kudo, K.; Fukui, H. *Journal of Chemical Physics* **2005**, *123*, 114102/1.

[29]   *Modern density functional theory: A tool for chemistry*; Seminario, J. M.; Politzer, P., Eds.; Elsevier Science: Amsterdam, 1995; Vol. 2.

[30]   Gauss, J.; Stanton, J. F. Electron-Correlated Approaches for the Calculation of NMR

Chemical Shifts. In *Advances in Chemical Physics*; Prigogine, I., Rice, S. A., Eds.; John

Wiley & Sons: Indianapolis, 2002; Vol. 123; pp 355.

[31]   Jameson, C. J.; De Dios, A.; Jameson, A. K. *Chemical Physics Letters* **1990**, *167*,

575.

[32]   Bieger, W.; Seifert, G.; Eschrig, H.; Grossmann, G. *Chemical Physics Letters* **1985**,

115, 275.

[33]   Friedrich, K.; Seifert, G.; Grossmann, G. *Zeitschrift fuer Physik D: Atoms, Molecules

and Clusters* **1990**, *17*, 45.

[34]   Schreckenbach, G.; Ziegler, T. *Journal of Physical Chemistry* **1995**, *99*, 606.

[35]   Mehring, M. *Principles of High Resolution NMR in Solids*, 2nd ed.; Springer-Verlag:

New York, 1983.

[36]   Anet, F. A. L.; O'Leary, D. J. *Concepts in Magnetic Resonance* **1991**, *3*, 193.

[37]   Herzfeld, J.; Berger, A. E. *Journal of Chemical Physics* **1980**, *73*, 6021.

[38]   Haeberlen, U. *High Resolution NMR in Solids, Supplement 1*; Academic Press: New

York, 1976.

[39]   Mason, J. *Solid State Nuclear Magnetic Resonance* **1993**, *2*, 285.

[40]   Bonhomme, C.; Livage, J. *Journal of Physical Chemistry A* **1998**, *102*, 375.

[41]   Radeglia, R. *Solid State Nuclear Magnetic Resonance* **1995**, *4*, 317.

[42]   Kroeker, S.; Eichele, K.; Wasylishen, R. E.; Britten, J. F. *Journal of Physical

Chemistry B* **1997**, *101*, 3727.

[43]   Vosegaard, T.; Skibsted, J.; Jakobsen, H. J. *Journal of Physical Chemistry A* **1999**,

103, 9144.

[44]   Eichele, K.; Wasylishen, R. E.; Corrigan, J. F.; Taylor, N. J.; Carty, A. J.; Feindel, K. W.; Bernard, G. M. *Journal of the American Chemical Society* **2002**, *124*, 1541.

[45]   Hester, R. K.; Ackerman, J. L.; Neff, B. L.; Waugh, J. S. *Physical Review Letters* **1976**, *36*, 1081.

[46]   Ishii, Y.; Terao, T.; Kainosho, M. *Chemical Physics Letters* **1996**, *256*, 133.

[47]   Yao, X.; Hong, M. *Journal of the American Chemical Society* **2002**, *124*, 2730.

[48]   Slichter, C. P. *Principles of Magnetic Resonance*; Harper & Row: New York, 1963.

[49]   Vaara, J.; Pyykko, P. *Journal of Chemical Physics* **2003**, *118*, 2973.

[50]   Flygare, W. H. *Journal of Chemical Physics* **1964**, *41*, 793.

[51]   Jameson, C. J.; Gutowsky, H. S. *Journal of Chemical Physics* **1964**, *40*, 1714.

[52]   Atkins, P. *Physical Chemistry*, 6th ed.; W. H. Freeman and Company: New York, 1998.

[53]   Note that the totally symmetric representation can be A, A_1, A_g, A_{1g}, etc.

[54]   Fowler, P. W.; Steiner, E.; Havenith, R. W. A.; Jenneskens, L. W. *Magnetic Resonance in Chemistry* **2004**, *42*, S68.

[55]   Karplus, M.; Pople, J. A. *Journal of Chemical Physics* **1963**, *38*, 2803.

[56]   Rozhenko, A. B.; Schoeller, W. W.; Povolotskii, M. I. *Magnetic Resonance in Chemistry* **1999**, *37*, 551.

[57]   Zilm, K. W.; Conlin, R. T.; Grant, D. M.; Michl, J. *Journal of the American Chemical Society* **1980**, *102*, 6672.

[58]   Chesnut, D. B.; Quin, L. D. *Journal of the American Chemical Society* **1994**, *116*, 9638.

[59]   Barrie, P. J.; Groombridge, C. J.; Mason, J.; Moore, E. A. *Chemical Physics Letters* **1994**, *219*, 491.

[60]   Wiberg, K. B.; Hammer, J. D.; Keith, T. A.; Zilm, K. *Tetrahedron Letters* **1997**, *38*, 323.

[61]   Wiberg, K. B.; Hammer, J. D.; Keith, T. A.; Zilm, K. *Journal of Physical Chemistry A* **1999**, *103*, 21.

[62]   Chesnut, D. B. *Chemical Physics* **1997**, *224*, 133.

[63]   Kaupp, M.; Malkina, O. L. *Journal of Chemical Physics* **1998**, *108*, 3648.

[64]   Gilbert, T. M.; Ziegler, T. *Journal of Physical Chemistry A* **1999**, *103*, 7535.

[65]   Wiberg, K. B.; Hammer, J. D.; Zilm, K. W.; Cheeseman, J. R.; Keith, T. A. *Journal of Physical Chemistry A* **1998**, *102*, 8766.

[66]   Grutzner, J. B. *Chemical Shift Theory. Orbital Symmetry and Charge Effects on Chemical Shifts*; Norell Press: Landisville, 1987.

[67]   Arduengo, A. J.; Dixon, D. A.; Kumashiro, K. K.; Lee, C.; Power, W. P.; Zilm, K. W. *Journal of the American Chemical Society* **1994**, *116*, 6361.

[68]   Wiberg, K. B.; Hammer, J. D.; Zilm, K. W.; Cheeseman, J. R. *Journal of Organic Chemistry* **1999**, *64*, 6394.

[69]   Schurko, R. W.; Hung, I.; Macdonald, C. L. B.; Cowley, A. H. *Journal of the American Chemical Society* **2002**, *124*, 13204.

[70]   Wiberg, K. B.; Hammer, J. D.; Zilm, K. W.; Keith, T. A.; Cheeseman, J. R.; Duchamp, J. C. *Journal of Organic Chemistry* **2004**, *69*, 1086.

[71]   Forgeron, M. A. M.; Wasylishen, R. E. *Journal of the American Chemical Society*

-134-

2006, *128*, 7817.

[72]   Guerra, C. F.; Snijders, J. G.; Te Velde, G.; Baerends, E. J. *Theoretical Chemistry Accounts* **1998**, *99*, 391.

[73]   te Velde, G.; Bickelhaupt, F. M.; Baerends, E. J.; Fonseca Guerra, C.; Van Gisbergen, S. J. A.; Snijders, J. G.; Ziegler, T. *Journal of Computational Chemistry* **2001**, *22*, 931.

[74]   ADF2005.01. ADF2005.01; SCM, Theoretical Chemistry, Vrije Universiteit: Amsterdam.

[75]   Wolinski, K.; Hinton, J. F.; Pulay, P. *Journal of the American Chemical Society* **1990**, *112*, 8251.

[76]   Kohn, W.; Sham, L. J. *Physical Review* **1965**, *140*, A1133.

[77]   Parr, R. G.; Yang, W. *Density-Functional Theory of Atoms and Molecules*; Oxford University Press: New York, 1989.

[78]   Wilk, L.; Vosko, S. H. *Physical Review A: Atomic, Molecular, and Optical Physics* **1977**, *15*, 1839.

[79]   Vosko, S. H.; Wilk, L.; Nusair, M. *Canadian Journal of Physics* **1980**, *58*, 1200.

[80]   Perdew, J. P. *Physical Review B* **1986**, *33*, 8822.

[81]   Perdew, J. P. *Physical Review B* **1986**, *34*, 7406.

[82]   Vignale, G.; Rasolt, M. *Physical Review Letters* **1987**, *59*, 2360.

[83]   Vignale, G.; Rasolt, M. *Physical Review Letters* **1989**, *62*, 115.

[84]   Lee, C.; Parr, R. G. *Physical Review A: Atomic, Molecular, and Optical Physics* **1990**, *42*, 193.

[85]   Perdew, J. P.; Burke, K.; Ernzerhof, M. *Physical Review Letters* **1996**, *77*, 3865.

[86]   Zhang, Y. K.; Yang, W. T. *Physical Review Letters* **1998**, *80*, 890.

[87]   Zhang, Y.; Wu, A.; Xu, X.; Yan, Y. *Chemical Physics Letters* **2006**, *421*, 383.

[88]   Baerends, E. J.; Autschbach, J.; Bérces, A.; Bo, C.; Boerrigter, P. M.; Cavallo, L.; Chong, D. P.; Deng, L.; Dickson, R. M.; Ellis, D. E.; van Faassen, M.; Fan, L.; Fischer, T. H.; Fonseca Guerra, C.; van Gisbergen, S. J. A.; Groeneveld, O. V.; Gritsenko, M.; Grüning, F. E.; Harris, F. E.; van den Hoek, P.; Jacobsen, H.; Jensen, L.; van Kessel, G.; Kootstra, F.; van Lenthe, E.; McCormack, D. A.; Michalak, V. P.; Osinga, V. P.; Patchkovskii, S.; Philipsen, P. H. T.; Post, D.; Pye, C. C.; Ravenek, W.; Ros, P.; Schipper, P. R. T.; Schreckenbach, G.; Snijders, J. G.; Solà, M.; Swart, M.; Swerhone, D.; te Velde, G.; Vernooijs, P.; Versluis, L.; Visser, O.; Wang, F.; van Wezenbeek, E.; Wiesenekker, G.; Wolff, S. K.; Woo, T. K.; Yakovlev, A. L.; Ziegler, T. ADF; 2005.01 ed.; SCM, Theoretical Chemistry, Vrije Universiteit: Amsterdam, 2005.

[89]   Schreckenbach, G.; Ziegler, T. *International Journal of Quantum Chemistry* **1997**, *61*, 899.

[90]   Wolff, S. K.; Ziegler, T. *Journal of Chemical Physics* **1998**, *109*, 895.

[91]   Schreckenbach, G.; Ziegler, T. *Journal of Physical Chemistry A* **1997**, *101*, 3388.

[92]   Becke, A. D. *Physical Review A* **1988**, *38*, 3098.

[93]   Lee, C.; Yang, W.; Parr, R. G. *Physical Review B* **1988**, *37*, 785.

[94]   Jackowski, K.; Raynes, W. T. *Molecular Physics* **1977**, *34*, 465.

[95]   Chesnut, D. B. *Chemical Physics Letters* **2003**, *380*, 251.

[96]   Ruud, K.; Åstrand, P. O.; Taylor, P. R. *Journal of the American Chemical Society*

2001, *123*, 4826.

[97] Orendt, A. M.; Facelli, J. C.; Beeler, A. J.; Reuter, K.; Horton, W. J.; Cutts, P.; Grant, D. M.; Michl, J. *Journal of the American Chemical Society* **1988**, *110*, 3386.

[98] Hindermann, D. K.; Cornwell, C. D. *Journal of Chemical Physics* **1968**, *48*, 4148.

[99] Gauss, J.; Stanton, J. F. *Journal of Chemical Physics* **1996**, *104*, 2574.

[100] Manninen, P.; Ruud, K.; Lantto, P.; Vaara, J. *Journal of Chemical Physics* **2005**, *122*, 114107/1.

[101] Manninen, P.; Ruud, K.; Lantto, P.; Vaara, J. *Journal of Chemical Physics* **2006**, *124*, 149901/1.

[102] Chan, J. C. C.; Eckert, H. *Theochem* **2001**, *535*, 1.

[103] De Leeuw, F. H.; Dymanus, A. *Journal of Molecular Spectroscopy* **1973**, *48*, 427.

[104] Ditchfield, R. *Chemical Physics* **1981**, *63*, 185.

[105] Jaszunski, M. *Chemical Physics Letters* **2004**, *385*, 122.

[106] Montana, A. J.; Zumbulyadis, N.; Dailey, B. P. *Journal of Chemical Physics* **1976**, *65*, 4756.

[107] Zumbulyadis, N.; Dailey, B. P. *Molecular Physics* **1973**, *26*, 777.

[108] Duncan, T. M. *A Compilation of Chemical Shift Anisotropies*; The Farragut Press: Chicago, 1990.

[109] Tossell, J. A.; Lazzeretti, P. *Journal of Chemical Physics* **1987**, *86*, 4066.

[110] Wasylishen, R. E.; Mooibroek, S.; Macdonald, J. B. *Journal of Chemical Physics* **1984**, *81*, 1057.

[111] Wasylishen, R. E.; Bryce, D. L. *Journal of Chemical Physics* **2002**, *117*, 10061.

[112] Vaara, J.; Lounila, J.; Ruud, K.; Helgaker, T. *Journal of Chemical Physics* **1998**, *109*, 8388.

[113] Jameson, C. J. *Nuclear Magnetic Resonance* **1989**, *18*, 1.

[114] Bruna, P. J.; Hachey, M. R. J.; Grein, F. *Theochem* **1997**, *400*, 177.

[115] Duer, M. J. *Introduction to Solid-State NMR Spectroscopy*; Blackwell Publishing: Cornwall, 2004.

[116] Zilm, K. W.; Grant, D. M. *Journal of the American Chemical Society* **1981**, *103*, 2913.

Chapter 4

Solid-State ^{23}Na NMR, X-ray Diffraction and Theoretical Studies upon the Polymeric Sodium Metallocenes CpNa and CpNa·THF

4.1 Introduction

Metallocenes are broadly defined as molecules which contain a metal atom that bonds in an η^x ($x = 1 - 5$) fashion to at least one configuration of the cyclopentadienyl anion ($Cp = C_5R_5^-$; R = H, Me, etc.). This anion is considered by some to be one of the most important ligands in organometallic chemistry.[1] Numerous studies have dealt with alkali-metal containing metallocenes due to their utility as reagents in many organometallic syntheses.[2-5] In addition, these types of metallocenes are interesting to study due to their wide range of structural motifs: they are present as both solvated[6-9] and unsolvated[10-12] polymeric chains, solvated oligomers[13,14] and monomers,[15,16] and are often constituents of mixed-metal metallocenes[17-19] and anionic sandwich complexes.[20,21] Some introductory texts on metallocenes begin with the characterization of ferrocene (Cp_2Fe), perhaps leading one to believe that ferrocene was the first isolated metallocene.[22] However, approximately fifty years prior to the initial synthesis[23] and characterisation[24,25] of ferrocene in the early 1950s, the first true metallocene complexes, $CpNa$[26] and CpK,[27] were prepared. Although a consensus was reached early on regarding the ionic nature of alkali-metal metallocenes, with a positively charged metal centre interacting with negatively charged Cp rings, a number of years passed before conclusive pictures were drawn regarding their molecular

-139-

structures.[28-33] Until very recently, although a great deal of effort has been directed towards a better understanding of this class of compounds,[5] a number of fine details, most notably intramolecular Cp' ring motion(s) (Cp' = Cp anion of variable ring substitution), and the temperature-dependent structural behaviour of the linear polymeric species, remained unpublished or unstudied. Thankfully, due to substantial advances in solid-state NMR characterisation techniques,[34-38] a number of these details have either been conclusively determined or hypothesized.[39,40]

In a previous work, several polymeric sodium metallocenes of the form Cp'Na were studied using solid-state ^{13}C and ^{23}Na NMR spectroscopy and, with the aid of computational modelling, in-depth discussions pertaining to (i) Cp' ring dynamics, (ii) temperature-dependent structural behaviour, (iii) sodium chemical shielding anisotropy (CSA) as well as (iv) chemical shielding (CS) and electric-field gradient (EFG) tensor magnitudes and orientations, were provided.[39] In addition, a bent base-substituted species, CpNa·THF, was identified (C_Q = 1.82(2) MHz; η_Q = 0.39(2), δ_{iso}([23]Na) = − 45.5(2) ppm) and its structure was proposed based upon computational modelling and available solid-state ^{13}C and ^{23}Na NMR data. This is noteworthy, as single crystals for many polymeric alkali-metal metallocenes are extremely difficult to isolate; hence, their structures have largely been deduced based upon synchrotron powder X-ray diffraction (pXRD) data and subsequent Rietveld analyses.[41]

Herein, we wish to extend the discussion on the solvated species as well as the base free version of this compound, CpNa (recently shown to act as an anionic initiator in a living photopolymerization process[42,43]), as CpNa·THF powder is often found in a mixture with

-140-

CpNa. A solid-state structure for CpNa·THF is proposed using refined single crystal XRD data and from this, comments are made for the first time regarding its large sodium CSA, and the origin and orientation of the EFG and CS tensors at the central sodium atom are discussed. The previously observed[39] sodium CSA in CpNa is defined more accurately using solid-state ^{23}Na NMR data acquired at several magnetic field strengths. New theoretical calculations upon CpNa·THF provide evidence for a strikingly different ^{23}Na EFG tensor orientation in the molecular frame from that proposed in earlier studies. Lastly, variable-temperature (VT) solid-state NMR data and VT pXRD experiments, in combination with detailed computational modelling, highlight the relationship between the molecular structure of CpNa as a function of temperature.

4.2 Experimental

4.2.1 CpNa·THF Crystal Isolation

A 2.0 M solution of CpNa dissolved in THF was purchased from Aldrich. While under nitrogen, a portion of this solution was decanted into a sample vial. In order to facilitate the slow evaporation of THF, this vial was placed inside a more voluminous container containing liquid THF, which was capped and left to equilibrate for two weeks. A crystal of CpNa·THF, suitable for single-crystal XRD experiments, was isolated from the vial.

4.2.2 Single-Crystal XRD

A colourless crystal, measuring 0.50 x 0.40 x 0.40 mm, was obtained as outlined

-141-

above. Due to sample sensitivity to air and moisture, it was flame-sealed in a capillary tube while the contents were still under nitrogen. The raw data was collected at $T = 173(2)$ K, using a Mo-Kα ($\lambda = 0.71069$ Å) graphite-monochromated radiation source with a Bruker APEX CCD area detector running the SMART data collection software.[44] The crystal produced the following unit cell parameters: $C_{18}H_{26}Na_2O_2$; $F_w = 320.37$ g mol^{-1}; orthorhombic; $Aba2$ ($a = 9.8242(15)$ Å, $b = 20.611(3)$ Å, $c = 9.3236(14)$ Å, $\alpha_c = \beta_c = \gamma_c = 90°$, $V = 1887.9(5)$ Å^3, $Z = 4$); $D_c = 1.127$ g cm^{-3}. 1826 total reflections, collected over the range $2.86 < \theta < 27.47°$, were used to determine the unit cell parameters. For formal data collection, a total of 8587 partial and complete reflections were collected over the range $1.98 < \theta < 27.57°$, covering the indices $h = -12$ to 12, $k = -26$ to 26 and $l = -12$ to 12. Sample rotation was performed (φ and ω) for both cell determination and data collection steps. Of the reflections collected, 2182 were symmetry independent. Data reduction was done using SAINT data reduction software.[45] The structure was solved for using direct methods with SHELXTL[46] and refined (full-matrix least squares on F_o^2) using SHELXL-97.[47] Overall quality factors (of the 1081 reflections with $I > 2\sigma I$) of the refined structure are: $R_1 = 0.0624$ and $wR_2 = 0.1346$ with a GooF of 0.994.

4.2.3 Powder XRD

Microcrystalline samples of CpNa and the mixed CpNa/CpNa·THF were prepared under nitrogen atmosphere, and were each flame-sealed in 1.0 mm capillary tubes. Data was collected at several temperature points, ranging from $T = 123(1)$ K to $T = 323(1)$ K, using a D8 DISCOVER powder X-ray diffractometer equipped with an Oxford Cryosystems 700

-142-

series cryostream plus cooler. The diffractometer utilizes a Cu-Kα_1 (λ = 1.54056 Å) radiation source with a Bruker AXS HI-STAR area detector running under the General Area Detector Diffractions System. pXRD powder pattern simulations were done using PowderCell 2.4.[48]

4.2.4 Solid-State NMR Spectroscopy

4.2.4.1 General NMR Parameters

Samples of CpNa and CpNa/CpNa·THF, the latter from the same vial which produced the single crystal used in XRD experiments, were ground into microcrystalline powders under nitrogen, packed tightly into 4 mm o. d. ZrO$_2$ rotors, and sealed with airtight caps. Spectra were obtained using 9.4 T (ν_0(^{1}H) $\approx$ 400 MHz) wide bore Varian Infinity+ and 11.7 T (ν_0(^{1}H) $\approx$ 500 MHz) standard bore Bruker AMX-500 NMR spectrometers at the University of Windsor, and a 21.1 T (ν_0(^{1}H) $\approx$ 900 MHz) standard bore Bruker AVANCE II NMR spectrometer at the Canadian National Ultrahigh-field NMR Facility for Solids in Ottawa. Varian/Chemagnetics double- and triple-resonance 4 mm MAS probes were used for all experiments conducted at B$_0$ = 9.4 T, while double-resonance 4 mm Bruker probes were used for experiments conducted at higher fields. Central-transition (CT) selective pulses used for ^{23}Na experiments are equal to the non-selective solution pulse widths after scaling by a factor of $(I + \frac{1}{2})^{-1}$.

4.2.4.2 ^{13}C CP/MAS NMR

Carbon chemical shifts were referenced to TMS (δ_{iso}(^{13}C) = 0.0 ppm), using the

-143-

downfield shift of adamantane (δ_{iso}(^{13}C) = 38.57 ppm) as an external secondary reference. Experiments were conducted at several MAS frequencies: 1.37, 2.41 and 4.4 kHz and employed proton saturation, cross-polarization (CP) and decoupling field strengths, v_1(^{1}H), of 82 – 104 kHz, ca. 45 kHz and ca. 55 kHz, respectively. Optimized parameters include a CP contact time ranging from 9 to 12 ms and recycle delays between 9 – 15 s. Experiments were conducted using a spectral width of 70.0 kHz, and 110 to 328 transients were collected and averaged.

4.2.4.3 ^{23}Na NMR

Sodium chemical shifts were referenced to a 1.0 M aqueous solution of NaCl (δ_{iso}(^{23}Na) = 0.0 ppm). A Hahn echo pulse sequence was used for all 1D static and MAS (v_{rot} = 10 - 11 kHz) experiments, using rotor-synchronized data collection where applicable. ^{23}Na $\pi/2$ pulses were optimised at various levels of amplification, leading to pulse widths ranging from 9.0 to 17.5 μs (v_1(^{23}Na) = 13.9 – 7.14 kHz). Experiments typically employed a spectral width of 50 kHz, continuous-wave proton decoupling using rf fields of 50 kHz, recycle delays of 4 – 6 s, and the collection of 400 – 2000 and 29 transients at standard- and ultrahigh-magnetic fields, respectively.

4.2.4.4 Spectral Simulations

Sodium-23 EFG and CS tensor parameters were determined using the analytical simulation program WSolids.[49] In select cases, numerical simulations were also conducted using SIMPSON.[50] All SIMPSON simulations employed the *direct* method of powder

-144-

averaging using the *zcw4180* crystal file and with the start and detect operators set equal to I_{1z} and I_{1c}, respectively. The number of gamma angles was set to 20 for MAS simulations. All error bounds were determined by the bidirectional variation of individual NMR parameters and best-fit spectra were obtained by minimizing the RMS difference between simulated and experimental spectra.

4.2.5 Theoretical Calculations

Atomic coordinates used for all calculations were taken from the available crystal structures.[10] Calculations were restricted to relatively small polymeric chains of CpNa ($[Cp_2Na]^-/[Cp_2Na_3]^+$) and CpNa·THF ($[Cp_2Na·THF]^-/[Cp_2Na_3·3THF]^+/$ $[Cp_3Na_3·3THF]/$ $[Cp_4Na_3·3THF]^-$) (see Appendix C, Tables in C.2.1 and C.2.2) and were performed using Dell Precision workstations running Red Hat Linux. Gaussian 98[51] and Gaussian 03[52] calculations used either restricted Hartree-Fock (RHF) or hybrid density functional theory (DFT). DFT calculations used Becke's three parameter hybrid functional with the correlation functional proposed by Lee, Yang and Parr, B3LYP.[53,54] All Gaussian calculations employed the standard polarized double-ζ and triple-ζ basis sets provided with the Gaussian software packages (6-31G**/6-311G**/6-311+G**/6-311++G**) on all non-sodium atoms. The sodium atoms were usually represented by standard basis sets, although select calculations used a well-tempered basis set (WTBS).[55,56] In order to convert the ^{23}Na quadrupolar coupling constant (C_Q) into MHz from atomic units,[57,58] the formula $C_Q = (eV_{33}Q/h) \times 9.71734 \times 10^{21}$ V m^{-2} was used, with $Q(^{23}Na) = 0.1054 \times 10^{-28}$ m^2 (*vide infra*), and where V_{33} is the largest component of the EFG tensor in its own principal axis system.

-145-

No standard method exists for referencing the absolute chemical shielding of sodium: the method used herein very closely corresponds to the procedure outlined in **2.2.3**. Sodium and carbon chemical shielding tensors were calculated using the gauge-including atomic orbitals (GIAO) method[59,60] and referenced against the theoretical isotropic shifts of $Na(OH_2)_6^+$ ($\delta_{iso}(^{23}Na) = 0.0$ ppm) and CO ($\delta_{iso}(^{13}C) = 187.1$ ppm), respectively (see Table C.2.3.1 for optimized $Na(OH_2)_6^+$ parameters). The point charges selected for use in embedded cluster molecular orbital (ECMO) calculations were based upon a Mulliken population analysis with the charges of the hydrogen atoms incorporated into the heavy atoms. This results in $q(Na)$ $= + 0.75$ e and $q(C) = -0.15$ e. A sphere of point charges 10 Å in diameter was used and the individual point charges were translated relative to a central $Cp_2Na_3^+$ cluster in accordance with the observed changes in the unit cell (checked for consistency using PowderCell 2.4). When modelling the possible temperature-dependent motions of a central sodium atom in CpNa, a single Cp_2Na^- cluster was used. The sodium atom was moved in steps of 0.03 Å towards the centroid of one of the Cp rings to mimic motion along the c-axis of the unit cell. For displacements in the ab-plane, the sodium atom was moved in 0.02 Å steps towards several different fixed points. The points chosen correspond to the ab-coordinates of the Cp ring carbons and the C-C bond midpoints.

Chemical shielding calculations were also carried out using pure DFT, as implemented in the Amsterdam Density Functional (ADF) program.[61-63] These calculations employed both the NMR[64-66] and EPR[67] modules using the TZ2P all-electron basis set provided in the ADF program on all atoms. These calculations used the "OPBE" generalized gradient approximation functional, recently shown to be the optimum non-hybrid DFT

-146-

method.[68] OPBE is the exchange functional of Cohen and Handy (OPTX),[69] along with the correlation functional of Perdew, Burke and Ernzerhof (PBE).[70]

4.3 Results and Discussion

4.3.1 Solid-State ^{23}Na NMR

As we were unable to isolate pure microcrystalline CpNa·THF, one- and two-dimensional (2D) solid-state ^{23}Na MAS NMR experiments were conducted on a mixed CpNa/CpNa·THF sample to determine the number of resolvable sodium sites in the sample, in addition to the EFG tensor parameters at the sodium atoms. The ^{23}Na MAS NMR spectra recorded at B_0 = 9.4 T and 11.7 T depict two sodium powder patterns, each clearly dominated by the second-order quadrupole interaction (Figure 4.1). Soft, CT-selective rf pulses are applied to reduce the appearance of nutation distortions in the spectra, as predicted[71] and observed[39] for cases where $v_{rf} \approx v_Q$. Simulations of the low-frequency (right) powder pattern reveal [23]Na EFG tensor and chemical shift parameters in accordance with the published parameters of CpNa,[39] while those of the high frequency pattern yield values for C_Q, η_Q and δ_{iso}([23]Na) which closely match those published for CpNa·THF (Table 4.1).

Sodium CSA in CpNa·THF was not previously investigated; hence, static ^{23}Na NMR experiments were also conducted on the mixed sample at two external magnetic fields (B_0 = 9.4 and 11.7 T; Figure 4.2) to determine the sodium CS tensor parameters of CpNa·THF, as well as the relative orientation between the sodium EFG and CS tensors. The sodium chemical shift range is relatively small and there are few literature examples of anisotropic

-147-

sodium chemical shielding.[39,72-75] Additionally, the observed magnitude of $\Omega(^{23}\text{Na})$ is often small, with the largest observed value equalling 20 ppm.[76]
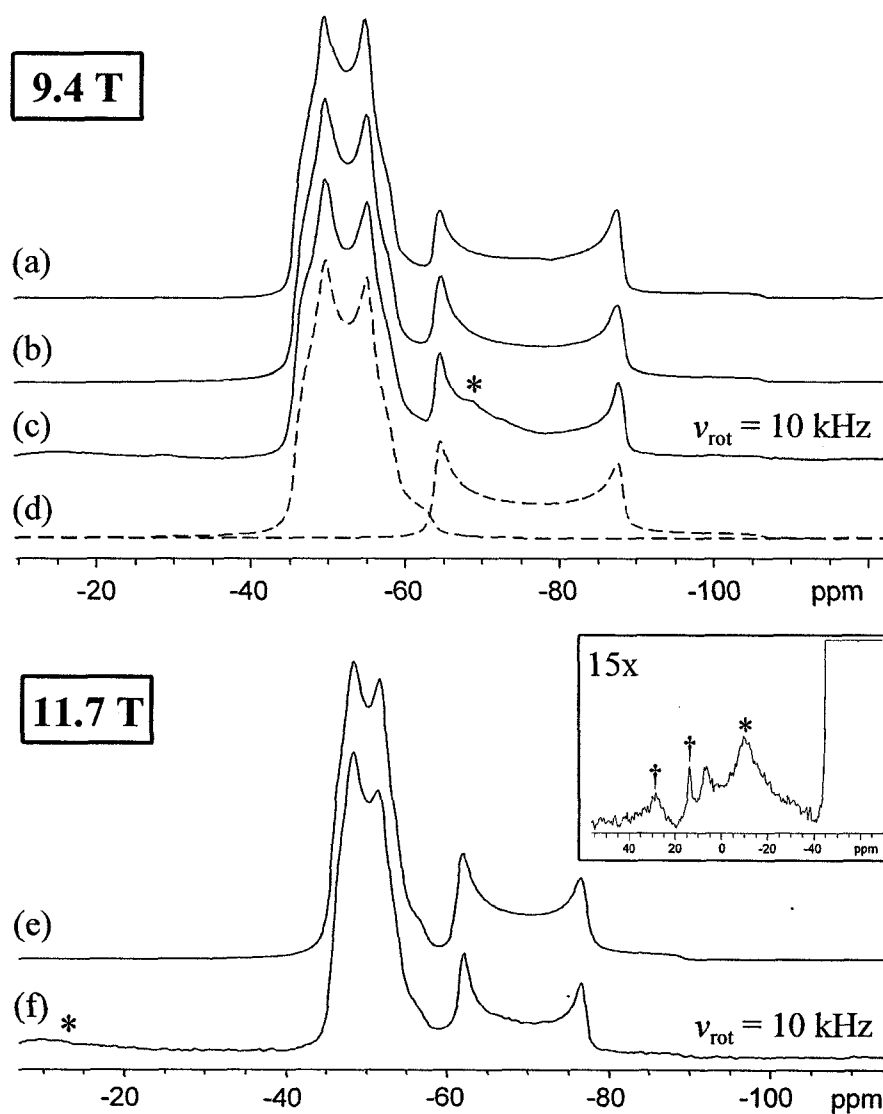
Figure 4.1 Solid-state ^{23}Na MAS NMR spectra of a mixed CpNa/CpNa·THF sample. Both numerical SIMPSON, (a), which accounts for finite pulse widths and sample rotation, and analytical WSolids, (b,e), simulations, which account for neither factor, closely match the experimental spectra acquired at $B_0 = 9.4$ T (c) and $B_0 = 11.7$ T (f). A de-convolution of the two sodium sites is provided in (d). Impurities are marked with asterisks. Inset: magnification (vertical scale multiplied by a factor of 15) of the high-frequency region of the experimental spectrum in (f), highlighting the impurity. Spinning sidebands are denoted with †.

-148-

Table 4.1 Experimental Sodium CS and EFG Tensor Parameters [a]

experiment	B_0 (T)	C_Q (MHz)	η_Q	Ω (ppm)	κ	δ_{iso} (ppm)
CpNa·THF						
MAS [b]	9.4	1.82(2)	0.37(2)	—	—	–45.4(3)
MAS [c]	9.4	1.82(2)	0.39(2)	—	—	–45.5(2)
MAS [b]	11.7	1.84(3)	0.39(3)	—	—	–45.1(3)
Static	9.4	—	—	18(3)	0.3(2)	—
Static	11.7	—	—	21(3)	0.2(2)	—
CpNa						
MAS [bd]	9.4	2.97(3)	0.03(3)	—	—	–57.6(3)
MAS [c]	9.4	2.97(3)	0.02(2)	—	—	–57.5(3)
MAS [bd]	11.7	3.00(3)	0.03(2)	—	—	–57.0(3)
Static [c]	9.4	—	—	12.5(30)	1.0 [e]	—
Static [d]	11.7	—	—	17(3)	0.9(1)	—
Static	11.7	—	—	14(2)	0.9(1)	–57.5(3)
Static	21.1	—	—	17.5(1.5)	0.8(1)	–58.2(4)

[a] Parameter definitions can be found in chapter 1.
[b] MAS frequency, ν_{rot} = 10 kHz.   [c] Taken from literature, see reference [39].
[d] Present in a mixture with CpNa·THF.   [e] Assumed based upon molecular symmetry.

Based upon analytical simulations of the powder patterns, it can be established that $\Omega(^{23}Na)$ for CpNa·THF is very close to 20 ppm, with observed values of 18(3) ppm and 21(3) ppm at B_0 = 9.4 and 11.7 T, respectively. Experimental determination of the sodium CS tensor symmetry (κ), and the relative orientation between the CS and EFG tensors (the Euler angles, α_e, β_e, and γ_e) are relatively uncommon, although they are often assumed based upon molecular symmetry. In the solvated sodium species, the CS tensor (B_0 = 9.4 T/B_0 = 11.7 T) deviates from axial symmetry ($\kappa(^{23}Na)$ = 0.3(2)/0.2(2)), and the EFG and CS tensor frames are clearly non-coincident: α_e = 75°(10)/80°(10), β_e = 80°(10)/85°(10), γ_e = 20°(10)/27°(5). Further discussion is provided in section **4.3.5**.
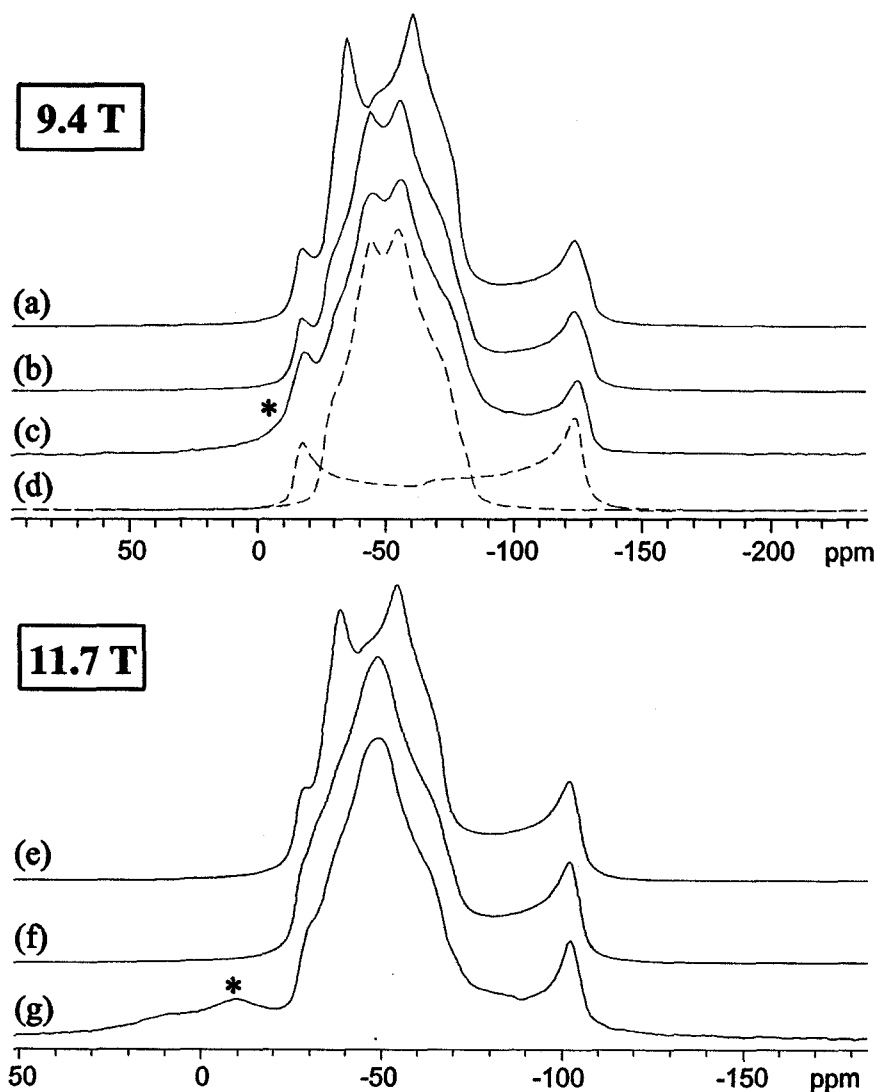
Figure 4.2 Static solid-state ^{23}Na NMR spectra of a mixed CpNa/CpNa·THF sample. Spectra acquired at (c) $B_0 = 9.4$ T and (g) $B_0 = 11.7$ T correspond closely to analytical simulations only if the effects of sodium CSA and non-coincident CS and EFG tensors are included (b,f). Simulations which do not include these effects for the CpNa·THF site (a,e) clearly do not match the experimental spectra. A de-convolution is provided in (d) for the spectrum acquired at $B_0 = 9.4$ T. Impurities are marked with asterisks.

The static ^{23}Na NMR spectrum acquired at $B_0 = 11.7$ T depicts a fairly intense impurity signal whose centre of gravity is –9.6 ppm. This signal also appears to be present

-150-

in the static ^{23}Na NMR spectrum of the mixed sample acquired at $\mathbf{B_0} = 9.4$ T, but is obscured by the powder pattern of CpNa·THF. ^{23}Na MAS experiments can resolve this peak (Figure 4.1, inset), but due to poor S/N, one is not able to comment upon the EFG parameters of this site. MQMAS experiments conducted at 9.4 T (see Supporting Information for MQMAS details; Figure C.1.2.1 and Table C.1.2.1) do not resolve the impurity site, possibly due to site disorder, a high $C_Q(^{23}$Na) value or a combination thereof. The mixed sample was also exposed to air and moisture in order to characterize sample degradation. Resultant ^{23}Na NMR spectra (Figure C.1.3) highlight a sodium environment very similar to Na$^+$, leading to the conclusion that upon exposure to air and moisture, the mixed sample adopts a simple salt structure. For the decomposed sample, $\delta_{iso}(^{23}$Na) = 1.6 ppm, clearly in contrast with the centre of gravity of the impurity signal before exposure to the atmosphere. It is postulated that the signal centred at −9.6 ppm corresponds either to sample degradation after exposure to oxygen, or thermal decomposition. The peak at +1.6 ppm represents a hydrated version of the decomposition product. As observed here, it is expected that hydration will produce an increase in chemical shift,[77] the magnitude of which varies, but is typically on the order of +10 ppm.

Static solid-state ^{23}Na NMR experiments were carried out on a nearly pure sample of CpNa in order to determine its sodium CS tensor parameters more accurately. High-field ($\mathbf{B_0}$ = 21.1 T) experiments were chosen as they will enhance the contribution that CSA makes to a quadrupolar-dominated powder pattern. Previous solid-state ^{23}Na NMR experiments on CpNa at $\mathbf{B_0}$ = 9.4 T resolve a small, axially-symmetric sodium CS tensor ($\Omega(^{23}$Na) = 12.5(30)/$\kappa(^{23}$Na) = 1.0),[39] where the axial-symmetry of the tensor is assumed

-151-

based upon molecular geometry. The account is very similar when one moves to a slightly higher magnetic field ($B_0 = 11.7$ T; see Table 4.1 and Figure 4.3b), however, when compared to the values obtained at a substantially higher magnetic field ($B_0 = 21.1$ T; Figure 4.3d), one observes that the CS tensor parameters now lie outside the error ranges associated with the moderate-field accounts.
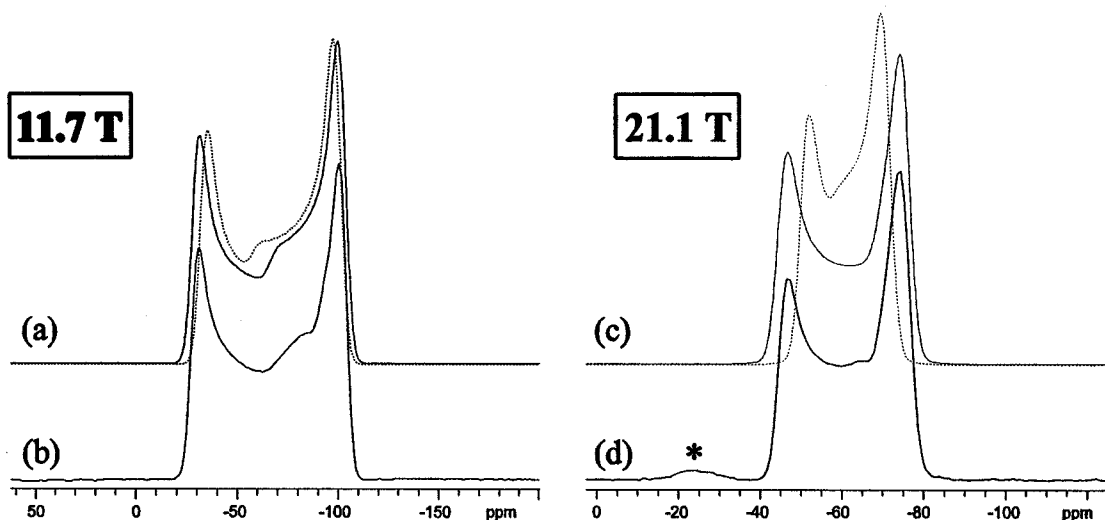
Figure 4.3 Static solid-state ^{23}Na NMR spectra of CpNa at (a,b) $B_0 = 11.7$ T and (c,d) $B_0 = 21.1$ T. Bottom traces (b,d) correspond to experimental spectra with top traces (a,c) representing analytical simulations using the parameters outlined in Table 4.1. Dotted line traces in (a) and (c) are equivalent to the solid line traces, but neglect CSA. Impurities are marked with asterisks.

The span of the sodium shielding tensor is significantly more pronounced ($\Omega(^{23}\text{Na}) = 17.5(1.5)$ ppm) and although it is still nearly axially-symmetric, it is clearly not of perfect axial symmetry ($\kappa(^{23}\text{Na}) = 0.8(1)$), as previously assumed. The high-field values are expected to be more reliable, as the broadening arising from the second-order quadrupolar interaction scales inversely with B_0, while the broadening from CSA is proportional to it.

-152-

At B_0 = 9.4 T, a Ω of 12.5 ppm represents approximately 7 % of the total powder pattern width, which is detectable, but with high relative error values (see Figure 4.3a). At high-field, the breadth of the powder pattern is reduced significantly (Δv = 11.3 kHz, as opposed to 18.9 kHz at 9.4 T), and a CSA of 17.5 ppm now accounts for about 37 % of the total powder pattern breadth (Figure 4.3c). The origins of the non-axial sodium shielding tensor of this complex are discussed in the theoretical section.

4.3.2   Crystal Structure of CpNa·THF

The refined crystal structure of CpNa·THF is presented in Figure 4.4. To date, only a handful of polymeric sodocene solvates have been structurally characterized using single-crystal XRD techniques. A number of these solvates possess Cp rings that contain large substituents, as observed in (benzyl)CpNa·THF and (cyclopentyl)CpNa·THF,[78] but only a single example can be found where the Cp ring is unsubstituted: CpNa·TMEDA (TMEDA = tetramethylethylenediamine).[32,33] As expected, a central sodium atom finds itself bonded to proximate anionic Cp rings in an η^5 fashion. Unsolvated alkali-metal metallocenes generally possess linear polymeric structures and in cases where the metal atom is only slightly polarizable, such as with CpLi and CpNa, the chains are straight and highly-ionic. The refined crystal structure of CpNa·THF is also found to form a polymeric chain-like structure, but it is zigzagging ($\angle$(Cp$_{cent}$-Na-Cp$_{cent}$) = 143.4°; where Cp$_{cent}$ is the geometric centre of the Cp ring), a structural change upon solvation that is also seen in CpNa·TMEDA. The crystal structures of solvated polymeric sodocenes determined thus far also show an increase in the Cp$_{cent}$-Na distance relative to CpNa. For example, the Cp$_{cent}$-Na distance in

-153-

CpNa has been measured to be 2.357 Å,[10] while the same parameter in CpNa·TMEDA and

CpNa·THF is 2.667 Å[32,33] and 2.455 Å, respectively.
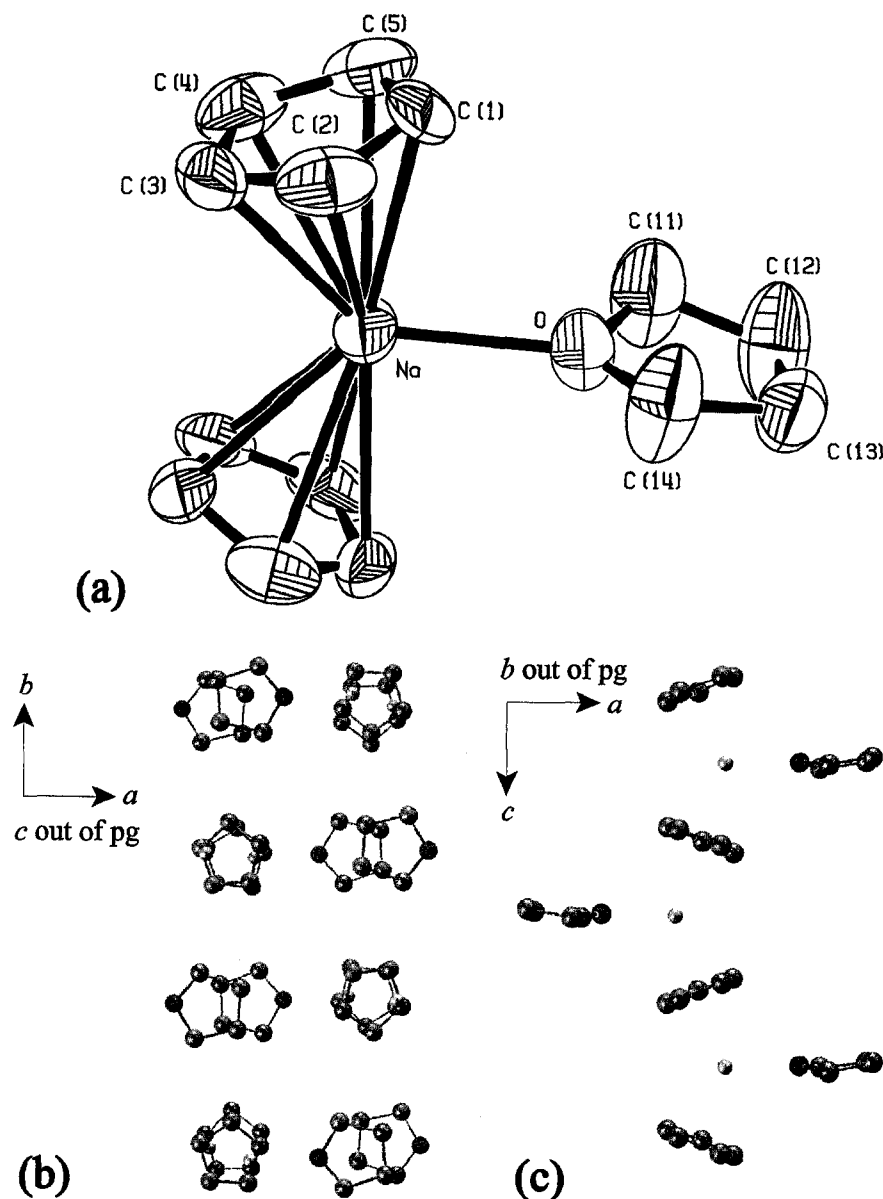
Figure 4.4 (a) ORTEP-3 rendering of CpNa. Thermal ellipsoids are shown at the 50% probability level. Atoms comprising the asymmetric unit are labelled. (b) View of the CpNa·THF unit cell along the c-crystallographic axis. (c) A view along the b-axis highlights the zigzagging linear polymeric nature of the molecule. Hydrogen atoms have been omitted in (a-c) to improve clarity.

-154-

The increase in Cp_{cent}-Na bond distance is clearly due to the presence of the donor THF ligand that coordinates directly to the sodium atom. This coordination increases the electron density at the sodium, thereby slightly electrostatically repulsing the anionic rings relative to CpNa. In contrast to the pronounced distance change ($\Delta(Cp_{cent}$-Na$) = +\ 0.310$ Å) upon coordination of the TMEDA ligand, there is only a modest Cp_{cent}-Na distance change ($\Delta(Cp_{cent}$-Na$) = +\ 0.098$ Å) when a THF molecule binds to the sodium atom. This is anticipated, as the sodium-THF interaction is relatively weak[33] and should produce only a modest change in the electronic configuration of the sodium valence. This weak interaction is also thought by us to be the main reason as to why it is so difficult to obtain samples of CpNa·THF that are not mixed with CpNa.

4.3.3　Variable-Temperature Powder XRD

4.3.3.1　CpNa

As CpNa·THF cannot be isolated as a pure microcrystalline powder and is instead found as a mixture with CpNa, VT pXRD experiments were also conducted upon a pure sample of CpNa to determine its unit cell parameter changes as a function of temperature. The unit cell dimensions of CpNa change slightly as a function of temperature (for associated pXRD spectra, see the Appendix, Figure C.1.4) and can be fit to a function which is linear in temperature (Figure 4.5). Unit cell changes were determined by observing the variation in the 2θ values associated with the (200), (020) and (002) peaks, as the distance between Bragg planes corresponding to the same Miller index is given by:

-155-

$$d = \frac{1}{\sqrt{(h/a)^2 + (k/b)^2 + (l/c)^2}}$$

[4.1]

Based upon previous solid-state ^{23}Na NMR data and computational modelling, it was concluded that CpNa should exhibit temperature-dependent structural changes, such that the Cp_{cent}–Na distance (and hence the c-axis of the unit cell) increases with decreasing temperature.

CpNa Unit Cell Lengths (a, b) vs. Temperature
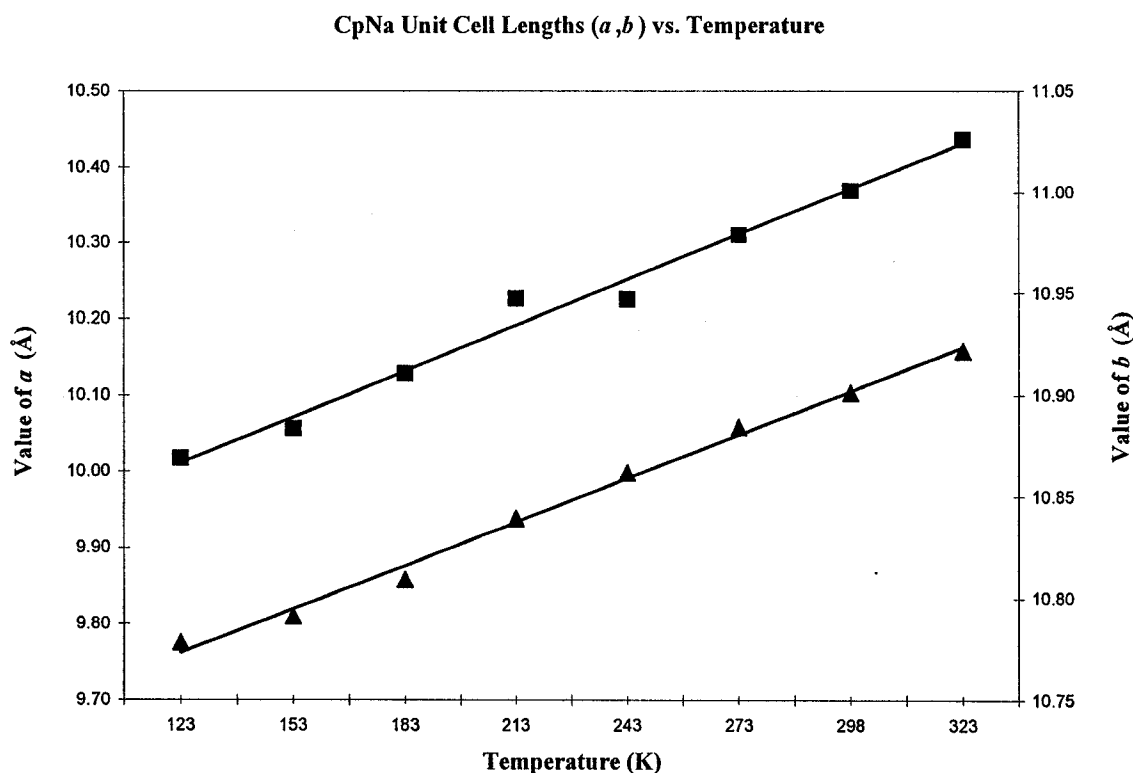
Figure 4.5 Plot of CpNa unit cell lengths as a function of temperature. The a (▲) and b (■) unit cell lengths can both be fit to linear functions in temperature: a(Å) = 0.0020T(K) + 9.5149; b(Å) = 0.0008T(K) + 10.7694.

-156-

Actual unit cell parameter changes observed through VT pXRD experiments are not in line with the earlier proposal. There is no correlation between the c unit cell length and temperature ($R^2 = 0.0651$, see Appendix C, Figure C.1.5), while the lengths of the a- and b-axes show strong linear correlations with temperature: $R^2 = 0.9946$ and 0.9834, respectively (Figure 4.5). Several scenarios regarding the mode of structural transformation are examined later in the theoretical section.

4.3.3.2 CpNa/CpNa·THF

Powder XRD experiments were also carried out upon the mixed CpNa/CpNa·THF sample (Figure C.1.6). The pXRD spectrum of the mixed sample was expected to include several peaks in the same positions as the pXRD spectrum of CpNa (Figure C.1.4), with additional peaks attributed to CpNa·THF. The observed pXRD spectrum does not fall in line with our expectations. The resultant spectrum, which was reproduced numerous times, does not show characteristic peaks associated with either CpNa (based upon its refined pXRD strucutre) or CpNa·THF (according to its single-crystal XRD structure). While sample impurities did exist according to solid-state ^{23}Na NMR, only a broad peak at $2\theta = 3.60°$ ($d = 24.5$ Å) can be attributed to decomposition of the sample upon exposure to air and moisture (Figure C.1.6b). The decomposition product upon atmospheric exposure should therefore be a sodium salt possessing little crystalline order. Additional low-angle peaks (asterisks in Figure C.1.6a) showed variability in their intensities over a number of samples, and thus they may correspond to sample decomposition prior to hydration. Although VT pXRD data was collected, unit cell parameters of the mixed sample cannot be defined;

hence, comments upon solid-state structural changes as a function of temperature cannot be made for this sample. A preliminary conclusion is that the solid-state structure of the mixed sample cannot be represented by individual microcrystalline regions of CpNa and CpNa·THF, but is rather a new polymorphic species (i.e., both constituents of the mixed sample crystallise in different space groups relative to when they are pure).

4.3.4 ^{13}C CP/MAS NMR

Spectra of the mixed microcrystalline sample were obtained at two MAS frequencies, revealing three isotropic signals (Figure 4.6). The isotropic resonance at $\delta_{iso}(^{13}C) = 104.3(2)$ ppm corresponds to the Cp ring carbon atoms of both CpNa and CpNa·THF (Table 4.2). The resolution of the ^{13}C CP/MAS NMR experiments do not allow for their differentiation (Figure 4.6, left inset), hinting that coordination of the THF ligand at the central sodium atom does not greatly perturb the electronic environment in the Cp rings, in line with the modest structural changes outlined earlier. Resonances at ca. 71.0(3)/69.6(3) ppm and 27.6(2) ppm are assigned to the α and β THF ring carbon atoms (Figure 4.6, right inset), respectively. Herzfeld-Berger analysis of the powder pattern which corresponds to the Cp ring carbons highlights an axially-symmetric shielding tensor ($\kappa(^{13}C) = +1.0$) of appreciable magnitude ($\Omega(^{13}C) = 121.1 \pm 8.0$ ppm). While it is noted that the span reported here for the CpNa·THF Cp ring carbons is actually slightly higher than observed in the pure CpNa complex, the errors associated with Herzfeld-Berger analysis reduce the significance of this discrepancy.[39] THF ring carbon atoms exhibit reduced CSA, relative to Cp ring carbons, in accordance with theoretical calculations (*vide infra*).

-158-
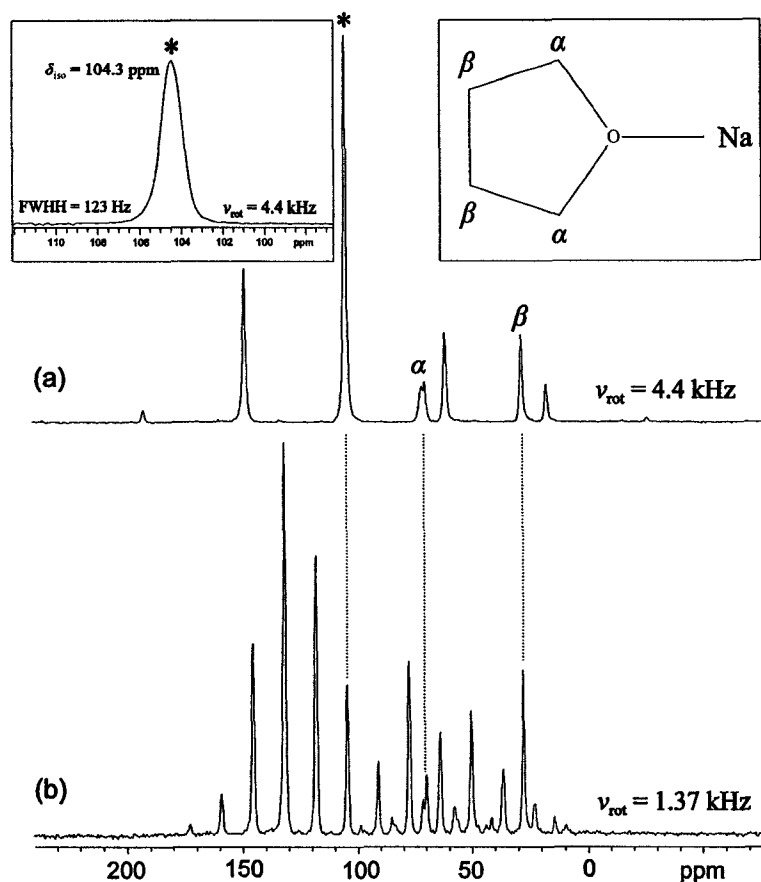
Figure 4.6 ^{13}C CP/MAS spectra of a mixed CpNa/CpNa·THF sample at (a) v_{rot} = 4.4 kHz and (b) v_{rot} = 1.37 kHz. The isotropic peak associated with the Cp ring carbons is denoted with an asterisk, carbon atoms in THF ring are denoted with symbols, and correspond to the carbon atoms shown in the right inset. Left inset: closeup of the isotropic Cp ring carbon signal prior to the application of line broadening.

Table 4.2 Experimental Carbon CS Tensor Parameters

molecule	site	δ_{11} (ppm)	δ_{22} (ppm)	δ_{33} (ppm)	δ_{iso} (ppm)	Ω (ppm)	κ
CpNa·THF	Cp	144.7	144.7	23.5	104.3(2)	121.1(8.0)	1.00
	α	—	—	—	71.0(3)/ 69.6(3)	—	—
	β	—	—	—	27.6(2)	—	—
CpNa [a]	Cp	141.0	138.8	33.8	104.5	107.1	0.96

[a] Taken from literature, see reference [39].

-159-

4.3.5 Theoretical Calculations

4.3.5.1 ^{23}Na EFG Tensor and Nuclear Electric Quadrupole Moment

Previous *ab initio* calculations of the ^{23}Na EFG tensor magnitude, symmetry and orientation in the molecular frame for CpNa·THF were carried out upon gas-phase, geometry-optimized structures,[39] as a crystal structure was unavailable at the time. With the crystal structure determined, results from calculations utilizing this structure are presented. Comparisons made between experimental and calculated ^{23}Na EFG tensor parameters are not intended to be quantitative, but will be used in a qualitative sense to illustrate which methodology combinations best reproduce the experimental parameters. Quantitative comparisons between experiment and theory are difficult, even viewed by some as not currently possible[79] due to the errors present in both the experimental and theoretical determination of nuclear parameters. A fair amount of discussion has been dedicated towards the value of the ^{23}Na nuclear electric quadrupole moment, $Q(^{23}$Na), which must be determined accurately to make quantitative comparisons. This parameter has been determined using a variety of experimental methods, including muonic X-ray experiments,[80] atomic nuclear hyperfine measurements,[81] nuclear scattering experiments,[82] and various theoretical treatments, including large-scale multiconfiguration Hartree-Fock (MCHF)[83] and configuration-interaction (CI) methods.[79] It is interesting to note that while the errors associated with each experimental and theoretical account are rather small (at most a few percent, omitting those for nuclear scattering experiments, which are often larger), the values determined by these methods do not typically compliment one another. This leads to a range of equally acceptable values for $Q(^{23}$Na), from $0.1006(20) \times 10^{-28}$ m^2, determined using

-160-

muonic X-ray experiments, to $0.1089(32) \times 10^{-28}$ m^2 from MCHF calculations. Thus, $Q(^{23}\text{Na})$ may be stated as anywhere in the region of $0.0986 - 0.1122 \times 10^{-28}$ m^2. In an effort to present calculated values which can be related meaningfully to experimental values, while at the same time not strongly favouring any measurement methodology, a median value of $Q(^{23}\text{Na}) = 0.1054 \times 10^{-28}$ m^2 is chosen.

4.3.5.2 ^{23}Na EFG Tensor Orientations

The orientation of the CpNa·THF ^{23}Na EFG tensor presented herein (Figure 4.7a-b) does not agree with earlier reports.[39] This may be due to the fact that the earlier study relied upon structures which were optimized in the gas-phase. It is noted here that as long as a basis set of at least 6-311G** quality is used (the orientation of the ^{23}Na EFG tensor when using double-ζ (DZ) basis sets does not converge when varying the cluster size or method), the ^{23}Na EFG tensor orientation does not vary significantly. V_{22} and V_{33} lie nearly in the ab-crystallographic plane, with V_{22} pointing near the sodium-oxygen bond axis (the ab-plane almost contains the THF molecule), while V_{11} is orientated close to the c-axis of the unit cell. Over all calculations, each principal component of the ^{23}Na EFG tensor points nearly along one of the crystallographic axes, with $\angle(V_{11}-\text{Na}-c)$, $\angle(V_{22}-\text{Na}-a)$ and $\angle(V_{33}-\text{Na}-b)$ ranging from $2.5° - 7.0°$, $3.6° - 6.7°$ and $2.0° - 3.7°$, respectively. The orientation of the EFG tensor in CpNa was reported earlier (Figure 4.7d).[39] For CpNa, the distinct V_{33} component points along the axis of chain propagation (the c-crystallographic axis), with V_{11} and V_{22} being oriented in electronically similar environments (hence, $\eta_Q \approx 0$) perpendicular to V_{33} (nearly perpendicular to the Cp rings).
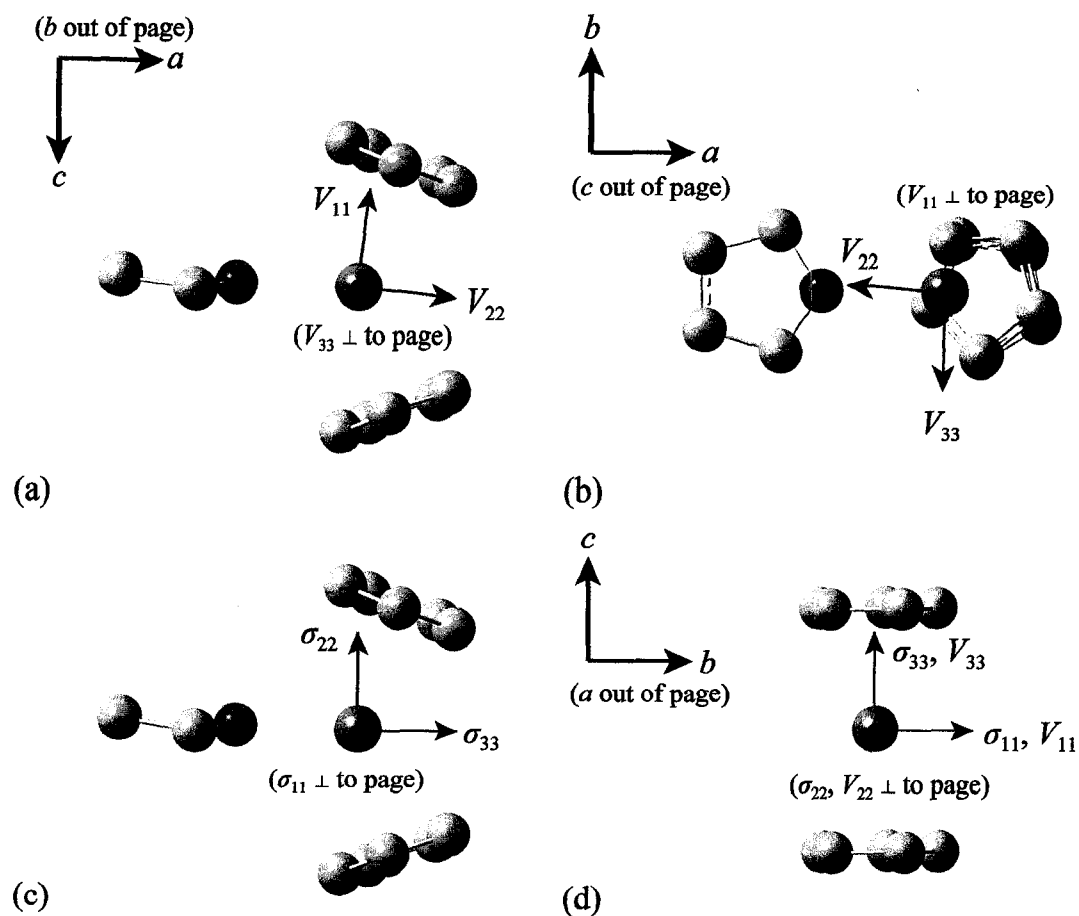
Figure 4.7 Calculated orientations of the ^{23}Na EFG ((a) = along b-crystallographic axis; (b) = along c-axis) and sodium CS (c) tensors for CpNa·THF, (d) as well as the sodium EFG and CS tensor orientations in CpNa. All hydrogen atoms have been removed to enhance clarity. When viewing the ^{23}Na EFG tensor of CpNa·THF along the c-axis, one carbon atom has been removed to better illustrate the tensor components.

4.3.5.3 The ^{23}Na Quadrupolar Coupling Constant of CpNa·THF

Calculated C_Q values fall into two regimes (Table 4.3/Table C.2.4.1): the lowest relative values are arrived at using DZ basis sets, with the highest values produced using triple-ζ (TZ) basis sets. Although experimental C_Q values are best reproduced using a DZ basis, additional considerations reduce ones confidence in them. As outlined above, the ^{23}Na

-162-

EFG tensor orientation does not converge across all calculations using a DZ basis set. Additionally, the range of calculated η_Q values is greater when comparing all DZ calculations (0.086 – 0.993) to all TZ calculations (0.333 – 0.923).

Table 4.3 Experimental & Theoretical ^{23}Na EFG Tensor Parameters for CpNa·THF ^{a}

cluster	basis set	V_{11} (au)	V_{22} (au)	V_{33} (au)	$\lvert C_Q \rvert$ (MHz)	η_Q
Experimental						
CpNa·THF	MAS - RT	—	—	—	1.82(2)	0.37(2)
CpNa·THF	MAS - 183 K	—	—	—	1.79	0.61
CpNa·THF	MAS - 153 K	—	—	—	1.78	0.70
RHF						
[Cp$_2$Na·THF]$^-$	6-311G**	0.0415	0.0763	−0.1178	2.918	0.2958
[Cp$_2$Na$_3$·3THF]$^+$	6-311G**	0.0087	0.1147	−0.1234	3.057	0.8585
Cp$_3$Na$_3$·3THF	6-311G**	0.0228	0.0991	−0.1219	3.018	0.6266
[Cp$_4$Na$_3$·3THF]$^-$	6-311G**	0.0353	0.0881	−0.1234	3.057	0.4279
[Cp$_2$Na·THF]$^-$	6-311+G**	0.0395	0.0790	−0.1185	2.935	0.3333
[Cp$_2$Na$_3$·3THF]$^+$	6-311+G**	0.0100	0.1146	−0.1246	3.087	0.8391
Cp$_3$Na$_3$·3THF	6-311+G**	0.0173	0.1060	−0.1233	3.053	0.7199
[Cp$_4$Na$_3$·3THF]$^-$	6-311+G**	0.0300	0.0945	−0.1245	3.083	0.5177
B3LYP						
[Cp$_2$Na·THF]$^-$	6-311G**	0.0361	0.0763	−0.1124	2.783	0.3583
[Cp$_2$Na$_3$·3THF]$^+$	6-311G**	0.0047	0.1154	−0.1201	2.974	0.9225
Cp$_3$Na$_3$·3THF	6-311G**	0.0118	0.1061	−0.1180	2.922	0.7994
[Cp$_4$Na$_3$·3THF]$^-$	6-311G**	0.0242	0.0958	−0.1201	2.973	0.5965
[Cp$_2$Na·THF]$^-$	6-311+G**	0.0359	0.0780	−0.1139	2.822	0.3700
[Cp$_2$Na$_3$·3THF]$^+$	6-311+G**	0.0062	0.1149	−0.1211	2.999	0.8983
Cp$_3$Na$_3$·3THF	6-311+G**	0.0126	0.1062	−0.1188	2.943	0.7871
[Cp$_4$Na$_3$·3THF]$^-$	6-311+G**	0.0255	0.0945	−0.1199	2.970	0.5754

^{a} Using standard (i.e., WTBS were not employed) basis sets on all atoms. Parameter definitions can be found in chapter 1.

Experimental C_Q values are overestimated by approximately 50 % by calculations using a TZ basis; hence, the choice of $Q(^{23}$Na) cannot account for the total discrepancy between

-163-

experimental and theoretical results. The bulk of the difference might be due to (i) medium-range interchain effects or (ii) the use of an insufficient basis set. In a previous study on polymeric potassocenes (see Chapter 2), it was shown that interchain effects were minimal and that the usage of a well-tempered basis set (WTBS) on the alkali-metal atom, in combination with the RHF method, resulted in a significant decrease in the calculated C_Q value at the potassium, producing better agreement with the experimental solid-state ^{39}K NMR values. Using a select number of basis set and methodology combinations, it is once again shown that the RHF/WTBS combination produces C_Q values that are good agreement with the experimental values (Table 4.4/Table C.2.4.2).

Table 4.4 Experimental & Theoretical ^{23}Na EFG Tensor Parameters for CpNa·THF [a]

cluster	basis set	V_{11} (au)	V_{22} (au)	V_{33} (au)	$|C_Q|$ (MHz)	η_Q
Experimental						
CpNa·THF	MAS - RT	—	—	—	1.82(2)	0.37(2)
CpNa·THF	MAS - 183 K	—	—	—	1.79	0.61
CpNa·THF	MAS - 153 K	—	—	—	1.78	0.70
RHF						
$[Cp_2Na\cdot THF]^-$	6-311G**	0.0308	0.0492	−0.0800	1.983	0.2300
$[Cp_2Na_3\cdot 3THF]^+$	6-311G**	0.0180	0.0629	−0.0808	2.002	0.5559
$Cp_3Na_3\cdot 3THF$	6-311G**	0.0201	0.0606	−0.0806	1.997	0.5026
$[Cp_2Na\cdot THF]^-$	6-311+G**	0.0225	0.0491	−0.0717	1.775	0.3711
$[Cp_2Na_3\cdot 3THF]^+$	6-311+G**	0.0015	0.0783	−0.0798	1.977	0.9624
$Cp_3Na_3\cdot 3THF$	6-311+G**	0.0517	0.0720	−0.0772	1.912	0.8661

[a] Using a WTBS on the sodium atom(s).

4.3.5.4 The ^{23}Na EFG Tensor Asymmetry of CpNa·THF

When comparing the calculated and experimental values of η_Q, one should note that

-164-

the crystal structure was determined at 173(2) K. According to earlier VT solid-state ^{23}Na

NMR experiments, this corresponds to an experimental η_Q value near 0.65, as opposed to the

room temperature value of 0.37(2).[39] The best correlation between experiment and theory

occurs when using the RHF method along with the neutral $Cp_3Na_3 \cdot 3THF$ cluster and a TZ

basis set on all atoms. The usage of anionic and cationic clusters appears to under- and over-

estimate the value associated with this parameter, respectively. The use of a WTBS on the

sodium atoms does not result in better correlation between experimental and calculated

values.

4.3.5.5 Reconciliation of VT NMR/pXRD Data for CpNa

The CpNa VT pXRD data do not allow one to arrive at conclusions that are

consistent with those reported earlier regarding the temperature-dependent structural

behaviour of CpNa, which supported an increasing Cp_{cent}–Na distance with decreasing

temperature.[39] Additional computational modelling is used in an attempt to reconcile the

VT pXRD and VT solid-state ^{23}Na NMR experimental data sets. The following alternative

models are considered: (i) medium-range interchain interactions, (ii) movement of the

sodium atom towards the Cp rings (nearly along the c-axis of the unit cell) and (iii)

movement of the sodium atom in directions perpendicular to the c-crystallographic axis.

The pXRD data illustrates that the length of the unit cell along the c-crystallographic

axis is invariant with respect to temperature, while the a and b values decrease with

decreasing temperature. As each CpNa chain lies adjacent to 6 other CpNa chains (see

Appendix C, Figure C.2.5.1), it is thought that medium-range (ca. 3.5 - 7 Å) electrostatic

-165-

interactions might play a role in changing the local electronic environment about the sodium atom. This model yields the following changes in ^{23}Na EFG tensor parameters (Figure 4.8a/Table C.2.5.1): as the lengths of the a- and b-crystallographic axes are decreased (modelling a decrease in system temperature), the value of C_Q remains largely invariant, while the value of η_Q increases. This model is in clear disagreement with previous solid-state ^{23}Na NMR observations and is rejected.

The next model looks at the possibility of the sodium atom moving towards one of the two proximate Cp rings (i.e., displacement nearly along the c-crystallographic axis; see Appendix C, Figure C.2.5.2), a type of motion which would be expected to increase in frequency and amplitude as the temperature of the system is increased. The calculations show that as the sodium atom moves towards one of the Cp rings, the value of C_Q decreases in a fashion that can be fit to a second-order polynomial function (Figure 4.8b). It is also seen that η_Q does not vary significantly until the displacement is nearly 0.5 Å from the experimentally determined position (see Figure 4.8b and Table C.2.5.2). The constant η_Q value is consistent with the solid-state ^{23}Na NMR data, however, a C_Q that is at a maximum at the crystallographic position, which is also the position at which the SCF system energy is minimized, rules out this type of behaviour.

-166-

(a)

^{23}Na EFG Tensor Parameters - ECMO calculations on CpNa

(b)

^{23}Na EFG Tensor Parameters - CpNa - Moving Na Towards Cp Ring
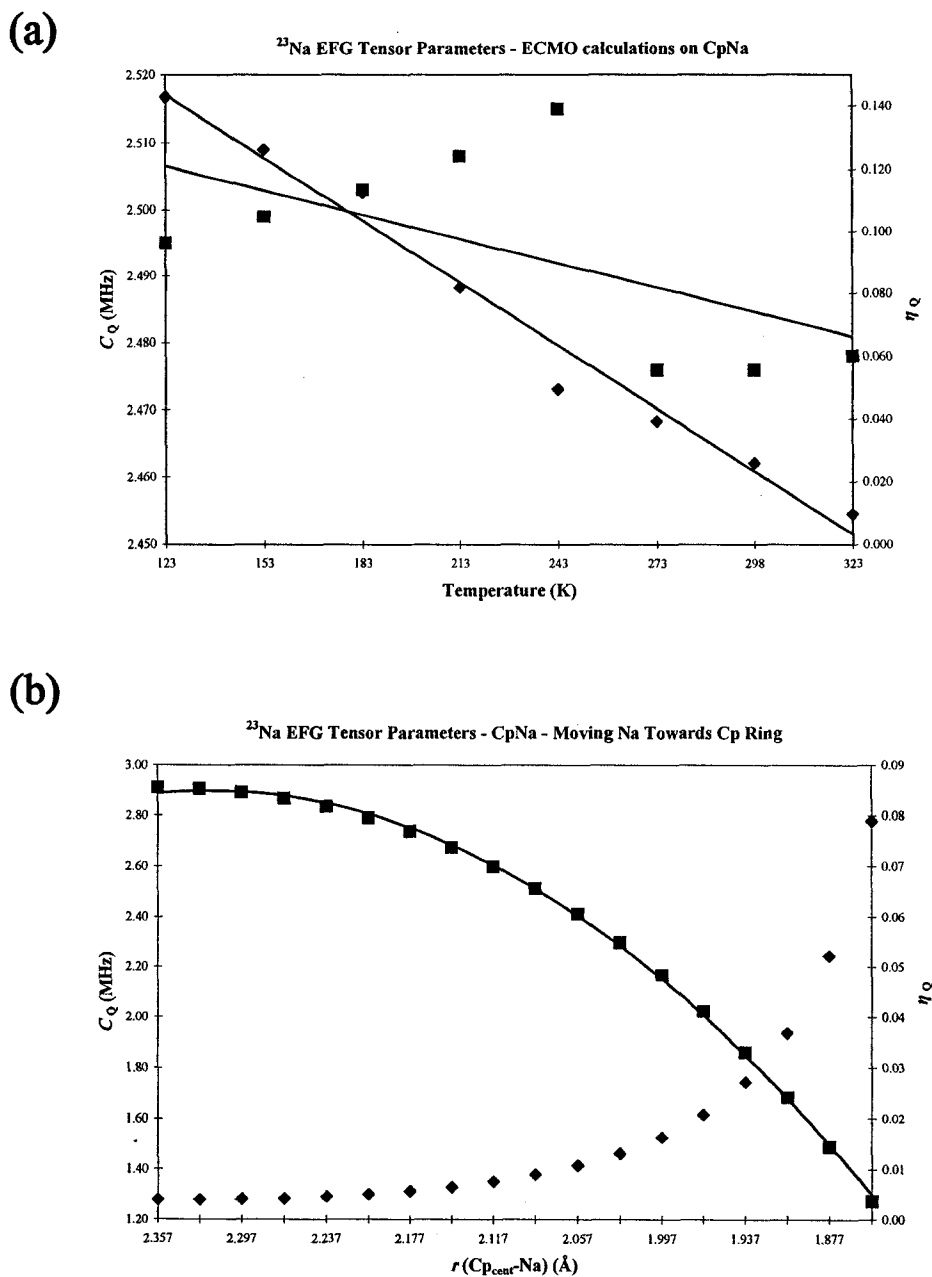
Figure 4.8 (a) ECMO calculations which attempt to incorporate medium-range electrostatic interactions show that C_Q (■) is invariant to temperature (C_Q(MHz) = –0.0037T(K) + 2.5103; R^2 = 0.3427), while η_Q (◆) should increase with decreasing temperature (η_Q = –0.0007T(K) + 0.2310; R^2 = 0.9835). (b) Movement of the sodium atom towards one Cp ring results in a decrease in the calculated C_Q value (■; C_Q(MHz = –0.0064r^2(Å^2) + 0.0288r(Å) + 2.8652; R^2 = 0.9993), while η_Q (◆) is essentially invariant until Δr(Cp$_{cent}$-Na) > 0.45 Å from the crystallographic value.

-167-

Lastly, we considered the possibility of the sodium atom undergoing a "side-to-side" motion perpendicular to the axis of chain propagation (see Figure C.2.5.3 for clarification of chosen displacements). A motion of this sort would also be expected to increase in amplitude as the temperature of the system is increased and was recently shown to be present in the structurally similar $Cp*_2Fe$ metallocene.[84] According to calculations upon an isolated Cp_2Na^- cluster (a representative example showing the change in C_Q and energy is provided in Figure 4.9a, for complete details, see Appendix C, Tables C.2.5.3 to C.2.5.12), as the sodium atom moves from its crystallographic position, the C_Q value is observed to increase, while the η_Q value changes only very slightly (below our experimental detection limits). It is expected that as the temperature increases, thermal energy available to the system would increase the amplitude of such a motion, hence giving rise to an increase in C_Q as temperature increases, in agreement with the NMR data. It is therefore concluded that the central sodium atom is undergoing a "side-to-side" motion perpendicular to the direction of chain propagation, a motion which increases in amplitude with increasing temperature (Figure 4.9b). The displacements from the equilibrium position at $T = 323$ K are thought to be about 0.1 Å to 0.2 Å greater than at $T = 153$ K, arrived at by matching the calculated and experimentally observed changes in $C_Q(^{23}Na)$.

4.3.5.6 Sodium Chemical Shielding Tensor in CpNa

The calculated orientation of the sodium CS tensor in CpNa (Figure 4.7d) agrees with that of an earlier report.[39] Two cases were considered in order to explain the experimentally observed non-axial nature of the sodium CS tensor, which contrasts with the previous

-168-

account.

(a)

C_Q and SCF Energy vs. Sodium Displacement in ab-plane

Displacement from Crystallographic Position in ab-plane (Å)

(b)
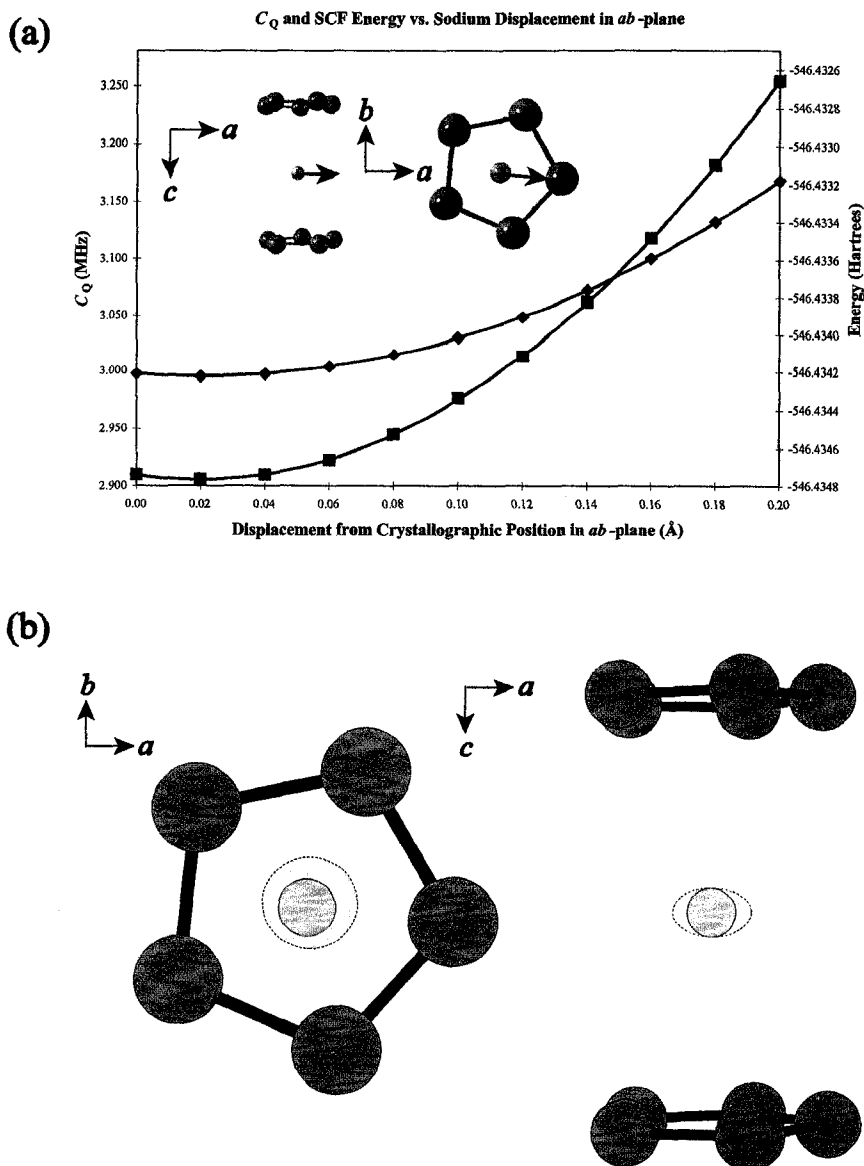
Figure 4.9 (a) Central sodium displacements perpendicular to the c-axis of the unit cell (i.e., the ab-plane; the displacement considered here is illustrated in the inset), result in energy (♦; E(Hartrees) = $1E^{-5}x^2(Å^2)$ - $5E^{-5}x(Å)$ - 546.43; R^2 = 0.9754) and C_Q (■; C_Q(MHz) = $0.0043x^2(Å^2)$ - $0.0168x(Å)$ + 2.9223; R^2 = 1.000) value increases, while η_Q does not vary significantly. A schematic of the proposed temperature-dependent motion is given in (b), where the lightly shaded dotted region represents the thermal displacement that the sodium atom is undergoing. As the temperature is decreased, this region becomes smaller, as indicated by the solid circle.

-169-

One model assumes that CpNa may be represented using the D_{5h} point group, an approximation which requires that the Cp_{cent}–Na–Cp_{cent} angle be set equal to the non-experimental value of 180.0°. The results of a DFT calculation (Tables 4.5 and C.2.6) show that the sodium shielding tensor is essentially perfectly axially symmetric ($\kappa(^{23}Na$, CpNa) = 0.994). A second model uses the experimentally determined Cp_{cent}–Na–Cp_{cent} angle of 177.7°. Using this parameter value means that CpNa is now best represented by the C_{2v} point group. A DFT calculation using this molecular conformation results in a slight variation of the sodium CS tensor symmetry, as $\kappa(^{23}Na$, CpNa) now equals 0.964. A change of this magnitude is beneath our detection capabilities, but is still significant, as shown below. By altering the symmetry of the molecule, it is perhaps of little surprise that $\kappa(^{23}Na)$ changes as well, but the origins are not well defined. By comparing the shielding values associated with CpNa when represented by the D_{5h} and C_{2v} point groups, it can be established that alteration of the Cp_{cent}–Na–Cp_{cent} value does not produce a significant change in any of the principal components of σ^d and that the variation in κ is due entirely to changing σ^p contributions. It is also seen that σ^d retains its near-perfect axial symmetry. However, as σ^p contributions arise primarily from the symmetry-allowed mixing of MO pairs (induced by the application of B_0), it is clear that there must be slight variations in the MO eigenvalues and overlap coefficients. There are no dominant contributions to σ^p in CpNa, thus making a detailed MO-by-MO analysis uninformative. It can be noted, however, that when going from D_{5h} to C_{2v} symmetry, previously doubly-degenerate E_1' and E_1'' MOs split into singly-degenerate MOs. Additionally, the D_{5h} point group contains only two rotational operators, ($\hat{R}_x, \hat{R}_y$) and $\hat{R}_z$, while the C_{2v} point group has three: $\hat{R}_x$, $\hat{R}_y$, and $\hat{R}_z$. Thus, when represented by the

-170-

C_{2v} point group, there is a clear symmetry-based distinction between the CS tensor principal components $\perp$ to σ_{33}, and that this distinction is not made when the molecule possesses D_{5h} point symmetry. As the contributions to σ_{33} remain largely unchanged upon this variation in symmetry; the change in $\kappa(^{23}\text{Na})$ is brought about entirely due to changes in σ^p, which arise because of the loss in degeneracy in the $(\hat{R}_x, \hat{R}_y)$ rotational operator and the E_1' and E_1'' MOs.

Table 4.5 Contributions to Sodium CS Tensor in the Tensor PAS (ppm) - CpNa [a]

Contribution	σ_{11} (ppm)	σ_{22} (ppm)	σ_{33} (ppm)	σ_{iso} (ppm)	Ω (ppm)	κ
CpNa (D_{5h})						
σ^d (total)	621.08	621.10	631.87	624.68	—	—
σ^p (gauge)	7.97	7.98	3.75	6.57	—	—
σ^p (occ – occ)	53.56	52.97	11.05	39.19	—	—
σ^p (occ – vir)	−67.17	−66.54	−4.93	−46.21	—	—
σ^p (total)	−5.64	−5.58	9.87	−0.45	—	—
σ_{tot} (total)	615.44	615.52	641.74	624.23	26.30	0.994
CpNa (C_{2v})						
σ^d (total)	621.20	621.21	631.87	624.76	—	—
σ^p (gauge)	7.95	7.96	3.82	6.58	—	—
σ^p (occ – occ)	52.46	53.35	11.50	39.10	—	—
σ^p (occ – vir)	−65.60	−66.02	−5.41	−45.68	—	—
σ^p (total)	−5.19	−4.71	9.91	0.00	—	—
σ_{tot} (total)	616.02	616.50	641.78	624.77	25.76	0.964

[a] Pure DFT calculation using a Cp_2Na^- cluster, TZ2P basis on all atoms and OPBE method.

4.3.5.7 Sodium Chemical Shielding Tensor in CpNa·THF

The orientation of the sodium CS tensor in the molecular frame is provided in Figure 4.7c. As was the case with the ^{23}Na EFG tensor, the principal components lie very close to the crystallographic axes, with calculated values ranging from $\angle(\sigma_{11}\text{–Na–}b) = 1$ to $4°$,

-171-

$\Delta(\sigma_{22}-\text{Na}-c) = 6$ to $12°$ and $\Delta(\sigma_{33}-\text{Na}-a) = 6$ to $12°$. This orientation was observed over

all calculations, provided a triple-ζ basis set was used. All calculations provided roughly

similar sodium CS parameters (Table 4.6), and were in moderately good agreement with

experimental findings.

Table 4.6 Experimental & Theoretical Sodium CS Tensor Parameters for CpNa·THF

cluster	basis set	δ_{11} (ppm)	δ_{22} (ppm)	δ_{33} (ppm)	δ_{iso} (ppm)	σ_{iso} (ppm)	Ω (ppm)	κ
Experimental								
CpNa·THF	static - 9.4 T	—	—	—	−45.8	—	18(3)	0.3(2)
CpNa·THF	static - 11.7 T	—	—	—	−45.1	—	21(3)	0.2(2)
RHF								
[Cp$_2$Na·THF]$^-$	6-31G**	−61.99	−66.33	−90.48	−72.93	638.16	28.49	0.70
[Cp$_2$Na$_3$·3THF]$^+$	6-31G**	−54.36	−64.80	−87.65	−68.94	634.17	33.30	0.37
[Cp$_2$Na·THF]$^-$	6-311G**	−62.37	−65.56	−91.60	−73.18	635.65	29.23	0.78
[Cp$_2$Na·THF]$^-$	6-311+G**	−62.38	−65.63	−91.84	−73.28	635.87	29.46	0.78
[Cp$_2$Na·THF]$^-$	6-311++G**	−62.27	−65.53	−91.82	−73.21	635.88	29.55	0.78
B3LYP								
[Cp$_2$Na·THF]$^-$	6-31G**	−82.76	−84.94	−112.61	−93.44	630.63	29.86	0.85
[Cp$_2$Na$_3$·3THF$^+$]	6-31G**	−81.93	−85.27	−118.86	−95.35	632.54	36.93	0.82
[Cp$_2$Na·THF]$^-$	6-311G**	−67.32	−72.84	−98.24	−79.47	624.93	30.92	0.64
[Cp$_2$Na$_3$·3THF]$^+$	6-311G**	−65.14	−71.11	−99.82	−78.69	624.15	34.68	0.66
[Cp$_2$Na·THF]$^-$	6-311+G**	−68.21	−74.16	−100.07	−80.81	625.61	31.86	0.63
[Cp$_2$Na·THF]$^-$	6-311++G**	−68.61	−74.04	−100.28	−80.98	625.78	31.68	0.66

CpNa·THF was also found to typically be de-shielded relative to CpNa (as observed

experimentally), using the CpNa sodium shielding data provided by Willans and Schurko.[39]

Notable trends over all calculations include: (i) calculated isotropic sodium chemical shifts

are shielded by ca. 30-40 ppm, (ii) produce CS tensor spans approximately 50 % greater than

the experimental values, and predict a high sodium CS tensor skew (κ ranges from 0.64 -

0.85 over all but one calculation). Computations involving larger basis sets (i.e., WTBS) and

cluster sizes were attempted, but did not converge, likely due to computational memory

-172-

limitations.

4.3.5.8 Sodium CS/EFG Euler Angles in CpNa·THF

According to simulations of the CpNa·THF site in the static solid-state ^{23}Na NMR

spectra of the mixed sample, the CS and EFG tensors of CpNa·THF are non-coincident.

Provided a triple-ζ basis set is used on all atoms, the orientations of the respective EFG and

CS tensors vary only slightly, and hence, the Euler angles determined by each calculation

do not vary with respect to one another in a very pronounced fashion. Average calculated

values over all computations that used a triple-ζ basis are (standard deviations in

parentheses): $\alpha_e = 95.3(1.6)°$, $\beta_e = 88.6(0.3)°$ and $\gamma_e = 10.8(3.1)°$, in fair (α_e and γ_e) to very

good (β_e) agreement with experimental findings.

4.3.5.9 Carbon Chemical Shielding Tensors in CpNa·THF

Herzfeld-Berger analysis of the Cp ring carbons indicates that $\delta_{11} = \delta_{22} = 144.7$ ppm,

while δ_{33} is distinct at 23.5 ppm. The Cp ring carbon atoms are expected to be undergoing

rapid five-fold reorientations at room temperature,[85] allowing for the existence of two

distinct Cp ring carbon environments, one parallel to the ring and one perpendicular to it.

In accordance with previous solid-state NMR experiments upon similar systems,[39,86-89] we

also expect that the most shielded component, δ_{33}, would point perpendicular to the Cp ring,

with δ_{11} and δ_{22} oriented parallel to the ring. Calculated carbon CS tensor values for the Cp

ring carbon atoms are provided in Table 4.7.

-173-

Table 4.7 Experimental & Theoretical Carbon CS Tensor Parameters for Cp Ring Carbon Nuclei in CpNa·THF

cluster	basis set	δ_{11} (ppm)	δ_{22} (ppm)	δ_{33} (ppm)	δ_{iso} (ppm)	σ_{iso} (ppm)	$(\delta_{11} + \delta_{22})/2$ (ppm)	Ω' [a] (ppm)
Experimental								
CpNa·THF	static - 9.4 T	144.7	144.7	23.5	104.3	—	144.7	121.1
RHF								
[Cp$_2$Na·THF]$^-$	6-31G**	162.63	95.87	−7.00	83.83	113.76	129.25	136.25
[Cp$_2$Na$_3$·3THF]$^+$	6-31G**	164.23	99.42	−9.15	84.83	112.76	131.82	140.98
[Cp$_2$Na·THF]$^-$	6-311G**	166.21	89.92	−17.24	79.63	99.78	128.06	145.30
[Cp$_2$Na·THF]$^-$	6-311+G**	167.52	90.65	−16.92	80.41	99.11	129.08	146.00
[Cp$_2$Na·THF]$^-$	6-311++G**	167.61	90.83	−16.94	80.50	99.02	129.22	146.16
B3LYP								
[Cp$_2$Na·THF]$^-$	6-31G**	163.86	102.22	5.41	90.50	106.83	133.04	127.64
[Cp$_2$Na$_3$·3THF]$^+$	6-31G**	168.37	106.21	2.96	92.51	104.82	137.29	134.33
[Cp$_2$Na·THF]$^-$	6-311G**	168.65	93.15	−9.40	84.13	90.65	130.90	140.29
[Cp$_2$Na$_3$·3THF]$^+$	6-311G**	170.42	95.55	−8.24	85.91	89.88	132.99	141.23
[Cp$_2$Na·THF]$^-$	6-311+G**	170.73	95.65	−8.19	86.06	89.73	133.19	141.37
[Cp$_2$Na·THF]$^-$	6-311++G**	170.42	95.55	−8.24	85.91	89.88	132.99	141.23

[a] Ω' calculated using averaged value of $(\delta_{11} + \delta_{22})/2$ in place of δ_{11}. When such an assumption is made, $\kappa = 1.00$.

CSA of the THF ring carbons was not experimentally measured and is hence not discussed herein (see Table C.2.7 for calculated carbon CS tensor principal components of the THF ring carbon nuclei). Correlation between experimental and calculated values is fair for all three carbon sites, with calculated $\delta_{iso}(^{13}C)$ values typically being shielded by about 20 ppm to 30 ppm, and span values for the Cp ring carbon nuclei about 15 % above experimental measurements.

4.4   Conclusions

Temperature-dependent structural changes in CpNa are not in line with previous models. The CpNa unit cell exhibits a temperature dependence, such that the a and b unit cell magnitudes decrease with decreasing temperature, while the c unit cell length shows no variation. The variation in the unit cell with temperature is not responsible for previously measured temperature-dependent $C_Q(^{23}Na)$ values, which are due rather to a fast sodium atom vibrational motion in the ab plane of the unit cell ($\perp$ to the Cp rings).

The crystal structure of the thermally unstable polymeric sodium solvate, CpNa·THF has been determined. Thermal instability is due to very weak coordination of the THF ligand to the central sodium atom, resulting in solid-state ^{23}Na NMR and pXRD experiments being conducted on a mixed CpNa/CpNa·THF sample. Powder XRD experiments on the mixed sample do not resolve the presence of either microcrystalline CpNa or CpNa·THF although solid-state ^{23}Na experiments clearly establish the presence of CpNa. It is thought that CpNa and CpNa·THF in the mixed sample each crystallise in new space groups, relative to pure substances of each.

-175-

Static solid-state ^{23}Na NMR spectra of both CpNa and the mixed sample exhibit pronounced non-axial sodium CSA. The CS and EFG tensor frames in the THF-solvated species are non-coincident, in good agreement with theoretical findings. Solid-state ^{13}C NMR experiments on the mixed sample establish the presence of THF and that although the Cp ring carbon atoms of CpNa and CpNa·THF cannot be differentiated, they are undergoing rapid, 5-fold, reorientational motions. Solid-state ^{23}Na NMR and pXRD experiments are useful in identifying the presence and identity of sample decomposition products.

-176-

Bibliography

[1]   Leal, J. P.; Cachata, V.; Carvalho, A. *European Journal of Inorganic Chemistry*
2001, 1587.

[2]   Wardell, J. L. In *Comprehensive Organometallic Chemistry*; Wilkinson, G., Stone,
F. G. A., Eds.; Pergamon Press: Oxford, 1982.

[3]   Weiss, E. *Angewandte Chemie-International Edition in English* **1993**, *32*, 1501.

[4]   Beswick, M. A. In *Comprehensive Organometallic Chemistry II*; Abel, E. W., Stone,
F. G. A., Wilkinson, G., Eds.; Elsevier Science Ltd.: Oxford, 1995.

[5]   Harder, S. *Coordination Chemistry Reviews* **1998**, *176*, 17.

[6]   Rabe, G.; Roesky, H. W.; Stalke, D.; Pauer, F.; Sheldrick, G. M. *Journal of
Organometallic Chemistry* **1991**, *403*, 11.

[7]   Schaefer, W. P.; Cotter, W. D.; Bercaw, J. E. *Acta Crystallographica Section C-
Crystal Structure Communications* **1993**, *49*, 1489.

[8]   Herberich, G. E.; Fischer, A. *Organometallics* **1996**, *15*, 58.

[9]   Jordan, V.; Behrens, U.; Olbrich, F.; Weiss, E. *Journal of Organometallic Chemistry*
1996, *517*, 81.

[10]   Dinnebier, R. E.; Behrens, U.; Olbrich, F. *Organometallics* **1997**, *16*, 3855.

[11]   Dinnebier, R. E.; Olbrich, F.; van Smaalen, S.; Stephens, P. W. *Acta
Crystallographica, Section B: Structural Science* **1997**, *B53*, 153.

[12]   Dinnebier, R. E.; Olbrich, F.; Bendele, G. M. *Acta Crystallographica, Section C:
Crystal Structure Communications* **1997**, *C53*, 699.

[13]   Lin, G.; Wong, W.-T. *Polyhedron* **1994**, *13*, 3027.

[14]   Dohmeier, C.; Baum, E.; Ecker, A.; Koeppe, R.; Schnoeckel, H. *Organometallics* **1996**, *15*, 4702.

[15]   Jutzi, P.; Leffers, W.; Pohl, S.; Saak, W. *Chemische Berichte* **1989**, *122*, 1449.

[16]   Chen, H.; Jutzi, P.; Leffers, W.; Olmstead, M. M.; Power, P. P. *Organometallics* **1991**, *10*, 1282.

[17]   Davidson, M. G.; Stalke, D.; Wright, D. S. *Angewandte Chemie* **1992**, *104*, 1265.

[18]   Paver, M. A.; Russell, C. A.; Stalke, D.; Wright, D. S. *Journal of the Chemical Society, Chemical Communications* **1993**, 1349.

[19]   Armstrong, D. R.; Herbst-Irmer, R.; Kuhn, A.; Moncrieff, D.; Paver, M. A.; Russel, C. A.; Stalke, D.; Steiner, A.; Wright, D. S. *Angewandte Chemie* **1993**, *105*, 1807.

[20]   Harder, S.; Prosenc, M. H.; Rief, U. *Organometallics* **1996**, *15*, 118.

[21]   Harder, S.; Prosenc, M. H. *Angewandte Chemie, International Edition in English* **1996**, *35*, 97.

[22]   Long, N. J. *Metallocenes: An introduction to sandwich complexes*; Copp Clark Professional: Toronto, 1998.

[23]   Kealy, T. J.; Paulson, P. L. *Nature (London, United Kingdom)* **1951**, *168*, 1039.

[24]   Wilkinson, G.; Rosenblum, M.; Whiting, M. C.; Woodward, R. B. *Journal of the American Chemical Society* **1952**, *74*, 2125.

[25]   Fischer, E. O.; Pfab, W. *Zeitschrift fuer Naturforschung* **1952**, *7b*, 377.

[26]   Thiele, J. *Berichte der Deutschen Chemischen Gesellschaft* **1900**, *33*, 666.

[27]   Thiele, J. *Berichte der Deutschen Chemischen Gesellschaft* **1901**, *34*, 68.

[28]   Fritz, H. P.; Schneider, R. *Chemische Berichte* **1960**, *93*, 1171.

[29]   Fritz, H. P.; Schafer, L. *Chemische Berichte* **1964**, *97*, 1829.

[30]   Cox, R. H.; Terry, H. W.; Harrison, L. W. *Journal of the American Chemical Society* **1971**, *93*, 3297.

[31]   Ford, W. T. *Journal of Organometallic Chemistry* **1971**, *32*, 27.

[32]   Aoyagi, T.; Shearer, H. M. M.; Wade, K.; Whitehead, G. *Journal of the Chemical Society, Chemical Communications* **1976**, 164.

[33]   Aoyagi, T.; Shearer, H. M. M.; Wade, K.; Whitehead, G. *Journal of Organometallic Chemistry* **1979**, *175*, 21.

[34]   Larsen, F. H.; Jakobsen, H. J.; Ellis, P. D.; Nielsen, N. C. *Journal of Magnetic Resonance* **1998**, *131*, 144.

[35]   Kentgens, A. P. M.; Verhagen, R. *Chemical Physics Letters* **1999**, *300*, 435.

[36]   Madhu, P. K.; Goldbourt, A.; Frydman, L.; Vega, S. *Chemical Physics Letters* **1999**, *307*, 41.

[37]   Lipton, A. S.; Sears, J. A.; Ellis, P. D. *Journal of Magnetic Resonance* **2001**, *151*, 48.

[38]   Schurko, R. W.; Hung, I.; Widdifield, C. M. *Chemical Physics Letters* **2003**, *379*, 1.

[39]   Willans, M. J.; Schurko, R. W. *Journal of Physical Chemistry B* **2003**, *107*, 5144.

[40]   Widdifield, C. M.; Schurko, R. W. *Journal of Physical Chemistry B* **2005**, *109*, 6875.

[41]   Rietveld, H. M. *Journal of Applied Crystallography* **1969**, *2*, 65.

[42]   Freemantle, M. Sunlight Controls Polymer Growth. In *Chemical and Engineering News*, 2006; Vol. 84; pp 9.

[43]   Tanabe, M.; Vandermeulen, G. W. M.; Chan, W. Y.; Cyr, P. W.; Vanderark, L.;

Rider, D. A.; Manners, I. *Nature Materials* **2006**, *5*, 467.

[44]   SMART. Program for Data Collection and Cell Refinement; Bruker AXS Inc.: Madison, WI, 2001.

[45]   SAINT. Program for Data Reduction; Bruker AXS Inc.: Madison, WI, 2001.

[46]   Sheldrick, G. M. SHELXTL: Program for Crystal Structure Solution; Bruker AXS Inc.: Madison, WI, 2001.

[47]   Sheldrick, G. M. SHELXL-97: Program for Crystal Structure Refinement; Universitat Gottingen: Gottingen, 1997.

[48]   Kraus, W.; Nolze, G. PowderCell for Windows; 2.4 ed.; Federal Institute for Materials Research and Testing: Berlin, 2000.

[49]   Eichele, K.; Wasylishen, R. E. WSolids; 2.2.13 ed.; Dalhousie University: Halifax, N.S., 1998.

[50]   Bak, M.; Rasmussen, J. T.; Nielsen, N. C. *Journal of Magnetic Resonance* **2000**, *147*, 296.

[51]   Frisch, M. J.; Trucks, G. W.; Schlegel, H. B.; Scuseria, G. E.; Robb, M. A.; Cheeseman, J. R.; Zakrzewski, V. G.; Montgomery, J., J. A.; Stratmann, R. E.; Burant, J. C.; Dapprich, S.; Millam, J. M.; Daniels, A. D.; Kudin, K. N.; Strain, M. C.; Farkas, O.; Tomasi, J.; Barone, V.; Cossi, M.; Cammi, R.; Mennucci, B.; Pomelli, C.; Adamo, C.; Clifford, S.; Ochterski, J.; Petersson, G. A.; Ayala, P. Y.; Cui, Q.; Morokuma, K.; Malick, D. K.; Rabuck, A. D.; Raghavachari, K.; Foresman, J. B.; Cioslowski, J.; Ortiz, J. V.; Baboul, A. G.; Stefanov, B. B.; Liu, G.; Liashenko, A.; Piskorz, P.; Komaromi, I.; Gomperts, R.; Martin, R. L.; Fox, D. J.; Keith, T.; Al-Laham, M. A.; Peng, C. Y.; Nanayakkara, A.; Challacombe,

M.; Gill, P. M. W.; Johnson, B.; Chen, W.; Wong, M. W.; Andres, J. L.; Gonzalez, C.; Head-Gordon, M.; Replogle, E. S.; Pople, J. A. Gaussian 98; Revision A.9 ed.; Gaussian, Inc.: Pittsburgh, PA, 1998.

[52]   Frisch, M. J.; Trucks, G. W.; Schlegel, H. B.; Scuseria, G. E.; Robb, M. A.; Cheeseman, J. R.; Montgomery, J., J. A.; Vreven, T.; Kudin, K. N.; Burant, J. C.; Millam, J. M.; Iyengar, S. S.; Tomasi, J.; Barone, V.; Mennucci, B.; Cossi, M.; Scalmani, G.; Rega, N.; Petersson, G. A.; Nakatsuji, H.; Hada, M.; Ehara, M.; Toyota, K.; Fukuda, R.; Hasegawa, J.; Ishida, M.; Nakajima, T.; Honda, Y.; Kitao, O.; Nakai, H.; Klene, M.; Li, X.; Knox, J. E.; Hratchian, H. P.; Cross, J. B.; Adamo, C.; Jaramillo, J.; Gomperts, R.; Stratmann, R. E.; Yazyev, O.; Austin, A. J.; Cammi, R.; Pomelli, C.; Ochterski, J. W.; Ayala, P. Y.; Morokuma, K.; Voth, G. A.; Salvador, P.; Dannenberg, J. J.; Zakrzewski, V. G.; Dapprich, S.; Daniels, A. D.; Strain, M. C.; Farkas, O.; Malick, D. K.; Rabuck, A. D.; Raghavachari, K.; Foresman, J. B.; Ortiz, J. V.; Cui, Q.; Baboul, A. G.; Clifford, S.; Cioslowski, J.; Stefanov, B. B.; Liu, G.; Liashenko, A.; Piskorz, P.; Komaromi, I.; Martin, R. L.; Fox, D. J.; Keith, T.; Al-Laham, M. A.; Peng, C. Y.; Nanayakkara, A.; Challacombe, M.; Gill, P. M. W.; Johnson, B.; Chen, H.; Wong, M. W.; Gonzalez, C.; Pople, J. A. Gaussian 03; Rev. B.03 ed.; Gaussian, Inc.: Pittsburgh, 2003.

[53]   Becke, A. D. *Physical Review A* **1988**, *38*, 3098.

[54]   Lee, C.; Yang, W.; Parr, R. G. *Physical Review B* **1988**, *37*, 785.

[55]   Huzinaga, S.; Miguel, B. *Chemical Physics Letters* **1990**, *175*, 289.

[56]   Huzinaga, S.; Klobukowski, M. *Chemical Physics Letters* **1993**, *212*, 260.

[57]   Brown, R. D.; Head-Gordon, M. P. *Molecular Physics* **1987**, *61*, 1183.

-181-

[58]   Cummins, P. L.; Bacskay, G. B.; Hush, N. S. *Molecular Physics* **1987**, *62*, 193.

[59]   Ditchfield, R. *Molecular Physics* **1974**, *27*, 789.

[60]   Wolinski, K.; Hinton, J. F.; Pulay, P. *Journal of the American Chemical Society* **1990**, *112*, 8251.

[61]   Guerra, C. F.; Snijders, J. G.; Te Velde, G.; Baerends, E. J. *Theoretical Chemistry Accounts* **1998**, *99*, 391.

[62]   te Velde, G.; Bickelhaupt, F. M.; Baerends, E. J.; Fonseca Guerra, C.; Van Gisbergen, S. J. A.; Snijders, J. G.; Ziegler, T. *Journal of Computational Chemistry* **2001**, *22*, 931.

[63]   Baerends, E. J.; Autschbach, J.; Bérces, A.; Bo, C.; Boerrigter, P. M.; Cavallo, L.; Chong, D. P.; Deng, L.; Dickson, R. M.; Ellis, D. E.; van Faassen, M.; Fan, L.; Fischer, T. H.; Fonseca Guerra, C.; van Gisbergen, S. J. A.; Groeneveld, O. V.; Gritsenko, M.; Grüning, F. E.; Harris, F. E.; van den Hoek, P.; Jacobsen, H.; Jensen, L.; van Kessel, G.; Kootstra, F.; van Lenthe, E.; McCormack, D. A.; Michalak, V. P.; Osinga, V. P.; Patchkovskii, S.; Philipsen, P. H. T.; Post, D.; Pye, C. C.; Ravenek, W.; Ros, P.; Schipper, P. R. T.; Schreckenbach, G.; Snijders, J. G.; Solà, M.; Swart, M.; Swerhone, D.; te Velde, G.; Vernooijs, P.; Versluis, L.; Visser, O.; Wang, F.; van Wezenbeek, E.; Wiesenekker, G.; Wolff, S. K.; Woo, T. K.; Yakovlev, A. L.; Ziegler, T. ADF; 2005.01 ed.; SCM, Theoretical Chemistry, Vrije Universiteit: Amsterdam, 2005.

[64]   Schreckenbach, G.; Ziegler, T. *Journal of Physical Chemistry* **1995**, *99*, 606.

[65]   Schreckenbach, G.; Ziegler, T. *International Journal of Quantum Chemistry* **1997**, *61*, 899.

[66]   Wolff, S. K.; Ziegler, T. *Journal of Chemical Physics* **1998**, *109*, 895.

[67]   Schreckenbach, G.; Ziegler, T. *Journal of Physical Chemistry A* **1997**, *101*, 3388.

[68]   Zhang, Y.; Wu, A.; Xu, X.; Yan, Y. *Chemical Physics Letters* **2006**, *421*, 383.

[69]   Cohen, A. J.; Handy, N. C. *Chemical Physics Letters* **2000**, *316*, 160.

[70]   Perdew, J. P.; Burke, K.; Ernzerhof, M. *Physical Review Letters* **1996**, *77*, 3865.

[71]   Dumazy, Y.; Amoureux, J.-P.; Fernandez, C. *Molecular Physics* **1997**, *90*, 959.

[72]   Sagnowski, S. F.; Ogar, J. *Physica Status Solidi B: Basic Research* **1981**, *107*, K125.

[73]   Sagnowski, S. F.; Sulek, Z.; Stachura, M.; Ogar, J. *Zeitschrift fuer Physik B: Condensed Matter* **1982**, *46*, 123.

[74]   Wong, A.; Wu, G. *Journal of Physical Chemistry A* **2000**, *104*, 11844.

[75]   Wong, A.; Whitehead, R. D.; Gan, Z.; Wu, G. *Journal of Physical Chemistry A* **2004**, *108*, 10551.

[76]   Jost, S.; Gunther, H. *Magnetic Resonance in Chemistry* **2003**, *41*, 373.

[77]   Dickinson, L. C.; MacKnight, W. J.; Connolly, J. M.; Chien, J. C. W. *Polymer Bulletin (Berlin, Germany)* **1987**, *17*, 459.

[78]   Zhang, B.; Jin, Z.; Wang, Y.; Wei, G.; Chen, W. *Chemical Research in Chinese Universities* **1992**, *8*, 15.

[79]   Jönsson, P.; Ynnermann, A.; Fischer, C. F.; Godefroid, M. R.; Olsen, J. *Physical Review A: Atomic, Molecular, and Optical Physics* **1996**, *53*, 4021.

[80]   Jeckelmann, B.; Beer, W.; Beltrami, I.; De Boer, F. W. N.; De Chambrier, G.; Goudsmit, P. F. A.; Kern, J.; Leisi, H. J.; Ruckstuhl, W.; Vacchi, A. *Nuclear Physics A* **1983**, *A408*, 495.

-183-

[81]   Yei, W.; Sieradzan, A.; Havey, M. D. *Physical Review A: Atomic, Molecular, and Optical Physics* **1993**, *48*, 1909.

[82]   Schwalm, D.; Warburton, E. K.; Olness, J. W. *Nuclear Physics A* **1977**, *A293*, 425.

[83]   Sundholm, D.; Olsen, J. *Physical Review Letters* **1992**, *68*, 927.

[84]   Herber, R. H.; Nowik, I.; Kahlenberg, V.; Kopacka, H.; Schottenberger, H. *European Journal of Inorganic Chemistry* **2006**, *2006*, 3255.

[85]   Orendt, A. M.; Facelli, J. C.; Jiang, Y. J.; Grant, D. M. *Journal of Physical Chemistry A* **1998**, *102*, 7692.

[86]   Wemmer, D. E.; Ruben, D. J.; Pines, A. *Journal of the American Chemical Society* **1981**, *103*, 28.

[87]   Kwon, O.; McKee, M. L. *Journal of Physical Chemistry A* **2001**, *105*, 10133.

[88]   Schurko, R. W.; Hung, I.; Macdonald, C. L. B.; Cowley, A. H. *Journal of the American Chemical Society* **2002**, *124*, 13204.

[89]   Hung, I.; Schurko, R. W. *Solid State Nuclear Magnetic Resonance* **2003**, *24*, 78.

-184-

Chapter 5

General Conclusions

In supplement to the conclusions offered in each chapter, it is clear from the studies presented in Chapters 2 through 4 that solid-state NMR techniques are very sensitive probes of molecular structure. Independent of the observe nuclide, measurable NMR parameters, which can be associated with CS and EFG tensors, are related to molecular structure by performing detailed *Ab Initio* analyses. Substantial information pertaining to both molecular structure and temperature-dependent structural changes and dynamics can be obtained if one uses XRD and solid-state NMR data in tandem. It must also be stressed that it is very important to understand the available physical models pertaining to chemical shielding as computational methodologies are nearly at the point where one can make quantitative chemical shielding predictions. With knowledge of this sort, measured CS tensor information in the solid-state should prove to be a very accurate probe of MO eigenstates and eigenvalues, which can be directly related to the types of bonding interactions that are being experienced at a desired NMR-active nucleus.

Appendix A

Supporting Information - A Solid-State ^{39}K and ^{13}C NMR Study of Polymeric Potassium Metallocenes

A.1   Supporting Experimental Information

CpK

Index	Calc (Å)	Obs (Å)	Error (%)
101	7.233	7.243	0.14
200	4.987	4.972	0.30
210	4.481	4.456	0.56
21$\bar{1}$	4.106	4.091	0.37
103	3.304	3.299	0.15
21$\bar{3}$	2.754	2.753	0.04
004	2.626	2.622	0.15
204	2.323	2.326	0.13
32$\bar{3}$	2.171	2.170	0.05
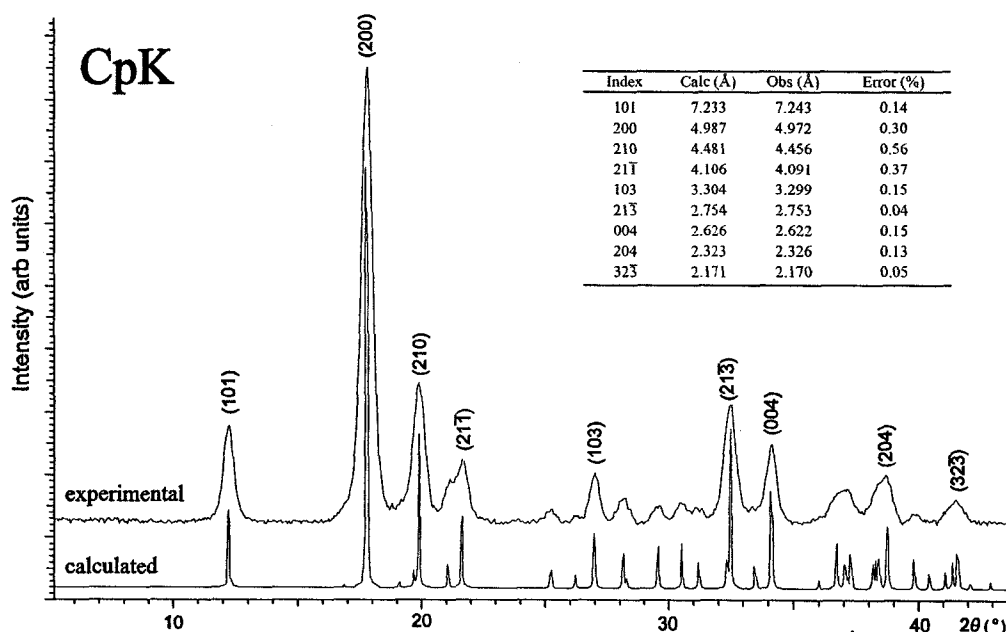
Figure A.1.1 Powder XRD spectrum of cyclopentadienyl potassium (CpK). Both CpK and Cp*K were packed into 0.7 mm capillary tubes and sealed under N_2 atmosphere prior to running pXRD experiments. Experiments were conducted at the University of Windsor on a D8 Discover powder X-ray diffractometer (Cu-Kα_2 source), using the general area detector diffractions system. Analogous samples of this material were used in subsequent ^{13}C CP/MAS NMR as well as all ^{39}K NMR experiments. Sample purity is verified by comparing the observed spectrum (top trace) to one which is calculated (bottom trace)[1] based upon the refined powder XRD structure of CpK.[2] The inset table highlights the quantitative agreement (well within experimental error) between the two data sets (the d-spacings associated with several important Miller indices were compared).

-186-
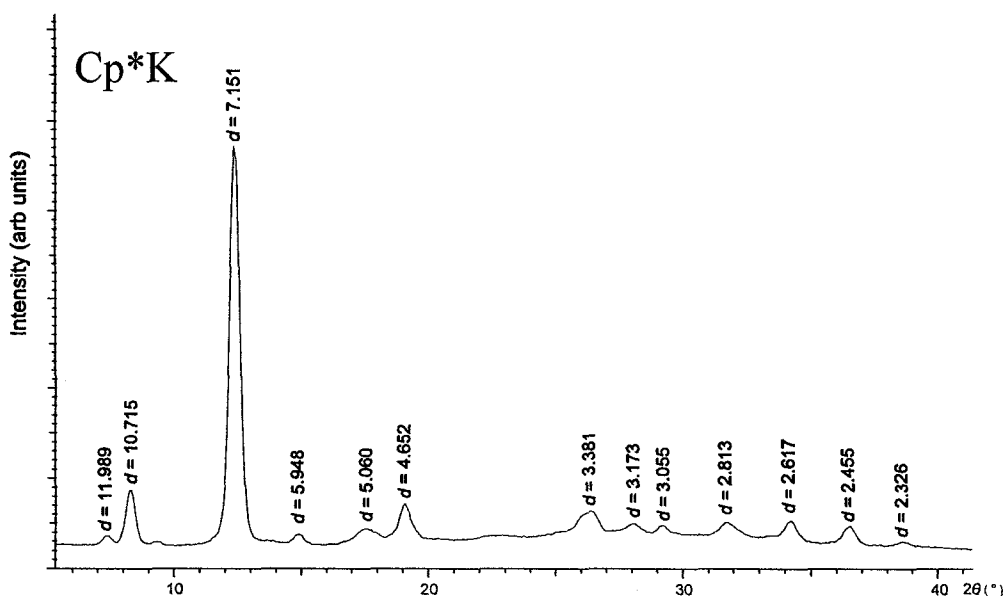
Figure A.1.2 Powder XRD spectrum of pentamethylcyclopentadienyl potassium (Cp*K). Experiments were conducted using the same experimental setup as with CpK. Analogous samples of this material were used in subsequent ^{13}C CP/MAS NMR as well as ^{39}K QCPMG NMR experiments. Sample purity was determined in a qualitative fashion, as the observed spectrum matches very closely with the findings of Dinnebier et al.[3]
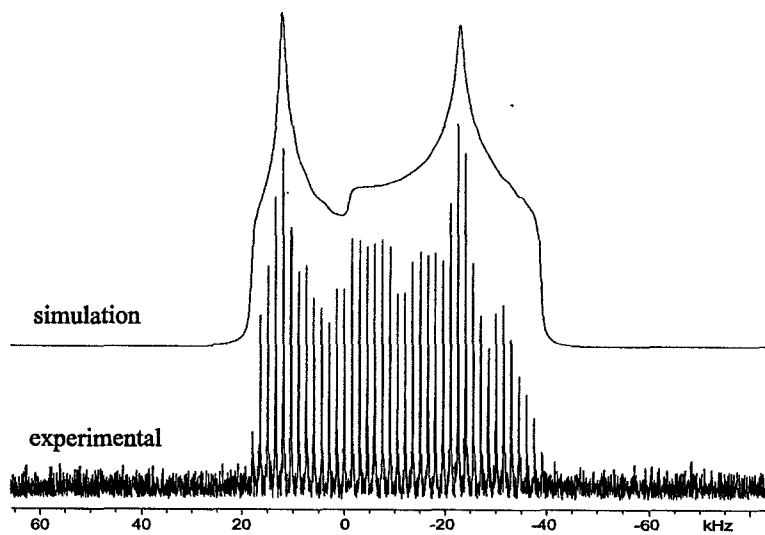
Figure A.1.3 Initial static ^{39}K QCPMG NMR powder pattern of CpK. Top trace was analytically simulated using WSolids and supplied the necessary parameters for DFS/QCPMG experiments.

-187-

No CSA, 61.5 kHz wide

$\beta_c = 0°$, 63.0 kHz wide

$\beta_c = 90°$, 60.0 kHz wide
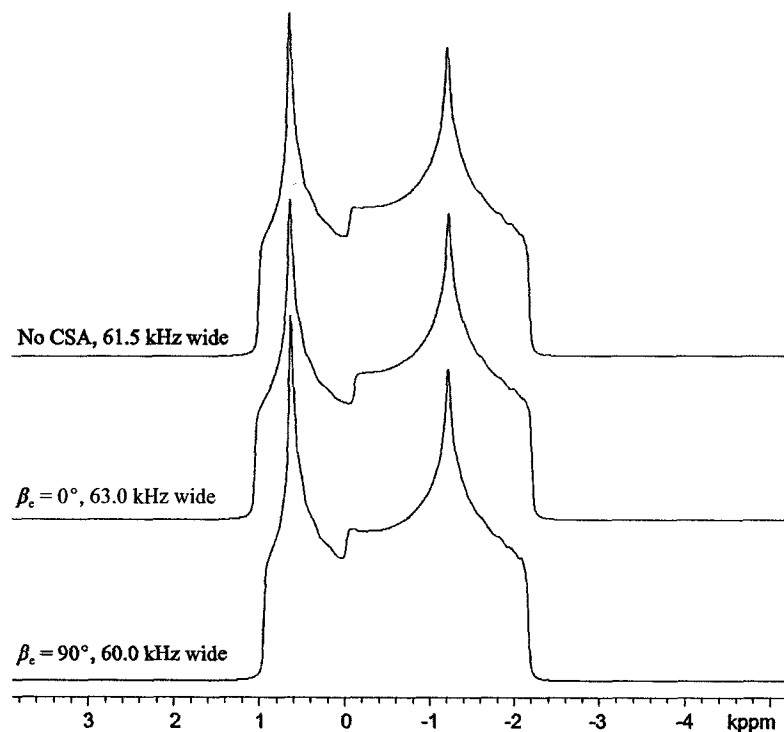
Figure A.1.4 Analytical simulations showing the minor contribution of potassium CSA to the overall static ^{39}K NMR powder pattern of CpK. Theoretical calculations point towards a maximum Ω value of about 60 ppm. The top trace is the ^{39}K NMR simulation without considering the effects of CSA, while the middle and bottom traces set $\Omega = 100$ ppm. Signal broadening caused by this amount of CSA is estimated to account for a maximum of 2.4 % of the total powder pattern breadth, below our current detection limits.

(a) $v_{rot} = 3.0$ kHz

(b) $v_{rot} = 7.0$ kHz
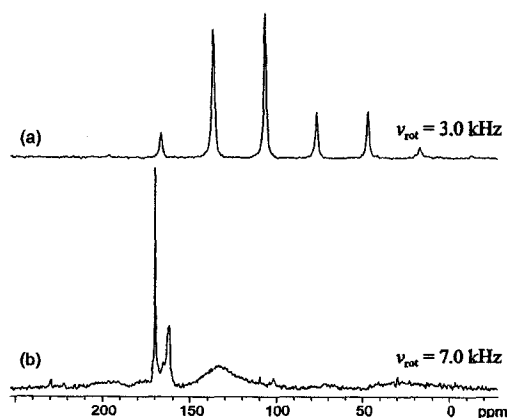
Figure A.1.5 ^{13}C CP/MAS experiments on the same sample of CpK depict drastically different carbon environments when the sample is (a) pure and (b) degraded, having been exposed to both air and moisture.

-188-
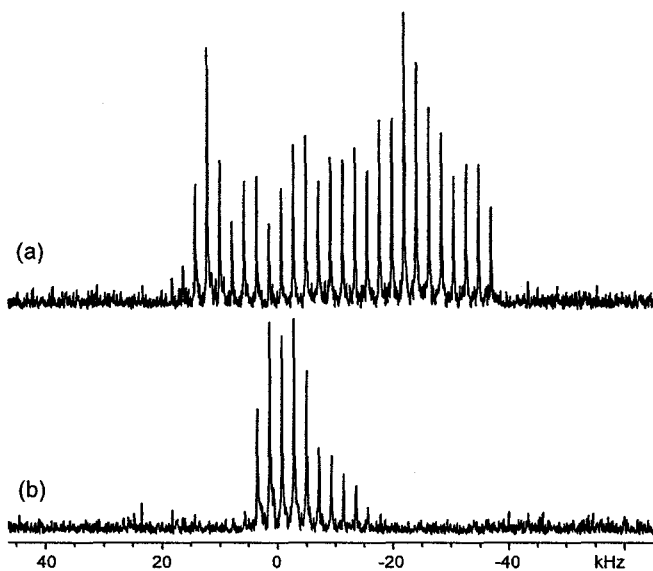
Figure A.1.6 Static ^{39}K QCPMG NMR experiments upon the same sample of CpK as depicted in Figure A.1.5, both (a) before and (b) after exposing the sample to air and moisture. A qualitative analysis of the spectra leads one to the conclusion that the potassium environments in each are completely distinct, thus illustrating the utility of ^{39}K QCPMG NMR experiments as it pertains to sample purity determination.
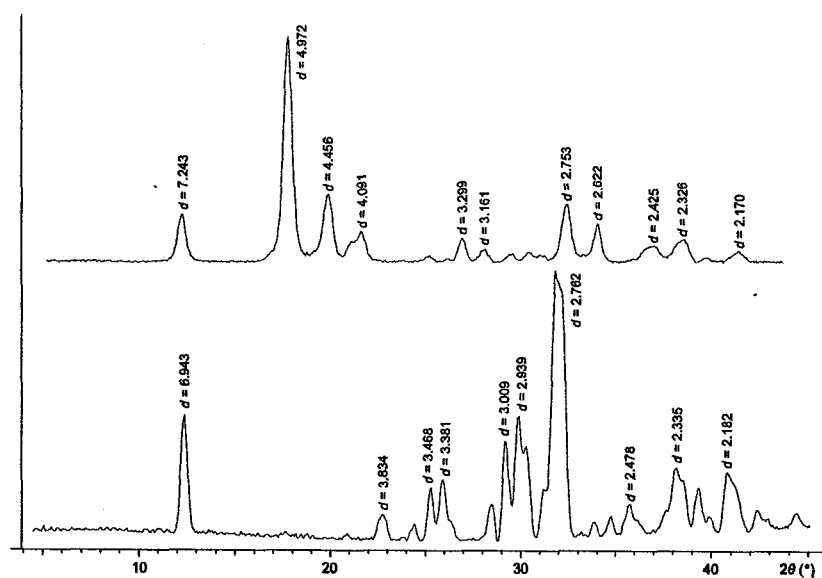
Figure A.1.7 Powder XRD spectra acquired using the same experimental setup as was mentioned in Figures A.1.1 and A.1.2. The bottom trace was acquired using the same samples as in Figures A.1.5 and A.1.6 (after exposure to air and moisture) and shows a significantly different diffraction pattern than was isolated in the known pure sample (top trace).

-189-

A.2 Supporting *Ab Initio* Information

A.2.1 CpK Cluster Coordinates Used for *Ab Initio* Calculations

Table A.2.1.1 Standard Orientation of Cp_2K^- Cluster (Cartesian)

atom	x (Å)	y (Å)	z (Å)	atom	x (Å)	y (Å)	z (Å)
K	-0.004021	-0.793769	-0.038041	H	2.395892	0.809006	-0.993551
C	2.395892	0.809006	-0.993551	H	2.234657	1.277854	0.310713
C	2.234657	1.277854	0.310713	H	2.619420	0.260201	1.184922
C	2.619420	0.260201	1.184922	H	3.018096	-0.836551	0.421180
C	3.018096	-0.836551	0.421180	H	2.881046	-0.497601	-0.925430
C	2.881046	-0.497601	-0.925430	H	-3.172198	-0.625955	-1.973068
C	-2.916703	-0.224821	-1.037059	H	-3.582919	-1.766106	0.360036
C	-3.133894	-0.830181	0.201202	H	-2.673368	-0.149951	2.224881
C	-2.651428	0.027787	1.190657	H	-1.701340	1.988335	1.043619
C	-2.136520	1.162380	0.564018	H	-2.009198	1.693977	-1.551128
C	-2.299351	1.006403	-0.813001				

Table A.2.1.2 Standard Orientation of $Cp_2K_3^+$ Cluster (Cartesian)

atom	x (Å)	y (Å)	z (Å)	atom	x (Å)	y (Å)	z (Å)
K	0.009242	1.160449	-0.010638	C	2.167670	-1.007981	-0.231676
K	5.293007	-0.772540	0.000343	H	3.130613	1.480041	1.662910
K	-5.209107	-0.942777	-0.010963	H	3.400007	1.945985	-0.910893
C	2.882695	0.818673	0.886440	H	2.130513	-0.934399	1.950944
C	3.025131	1.065673	-0.479477	H	2.567128	-0.180741	-2.213135
C	2.351799	-0.462725	1.039431	H	1.782061	-1.961410	-0.444017
C	-2.348316	-0.503334	0.884052	H	-2.079163	-1.152213	1.663982
C	-2.197834	-0.752797	-0.480554	H	-1.794591	-1.622763	-0.907348
C	-2.675185	0.357064	-1.177298	H	-2.695838	0.468951	-2.220729
C	-3.122062	1.293262	-0.243630	H	-3.538347	2.232559	-0.460968
C	-2.920470	0.760976	1.030322	H	-3.157002	1.230037	1.939352
C	2.584056	-0.062736	-1.170312				

Table A.2.1.3 Standard Orientation of Cp_3K_3 Cluster (Cartesian)

atom	x (Å)	y (Å)	z (Å)	atom	x (Å)	y (Å)	z (Å)
K	1.662526	1.113864	-0.005665	C	-5.906123	0.697411	1.038755
K	6.929610	-0.864280	-0.014372	H	-1.469899	1.348554	1.667098
K	-3.573580	-0.944892	-0.010860	H	3.801244	-1.158530	1.656570

-190-

atom	x (Å)	y (Å)	z (Å)	atom	x (Å)	y (Å)	z (Å)
C	-1.205719	0.698033	0.886836	H	-6.701946	-1.239141	1.660081
C	4.055368	-0.498673	0.880821	H	-1.748552	1.823589	-0.904047
C	-6.447822	-0.579284	0.884332	H	3.529778	-1.620073	-0.917808
C	-1.353063	0.949875	-0.477675	H	-6.973412	-1.700685	-0.914296
C	3.911835	-0.743343	-0.485401	H	-0.864222	-0.274670	-2.218483
C	-6.591355	-0.823955	-0.481890	H	4.381734	0.500520	-2.217707
C	-0.884687	-0.163455	-1.174976	H	-6.121457	0.419909	-2.214196
C	4.363033	0.381820	-1.174993	H	-0.038089	-2.046828	-0.459548
C	-6.140158	0.301209	-1.171482	H	5.180666	2.272991	-0.446565
C	-0.446503	-1.104188	-0.241747	H	-5.322524	2.192380	-0.443054
C	4.786778	1.322717	-0.235283	H	-0.412631	-1.043031	1.941310
C	-5.716412	1.242105	-0.231772	H	4.821699	1.247053	1.947303
C	-0.644483	-0.571233	1.032492	H	-5.681481	1.166442	1.950814
C	4.597068	0.778023	1.035244				

Table A.2.1.4 Standard Orientation of $Cp_4K_3^-$ Cluster (Cartesian)

atom	x (Å)	y (Å)	z (Å)	atom	x (Å)	y (Å)	z (Å)
K	0.044765	1.106134	-0.016143	C	-2.893180	0.780282	1.027264
K	5.280650	-0.952996	-0.001320	H	3.173717	1.355954	1.655115
K	-5.222530	-0.871307	-0.007767	H	-7.329463	1.437643	1.648668
C	2.909630	0.698316	0.880810	H	8.405486	-1.232250	1.672978
C	-7.593551	0.780005	0.874364	H	-2.097694	-1.150562	1.666532
C	8.151595	-0.579525	0.891143	H	3.452956	1.807312	-0.920237
C	-2.351586	-0.497837	0.884696	H	-7.050224	1.889001	-0.926684
C	3.057284	0.937589	-0.485928	H	8.677438	-1.717468	-0.896991
C	-7.445897	1.019278	-0.492374	H	-1.825742	-1.635779	-0.903438
C	8.295385	-0.836759	-0.472742	H	2.568673	-0.302855	-2.215507
C	-2.207795	-0.755071	-0.479188	H	-7.934507	-0.221166	-2.221954
C	2.588933	-0.182054	-1.173063	H	7.825981	0.391177	-2.216507
C	-7.914247	-0.100366	-1.179510	H	-2.677199	0.472866	-2.222954
C	7.844453	0.282065	-1.172742	H	1.741983	-2.058681	-0.440529
C	-2.658728	0.363754	-1.179188	H	-8.761197	-1.976992	-0.446975
C	2.150453	-1.114122	-0.231317	H	7.026872	2.179939	-0.461900
C	-8.352727	-1.032433	-0.237763	H	-3.476308	2.261628	-0.468347
C	7.420613	1.231605	-0.241809	H	2.116134	-1.032897	1.951079
C	-3.082567	1.313294	-0.248256	H	-8.387046	-0.951208	1.944632
C	2.348226	-0.569497	1.038010	H	7.385230	1.176012	1.941373
C	-8.154955	-0.487808	1.031564	H	-3.117950	1.257701	1.934926
C	7.610001	0.698593	1.033711				

-191-

Table A.2.1.5 Standard Orientation of Cp_4K_4 Cluster (Cartesian)

atom	x (Å)	y (Å)	z (Å)	atom	x (Å)	y (Å)	z (Å)
K	−0.933927	−1.028657	−0.008140	C	−8.511379	−0.828850	1.036356
K	9.567359	−0.813006	−0.010327	C	1.989907	−0.613199	1.034170
K	−6.226013	0.881613	−0.008165	H	−4.058598	−1.356433	1.663474
K	4.275273	1.097264	−0.010351	H	6.442688	−1.140782	1.661287
C	−3.812818	−0.696467	0.885133	H	−9.361544	1.082683	1.663156
C	6.688468	−0.480816	0.882947	H	1.139742	1.298334	1.660969
C	−9.088859	0.432502	0.885541	H	−4.323571	−1.831709	−0.909081
C	1.412426	0.648153	0.883355	H	6.177714	−1.616058	−0.911268
C	−3.952909	−0.948418	−0.480122	H	−9.645748	1.543830	−0.909918
C	6.548377	−0.732767	−0.482309	H	0.855538	1.759481	−0.912104
C	−9.239145	0.676977	−0.479989	H	−3.498683	0.294456	−2.217312
C	1.262141	0.892627	−0.482176	H	7.002603	0.510107	−2.219499
C	−3.516073	0.179691	−1.174135	H	−8.734237	−0.548125	−2.215812
C	6.985213	0.395342	−1.176321	H	1.767049	−0.332474	−2.217998
C	−8.756348	−0.433015	−1.172762	H	−2.722976	2.084114	−0.453143
C	1.744938	−0.217364	−1.174948	H	7.778310	2.299765	−0.455329
C	−3.104656	1.129705	−0.238126	H	−7.885751	−2.302473	−0.449679
C	7.396629	1.345356	−0.240313	H	2.615535	−2.086822	−0.451866
C	−8.306297	−1.364300	−0.235711	H	−3.069219	1.063215	1.944750
C	2.194989	−1.148649	−0.237897	H	7.432066	1.278866	1.942563
C	−3.287612	0.587696	1.034538	H	−8.273669	−1.293994	1.947090
C	7.213674	0.803346	1.032351	H	2.227616	−1.078343	1.944903

A.2.2 Calculated SCF Energies for CpK Clusters

Table A.2.2.1 Standard Basis Sets on All Atoms

cluster	method	basis	ECMO	SCF energy (Hartrees)
Cp_2K^-	RHF	6-31G**	N	−983.62157120
Cp_2K^-	RHF	6-311G**	N	−983.72997163
Cp_2K^-	RHF	6-311+G**	N	−983.74082143
Cp_2K^-	RHF	6-311++G**	N	−983.74098100
Cp_2K^-	B3LYP	6-31G**	N	−987.01611218
Cp_2K^-	B3LYP	6-311G**	N	−987.15225290
Cp_2K^-	B3LYP	6-311+G**	N	−987.16352648
Cp_2K^-	B3LYP	6-311++G**	N	−987.16375493
$Cp_2K_3^+$	RHF	6-31G**	N	−2181.82339819
$Cp_2K_3^+$	RHF	6-311G**	N	−2181.98826343
$Cp_2K_3^+$	RHF	6-311+G**	N	−2181.99184861
$Cp_2K_3^+$	RHF	6-311+G**	Y^a	−2181.99184737
$Cp_2K_3^+$	RHF	6-311+G**	Y^b	−2181.99184737

cluster	method	basis	ECMO	SCF energy (Hartrees)
$Cp_2K_3^+$	RHF	6-311++G**	N	–2181.99195906
$Cp_2K_3^+$	B3LYP	6-31G**	N	–2186.72659309
$Cp_2K_3^+$	B3LYP	6-311G**	N	–2186.93244165
$Cp_2K_3^+$	B3LYP	6-311+G**	N	–2186.93658819
$Cp_2K_3^+$	B3LYP	6-311+G**	Y^a	–2202.73467758
$Cp_2K_3^+$	B3LYP	6-311+G**	Y^b	–2213.65452163
$Cp_2K_3^+$	B3LYP	6-311++G**	N	–2186.93677859
Cp_3K_3	RHF	6-31G**	N	–2374.15543732
Cp_3K_3	RHF	6-311G**	N	–2374.35836062
Cp_3K_3	RHF	6-311+G**	N	–2374.36674590
Cp_3K_3	RHF	6-311++G**	N	–2374.36696583
Cp_3K_3	B3LYP	6-31G**	N	–2380.38060898
Cp_3K_3	B3LYP	6-311G**	N	–2380.63458669
Cp_3K_3	B3LYP	6-311+G**	N	–2380.64362749
Cp_3K_3	B3LYP	6-311++G**	N	–2380.64396332
$Cp_4K_3^-$	RHF	6-31G**	N	–2566.44664816
$Cp_4K_3^-$	RHF	6-311G**	N	–2566.68735624
$Cp_4K_3^-$	RHF	6-311+G**	N	–2566.70050512
$Cp_4K_3^-$	RHF	6-311++G**	N	–2566.70080148
$Cp_4K_3^-$	B3LYP	6-31G**	N	–2573.99335368
$Cp_4K_3^-$	B3LYP	6-311G**	N	–2574.29517716
$Cp_4K_3^-$	B3LYP	6-311+G**	N	–2574.30913723
$Cp_4K_3^-$	B3LYP	6-311++G**	N	–2574.30958056
Cp_4K_4	RHF	6-31G**	N	–3165.55934502
Cp_4K_4	RHF	6-311G**	N	–3165.82870666
Cp_4K_4	RHF	6-311+G**	N	–3165.83859579
Cp_4K_4	RHF	6-311++G**	N	–3165.83885896
Cp_4K_4	B3LYP	6-31G**	N	–3173.85957799
Cp_4K_4	B3LYP	6-311G**	N	–3174.19527174
Cp_4K_4	B3LYP	6-311+G**	N	–3174.20814943
Cp_4K_4	B3LYP	6-311++G**	N	–3174.20860132

a Mulliken point charges used
b standard point charges used

Table A.2.2.2 A Well-Tempered Basis Set (WTBS) on Potassium Atoms

cluster	method	basis	SCF energy (Hartrees)
Cp_2K^-	RHF	6-31G**	–983.64288510
Cp_2K^-	RHF	6-311G**	–983.73157534
Cp_2K^-	RHF	6-311+G**	–983.74953005
Cp_2K^-	RHF	6-311++G**	–983.74969772
Cp_2K^-	B3LYP	6-31G**	–987.02077972
Cp_2K^-	B3LYP	6-311G**	–987.14288666
Cp_2K^-	B3LYP	6-311+G**	–987.16354069

cluster	method	basis	SCF energy (Hartrees)
Cp_2K^-	B3LYP	6-311++G**	−987.16385822
$Cp_2K_3^+$	RHF	6-31G**	−2181.92627114
$Cp_2K_3^+$	RHF	6-311G**	−2182.01233405
$Cp_2K_3^+$	RHF	6-311+G**	−2182.02307137
$Cp_2K_3^+$	RHF	6-311++G**	−2182.02315382
$Cp_2K_3^+$	B3LYP	6-31G**	−2186.80723399
$Cp_2K_3^+$	B3LYP	6-311G**	−2186.92801625
$Cp_2K_3^+$	B3LYP	6-311+G**	−2186.94145074
$Cp_2K_3^+$	B3LYP	6-311++G**	−2186.94167627
Cp_3K_3	RHF	6-31G**	−2374.24479231
Cp_3K_3	RHF	6-311G**	−2374.37536116
Cp_3K_3	RHF	6-311+G**	−2374.39559911
Cp_3K_3	RHF	6-311++G**	−2374.39582301
Cp_3K_3	B3LYP	6-31G**	−2380.43989151
Cp_3K_3	B3LYP	6-311G**	−2380.62133340
Cp_3K_3	B3LYP	6-311+G**	−2380.64560894
Cp_3K_3	B3LYP	6-311++G**	−2380.64609320
$Cp_4K_3^-$	RHF	6-31G**	−2566.52588984
$Cp_4K_3^-$	RHF	6-311G**	−2566.69998943
$Cp_4K_3^-$	RHF	6-311+G**	−2566.72839244
$Cp_4K_3^-$	RHF	6-311++G**	−2566.72870817
$Cp_4K_3^-$	B3LYP	6-31G**	−2574.03434910
$Cp_4K_3^-$	B3LYP	6-311G**	−2574.27629481
$Cp_4K_3^-$	B3LYP	6-311+G**	−2574.30990889
$Cp_4K_3^-$	B3LYP	6-311++G**	−2574.31058486
Cp_4K_4	RHF	6-31G**	−3165.67929719
Cp_4K_4	RHF	6-311G**	−3165.85229922
Cp_4K_4	RHF	6-311+G**	−3165.87737297
Cp_4K_4	RHF	6-311++G**	−3165.87763315
Cp_4K_4	B3LYP	6-31G**	−3173.93996724
Cp_4K_4	B3LYP	6-311G**	−3174.18064224
Cp_4K_4	B3LYP	6-311+G**	−3174.21094556
Cp_4K_4	B3LYP	6-311++G**	−3174.21156950

A.2.3 Optimized $K(OH_2)_6^+$ Coordinates

Table A.2.3.1 Standard Basis Sets on All Atoms (O_h Symmetry)

method	basis	r(K–O) (Å)	r(O–H) (Å)	∠(H-O-H) (°)
RHF	6-31G**	2.8030	0.9442	106.43
RHF	6-311G**	2.7874	0.9424	106.11
RHF	6-311+G**	2.8181	0.9429	106.25
RHF	6-311++G**	2.8184	0.9429	106.24

-194-

method	basis	r(K–O) (Å)	r(O–H) (Å)	$\angle$(H-O-H) (°)
B3LYP	6-31G**	2.7435	0.9653	104.97
B3LYP	6-311G**	2.7225	0.9625	105.17
B3LYP	6-311+G**	2.7748	0.9633	105.31
B3LYP	6-311++G**	2.7747	0.9633	105.31

Table A.2.3.2 A WTBS on Potassium Atoms (O_h Symmetry)

method	basis	r(K–O) (Å)	r(O–H) (Å)	$\angle$(H-O-H) (°)
RHF	6-31G**	2.7837	0.9439	106.10
RHF	6-311G**	2.7794	0.9423	105.89
RHF	6-311+G**	2.8364	0.9428	106.24
RHF	6-311++G**	2.8383	0.9428	106.24
B3LYP	6-31G**	2.7287	0.9649	104.46
B3LYP	6-311G**	2.7172	0.9624	104.78
B3LYP	6-311+G**	2.8014	0.9632	105.30
B3LYP	6-311++G**	2.8000	0.9632	105.30

A.2.4 Example of Z-matrix Used for "dynamic" *Ab Initio* Calculations

```
k
xx    1    xxk2
xx    1    xxk3    2    xxkxx3
xx    3    xxxx4   1    xxxxk4   2    dih4
xx    1    xxk3    2    xxkxx3   3    dih4
xx    5    xxxx4   1    xxxxk4   2    dih4
k     3    xxk3    4    kxxxx7   1    dih4
k     5    xxk3    6    kxxxx7   1    dih4
c     3    cxx9    7    cxxk9    2    dih9
c     9    cc10    3    ccxx10   7    dih10
c     10   cc10    9    ccc11    3    dih11
c     11   cc10    10   ccc11    9    dih11
c     12   cc10    11   ccc11    10   dih11
c     5    cxx9    8    cxxk9    2    dih11
c     14   cc10    5    ccxx10   8    dih10
c     15   cc10    14   ccc11    5    dih11
c     16   cc10    15   ccc11    14   dih11
c     17   cc10    16   ccc11    15   dih11
h     10   hc19    11   hcc19    12   dih4
h     9    hc19    10   hcc19    19   dih11
h     13   hc19    9    hcc19    20   dih11
h     12   hc19    13   hcc19    21   dih11
h     11   hc19    12   hcc19    22   dih11
h     18   hc19    17   hcc19    16   dih4
h     14   hc19    18   hcc19    24   dih11
h     15   hc19    14   hcc19    25   dih11
h     16   hc19    15   hcc19    26   dih11
h     17   hc19    16   hcc19    27   dih11
```

-195-

xxk2	2.500000
xxk3	2.813000
xxkxx3	111.030
xxxx4	2.500000
xxxxk4	84.560
dih4	180.000
kxxxx7	90.000
cxx9	1.187080
cxxk9	90.000
dih9	0.000
cc10	1.395500
ccxx10	54.000
dih10	90.000
ccc11	108.000
dih11	0.000
hc19	1.050000
hcc19	126.000

A.2.5 Additional Basis Set/Methodology Combinations

Table A.2.5.1 Experimental and Theoretical ^{39}K EFG Tensor Parameters for CpK

cluster	method	basis set	V_{11} (au)	V_{22} (au)	V_{33} (au)	$|C_Q|$ (MHz)	η_Q
CpK	exp	static	—	—	—	2.55(6)	0.28(3)
CpK	exp	MAS	—	—	—	2.67(8)	0.29(3)
Cp_2K^-	RHF	6-31G**	−0.0645	−0.0818	0.1463	1.891	0.1180
$Cp_2K_3^+$	RHF	6-31G**	−0.0504	−0.0779	0.1284	1.659	0.2143
Cp_3K_3	RHF	6-31G**	−0.0556	−0.0779	0.1335	1.725	0.1668
$Cp_4K_3^-$	RHF	6-31G**	−0.0595	−0.0791	0.1385	1.791	0.1416
Cp_4K_4	RHF	6-31G**	−0.0584	−0.0782	0.1367	1.766	0.1450
Cp_2K^-	RHF	6-311G**	−0.1388	−0.1792	0.3179	4.109	0.1270
$Cp_2K_3^+$	RHF	6-311G**	−0.1010	−0.1541	0.2550	3.296	0.2082
Cp_3K_3	RHF	6-311G**	−0.1104	−0.1598	0.2702	3.492	0.1828
$Cp_4K_3^-$	RHF	6-311G**	−0.1222	−0.1675	0.2897	3.744	0.1567
Cp_4K_4	RHF	6-311G**	−0.1171	−0.1637	0.2807	3.628	0.1660
Cp_2K^-	RHF	6-311+G**	−0.1345	−0.1709	0.3054	3.947	0.1191
Cp_2K^-	RHF	6-311+G** §	−0.0621	−0.1114	0.1735	2.242	0.2842
$Cp_2K_3^+$	RHF	6-311+G**	−0.0990	−0.1506	0.2496	3.225	0.2069
$Cp_2K_3^+$	RHF†	6-311+G**	−0.0759	−0.0839	0.1598	2.066	0.0505
$Cp_2K_3^+$	RHF‡	6-311+G**	−0.0764	−0.0845	0.1610	2.080	0.0501
$Cp_2K_3^+$	RHF	6-311+G** §	−0.0523	−0.1071	0.1594	2.060	0.3438
Cp_3K_3	RHF	6-311+G**	−0.1081	−0.1565	0.2646	3.419	0.1832
Cp_3K_3	RHF	6-311+G** §	−0.0556	−0.1085	0.1640	2.120	0.3223
$Cp_4K_3^-$	RHF	6-311+G**	−0.1196	−0.1644	0.2840	3.671	0.1577
$Cp_4K_3^-$	RHF	6-311+G** §	−0.0601	−0.1116	0.1717	2.219	0.2995
Cp_4K_4	RHF	6-311+G**	−0.1145	−0.1608	0.2754	3.559	0.1683

cluster	method	basis set	V_{11} (au)	V_{22} (au)	V_{33} (au)	$|C_Q|$ (MHz)	η_Q
Cp_4K_4	RHF	6-311+G** §	−0.0584	−0.1104	0.1688	2.182	0.3083
Cp_2K^-	RHF	6-311++G**	−0.1352	−0.1706	0.3058	3.952	0.1155
Cp_2K^-	RHF	6-311++G** §	−0.0607	−0.1128	0.1735	2.243	0.3002
$Cp_2K_3^+$	RHF	6-311++G**	−0.0993	−0.1514	0.2507	3.239	0.2079
$Cp_2K_3^+$	RHF	6-311++G** §	−0.0515	−0.1074	0.1588	2.053	0.3518
Cp_3K_3	RHF	6-311++G**	−0.1084	−0.1574	0.2657	3.434	0.1843
Cp_3K_3	RHF	6-311++G** §	−0.0542	−0.1091	0.1633	2.110	0.3366
$Cp_4K_3^-$	RHF	6-311++G**	−0.1201	−0.1653	0.2853	3.687	0.1584
$Cp_4K_3^-$	RHF	6-311++G** §	−0.0584	−0.1128	0.1712	2.212	0.3176
Cp_4K_4	RHF	6-311++G**	−0.1149	−0.1617	0.2765	3.574	0.1693
Cp_4K_4	RHF	6-311++G** §	−0.0565	−0.1118	0.1683	2.175	0.3283
Cp_2K^-	B3YLP	6-31G**	−0.0577	−0.0614	0.1191	1.539	0.0315
Cp_2K^-	B3YLP	6-31G** §	−0.0690	−0.0948	0.1638	2.117	0.1579
$Cp_2K_3^+$	B3LYP	6-31G**	−0.0415	−0.0551	0.0966	1.249	0.1410
$Cp_2K_3^+$	B3LYP	6-31G** §	−0.0568	−0.0854	0.1422	1.837	0.2012
Cp_3K_3	B3LYP	6-31G**	−0.0470	−0.0546	0.1016	1.313	0.0754
Cp_3K_3	B3LYP	6-31G** §	−0.0593	−0.0862	0.1455	1.880	0.1851
$Cp_4K_3^-$	B3LYP	6-31G**	−0.0514	−0.0559	0.1072	1.385	0.0420
$Cp_4K_3^-$	B3LYP	6-31G** §	−0.0618	−0.0870	0.1488	1.923	0.1693
Cp_4K_4	B3LYP	6-31G**	−0.0499	−0.0552	0.1050	1.357	0.0503
Cp_4K_4	B3LYP	6-31G** §	−0.0606	−0.0862	0.1468	1.897	0.1739
Cp_2K^-	B3LYP	6-311G**	−0.1385	−0.1699	0.3084	3.985	0.1017
Cp_2K^-	B3LYP	6-311G** §	−0.0675	−0.0937	0.1612	2.083	0.1624
$Cp_2K_3^+$	B3LYP	6-311G**	−0.0976	−0.1447	0.2423	3.131	0.1947
$Cp_2K_3^+$	B3LYP	6-311G** §	−0.0545	−0.0866	0.1411	1.823	0.2280
Cp_3K_3	B3LYP	6-311G**	−0.1072	−0.1499	0.2572	3.323	0.1660
Cp_3K_3	B3LYP	6-311G** §	−0.0571	−0.0873	0.1444	1.866	0.2089
$Cp_4K_3^-$	B3LYP	6-311G**	−0.1198	−0.1579	0.2778	3.590	0.1372
$Cp_4K_3^-$	B3LYP	6-311G** §	−0.0606	−0.0885	0.1490	1.926	0.1872
Cp_4K_4	B3LYP	6-311G**	−0.1142	−0.1538	0.2680	3.464	0.1479
Cp_4K_4	B3LYP	6-311G** §	−0.0591	−0.0876	0.1467	1.896	0.1945
Cp_2K^-	B3LYP	6-311+G**	−0.1317	−0.1622	0.2938	3.798	0.1039
Cp_2K^-	B3LYP	6-311+G** §	−0.0385	−0.0849	0.1234	1.594	0.3767
$Cp_2K_3^+$	B3LYP	6-311+G**	−0.0943	−0.1415	0.2357	3.047	0.2001
$Cp_2K_3^+$	B3LYP†	6-311+G**	−0.0849	−0.1252	0.2102	2.716	0.1917
$Cp_2K_3^+$	B3LYP‡	6-311+G**	−0.0714	−0.1151	0.1865	2.410	0.2340
$Cp_2K_3^+$	B3LYP	6-311+G** §	−0.0273	−0.0799	0.1071	1.384	0.4911
Cp_3K_3	B3LYP	6-311+G**	−0.1034	−0.1471	0.2505	3.237	0.1744
Cp_3K_3	B3LYP	6-311+G** §	−0.0303	−0.0815	0.1118	1.445	0.4574
$Cp_4K_3^-$	B3LYP	6-311+G**	−0.1156	−0.1553	0.2709	3.500	0.1466
$Cp_4K_3^-$	B3LYP	6-311+G** §	−0.0361	−0.0854	0.1215	1.570	0.4065
Cp_4K_4	B3LYP	6-311+G**	−0.1102	−0.1516	0.2617	3.383	0.1583
Cp_4K_4	B3LYP	6-311+G** §	−0.0342	−0.0841	0.1183	1.528	0.4223
Cp_2K^-	B3LYP	6-311++G**	−0.1325	−0.1619	0.2943	3.804	0.0999

-197-

cluster	method	basis set	V_{11} (au)	V_{22} (au)	V_{33} (au)	$|C_Q|$ (MHz)	η_Q
Cp_2K^-	B3LYP	6-311++G** [§]	−0.0383	−0.0875	0.1258	1.626	0.3918
$Cp_2K_3^+$	B3LYP	6-311++G**	−0.0945	−0.1425	0.2370	3.062	0.2026
$Cp_2K_3^+$	B3LYP	6-311++G** [§]	−0.0269	−0.0813	0.1081	1.398	0.5028
Cp_3K_3	B3LYP	6-311++G**	−0.1036	−0.1482	0.2518	3.254	0.1771
Cp_3K_3	B3LYP	6-311++G** [§]	−0.0301	−0.0835	0.1136	1.468	0.4702
$Cp_4K_3^-$	B3LYP	6-311++G**	−0.1159	−0.1564	0.2723	3.519	0.1489
$Cp_4K_3^-$	B3LYP	6-311++G** [§]	−0.0357	−0.0885	0.1241	1.604	0.4254
Cp_4K_4	B3LYP	6-311++G**	−0.1104	−0.1527	0.2630	3.399	0.1608
Cp_4K_4	B3LYP	6-311++G** [§]	−0.0337	−0.0873	0.1210	1.563	0.4430

[†] Denotes ECMO calculation using Mulliken point charges.

[‡] Denotes ECMO calculation using standard point charges.

[§] Denotes WTBS on the potassium atom(s).

Table A.2.5.2 Experimental and Theoretical Potassium Chemical Shielding Tensor Parameters for CpK

cluster	method	basis set	δ_{11} (ppm)	δ_{22} (ppm)	δ_{33} (ppm)	δ_{iso} (ppm)	σ_{iso} (ppm)	Ω (ppm)	κ
CpK	exp	static	—	—	—	−100(20)	—	—	—
CpK	exp	MAS	—	—	—	−75(30)	—	—	—
Cp_2K^-	RHF	6-31G**	−62.85	−112.36	−114.33	−96.51	1367.41	51.48	−0.92
Cp_2K^-	RHF	6-31G** [a]	−18.81	−26.46	−33.94	−26.40	1323.68	15.13	−0.01
Cp_3K_3	RHF	6-31G**	−69.84	−109.00	−110.63	−96.49	1367.39	40.79	−0.92
Cp_3K_3	RHF	6-31G** [a]	−31.87	−37.58	−40.76	−36.74	1334.02	8.89	−0.28
$Cp_4K_3^-$	RHF	6-31G**	−70.19	−106.76	−112.57	−96.51	1367.41	42.38	−0.73
$Cp_4K_3^-$	RHF	6-31G** [a]	−30.22	−35.39	−41.48	−35.70	1332.98	11.25	0.08
Cp_4K_4	RHF	6-31G**	−69.86	−104.81	−112.38	−95.68	1366.58	42.52	−0.64
Cp_4K_4	RHF	6-31G** [a]	−31.07	−36.97	−40.92	−36.32	1333.60	9.85	−0.20
Cp_2K^-	RHF	6-311G**	−79.58	−138.25	−142.77	−120.20	1372.57	63.19	−0.86
Cp_2K^-	RHF	6-311G** [a]	−30.77	−39.96	−50.79	−40.51	1331.78	20.02	0.08
Cp_3K_3	RHF	6-311G**	−84.61	−126.53	−129.76	−113.63	1366.00	45.15	−0.86
Cp_3K_3	RHF	6-311G** [a]	−37.73	−45.28	−52.04	−45.02	1336.29	14.31	−0.06
$Cp_4K_3^-$	RHF	6-311G**	−84.78	−125.13	−131.23	−113.72	1366.09	46.45	−0.74
$Cp_4K_3^-$	RHF	6-311G** [a]	−37.63	−44.56	−52.37	−44.85	1336.12	14.74	0.06
Cp_4K_4	RHF	6-311G**	−84.46	−123.88	−130.73	−113.02	1365.39	46.26	−0.70
Cp_4K_4	RHF	6-311G** [a]	−38.09	−45.00	−52.23	−45.11	1336.38	14.14	0.02
Cp_2K^-	RHF	6-311+G**	−85.27	−134.96	−139.43	−119.89	1369.46	54.15	−0.83
Cp_2K^-	RHF	6-311+G** [a]	−66.67	−108.87	−114.88	−96.81	1367.23	48.21	−0.75
Cp_3K_3	RHF	6-311+G**	−88.05	−123.87	−126.47	−112.79	1362.37	38.42	−0.86
Cp_3K_3	RHF	6-311+G** [a]	−68.70	−90.54	−99.78	−86.34	1356.76	31.08	−0.41
$Cp_4K_3^-$	RHF	6-311+G**	−88.34	−125.48	−128.12	−113.98	1363.56	39.78	−0.87
$Cp_4K_3^-$	RHF	6-311+G** [a]	−66.32	−90.61	−102.15	−86.36	1356.78	35.83	−0.36
Cp_4K_4	RHF	6-311+G**	−88.05	−124.14	−127.39	−113.20	1362.78	39.35	−0.83

-198-

cluster	method	basis set	δ_{11} (ppm)	δ_{22} (ppm)	δ_{33} (ppm)	δ_{iso} (ppm)	σ_{iso} (ppm)	Ω (ppm)	κ
Cp$_4$K$_4$	RHF	6-311+G** [a]	−67.13	−89.90	−102.03	−86.35	1356.77	34.90	−0.30
Cp$_2$K$^-$	RHF	6-311++G**	−86.33	−133.16	−140.01	−119.83	1368.48	53.68	−0.74
Cp$_2$K$^-$	RHF	6-311++G** [a]	−69.49	−105.74	−112.58	−95.94	1366.40	43.09	−0.68
Cp$_3$K$_3$	RHF	6-311++G**	−89.22	−121.99	−126.83	−112.68	1361.33	37.61	−0.74
Cp$_3$K$_3$	RHF	6-311++G** [a]	−71.74	−91.25	−98.03	−87.01	1357.47	26.29	−0.48
Cp$_4$K$_3^-$	RHF	6-311++G**	−90.23	−123.13	−127.68	−113.68	1362.33	37.45	−0.76
Cp$_4$K$_3^-$	RHF	6-311++G** [a]	−70.12	−87.93	−97.48	−85.18	1355.64	27.36	−0.30
Cp$_4$K$_4$	RHF	6-311++G**	−89.93	−122.07	−127.37	−113.12	1361.77	37.44	−0.72
Cp$_4$K$_4$	RHF	6-311++G** [a]	−70.21	−88.30	−98.36	−85.62	1356.08	28.15	−0.29
Cp$_2$K$^-$	B3YLP	6-31G**	−73.26	−117.85	−125.22	−105.44	1352.41	51.96	−0.72
Cp$_2$K$^-$	B3YLP	6-31G** [a]	−2.96	−14.39	−23.23	−13.53	1314.02	20.27	−0.13
Cp$_3$K$_3$	B3LYP	6-31G**	−87.01	−127.04	−133.28	−115.78	1362.75	46.27	−0.73
Cp$_3$K$_3$	B3LYP	6-31G** [a]	−27.97	−35.08	−36.73	−33.26	1333.75	8.76	−0.62
Cp$_4$K$_3^-$	B3LYP	6-31G**	−86.28	−122.78	−135.67	−114.91	1361.88	49.39	−0.48
Cp$_4$K$_3^-$	B3LYP	6-31G** [a]	−24.91	−30.71	−37.79	−31.14	1331.63	12.88	0.10
Cp$_4$K$_4$	B3LYP	6-31G**	−85.97	−118.42	−133.80	−112.73	1359.70	47.83	−0.36
Cp$_4$K$_4$	B3LYP	6-31G** [a]	−26.84	−33.14	−38.14	−32.71	1333.20	11.30	−0.12
Cp$_2$K$^-$	B3LYP	6-311G**	−99.97	−136.75	−146.59	−127.77	1341.34	46.63	−0.58
Cp$_2$K$^-$	B3LYP	6-311G** [a]	−16.94	−25.22	−40.61	−27.59	1317.14	23.67	0.30
Cp$_3$K$_3$	B3LYP	6-311G**	−111.41	−135.28	−140.90	−129.20	1342.77	29.49	−0.62
Cp$_3$K$_3$	B3LYP	6-311G** [a]	−29.68	−37.37	−46.99	−38.01	1327.56	17.31	0.11
Cp$_4$K$_3^-$	B3LYP	6-311G**	−109.77	−132.02	−142.58	−128.12	1341.70	32.81	−0.36
Cp$_4$K$_3^-$	B3LYP	6-311G** [a]	−29.00	−36.16	−47.89	−37.68	1327.23	18.89	0.24
Cp$_4$K$_4$	B3LYP	6-311G**	−109.99	−130.53	−140.97	−127.16	1340.73	30.98	−0.33
Cp$_4$K$_4$	B3LYP	6-311G** [a]	−29.88	−37.31	−47.73	−38.31	1327.86	17.85	0.17
Cp$_2$K$^-$	B3LYP	6-311+G**	−103.27	−129.05	−138.70	−123.67	1338.53	35.43	−0.46
Cp$_2$K$^-$	B3LYP	6-311+G** [a]	−75.36	−110.73	−119.58	−101.89	1351.10	44.22	−0.60
Cp$_3$K$_3$	B3LYP	6-311+G**	−111.65	−130.80	−135.75	−126.07	1340.93	24.10	−0.59
Cp$_3$K$_3$	B3LYP	6-311+G** [a]	−86.10	−109.93	−112.77	−102.93	1352.14	26.67	−0.79
Cp$_4$K$_3^-$	B3LYP	6-311+G**	−110.50	−131.23	−138.39	−126.71	1341.57	27.89	−0.49
Cp$_4$K$_3^-$	B3LYP	6-311+G** [a]	−83.50	−109.47	−115.25	−102.74	1351.95	31.75	−0.64
Cp$_4$K$_4$	B3LYP	6-311+G**	−109.93	−128.93	−136.43	−125.09	1339.95	26.50	−0.43
Cp$_4$K$_4$	B3LYP	6-311+G** [a]	−84.90	−109.41	−116.24	−103.52	1352.73	31.34	−0.56
Cp$_2$K$^-$	B3LYP	6-311++G**	−105.01	−127.86	−140.56	−124.48	1337.56	35.55	−0.29
Cp$_2$K$^-$	B3LYP	6-311++G** [a]	−82.25	−105.25	−114.62	−100.71	1344.59	32.37	−0.42
Cp$_3$K$_3$	B3LYP	6-311++G**	−114.21	−130.94	−140.02	−128.39	1341.47	25.81	−0.30
Cp$_3$K$_3$	B3LYP	6-311++G** [a]	−94.62	−105.71	−109.90	−103.41	1347.29	15.28	−0.45
Cp$_4$K$_3^-$	B3LYP	6-311++G**	−114.11	−132.05	−142.56	−129.57	1342.65	28.45	−0.26
Cp$_4$K$_3^-$	B3LYP	6-311++G** [a]	−92.25	−103.87	−109.64	−101.65	1345.53	17.39	−0.24
Cp$_4$K$_4$	B3LYP	6-311++G**	−114.52	−131.50	−142.06	−129.36	1342.44	27.54	−0.23
Cp$_4$K$_4$	B3LYP	6-311++G** [a]	−93.71	−103.77	−111.93	−103.14	1347.02	18.22	−0.10

[a] A WTBS on the potassium atom(s).

-199-

Table A.2.5.3 Experimental and Theoretical Carbon Chemical Shielding Parameters for CpK

cluster	method	basis set	δ_{11} (ppm)	δ_{22} (ppm)	δ_{33} (ppm)	δ_{iso} (ppm)	σ_{iso} (ppm)	Ω (ppm)	κ	$(\delta_{11}+\delta_{22})/2$ (ppm)	Ω' [a] (ppm)
CpK	exp	MAS	146.7	144.3	27.7	106.2	—	119.0	0.97	—	—
Cp_2K^-	RHF	6-31G**	169.73	99.60	8.37	92.57	105.02	161.36	0.13	134.67	126.29
Cp_2K^-	RHF	6-31G** [b]	170.63	102.74	8.42	93.93	103.66	162.21	0.16	136.68	128.26
Cp_3K_3	RHF	6-31G**	172.30	101.23	5.86	93.13	104.46	166.44	0.15	136.76	130.90
Cp_3K_3	RHF	6-31G** [b]	172.37	108.25	5.73	95.45	102.14	166.64	0.23	140.31	134.58
$Cp_4K_3^-$	RHF	6-31G**	171.68	100.07	6.21	92.65	104.94	165.47	0.13	135.87	129.66
$Cp_4K_3^-$	RHF	6-31G** [b]	172.05	106.69	6.08	94.94	102.65	165.97	0.21	139.37	133.29
Cp_4K_4	RHF	6-31G**	172.56	101.23	5.35	93.05	104.54	167.20	0.15	136.89	131.54
Cp_4K_4	RHF	6-31G** [b]	172.53	108.59	5.21	95.45	102.14	167.32	0.24	140.56	135.35
Cp_2K^-	RHF	6-311G**	173.77	89.92	−1.60	87.36	92.05	175.38	0.04	131.84	133.45
Cp_2K^-	RHF	6-311G** [b]	174.50	89.29	−1.74	87.35	92.06	176.24	0.03	131.90	133.64
Cp_3K_3	RHF	6-311G**	175.72	96.87	−4.02	89.52	89.89	179.74	0.12	136.29	140.31
Cp_3K_3	RHF	6-311G** [b]	176.22	96.28	−4.30	89.40	90.01	180.51	0.11	136.25	140.54
$Cp_4K_3^-$	RHF	6-311G**	175.19	94.52	−3.78	88.64	90.77	178.98	0.10	134.86	138.64
$Cp_4K_3^-$	RHF	6-311G** [b]	175.88	94.15	−4.01	88.68	90.73	179.89	0.09	135.02	139.02
Cp_4K_4	RHF	6-311G**	175.92	97.46	−4.53	89.62	89.79	180.45	0.13	136.69	141.22
Cp_4K_4	RHF	6-311G** [b]	176.43	96.83	−4.81	89.48	89.93	181.24	0.12	136.63	141.44
Cp_2K^-	RHF	6-311+G**	176.37	91.61	−1.50	88.82	90.70	177.87	0.05	133.99	135.49
Cp_2K^-	RHF	6-311+G** [b]	176.69	90.96	−1.66	88.66	90.86	178.35	0.04	133.83	135.49
Cp_3K_3	RHF	6-311+G**	177.75	98.88	−3.83	90.93	88.59	181.58	0.13	138.31	142.15
Cp_3K_3	RHF	6-311+G** [b]	177.83	97.58	−4.13	90.43	89.09	181.95	0.12	137.70	141.83
$Cp_4K_3^-$	RHF	6-311+G**	177.36	96.45	−3.61	90.06	89.46	180.96	0.11	136.90	140.51
$Cp_4K_3^-$	RHF	6-311+G** [b]	177.53	95.64	−3.88	89.77	89.75	181.41	0.10	136.59	140.46
Cp_4K_4	RHF	6-311+G**	177.89	99.43	−4.33	91.00	88.52	182.22	0.14	138.66	142.99
Cp_4K_4	RHF	6-311+G** [b]	177.95	98.23	−4.64	90.52	89.00	182.59	0.13	138.09	142.73
Cp_2K^-	RHF	6-311++G**	176.39	91.78	−1.54	88.87	90.65	177.93	0.05	134.08	135.62
Cp_2K^-	RHF	6-311++G** [b]	176.69	90.95	−1.73	88.64	90.88	178.41	0.04	133.82	135.55
Cp_3K_3	RHF	6-311++G**	177.86	99.02	−3.89	91.00	88.52	181.75	0.13	138.44	142.32

cluster	method	basis set	δ_{11} (ppm)	δ_{22} (ppm)	δ_{33} (ppm)	δ_{iso} (ppm)	σ_{iso} (ppm)	Ω (ppm)	κ	$(\delta_{11}+\delta_{22})/2$ (ppm)	Ω' [a] (ppm)
Cp₃K₃	RHF	6-311++G** [b]	177.94	97.75	-4.21	90.49	89.03	182.16	0.12	137.85	142.06
Cp₄K₃⁻	RHF	6-311++G**	177.48	96.64	-3.66	90.16	89.36	181.14	0.11	137.06	140.72
Cp₄K₃⁻	RHF	6-311++G** [b]	177.64	95.75	-3.95	89.81	89.71	181.59	0.10	136.70	140.65
Cp₄K₄	RHF	6-311++G**	178.03	99.58	-4.37	91.08	88.44	182.40	0.14	138.80	143.18
Cp₄K₄	RHF	6-311++G** [b]	178.09	98.41	-4.72	90.59	88.93	182.81	0.13	138.25	142.97
Cp₂K⁻	B3YLP	6-31G**	169.44	106.35	22.01	99.27	98.06	147.43	0.14	137.90	115.89
Cp₂K⁻	B3YLP	6-31G** [b]	171.13	110.51	21.73	101.12	96.21	149.39	0.19	140.82	119.08
Cp₃K₃	B3LYP	6-31G**	173.20	107.45	19.51	100.05	97.28	153.69	0.14	140.32	120.81
Cp₃K₃	B3LYP	6-31G** [b]	173.58	116.79	14.87	101.75	95.58	158.71	0.28	145.18	130.32
Cp₄K₃⁻	B3LYP	6-31G**	172.14	106.01	19.92	99.36	97.97	152.22	0.13	139.08	119.16
Cp₄K₃⁻	B3LYP	6-31G** [b]	172.86	114.03	19.37	102.09	95.24	153.49	0.23	143.45	124.07
Cp₄K₄	B3LYP	6-31G**	173.02	106.03	17.39	98.81	98.52	155.63	0.14	139.52	122.14
Cp₄K₄	B3LYP	6-31G** [b]	173.52	116.44	16.49	102.15	95.18	157.02	0.27	144.98	128.49
Cp₂K⁻	B3LYP	6-311G**	175.20	94.07	8.55	92.61	82.17	166.65	0.03	134.63	126.08
Cp₂K⁻	B3LYP	6-311G** [b]	176.69	92.63	8.29	92.54	82.24	168.40	0.00	134.66	126.37
Cp₃K₃	B3LYP	6-311G**	177.73	101.99	6.05	95.26	79.52	171.68	0.12	139.86	133.81
Cp₃K₃	B3LYP	6-311G** [b]	178.82	100.03	5.57	94.81	79.97	173.25	0.09	139.43	133.86
Cp₄K₃⁻	B3LYP	6-311G**	176.84	99.13	6.34	94.10	80.68	170.49	0.09	137.98	131.64
Cp₄K₃⁻	B3LYP	6-311G** [b]	178.29	97.65	5.48	93.80	80.98	172.81	0.07	137.97	132.49
Cp₄K₄	B3LYP	6-311G**	177.65	103.75	6.71	96.03	78.75	170.94	0.14	140.70	133.99
Cp₄K₄	B3LYP	6-311G** [b]	178.94	100.43	5.05	94.81	79.97	173.89	0.10	139.69	134.63
Cp₂K⁻	B3LYP	6-311+G**	178.66	97.04	9.44	95.05	80.74	169.22	0.04	137.85	128.41
Cp₂K⁻	B3LYP	6-311+G** [b]	178.94	96.00	9.16	94.70	81.09	169.77	0.02	137.47	128.30
Cp₃K₃	B3LYP	6-311+G**	180.39	105.22	7.07	97.56	78.23	173.31	0.13	142.80	135.73
Cp₃K₃	B3LYP	6-311+G** [b]	180.30	102.78	6.58	96.55	79.24	173.72	0.11	141.54	134.96
Cp₄K₃⁻	B3LYP	6-311+G**	179.68	102.24	7.34	96.42	79.37	172.34	0.10	140.96	133.62
Cp₄K₃⁻	B3LYP	6-311+G** [b]	179.81	100.71	6.90	95.81	79.98	172.91	0.09	140.26	133.36
Cp₄K₄	B3LYP	6-311+G**	180.25	105.29	6.64	97.39	78.40	173.61	0.14	142.77	136.13
Cp₄K₄	B3LYP	6-311+G** [b]	180.34	103.31	6.08	96.58	79.21	174.26	0.12	141.83	135.75
Cp₂K⁻	B3LYP	6-311++G**	178.50	97.03	9.44	94.99	80.80	169.06	0.04	137.76	128.33

cluster	method	basis set	δ_{11} (ppm)	δ_{22} (ppm)	δ_{33} (ppm)	δ_{iso} (ppm)	σ_{iso} (ppm)	Ω (ppm)	κ	$(\delta_{11} + \delta_{22})/2$ (ppm)	Ω' [a] (ppm)
Cp_2K^-	B3LYP	6-311++G** [b]	178.94	95.64	9.14	94.50	81.29	169.60	0.02	137.19	128.05
Cp_3K_3	B3LYP	6-311++G**	180.31	105.15	7.08	97.51	78.28	173.23	0.13	142.73	135.65
Cp_3K_3	B3LYP	6-311++G** [b]	180.09	102.58	6.55	96.41	79.38	173.54	0.11	141.34	134.78
$Cp_4K_3^-$	B3LYP	6-311++G**	179.57	102.46	7.34	96.46	79.33	172.23	0.10	141.02	133.68
$Cp_4K_3^-$	B3LYP	6-311++G** [b]	179.57	100.65	6.87	95.70	80.09	172.70	0.09	140.11	133.24
Cp_4K_4	B3LYP	6-311++G**	180.35	105.59	6.69	97.54	78.25	173.65	0.14	142.97	136.27
Cp_4K_4	B3LYP	6-311++G** [b]	180.11	103.09	6.06	96.42	79.37	174.05	0.12	141.60	135.55

[a] Ω' calculated using averaged value of $(\delta_{11} + \delta_{22})/2$ in place of δ_{11}.

[b] A WTBS on the potassium atom(s).

Bibliography

[1]   Kraus, W.; Nolze, G. PowderCell for Windows; 2.4 ed.; Federal Institute for Materials Research and Testing: Berlin, 2000.

[2]   Dinnebier, R. E.; Behrens, U.; Olbrich, F. *Organometallics* **1997**, *16*, 3855.

[3]   Dinnebier, R. E., Private Communication.

Appendix B

Supporting Information - Understanding Chemical Shielding using Group Symmetry Representations, MO Analysis and Modern Density-Functional Theory

Table B.1 Calculated and Experimental Structural Data

molecule	parameter [a]	DZ basis [b]	TZ2P basis	expt [c]
C_2H_4	r(CC)	1.341	1.335	1.339
	r(CH)	1.091	1.089	1.085
	$\measuredangle$(HCH)	116.4	116.6	117.8
HF	r(HF)	0.975	0.936	0.917
H_2O	r(OH)	0.996	0.972	0.958
	$\measuredangle$(HOH)	107.4	104.4	104.5
CO	r(CO)	—	1.137	1.128
H_2CO	r(CO)	—	1.213	1.208
	r(HC)	—	1.115	1.116
	$\measuredangle$(HCH)	—	116.3	116.5
PF_3	r(PF)	1.773	1.607	1.570 [1]
	$\measuredangle$(FPF)	96.8	97.7	97.8 [1]

[a] All bond distances are reported in Angstroms (Å), all angles are in degrees (°).
[b] Basis sets are defined in **3.3**.
[c] Experimental molecular geometries were taken from reference [2], except where noted.

Table B.2 D_{2h} Character Table with Applicable Rotational Operators ($\hat{R}_n$)

D_{2h}	E	$C_2(z)$	$C_2(y)$	$C_2(x)$	i	$\sigma(xy)$	$\sigma(xz)$	$\sigma(yz)$	operator [a]
A_g	1	1	1	1	1	1	1	1	—
B_{1g}	1	1	−1	−1	1	1	−1	−1	R_z
B_{2g}	1	−1	1	−1	1	−1	1	−1	R_y
B_{3g}	1	−1	−1	1	1	−1	−1	1	R_x
A_u	1	1	1	1	−1	−1	−1	−1	—
B_{1u}	1	1	−1	−1	−1	−1	1	1	—
B_{2u}	1	−1	1	−1	−1	1	−1	1	—
B_{3u}	1	−1	−1	1	−1	1	1	−1	—

[a] For brevity, the operator caret symbol has been dropped when denoting rotational operators in tables.

Table B.3 C_2H_4 - Fragment Orbital (FO) Contributions to Significant Shielding MOs [a]

MO energy (eV)	ψ_p [b]	MO	%	FO [c]	atm [d]	MO energy (eV)	ψ_p	MO	%	FO	atm
−269.60	1	$1a_{1g}$	100.0	$1s$	C	4.31	15	$2b_{1u}*$	101.0	$3p_z$	C
−269.58	2	$1b_{3u}$	100.0	$1s$	C	6.32	18	$6a_{1g}*$	32.1	$3p_x$	C
−18.54	3	$2a_{1g}$	69.8	$2s$	C				24.9	$2s$	H
			23.1	$1s$	H				21.5	$1s$	H
			8.1	$2p_x$	C				11.1	$2p_y$	H
−14.05	4	$2b_{3u}$	51.4	$1s$	H				8.3	$2s$	C
			33.4	$2s$	C	7.91	19	$2b_{2g}*$	117.4	$3p_z$	C
			14.3	$2p_x$	C				−15.4	$2p_z$	C
			−5.6	$3p_x$	C	12.16 [e]	23	$3b_{1g}*$	87.1	$2s$	H
−11.29	5	$1b_{2u}$	53.1	$2p_y$	C				61.3	$3p_y$	C
			48.8	$1s$	H				−59.5	$1s$	H
−10.07	6	$3a_{1g}$	59.4	$2p_x$	C				−21.6	$2p_y$	C
			31.0	$1s$	H				14.4	$2p_x$	H
			9.5	$3p_x$	C	13.59 [e]	24	$6b_{3u}*$	175.7	$3p_x$	C
−8.43	7	$1b_{1g}$	69.2	$1s$	H				−56.7	$2p_x$	C
			25.9	$2p_y$	C				−53.4	$1s$	H
−6.52	8	$1b_{1u}$	95.4	$2p_z$	C				12.2	$4p_x$	C
−0.89	9	$1b_{2g}*$	98.7	$2p_z$	C				10.6	$2s$	H
			−8.4	$3p_z$	C						
			7.7	$2p_z$	H						
0.45	10	$4a_{1g}*$	75.8	$2s$	H						
			35.0	$1s$	H						
			−17.2	$3s$	C						
			5.5	$2p_x$	C						

[a] Includes FOs which constitute more than 5.0 % of the MO.
[b] Wave functions are numbered according to increasing energy, with 1 representing the lowest energy eigenstate.
[c] Fragment orbitals are unique to ADF software. They are symmetry-adapted combinations of AOs and serve as the building blocks for the eventual MOs.
[d] Atom(s) from which the fragment is derived.
[e] There are numerous contributions to this MO, only the top 5 are shown.

-205-

Table B.4 $C_{\infty v}$ Character Table with Applicable Rotation Operators ($\hat{R}_n$)

$C_{\infty v}$	E	$2\,C_\infty$	$\cdots$	$\infty\,\sigma_v$	operator
$A_1 \equiv \Sigma^+$	1	1	$\cdots$	1	—
$A_2 \equiv \Sigma^-$	1	1	$\cdots$	−1	R_z
$E_1 \equiv \Pi$	2	$2\cos\varphi$	$\cdots$	0	(R_x, R_y)
$E_2 \equiv \Delta$	2	$2\cos 2\varphi$	$\cdots$	0	—
$E_3 \equiv \Phi$	2	$2\cos 3\varphi$	$\cdots$	0	—
$\cdots$	$\cdots$	$\cdots$	$\cdots$	$\cdots$	$\cdots$
E_n	2	$2\cos n\varphi$	$\cdots$	0	—

Table B.5 HF - FO Contributions to Significant Shielding MOs [a]

MO energy (eV)	ψ_p	MO	%	FO	atm	MO energy (eV)	ψ_p	MO	%	FO	atm
−660.72	1	1σ	100.0	$1s$	F	5.61	8	$6\sigma^*$	87.8	$2s$	H
−29.81	2	2σ	87.8	$2s$	F				12.8	$2p_z$	F
			7.5	$1s$	H				7.5	$1s$	H
−13.36	3	3σ	76.9	$2p_z$	F	11.07	9	$2\pi_x^*$	59.3	$3p_x$	F
			11.1	$1s$	H				38.4	$2p_x$	H
			7.4	$2s$	F	11.07	10	$2\pi_y^*$	59.3	$3p_y$	F
−9.62	4	$1\pi_x$	97.6	$2p_x$	F				38.4	$2p_y$	H
−9.62	5	$1\pi_y$	97.6	$2p_y$	F						
−1.01	6	$4\sigma^*$	45.0	$1s$	H						
			36.1	$2s$	H						
			9.3	$2p_z$	H						

[a] Includes FOs which constitute more than 5.0 % of the MO.

Table B.6 C_{3v} Character Table with Applicable Rotation Operators ($\hat{R}_n$)

C_{3v}	E	$2\,C_3$	$3\,\sigma_v$	operator
A_1	1	1	1	—
A_2	1	1	−1	R_z
E	2	−1	0	(R_x, R_y)

-206-

Table B.7 PF$_3$ - FO Contributions to Significant Shielding MOs [a]

MO energy (eV)	ψ_p	MO	%	FO	atm	MO energy (eV)	ψ_p	MO	%	FO	atm
−2082.1	1	1a₁	100.0	1s	P	−1.54	23	7e(2)*	92.1	3p_y	P
−175.45	5	3a₁	100.0	2s	P				−15.4	3s	F
−127.08	6	2e(1)	100.0	2p_x	P				7.7	4p_y	P
−127.08	7	2e(2)	100.0	2p_y	P				6.7	3d_yz	P
−126.88	8	4a₁	99.9	2p_z	P				6.1	2p_z	F
−13.62	13	4e(1)	54.7	2p_y	F	3.12	28	11a₁*	53.3	4p_z	P
			22.9	2p_z	F				18.8	2p_x	F
			12.0	3p_x	P				18.1	3p_z	P
−13.62	14	4e(2)	54.7	2p_x	F				17.4	3s	P
			22.9	2p_z	F				−8.1	3p_x	F
			12.0	3p_y	P				5.5	3s	F
−8.09	21	8a₁	35.8	3s	P						
			31.7	2p_z	F						
			25.9	3p_z	P						
−1.54	22	7e(1)*	92.1	3p_x	P						
			−15.4	3s	F						
			7.7	4p_x	P						
			6.7	3d_xz	P						
			6.1	2p_z	F						

[a] Includes FOs which constitute more than 5.0 % of the MO.

Table B.8 C_{2v} Character Table with Applicable Rotation Operators ($\hat{R}_n$)

C_{2v}	E	C_2	$\sigma_v(xz)$	$\sigma_v'(yz)$	operator
A_1	1	1	1	1	—
A_2	1	1	−1	−1	R_z
B_1	1	−1	1	−1	R_y
B_2	1	−1	−1	1	R_x

Table B.9 H_2O - FO Contributions to Significant Shielding MOs [a]

MO energy (eV)	ψ_p	MO	%	FO	atm	MO energy (eV)	ψ_p	MO	%	FO	atm
-511.00	1	$1a_1$	100.0	$1s$	O	6.32	9	$3b_2$*	51.5	$2s$	H
-25.05	2	$2a_1$	76.6	$2s$	O				26.7	$2p_y$	O
			16.6	$1s$	H				22.0	$1s$	H
-13.00	3	$1b_2$	62.0	$2p_y$	O				6.2	$2p_z$	H
			32.2	$1s$	H	8.37	10	$6a_1$*	96.6	$3p_z$	O
-9.23	4	$3a_1$	77.0	$2p_z$	O				37.8	$2p_z$	H
			11.0	$2s$	O				-26.7	$3s$	O
			6.2	$1s$	H				-6.8	$2p_y$	H
-7.16	5	$1b_1$	93.9	$2p_x$	O				6.8	$2s$	O
			5.4	$2p_x$	H	9.86	11	$2b_1$*	84.9	$3p_x$	O
-0.84	6	$4a_1$*	50.9	$2s$	H				12.5	$2p_x$	H
			31.9	$1s$	H						
			5.4	$2p_y$	H						
5.95	8	$5a_1$*	50.2	$2s$	H						
			44.1	$1s$	H						
			13.1	$2p_z$	O						
			-10.7	$3s$	O						
			7.5	$2s$	O						
			-6.9	$3p_z$	O						

[a] Includes FOs which constitute more than 5.0 % of the MO.

Bibliography

[1]   Morino, Y.; Kuchitsu, K.; Moritani, T. *Inorganic Chemistry* **1969**, *8*, 867.

[2]   Hehre, W. J.; Radom, L.; Schleyer, P. v. R.; Pople, J. A. *Ab Initio Molecular Orbital Theory*; John Wiler & Sons: Toronto, 1986.

Appendix C

Supporting Information - Solid-State ^{23}Na NMR, X-ray Diffraction and Theoretical Studies upon the Polymeric Sodium Metallocenes CpNa and CpNa·THF

C.1 Supporting Experimental Information

C.1.1 MQMAS Experimental Details

2D MQMAS[1,2] experiments were used to resolve the two distinct powder patterns in a mixed sample of CpNa and CpNa·THF. The MQMAS variant applied here uses amplitude-modulated pulses during the triple- to single-quantum coherence conversion. High power ($v_1(^{23}$Na$) \approx 150$ kHz) 3Q excitation and 3Q – 1Q coherence transfer pulse widths of 3.4 and 0.9 μs were used. MQMAS experiments were conducted at $v_{rot} = 14$ kHz with quarter-rotor synchronization in the indirect dimension, yielding a spectral width in the indirect dimension of 56 kHz. 48 transients were collected and averaged per t_2 slice, with 128 t_1 points comprising the indirect dimension. With a calibrated recycle delay of 6 s, the total acquisition time was ca. 20 hours. Spectra were processed using the hypercomplex method[3] with appropriate shearing.

C.1.2 MQMAS Results and Discussion

MQMAS NMR experiments were conducted at $B_0 = 9.4$ T, in the hopes that the ^{23}Na EFG tensor parameters of the solvated species could be measured more accurately and to determine the presence of any additional signals which might be unresolvable in the one-dimensional experiments. After extracting the row of data corresponding to the CpNa·THF pattern, analytical simulations produce ^{23}Na EFG tensor parameters which are in reasonable agreement with the parameters isolated

-209-

in earlier experiments (C_Q = 1.84(4); η_Q = 0.31(4); see Figure C.1.2.1). The small differences

between the two sets of experimental data can be partially attributed to frictional heating caused by

rotating the sample at the magic angle, as the MQMAS experiment was conducted at 14 kHz, while

the MAS experiment used v_{rot} = 10 kHz. While nominal sample heating is expected at the lower

spinning frequency, substantially more heating is to be expected at the higher spin rate.[4] As

CpNa·THF exhibits very pronounced temperature-dependent ^{23}Na EFG tensor parameters, these

modest temperature differences may cause measurable differences in the observed powder pattern

shapes. In fact, if one considers the ^{23}Na MAS parameters isolated in the MQMAS experiment with

those observed for CpNa·THF at T = 323 K in a previous report[5] (see Table C.1.2.1) it is seen that

the observed data compare rather well. The MQMAS experiment was also unable to adequately

resolve the suspected impurity phase.
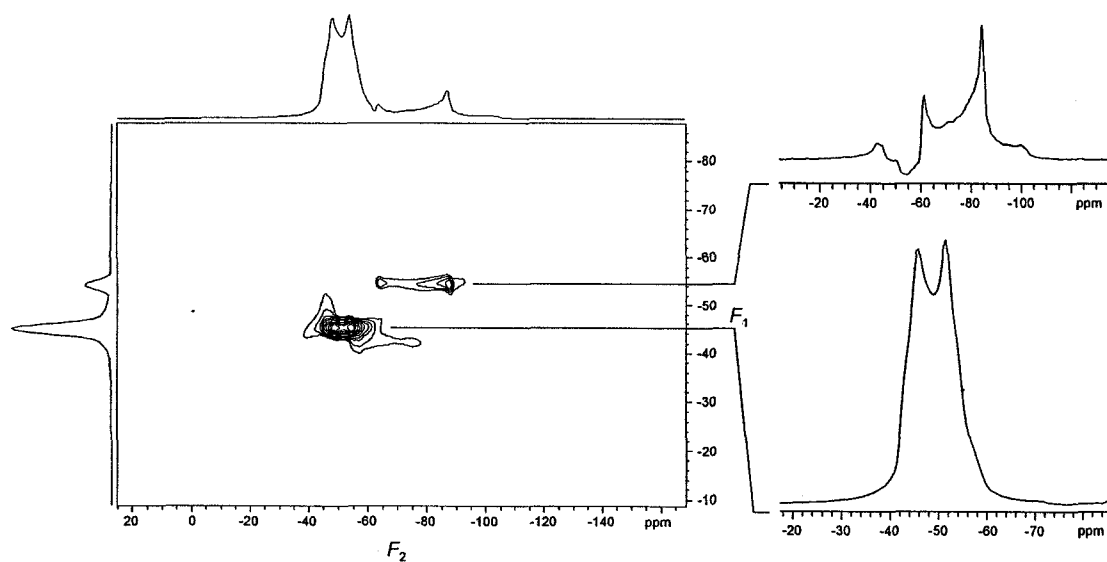
Figure C.1.2.1 Solid-state 3QMAS ^{23}Na NMR spectrum of a mixed CpNa/CpNa·THF sample (left) acquired at v_{rot} = 14 kHz. Two sodium sites are resolvable and analytical WSolids simulations (not shown) produce parameters which closely match CpNa (top right) and CpNa·THF (bottom right).

-210-

Table C.1.2.1 Additional Experimental Sodium CS and EFG Tensor Parameters [a]

experiment	temp (K)	C_Q (MHz)	η_Q	Ω (ppm)	κ	δ_{iso} (ppm)
CpNa·THF						
3QMAS [b]	293	1.84(4)	0.31(4)	—	—	–44.7(5)
MAS [c]	323	1.82	0.34	—	—	–44.7
CpNa						
3QMAS [b]	293	2.98(5)	0.04(4)	—	—	–57.0(5)
MAS [c]	323	2.99	0.03	—	—	–57.0

[a] Parameter definitions can be found in chapter 1.
[b] MAS frequency, $v_{rot} = 14$ kHz. [c] taken from literature, see reference .
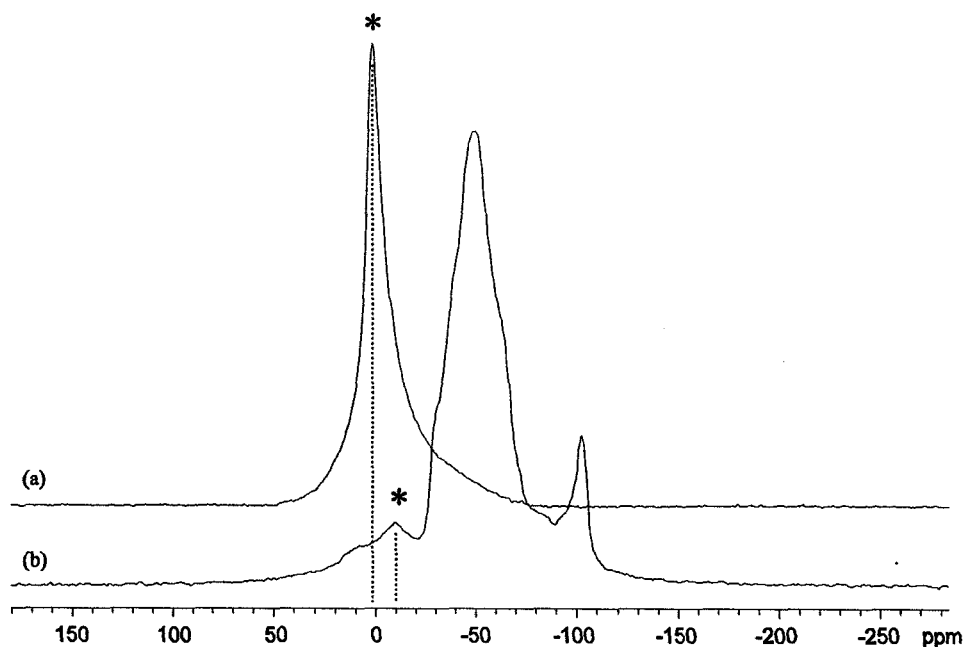
Figure C.1.3 Static solid-state ^{23}Na NMR spectra of a mixed CpNa/CpNa·THF sample both before (b) and after (a) exposure to air and moisture. Before exposure, a suspected impurity phase is observed at $\delta(^{23}$Na$) = -9.6$ ppm (asterisk in (a)), which shifts to +1.6 ppm (asterisk in (b)) after exposure to air and moisture for 2 h.

-211-
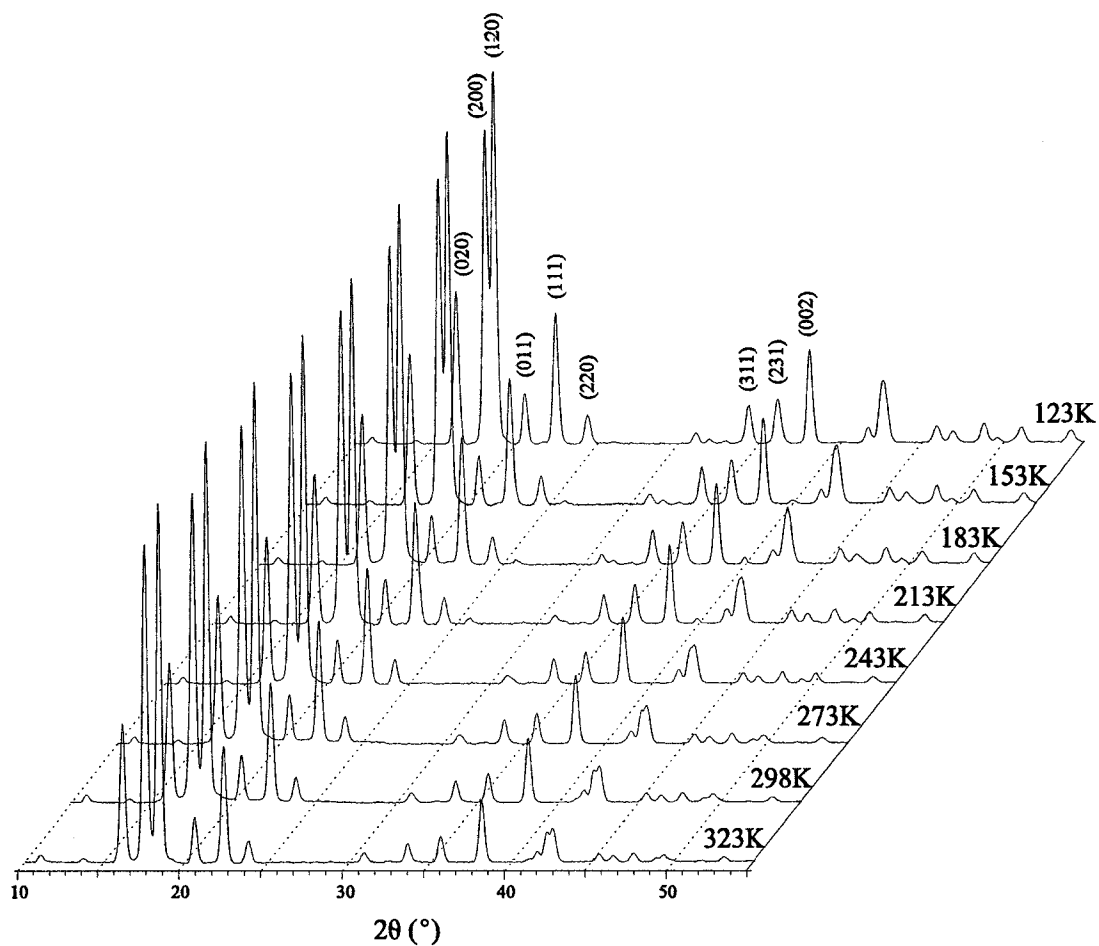
Figure C.1.4 Powder XRD spectra of a pure sample of CpNa acquired over the temperature range $T = 123 - 323$ K shows that there is a slight temperature-dependence of the a and b unit cell parameters.

-212-

(a)

CpNa Unit Cell Length (*c*) vs. Temperature

(b)

Cell Volume vs. Temperature
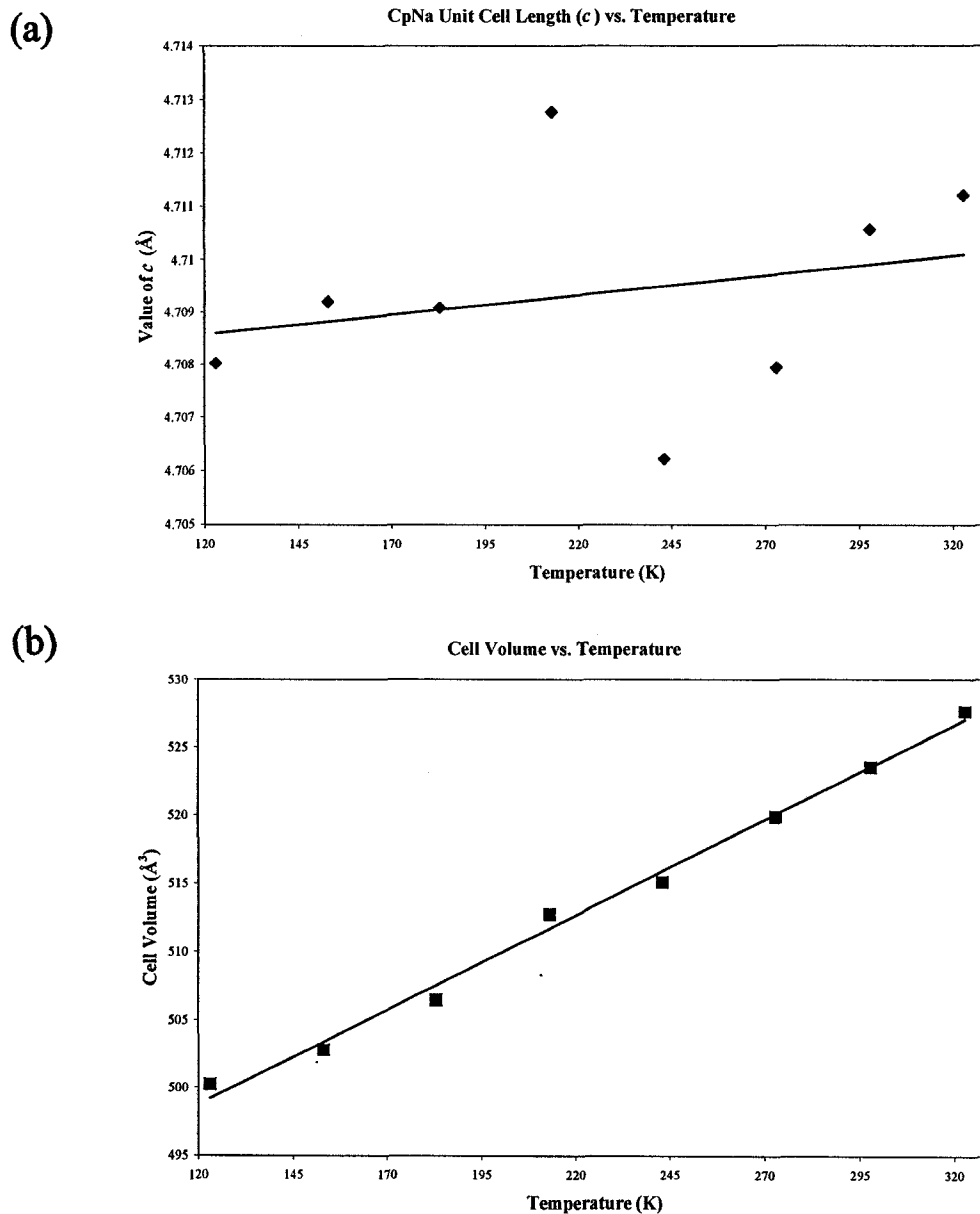
Figure C.1.5 According to VT pXRD data acquired for CpNa, (a) the c (◆) unit cell length is not a function of temperature ($R^2 = 0.0651$), but due to the temperature dependence of a and b, (b) the unit cell volume (■) is a linear function of temperature ($V(\text{Å}^3) = 0.139T(\text{K}) + 482.049$; $R^2 = 0.9932$).

-213-
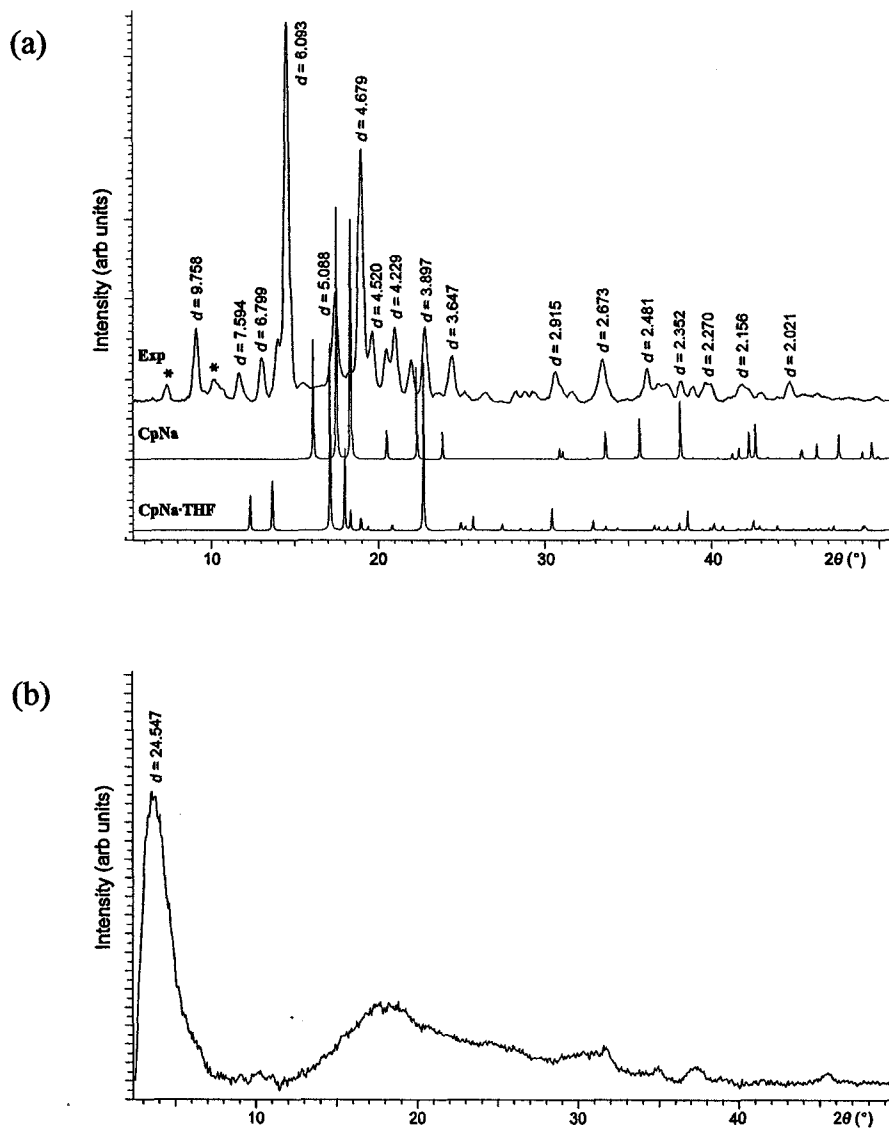
Figure C.1.6 pXRD spectra of a sample of CpNa/CpNa·THF both (a) before and (b) after exposure to air and moisture. (a) clearly shows that the experimental pXRD spectrum of the mixed sample (top trace) cannot be readily interpreted as a linear combination of the pXRD spectra that should be produced by pure CpNa (middle trace) and pure CpNa·THF (bottom trace). Asterisks highlight peaks which are thought to correspond to an impurity phase. After the sample is exposed to air and moisture for ca. 2 h, (b) the microcrystalline structure degrades nearly completely, resulting in a pXRD spectrum composed of one broad peak at $2\theta = 3.60°$.

-214-

C.2 Supporting Theoretical Information

C.2.1 CpNa·THF Cluster Coordinates Used for Theoretical Calculations

Table C.2.1.1 Standard Orientation of [Cp₂Na·THF]⁻ Cluster (Cartesian)

atom	x (Å)	y (Å)	z (Å)	atom	x (Å)	y (Å)	z (Å)
Na	0.723382	0.002173	−0.024575	H	−0.449758	3.003138	0.642601
O	−1.596602	−0.013557	−0.021493	H	1.305364	−2.316273	2.089563
C	2.264173	−2.041348	−0.822360	H	1.440598	2.350558	2.085474
C	0.811078	2.584323	−0.918399	H	0.552229	−2.734753	−1.819948
C	2.527386	−1.889355	0.497317	H	2.660138	1.983198	−1.709837
C	0.389946	2.718582	0.361661	H	−0.332994	−3.067316	0.441908
C	1.419674	−2.309619	1.166290	H	3.294601	1.690016	0.639995
C	1.433331	2.354062	1.155163	H	−2.103274	0.556062	1.750462
C	0.981277	−2.551673	−1.015150	H	−2.212032	−0.997771	1.518965
C	2.132269	2.141480	−0.960435	C	−3.786337	0.029296	0.723560
C	0.504573	−2.719263	0.237679	C	−3.804256	0.062256	−0.699019
C	2.469330	1.994979	0.339503	H	−2.291568	−1.069767	−1.479076
C	−2.353667	−0.129142	1.111109	H	−2.137699	0.461492	−1.812660
C	−2.389588	−0.172679	−1.122658	H	−4.312787	−0.715975	1.053775
H	2.857682	−1.833958	−1.509021	H	−4.149663	0.851521	1.088132
H	0.290805	2.762851	−1.669538	H	−4.118290	0.923094	−1.016097
H	3.313275	−1.562663	0.872365	H	−4.386143	−0.630306	−1.050360

Table C.2.1.2. Standard Orientation of [Cp₂Na₃·3THF]⁺ Cluster (Cartesian)

atom	x (Å)	y (Å)	z (Å)	atom	x (Å)	y (Å)	z (Å)
Na	−0.055855	1.580008	−0.104233	H	2.949534	2.691552	0.643617
O	−0.060472	3.894716	0.052875	C	2.290552	0.781785	1.029284
C	−0.174396	4.575467	1.233084	H	2.286327	0.712804	1.956853
C	−0.213880	4.759835	−0.993426	C	2.078299	0.225908	−1.128555
H	0.507559	4.279805	1.855369	H	1.919721	−0.250238	−1.911579
H	−1.044400	4.411320	1.629405	C	−4.676592	−3.079171	1.172443
C	−0.009361	6.029895	0.941751	C	4.644951	−2.883490	1.163918
C	0.027096	6.142086	−0.476451	H	−4.007415	−2.765890	1.799958
H	−1.110806	4.690090	−1.356836	H	5.314127	−2.570209	1.791432
H	0.419345	4.551193	−1.697733	H	−5.552573	−2.958491	1.571210
H	−0.751734	6.536921	1.305140	H	3.768969	−2.762810	1.562685
H	0.814901	6.364202	1.330807	C	1.927926	−0.195999	0.145923
H	0.889978	6.472261	−0.770758	H	1.618491	−1.037897	0.390519
H	−0.662988	6.749382	−0.789356	C	−4.450798	−4.520179	0.856241

-215-

atom	x (Å)	y (Å)	z (Å)	atom	x (Å)	y (Å)	z (Å)
C	−2.105347	0.105611	−1.005463	C	4.870745	−4.324498	0.847716
H	−1.899608	−0.442022	−1.727665	H	−5.171118	−5.064063	1.210604
C	−1.957819	−0.246383	0.294029	H	4.150425	−4.868382	1.202079
C	−2.609183	1.400960	−1.113360	H	−3.613098	−4.826247	1.239797
H	−1.634640	−1.056030	0.616533	H	5.708444	−4.630566	1.231272
C	−2.373022	0.817510	1.034694	C	−4.410188	−4.606377	−0.563664
H	−2.787877	1.883408	−1.888151	C	4.911354	−4.410696	−0.572190
C	−2.776662	1.794244	0.168120	H	−3.534312	−4.894963	−0.863286
H	−2.379802	0.870318	1.963309	H	5.787230	−4.699283	−0.871812
H	−3.121053	2.618098	0.427023	H	−5.074293	−5.236623	−0.887198
Na	−4.684288	−0.058857	−0.113206	H	4.247249	−5.040942	−0.895724
Na	4.637254	0.136824	−0.121731	C	−4.709110	−3.226778	−1.056919
O	−4.591750	−2.374078	0.004136	C	4.612433	−3.031097	−1.065444
O	4.729793	−2.178397	−0.004389	H	−5.608303	−3.188490	−1.419400
C	2.527394	1.539208	−0.998253	H	3.713239	−2.992809	−1.427926
H	2.709720	2.107308	−1.710873	H	−4.085448	−2.979697	−1.757311
C	2.660496	1.874717	0.307144	H	5.236094	−2.784016	−1.765837

Table C.2.1.3 Standard Orientation of Cp₃Na₃·3THF Cluster (Cartesian)

atom	x (Å)	y (Å)	z (Å)	atom	x (Å)	y (Å)	z (Å)
Na	0.790188	1.550874	−0.093384	H	−0.381979	4.306480	1.647799
Na	−3.712543	−0.407012	−0.072170	H	−4.365116	−3.359992	1.616946
Na	5.572351	0.438738	−0.142600	H	4.919778	−2.514242	1.546516
O	0.625086	3.859634	0.064578	C	−1.937064	1.574733	0.197129
O	−3.457874	−2.710117	0.043727	C	−6.390196	−0.928078	0.213372
O	5.827020	−1.864367	−0.026703	C	2.894698	−0.082328	0.142943
C	−1.157365	−0.063058	−0.981494	H	−2.336379	2.372571	0.458610
C	−5.920918	0.844611	−0.934144	H	2.646408	−0.943742	0.389290
C	3.363976	1.690362	−1.004573	C	0.532978	5.993269	0.953857
H	−0.918722	−0.595075	−1.705245	C	−3.161822	−4.841057	0.894109
H	−5.783432	1.423974	−1.647757	C	6.123072	−3.995306	0.823680
H	3.501462	2.269724	−1.718187	H	−0.240534	6.447287	1.322355
C	−0.976983	−0.403758	0.316862	H	5.444840	−4.588097	1.182629
C	−5.802869	1.188732	0.370459	H	1.334470	6.384328	1.337544
C	3.482026	2.034483	0.300029	H	−2.302271	−5.087874	1.271978
H	−0.595948	−1.188842	0.636920	C	0.552074	6.107578	−0.464516
H	−5.569308	2.023783	0.705295	C	−3.124750	−4.924363	−0.526066
H	3.715587	2.869534	0.634865	C	6.160145	−4.078613	−0.596495
C	−1.460482	0.628644	1.060651	H	1.387831	6.497136	−0.764435
C	−6.090819	0.072724	1.094652	H	−2.232883	−5.151151	−0.831607
C	3.194075	0.918475	1.024223	H	−0.180778	6.665198	−0.772608
H	−1.464749	0.680950	1.989309	H	5.539504	−4.753705	−0.915832

atom	x (Å)	y (Å)	z (Å)	atom	x (Å)	y (Å)	z (Å)
H	−6.084045	0.003716	2.022204	C·	0.404715	4.711824	−0.980371
H	3.200849	0.849467	1.951774	C	−3.522500	−3.569043	−1.016829
C	−1.751081	1.193959	−1.085577	C	5.762394	−2.723293	−1.087258
C	−6.278122	−0.496843	−1.061927	H	−0.487556	4.579614	−1.337834
C	3.006773	0.348908	−1.132356	H	−4.424566	−3.593642	−1.373310
H	−1.968162	1.662676	−1.858990	H	4.860328	−2.747891	−1.443740
H	−6.408293	−0.982979	−1.844049	H	1.046254	4.547808	−1.688946
H	2.876602	−0.137228	−1.914479	H	−2.922279	−3.279115	−1.721264
C	0.471791	4.530901	1.245762	H	6.362615	−2.433364	−1.791693
C	−3.485522	−3.419286	1.212320	H	−6.638486	−1.789493	0.459720
C	5.799372	−2.573536	1.141891	H	−3.840054	−5.433848	1.253059
H	1.176845	4.283620	1.863393	H	−3.745390	−5.599455	−0.845402
H	−2.835678	−3.06000	1.835484	H	6.982624	−4.242124	1.201548
H	6.449216	−2.214249	1.765054	H	7.052011	−4.305401	−0.902037

Table C.2.1.4 Standard Orientation of [Cp$_4$Na$_3$·3THF]$^-$ Cluster (Cartesian)

atom	x (Å)	y (Å)	z (Å)	atom	x (Å)	y (Å)	z (Å)
Na	−0.019450	1.387429	−0.070385	C	−7.396198	−0.433997	0.181015
O	0.023360	3.701325	0.092813	O	4.688065	−2.468601	0.020930
C	−2.098448	−0.042245	−0.976076	C	7.225150	−0.037795	−0.981430
C	2.562722	1.295996	−0.963773	C	7.365916	−0.395172	0.317184
C	−1.957682	−0.399621	0.322537	C	6.971442	0.674088	1.060317
C	2.703165	1.624296	0.342529	C	6.748026	1.267895	−1.086061
C	−2.352155	0.669638	1.065671	C	6.588215	1.661166	0.196402
C	2.309706	0.538272	1.061496	C	−4.735216	−3.179320	1.192707
C	−2.575571	1.263446	−1.080707	C	−4.769999	−3.320376	−1.037045
C	2.086827	−0.007469	−1.097659	C	4.588381	−3.174871	1.187353
C	−2.735383	1.656716	0.201755	C	4.553598	−3.315926	−1.042399
C	1.927399	−0.429547	0.175661	H	−4.059037	−2.881480	1.821234
C	−0.076976	4.381169	1.274778	H	−5.608673	−3.041745	1.591540
C	−0.111915	4.572152	−0.951251	C	−4.537980	−4.623821	0.872777
H	0.599490	4.069947	1.896476	C	−4.499606	−4.707106	−0.547339
H	−0.950299	4.233862	1.670417	H	−5.668095	−3.262699	−1.399681
C	0.118896	5.832665	0.987320	H	−4.140233	−3.084301	−1.736607
C	0.157187	5.947808	−0.430571	H	5.264560	−2.877030	1.815880
H	−1.009960	4.521776	−1.315098	H	3.714924	−3.037295	1.586187
H	0.518065	4.352416	−1.655924	C	4.785617	−4.619372	0.867423
H	−0.613983	6.353856	1.351831	C	4.823991	−4.702657	−0.552692
H	0.948770	6.148971	1.377490	H	3.655502	−3.258249	−1.405035
H	1.026760	6.260984	−0.723762	H	5.183364	−3.079851	−1.741961
H	−0.519259	6.569951	−0.742073	H	−5.270365	−5.153744	1.225502
Na	−4.680523	−0.156119	−0.084990	H	−3.707805	−4.948015	1.255765

-217-

atom	x (Å)	y (Å)	z (Å)	atom	x (Å)	y (Å)	z (Å)
H	-1.903742	-0.592062	-1.701719	H	-3.629732	-5.012811	-0.847469
H	-1.652217	-1.217552	0.642990	H	-5.175459	-5.322745	-0.872720
H	-2.359096	0.720133	1.994620	H	4.053232	-5.149295	1.220149
H	-2.744998	1.751490	-1.854276	H	5.615792	-4.943565	1.250412
H	-3.062889	2.486778	0.462728	H	5.693865	-5.008361	-0.852823
Na	4.643075	-0.151669	-0.090344	H	4.148138	-5.318295	-0.878073
H	2.756902	1.862128	-1.676903	H	-6.566695	1.857678	-1.671549
H	3.007853	2.435123	0.681244	H	-6.315744	2.430673	0.686598
H	2.302823	0.466954	1.989079	H	-7.020774	0.462504	1.994433
H	1.917851	-0.478205	-1.881979	H	-7.405746	-0.482655	-1.876625
H	1.600677	-1.265560	0.417952	H	-7.722920	-1.270010	0.423306
O	-4.635533	-2.473051	0.026284	H	7.419855	-0.587613	-1.707073
C	-6.760876	1.291546	-0.958419	H	7.671370	-1.213102	0.637636
C	-6.620432	1.619846	0.347883	H	6.964501	0.724583	1.989266
C	-7.013891	0.533822	1.066850	H	6.578599	1.755939	-1.859630
C	-7.236770	-0.011919	-1.092306	H	6.260708	2.491228	0.457374

C.2.2 Calculated SCF Energies for CpNa·THF Clusters

Table C.2.2.1 Standard Basis Sets on All Atoms

cluster	method	basis	SCF energy (Hartrees)
[Cp$_2$Na·THF]$^-$	RHF	6-31G**	-777.00686148
[Cp$_2$Na·THF]$^-$	RHF	6-311G**	-777.14178206
[Cp$_2$Na·THF]$^-$	RHF	6-311+G**	-777.15221449
[Cp$_2$Na·THF]$^-$	RHF	6-311++G**	-777.15254313
[Cp$_2$Na·THF]$^-$	B3LYP	6-31G**	-781.51619569
[Cp$_2$Na·THF]$^-$	B3LYP	6-311G**	-781.68854119
[Cp$_2$Na·THF]$^-$	B3LYP	6-311+G**	-781.69950179
[Cp$_2$Na·THF]$^-$	B3LYP	6-311++G**	-781.69986793
[Cp$_2$Na$_3$·3THF]$^+$	RHF	6-31G**	-1562.45484519
[Cp$_2$Na$_3$·3THF]$^+$	RHF	6-311G**	-1562.68060147
[Cp$_2$Na$_3$·3THF]$^+$	RHF	6-311+G**	-1562.68773499
[Cp$_2$Na$_3$·3THF]$^+$	B3LYP	6-31G**	-1570.72922991
[Cp$_2$Na$_3$·3THF]$^+$	B3LYP	6-311G**	-1571.01492558
[Cp$_2$Na$_3$·3THF]$^+$	B3LYP	6-311+G**	-1571.02355468
Cp$_3$Na$_3$·3THF	RHF	6-31G**	-1754.66592541
Cp$_3$Na$_3$·3THF	RHF	6-311G**	-1754.93291602
Cp$_3$Na$_3$·3THF	RHF	6-311+G**	-1754.94788410
Cp$_3$Na$_3$·3THF	B3LYP	6-31G**	-1764.25612999
Cp$_3$Na$_3$·3THF	B3LYP	6-311G**	-1764.59932390
Cp$_3$Na$_3$·3THF	B3LYP	6-311+G**	-1764.61128316
[Cp$_4$Na$_3$·3THF]$^-$	RHF	6-31G**	-1946.83900528

-218-

cluster	method	basis	SCF energy (Hartrees)
[Cp$_4$Na$_3$·3THF]$^-$	RHF	6-311G**	−1947.14336018
[Cp$_4$Na$_3$·3THF]$^-$	RHF	6-311+G**	−1947.16268972
[Cp$_4$Na$_3$·3THF]$^-$	B3LYP	6-31G**	−1957.74307042
[Cp$_4$Na$_3$·3THF]$^-$	B3LYP	6-311G**	−1958.12976775
[Cp$_4$Na$_3$·3THF]$^-$	B3LYP	6-311+G**	−1958.15305562

Table C.2.2.2 A Well-Tempered Basis Set (WTBS) on Sodium Atoms

cluster	method	basis	SCF energy (Hartrees)
[Cp$_2$Na·THF]$^-$	RHF	6-311G**	−777.14801320
[Cp$_2$Na·THF]$^-$	RHF	6-311+G**	−777.16309318
[Cp$_2$Na·THF]$^-$	B3LYP	6-311G**	−781.69012092
[Cp$_2$Na·THF]$^-$	B3LYP	6-311+G**	−781.70788959
[Cp$_2$Na$_3$·3THF]$^+$	RHF	6-311G**	−1562.70505624
[Cp$_2$Na$_3$·3THF]$^+$	RHF	6-311+G**	−1562.72046587
[Cp$_2$Na$_3$·3THF]$^+$	B3LYP	6-311G**	−1571.02475712
[Cp$_2$Na$_3$·3THF]$^+$	B3LYP	6-311+G**	−1571.04741793
Cp$_3$Na$_3$·3THF	RHF	6-311G**	−1754.95981356
Cp$_3$Na$_3$·3THF	RHF	6-311+G**	−1754.98043000
Cp$_3$Na$_3$·3THF	B3LYP	6-311G**	−1764.60843634
Cp$_3$Na$_3$·3THF	B3LYP	6-311+G**	−1764.63525187

C.2.3 Optimized Na(OH$_2$)$_6^+$ Coordinates

Table C.2.3.1 Standard Basis Sets on All Atoms (O_h Symmetry)

method	basis	r(Na–O) (Å)	r(O–H) (Å)	∠(H-O-H) (°)
RHF	6-31G**	2.3901	0.9439	107.06
RHF	6-311G**	2.3886	0.9422	106.75
RHF	6-311+G**	2.4060	0.9428	106.80
RHF	6-311++G**	2.4054	0.9427	106.78
B3LYP	6-31G**	2.3576	0.9647	105.85
B3LYP	6-311G**	2.3581	0.9621	105.96
B3LYP	6-311+G**	2.3865	0.9630	105.96
B3LYP	6-311++G**	2.3861	0.9630	105.96

C.2.4 Additional Basis Set/Methodology Combinations

Table C.2.4.1 Experimental & Theoretical ^{23}Na EFG Tensor Parameters for CpNa·THF ^{a}

cluster	basis set	V_{11} (au)	V_{22} (au)	V_{33} (au)	$|C_Q|$ (MHz)	η_Q
Experimental						
CpNa·THF	MAS - RT	—	—	—	1.82(2)	0.37(2)
CpNa·THF	MAS - 183 K	—	—	—	1.79	0.61
CpNa·THF	MAS - 153 K	—	—	—	1.78	0.70
RHF						
[Cp$_2$Na·THF]$^-$	6-31G**	0.0407	0.0483	−0.0890	2.204	0.0862
[Cp$_2$Na$_3$·3THF]$^+$	6-31G**	0.0267	0.0696	−0.0963	2.386	0.4446
Cp$_3$Na$_3$·3THF	6-31G**	0.0313	0.0641	−0.0954	2.363	0.3440
[Cp$_4$Na$_3$·3THF]$^-$	6-31G**	0.0379	0.0577	−0.0956	2.368	0.2075
[Cp$_2$Na·THF]$^-$	6-311++G**	0.0395	0.0791	−0.1186	2.937	0.3337
B3LYP						
[Cp$_2$Na·THF]$^-$	6-31G**	0.0125	0.0533	−0.0658	1.630	0.6194
[Cp$_2$Na$_3$·3THF]$^+$	6-31G**	−0.0050	−0.0733	0.0783	1.939	0.8722
Cp$_3$Na$_3$·3THF	6-31G**	−0.0002	−0.0710	0.0712	1.764	0.9932
[Cp$_4$Na$_3$·3THF]$^-$	6-31G**	0.0065	0.0649	−0.0713	1.766	0.8190
[Cp$_2$Na·THF]$^-$	6-311++G**	0.0359	0.0781	−0.1139	2.821	0.3705

^{a} Using standard (i.e., WTBS were not employed) basis sets on all atoms. Parameter definitions can be found in chapter 1.

Table C.2.4.2 Experimental & Theoretical ^{23}Na EFG Tensor Parameters for CpNa·THF ^{a}

cluster	basis set	V_{11} (au)	V_{22} (au)	V_{33} (au)	$|C_Q|$ (MHz)	η_Q
Experimental						
CpNa·THF	MAS - RT	—	—	—	1.82(2)	0.37(2)
CpNa·THF	MAS - 183 K	—	—	—	1.79	0.61
CpNa·THF	MAS - 153 K	—	—	—	1.78	0.70
B3LYP						
[Cp$_2$Na·THF]$^-$	6-311G**	0.0061	0.0370	−0.0431	1.067	0.7158
[Cp$_2$Na$_3$·3THF]$^+$	6-311G**	−0.0096	−0.0433	0.0529	1.311	0.6355
Cp$_3$Na$_3$·3THF	6-311G**	−0.0076	−0.0421	0.0497	1.230	0.6938
[Cp$_2$Na·THF]$^-$	6-311+G**	0.0103	0.0249	−0.0352	0.872	0.4129
[Cp$_2$Na$_3$·3THF]$^+$	6-311+G**	−0.0204	−0.0407	0.0611	1.514	0.3313
Cp$_3$Na$_3$·3THF	6-311+G**	−0.0172	−0.0369	0.0541	1.341	0.3648

^{a} Using a WTBS on the sodium atom(s).

-220-

C.2.5 Additional Information - Reconciliation of VT Data for CpNa
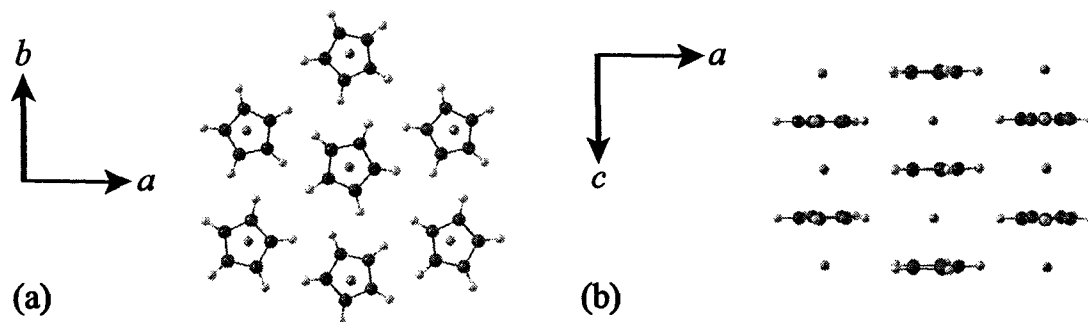
Figure C.2.5.1 The medium-range structure of CpNa shows (a) that each CpNa chain is proximate to six other chains and (b) that adjacent columns are staggered if one chooses to view an orientation perpendicular to the ac-crystallographic plane.

Table C.2.5.1 Theoretical ^{23}Na EFG Tensor Parameters - ECMO calculations on CpNa [a]

Temp [b] (K)	# of charges	V_{11} (au)	V_{22} (au)	V_{33} (au)	$|C_Q|$ (MHz)	η_Q
323	158	−0.0495	−0.0505	0.1001	2.478	0.0097
298	158	−0.0487	−0.0513	0.1000	2.476	0.0260
273	158	−0.0480	−0.0520	0.1000	2.476	0.0393
243	164	−0.0483	−0.0533	0.1016	2.515	0.0494
213	164	−0.0465	−0.0548	0.1013	2.508	0.0818
183	166	−0.0448	−0.0562	0.1011	2.503	0.1126
153	166	−0.0441	−0.0568	0.1009	2.499	0.1264
123	170	−0.0432	−0.0576	0.1008	2.495	0.1430

[a] ECMO calculations used a $Cp_2Na_3^+$ cluster, the RHF method and 6-311G** basis set on all atoms.
[b] The lengths of the a- and b-axes were varied so that they matched the pXRD-derived experimental values for the temperature shown.
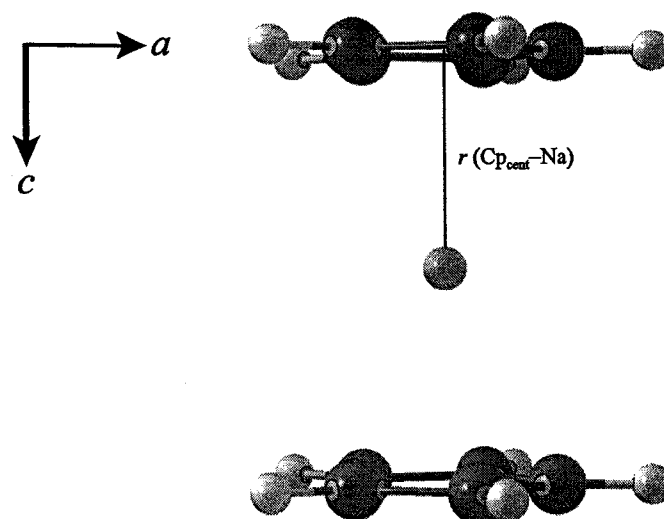
Figure C.2.5.2 Pictorial representation of moving the central sodium atom towards the centroid of one Cp ring (nearly along the c-axis of the unit cell).

Table C.2.5.2 Theoretical ^{23}Na EFG Tensor Parameters - Towards Cp Ring (CpNa) [a]

$r(Cp_{cent}-Na)$ (Å)	V_{11} (au)	V_{22} (au)	V_{33} (au)	$\lvert C_Q \rvert$ (MHz)	η_Q
2.357	−0.0585	−0.0590	0.1175	2.910	0.0039
2.327	−0.0584	−0.0589	0.1173	2.905	0.0039
2.297	−0.0581	−0.0586	0.1167	2.891	0.0040
2.267	−0.0576	−0.0581	0.1158	2.867	0.0041
2.237	−0.0570	−0.0574	0.1144	2.834	0.0045
2.207	−0.0561	−0.0566	0.1127	2.791	0.0050
2.177	−0.0550	−0.0556	0.1106	2.738	0.0056
2.147	−0.0537	−0.0543	0.1080	2.675	0.0064
2.117	−0.0521	−0.0529	0.1050	2.599	0.0075
2.087	−0.0503	−0.0512	0.1014	2.512	0.0089
2.057	−0.0482	−0.0492	0.0974	2.412	0.0107
2.027	−0.0458	−0.0470	0.0928	2.297	0.0130
1.997	−0.0431	−0.0445	0.0876	2.168	0.0162
1.967	−0.0400	−0.0417	0.0817	2.024	0.0207
1.937	−0.0366	−0.0386	0.0752	1.862	0.0272
1.907	−0.0327	−0.0352	0.0680	1.684	0.0368
1.877	−0.0285	−0.0316	0.0601	1.487	0.0522
1.847	−0.0237	−0.0277	0.0514	1.274	0.0789

[a] Calculations used a Cp_2Na^- cluster, the RHF method and 6-311G** basis set on all atoms.

-222-
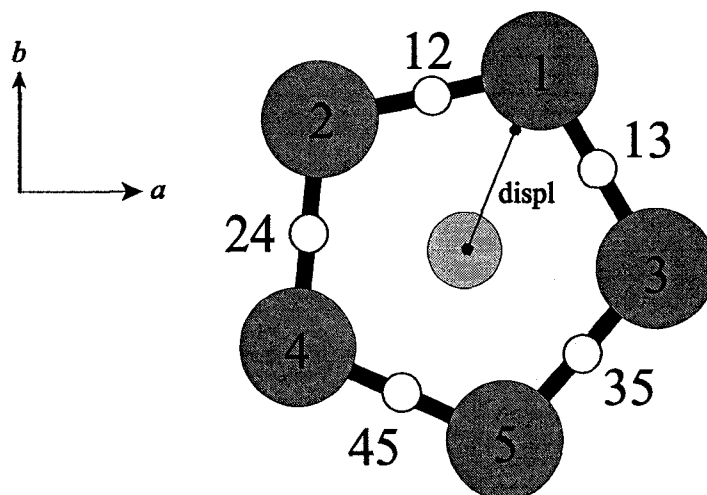
Figure C.2.5.3 Schematic of a single Cp_2Na^- cluster, as viewed along the c-axis of the unit cell. Calculations were carried out in which the central sodium atom was moved in the ab-plane along a number of different directions. The sodium atom was moved in small steps towards points which had identical ab-coordinates as the five unique carbon atoms (1,2,3,4,5) as well as the midpoints of the C-C bonds (12,13,24,35,45), while always maintaining the initial c coordinate of the sodium atom.

Table C.2.5.3 Theoretical ^{23}Na EFG Parameters - ab-plane - "Towards" 1 (CpNa)

displ ^{a} (Å)	V_{11} (au)	V_{22} (au)	V_{33} (au)	$|C_Q|$ (MHz)	η_Q	E (Hartrees)
0.02	−0.0584	−0.0585	0.1169	2.894	0.0009	−546.434184
0.04	−0.0582	−0.0583	0.1166	2.887	0.0006	−546.434279
0.06	−0.0583	−0.0583	0.1166	2.888	0.0004	−546.434273
0.08	−0.0584	−0.0586	0.1171	2.899	0.0017	−546.434242
0.10	−0.0586	−0.0592	0.1178	2.918	0.0054	−546.434185
0.12	−0.0588	−0.0601	0.1189	2.946	0.0107	−546.434101
0.14	−0.0592	−0.0613	0.1204	2.982	0.0175	−546.433992
0.16	−0.0595	−0.0627	0.1222	3.027	0.0256	−546.433857
0.18	−0.0600	−0.0644	0.1244	3.080	0.0350	−546.433697
0.20	−0.0605	−0.0663	0.1268	3.141	0.0453	−546.433511

^{a} Displacement from crystallographic position. The direction is determined using the diagram in above Figure.

-223-

Table C.2.5.4 Theoretical ^{23}Na EFG Parameters - *ab*-plane - "Towards" 2 (CpNa)

Displ (Å)	V_{11} (au)	V_{22} (au)	V_{33} (au)	$|C_Q|$ (MHz)	η_Q	E (Hartrees)
0.02	−0.0585	−0.0590	0.1175	2.909	0.0042	−546.434213
0.04	−0.0585	−0.0593	0.1178	2.917	0.0062	−546.434189
0.06	−0.0586	−0.0598	0.1185	2.934	0.0098	−546.434139
0.08	−0.0589	−0.0606	0.1195	2.959	0.0148	−546.434063
0.10	−0.0591	−0.0617	0.1208	2.993	0.0211	−546.433961
0.12	−0.0595	−0.0630	0.1225	3.035	0.0288	−546.433833
0.14	−0.0600	−0.0646	0.1246	3.086	0.0377	−546.433680
0.16	−0.0605	−0.0665	0.1270	3.145	0.0476	−546.433502
0.18	−0.0611	−0.0686	0.1297	3.212	0.0584	−546.433298
0.20	−0.0617	−0.0710	0.1327	3.287	0.0699	−546.433070

Table C.2.5.5 Theoretical ^{23}Na EFG Parameters - *ab*-plane - "Towards" 3 (CpNa)

Displ (Å)	V_{11} (au)	V_{22} (au)	V_{33} (au)	$|C_Q|$ (MHz)	η_Q	E (Hartrees)
0.02	−0.0585	−0.0589	0.1173	2.906	0.0033	−546.434224
0.04	−0.0585	−0.0590	0.1175	2.910	0.0047	−546.434211
0.06	−0.0586	−0.0595	0.1180	2.923	0.0076	−546.434172
0.08	−0.0587	−0.0602	0.1189	2.945	0.0120	−546.434107
0.10	−0.0590	−0.0611	0.1202	2.976	0.0178	−546.434016
0.12	−0.0593	−0.0623	0.1217	3.013	0.0247	−546.433903
0.14	−0.0598	−0.0639	0.1237	3.062	0.0333	−546.433757
0.16	−0.0603	−0.0657	0.1259	3.118	0.0429	−546.433589
0.18	−0.0608	−0.0677	0.1285	3.182	0.0533	−546.433396
0.20	−0.0615	−0.0699	0.1314	3.254	0.0646	−546.433179

Table C.2.5.6 Theoretical ^{23}Na EFG Parameters - *ab*-plane - "Towards" 4 (CpNa)

Displ (Å)	V_{11} (au)	V_{22} (au)	V_{33} (au)	$|C_Q|$ (MHz)	η_Q	E (Hartrees)
0.02	−0.0587	−0.0597	0.1183	2.932	0.0082	−546.434147
0.04	−0.0590	−0.0606	0.1196	2.962	0.0140	−546.434057
0.06	−0.0593	−0.0619	0.1212	3.001	0.0212	−546.433941
0.08	−0.0597	−0.0634	0.1231	3.048	0.0297	−546.433799
0.10	−0.0602	−0.0652	0.1253	3.103	0.0393	−546.433632
0.12	−0.0608	−0.0671	0.1279	3.167	0.0498	−546.433440
0.14	−0.0614	−0.0694	0.1308	3.239	0.0612	−546.433223
0.16	−0.0621	−0.0719	0.1340	3.318	0.0731	−546.432981
0.18	−0.0629	−0.0746	0.1375	3.406	0.0855	−546.432716
0.20	−0.0637	−0.0776	0.1413	3.500	0.0982	−546.432426

Table C.2.5.7 Theoretical ^{23}Na EFG Parameters - *ab*-plane - "Towards" 5 (CpNa)

Displ (Å)	V_{11} (au)	V_{22} (au)	V_{33} (au)	$|C_Q|$ (MHz)	η_Q	E (Hartrees)
0.02	-0.0587	-0.0596	0.1183	2.929	0.0074	-546.434154
0.04	-0.0589	-0.0605	0.1194	2.957	0.0131	-546.434071
0.06	-0.0592	-0.0616	0.1209	2.994	0.0200	-546.433963
0.08	-0.0596	-0.0631	0.1227	3.039	0.0281	-546.433828
0.10	-0.0601	-0.0648	0.1249	3.092	0.0375	-546.433669
0.12	-0.0606	-0.0667	0.1273	3.154	0.0478	-546.433483
0.14	-0.0612	-0.0689	0.1302	3.223	0.0589	-546.433274
0.16	-0.0619	-0.0714	0.1333	3.301	0.0707	-546.433039

Table C.2.5.8 Theoretical ^{23}Na EFG Parameters - *ab*-plane - "Towards" 13 (CpNa)

Displ (Å)	V_{11} (au)	V_{22} (au)	V_{33} (au)	$|C_Q|$ (MHz)	η_Q	E (Hartrees)
0.02	-0.0584	-0.0586	0.1170	2.897	0.0014	-546.434251
0.04	-0.0583	-0.0585	0.1168	2.892	0.0015	-546.434264
0.06	-0.0583	-0.0586	0.1169	2.896	0.0027	-546.434252
0.08	-0.0584	-0.0590	0.1175	2.909	0.0050	-546.434213
0.10	-0.0586	-0.0597	0.1183	2.931	0.0090	-546.434148
0.12	-0.0589	-0.0607	0.1196	2.961	0.0147	-546.434058
0.14	-0.0592	-0.0619	0.1211	3.000	0.0218	-546.433941
0.16	-0.0597	-0.0634	0.1230	3.047	0.0303	-546.433799
0.18	-0.0601	-0.0651	0.1253	3.103	0.0400	-546.433632
0.20	-0.0607	-0.0672	0.1279	3.166	0.0508	-546.433440

Table C.2.5.9 Theoretical ^{23}Na EFG Parameters - *ab*-plane - "Towards" 23 (CpNa)

Displ (Å)	V_{11} (au)	V_{22} (au)	V_{33} (au)	$|C_Q|$ (MHz)	η_Q	E (Hartrees)
0.02	-0.0584	-0.0586	0.1170	2.899	0.0021	-546.434244
0.04	-0.0583	-0.0586	0.1169	2.896	0.0025	-546.434251
0.06	-0.0584	-0.0588	0.1172	2.902	0.0039	-546.434232
0.08	-0.0585	-0.0593	0.1178	2.917	0.0066	-546.434187
0.10	-0.0587	-0.0600	0.1187	2.940	0.0109	-546.434116
0.12	-0.0590	-0.0610	0.1200	2.973	0.0168	-546.434019
0.14	-0.0594	-0.0623	0.1217	3.014	0.0242	-546.433896
0.16	-0.0598	-0.0639	0.1237	3.063	0.0330	-546.433748
0.18	-0.0603	-0.0657	0.1260	3.120	0.0428	-546.433574
0.20	-0.0609	-0.0678	0.1286	3.186	0.0537	-546.433376

Table C.2.5.10 Theoretical ^{23}Na EFG Parameters - ab-plane - "Towards" 35 (CpNa)

Displ (Å)	V_{11} (au)	V_{22} (au)	V_{33} (au)	$|C_Q|$ (MHz)	η_Q	E (Hartrees)
0.02	−0.0586	−0.0592	0.1178	2.918	0.0056	−546.434188
0.04	−0.0587	−0.0598	0.1185	2.935	0.0090	−546.434139
0.06	−0.0589	−0.0606	0.1195	2.960	0.0140	−546.434064
0.08	−0.0592	−0.0617	0.1209	2.994	0.0205	−546.433963
0.10	−0.0596	−0.0630	0.1226	3.036	0.0282	−546.433836
0.12	−0.0600	−0.0646	0.1247	3.087	0.0372	−546.433684
0.14	−0.0605	−0.0665	0.1270	3.146	0.0473	−546.433507
0.16	−0.0611	−0.0687	0.1297	3.213	0.0583	−546.433304
0.18	−0.0617	−0.0710	0.1328	3.288	0.0700	−546.433077
0.20	−0.0625	−0.0737	0.1361	3.371	0.0823	−546.432826

Table C.2.5.11 Theoretical ^{23}Na EFG Parameters - ab-plane - "Towards" 24 (CpNa)

Displ (Å)	V_{11} (au)	V_{22} (au)	V_{33} (au)	$|C_Q|$ (MHz)	η_Q	E (Hartrees)
0.02	−0.0586	−0.0594	0.1180	2.922	0.0064	−546.434176
0.04	−0.0588	−0.0600	0.1188	2.942	0.0105	−546.434116
0.06	−0.0590	−0.0609	0.1200	2.971	0.0162	−546.434029
0.08	−0.0593	−0.0621	0.1215	3.008	0.0232	−546.433917
0.10	−0.0597	−0.0636	0.1233	3.054	0.0315	−546.433779
0.12	−0.0602	−0.0653	0.1255	3.108	0.0410	−546.433615
0.14	−0.0607	−0.0673	0.1280	3.171	0.0515	−546.433426
0.16	−0.0613	−0.0695	0.1309	3.241	0.0628	−546.433213
0.18	−0.0620	−0.0720	0.1340	3.319	0.0749	−546.432975
0.20	−0.0627	−0.0748	0.1375	3.405	0.0874	−546.432713

Table C.2.5.12 Theoretical ^{23}Na EFG Parameters - ab-plane - "Towards" 45 (CpNa) ·

Displ (Å)	V_{11} (au)	V_{22} (au)	V_{33} (au)	$|C_Q|$ (MHz)	η_Q	E (Hartrees)
0.02	−0.0587	−0.0598	0.1185	2.935	0.0087	−546.434138
0.04	−0.0590	−0.0608	0.1190	2.968	0.0150	−546.434040
0.06	−0.0594	−0.0621	0.1215	3.010	0.0227	−546.433915
0.08	−0.0598	−0.0637	0.1235	3.060	0.0318	−546.433765
0.10	−0.0603	−0.0656	0.1259	3.118	0.0419	−546.433590
0.12	−0.0609	−0.0677	0.1286	3.185	0.0530	−546.433389
0.14	−0.0615	−0.0701	0.1316	3.259	0.0649	−546.433164
0.16	−0.0622	−0.0727	0.1349	3.341	0.0774	−546.432915
0.18	−0.0630	−0.0755	0.1385	3.431	0.0903	−546.432642
0.20	−0.0639	−0.0786	0.1425	3.528	0.1035	−546.432345

-226-

Table C.2.6 Significant σ^d Contributions to Sodium CS - CpNa, Arranged by MO [a]

ψ_p [b]	MO	σ_{11} (ppm)	σ_{22} (ppm)	σ_{33} (ppm)	σ_{iso} (ppm)	AO [c]	% AO
CpNa (D_{5h})							
1	$1a'$	376.2	376.2	376.2	376.2	$1s$	100.0
12	$3a'$	66.1	66.1	66.1	66.1	$2s$	99.8
13	$2e'(1)$	36.1	71.5	71.5	59.7	$2p_y$	99.9
14	$2e'(2)$	71.4	36.1	71.4	59.7	$2p_x$	99.9
15	$2a''$	70.7	70.7	35.9	59.0	$2p_z$	99.3
CpNa (C_{2v})							
1	$1a_1$	376.2	376.2	376.2	376.2	$1s$	100.0
12	$5a_1$	66.1	66.1	66.1	66.1	$2s$	99.8
13	$3b_2$	71.4	36.1	71.4	59.6	$2p_y$	99.9
14	$6a_1$	36.1	71.5	71.4	59.7	$2p_z$	99.9
15	$4b_1$	70.7	70.7	35.8	59.1	$2p_x$	99.4

[a] Pure DFT calculation using a Cp_2Na^- cluster, TZ2P basis on all atoms and OPBE method.

[b] Wave functions are numbered according to increasing energy, with 1 representing the lowest energy eigenstate.

[c] Atomic orbital which contributes the most character to the given MO.

Table C.2.7 Experimental & Theoretical Carbon CS Tensor Parameters for THF Ring Carbon Nuclei in CpNa·THF

cluster	site [a]	basis set	δ_{11} (ppm)	δ_{22} (ppm)	δ_{33} (ppm)	δ_{iso} (ppm)	σ_{iso} (ppm)	Ω (ppm)	κ
Experimental									
CpNa·THF	α	static - 9.4 T	—	—	—	71.0(3)/ 69.6(3)	—	—	—
	β	static - 9.4 T	—	—	—	27.6(2)	—	—	—
RHF									
[Cp$_2$Na·THF]$^-$	α	6-31G**	94.83	42.08	−20.24	38.89	158.70	115.07	0.08
	β		28.12	−19.67	−25.32	−5.62	203.21	53.44	−0.79
[Cp$_2$Na$_3$·3THF]$^+$	α	6-31G**	96.75	43.76	−20.93	39.86	157.73	117.68	0.10
	β		28.96	−20.07	−26.07	−5.72	203.31	55.04	−0.78
[Cp$_2$Na·THF]$^-$	α	6-311G**	85.28	31.99	−30.58	28.90	150.51	115.86	0.08
	β		19.00	−30.59	−36.67	−16.09	195.50	55.67	−0.78
[Cp$_2$Na·THF]$^-$	α	6-311+G**	85.96	32.81	−30.67	29.37	150.16	116.63	0.09
	β		19.38	−30.15	−36.17	−15.65	195.16	55.55	−0.78
[Cp$_2$Na·THF]$^-$	α	6-311++G**	86.05	32.70	−30.57	29.39	150.13	116.62	0.09
	β		19.37	−30.38	−36.32	−15.78	195.30	55.69	−0.79
B3LYP									
[Cp$_2$Na·THF]$^-$	α	6-31G**	112.62	56.24	−11.11	52.58	144.75	123.73	0.09
	β		41.50	−11.09	−15.87	4.85	192.48	57.37	−0.83
[Cp$_2$Na$_3$·3THF]$^+$	α	6-31G**	114.64	57.83	−12.25	53.41	143.92	126.88	0.11
	β		42.57	−11.47	−16.51	4.87	192.46	59.08	−0.83
[Cp$_2$Na·THF]$^-$	α	6-311G**	103.97	44.91	−25.76	41.04	133.74	129.73	0.09
	β		30.55	−26.86	−32.01	−9.44	184.22	62.56	−0.84
[Cp$_2$Na$_3$·3THF]$^+$	α	6-311G**	105.65	46.39	−24.77	42.42	133.37	130.42	0.09
	β		32.18	−25.55	−30.44	−7.94	183.73	62.62	−0.84
[Cp$_2$Na·THF]$^-$	α	6-311+G**	105.58	46.45	−24.87	42.39	133.40	130.45	0.09
	β		32.22	−25.44	−30.46	−7.89	183.69	62.68	−0.84

cluster	site [a]	basis set	δ_{11} (ppm)	δ_{22} (ppm)	δ_{33} (ppm)	δ_{iso} (ppm)	σ_{iso} (ppm)	Ω (ppm)	κ
[Cp$_2$Na·THF]$^-$	α	6-311++G**	105.65	46.39	−24.77	42.42	133.37	130.42	0.09
	β		32.18	−25.55	−30.44	−7.94	183.73	62.62	−0.84

[a] As outlined in the inset of figure 4.6.

-229-

Bibliography

[1]   Medek, A.; Harwood, J. S.; Frydman, L. *Journal of the American Chemical Society* **1995**, *117*, 12779.

[2]   Frydman, L.; Harwood, J. S. *Journal of the American Chemical Society* **1995**, *117*, 5367.

[3]   Massiot, D.; Touzo, B.; Trumeau, D.; Coutures, J. P.; Virlet, J.; Florian, P.; Grandinetti, P. J. *Solid State Nuclear Magnetic Resonance* **1996**, *6*, 73.

[4]   Langer, B.; Schnell, I.; Spiess, H. W.; Grimmer, A.-R. *Journal of Magnetic Resonance* **1999**, *138*, 182.

[5]   Willans, M. J.; Schurko, R. W. *Journal of Physical Chemistry B* **2003**, *107*, 5144.

Vita Auctoris

Cory M. Widdifield was born on October 8th, 1981 in Windsor, Ontario, Canada. He graduated from St. Thomas of Villanova Secondary School in June of 2000 and the University of Windsor with the degree of B. Sc[H] - Chemistry with Thesis in June of 2004. After the completion of his Master's degree requirements in late summer 2006, he will be attending Teacher's College starting September 2006.